UNIVERSITÀ DEGLI STUDI DI TRIESTE

XXIX CICLO DEL DOTTORATO DI RICERCA IN CHIMICA

NANOSTRUCTURED MATERIALS FOR ENVIRONMENTAL AND ENERGY-RELATED APPLICATIONS

Settore scientifico-disciplinare CHIM/03

DOTTORANDO

MATTEO MONAI

COORDINATORE

CHIAR. MO PROF. MAURO STENER

RELATORE

CHIAR.MO PROF. PAOLO FORNASIERO

TUTORI

CHIAR. MO PROF. RAYMOND J. GORTE

DR. TIZIANO MONTINI

ANNO ACCADEMICO 2015 / 2016

- "The most exciting phrase to hear in science […] is not 'Eureka!' but 'That's funny…'"

— Isaac Asimov

Table of Contents

0. Abstract

The world is facing an era of global environmental pollution, as a result of the tremendous population growth and the consequent massive fossil fuel-based energy consumption. A significant exploitation of renewable energies is needed to guarantee quality of human life and allow further sustainable growth, but this may take decades to happen. In order to mitigate the negative effect of human activities on the environment in the short- and mid-term, the development of more efficient technologies for emissions abatement and for renewable fuels production is imperative. Heterogeneous catalysis and photocatalysis are two key pillars of a multi-approach strategy to solve these issues.

During the last century, catalysts were explored by changing the formulation of multi-component systems in order to find the best performing material for a certain reaction. Since the late 90's, a new approach to catalytic systems improvement emerged: nano-catalysis. Exploiting the tools of nanotechnology, tailored nanostructured materials can now be produced, which show different properties in comparison to their bulky counterparts, often resulting in better catalytic performances. Furthermore, combining the elements of the periodic table in nano-alloys allows to expand the possibility of catalyst generation. Consistently with these approaches, the main focus of this thesis is the synthesis and characterization of well-defined nanostructured and hierarchical materials for environmental and energy-related applications, such as emissions control, biofuels synthesis and photocatalytic H_2 production. We show that structural control at the nanoscale is a great instrument for understanding reaction pathways, for studying the nature of catalytic active sites, and for synthesizing more selective, active and stable catalysts.

Two synthetic strategies were followed to acquire nanostructural control: a self-assembly method was employed to prepare hierarchical materials starting from functional nanoparticles, and advanced solvothermal methods were used to prepare monodisperse nanocrystals having controlled size and composition. State-of-the-art hierarchical Pd-based catalysts embedded by metal oxide promoters were tested for methane catalytic oxidation in the presence of poisoning compounds typically found in real applications. Detailed surface studies allowed to propose deactivation mechanisms and strategies to improve catalysts resistance to deactivation. Well-controlled nanostructured Pt-based alloys and Ni-Cu alloys showed improved activity, stability and selectivity for hydrodeoxygenation reactions of biomass-derived feedstocks to produce biofuels. The control of nanostructure was pivotal to understand the reason for such enhanced

performances. Finally, dye-sensitized photocatalysts were investigated in H_2 photocatalytic production under visible light, and state-of-the-art stability and activities were demonstrated.

All these findings greatly contributed to the development of catalytic materials for energy-related applications.

1. Introduction

Since the Great Acceleration of the 20th century, human activity has modified the environment on so many levels and to such an extent that we may have entered a new geological epoch - *Anthropocene* - as proposed by a growing number of researchers (*1*). As sensationalist as it may sound, the evidences of anthropogenic impact on the environment are striking, not only on a geological scale: climate forcing, rising sea levels, increasing CO_2 and CH_4 concentration in the atmosphere, erosion of the ozone layer and oceans acidification are just some examples of the fast transformations taking place since the last century. In response to this, a growing awareness about the fragility of the biosphere culminated in environmentalism as a political movement, and in the development of environmental laws and agreements meant to address pollution on an international scale (*2*). In this context, environmental science came alive as an active field of scientific investigation, focusing on pollution abatement, sustainable growth, technological impact on the environment and many other subjects.

The main thrust for the Great Acceleration came from the great progress in industrial catalysis of that time. The Haber-Bosch process for ammonia synthesis allowed the production of economic fertilizers and in turn boosted the growth in population. Later on, the industrial catalytic production of plastics and rubbers introduced completely new materials to the public consumption. The invention of the internal combustion engine and the widespread of cars pressed for petroleum industry growth and new catalytic systems to produce fuels and control noxious emissions. The dawn and rise of the electronics industry called for new materials and for miniaturization of integrated circuits, boosting research in optics, electronic properties of materials and nanostructured materials manufacturing. Aviation and space exploration stimulated research on innovative materials and on the control of their micro and nanostructure. All these innovations are tightly linked to scientific advances, and have lead to tremendous developments in microscopy, spectroscopy, crystallography and many other techniques.

Now, catalysis and material science are dealing with another main issue, which is the energy problem. Non-renewable fossil fuels such as coal, petroleum and natural gas make up more than 80 % of the primary energy consumption worldwide (*3*). The use of fossil fuels raises many environmental concerns, since their reserves are distributed unevenly on the planet, their extraction has severe impact on the soil, and because they produce CO_2 when burned, which in turn is the main greenhouse gas contributing to global warming. Combustion of fossil fuels also

produces other air pollutants, such as nitrogen oxides (NO_x), SO_2, volatile organic compounds (VOCs), and heavy metals.

Despite of these drawbacks, fossil fuels are still the most economic and widespread energy source, since renewable sources (such as hydroelectric, solar, wind, and geothermal) currently require more expensive production and processing technologies. Given the inertia of large energy systems, a significant shift to renewable sources may take decades. In order to mitigate the short and mid-term environmental impact of fossil fuels, two parallel strategies can be envisaged: the development of more efficient emissions control/storage systems and a shift towards more sustainable biofuels and energy carriers. These tasks are very complex, and no single strategy can be applied to answer the problem. However, catalysis, and heterogeneous catalysis, are the common keys to achieve such a target, thanks to recent advances in nanotechnology.

Nanotechnology is a field of research that encompasses science and engineering, and refers to the manipulation of matter on an atomic and molecular scale. Nanotechnologic materials are already finding applications in electronics, biology, materials science, medicinal chemistry and catalysis, and they can be used to exploit energy production processes in a more sustainable way than the present ones, also in terms of pollutant emissions. For what heterogeneous catalysis is concerned, many nanotechnologic materials have already been proved to be more active and selective than their classical counterparts in the desired catalytic process, such as hydrogen production (*4*, *5*), steam reforming (*4*), catalytic oxidation (*6*–*8*), *etc.*

Accordingly, the present work is focused on the synthesis and characterization of well-defined nanostructured and hierarchical materials for environmental and energy-related applications, such as emissions control, biofuels synthesis and photocatalytic H_2 production. We show that structural control at the nanoscale is a great instrument for understanding reaction pathways, for studying the nature of catalytic active sites, and for synthesizing more selective, active and stable catalysts. The aim of this introductory chapter is to underline the objectives of the present study and to provide the reader with a general survey of the matter of interest of this thesis.

1.1 Emissions Control: Methane Catalytic Oxidation

Emissions control is not a new concept: since the original Clean Air Act[1] of the '70s, catalytic technologies for noxious emissions abatement substantially improved the quality of life, especially in urban areas (*9*), where the emission levels of hydrocarbons (HCs), carbon monoxide (CO) and nitrogen oxides (NO_x) from automobiles have decreased by more than 90% (in 2004) (*10*).

[1] The Clean Air Act excludes methane from the emission standards, since it does not significantly participate in photochemical reactions.

Nowadays, clean air is considered to be a fundamental requirement for human health and wellbeing. However, the challenge remains to reduce the emission levels of pollutants such as volatile organic compounds (VOCs), particulate matter (PM), ammonia, nitrogen oxides and ozone (O_3) even further. These compounds arise (directly or indirectly) from natural sources and from many human activities, comprising agricultural activity, combustion processes, transportation, solvent usage, industrial processes, *etc*. (*11*). Transportation is one of the main sources of air pollution in Europe, particularly in cities and urban areas such as towns, airports and sea ports (*12*). According to the revised Gothenburg Protocol (4 May 2012)[2], between 2005 and 2020 the EU member states must jointly cut their emissions of volatile organic compounds by 28%, together with sulfur dioxide by 59%, nitrogen oxides by 42%, ammonia by 6%, and particles by 22%.

In this work, we focus on the catalytic abatement of methane (CH_4), one of the most climate-impacting VOC. VOCs are organic species that evaporate steadily at room temperature and participate in atmospheric photochemical reactions, excluding carbon monoxide, carbon dioxide, carbonic acid, metallic carbides or carbonates, and ammonium carbonate[3]. Because of the very large number of individual air pollutants that come within the definition of VOCs, their importance as a class of ambient air pollutants has only recently become recognized (*13*).

After carbon dioxide, methane is the most important contributor to radiative climate forcing, especially if including its indirect effect due to chemical reaction with hydroxyl radicals (˙OH) in the atmosphere (*14*). Methane concentrations in the atmosphere have raised exponentially in the last century, going from a preindustrial concentration near 700 ppb to a present-day value of 1745 ppb (*13*, *14*). In line with this, satellite retrievals and surface observations have shown that U.S. methane emissions increased by more than 30% over the 2002–2014 period (*15*). However, this increase cannot be readily attributed to any specific source type, and the Environmental Protection Agency (EPA) indicate no significant trend in U.S. anthropogenic methane emissions from 2002 to present. This may be due to the fact that methane is a well-mixed pollutant globally, so that ambient concentrations may not strictly be related to regional emissions. New worldwide regulations are therefore needed, revising the proposals of the Kyoto Protocol and the United Nations Framework Convention on Climate Change (UNFCCC).

Many technologies for VOCs abatement have been developed for a wide range of applications, such as solids adsorbents and other capture devices, condensers, membranes, biodegradation methods and thermal or catalytic oxidation (*16*). However, each technology can be

[2] Protocol was finalized at a meeting of the parties to the Convention on Long-range Transboundary Air Pollution (CLRTAP) in Geneva. http://www.airclim.org/acidnews/new-gothenburg-protocol-adopted

[3] As of 03/29/2013, Electronic Code of Federal Regulations, 40 CFR 51.100(s) - Definition - Volatile organic compounds (VOC).
http://www.ecfr.gov/cgi-bin/text idx?c=ecfr&rgn=div8&view=text&node=40:2.0.1.1.2.3.8.1&idno=40

applied for a specific range of organic compounds, concentrations, and emission sources (*17*, *18*). For example, low-temperature condensation is energy intensive and limited to treatment of evaporative solvents, while biochemical methods are selective and concentration sensitive. One of the most versatile and economical VOC removal technologies is catalytic oxidation (*19*), because it can operate with dilute VOCs effluent streams (<1% VOCs) and at much lower temperatures and higher selectivity than conventional thermal incineration, with consequent limited emissions of NO_x. Some limitations of this abatement technique include the disposal of the spent catalyst materials (if not recyclable), catalyst poisoning by non-VOC materials, aging and leaching of the catalyst (*18*). Also, to date no commercial technology exists able to control methane emission at medium-low temperature (350-400°C). Therefore, the development of new effective methods for VOCs abatement, and methane in particular, is mandatory.

Presently, between 50 and 90% of the total HCs emissions from modern cars equipped with three-way catalysts (TWC) are released during the cold start, *i.e.* when the engine is still cold and the catalyst temperature is low (*10*). Indeed, the most critical factor for efficient conversion is the temperature of the catalyst. After start-up, the hot engine exhausts heat up the catalyst to a temperature high enough to initiate the catalytic reactions, called the light-off temperature, which sets an approximate limit between the kinetically and mass transport controlled temperature regimes for the catalytic reactions. During low speed driving condition CH_4 emissions are 5 times as much as the emissions at high speed (*20*). Even in the case of natural gas vehicles (NGVs), that offer significant environmental advantages over gasoline and diesel (*21*), the problem of unburned methane emissions represents a serious ecological hazard, especially during the sold start (*22*). Indeed, methane is the principal hydrocarbon species emitted by NGV, reflecting the fuel CH_4/NMHC (non-methane hydrocarbons) ratio, typically 93% methane, 5% NMHC(*23*).

A number of approaches have been proposed to improve the emission control during cold-start, such as increasing catalysts activity and developing technical solutions that more indirectly improve the efficiency of the abatement system. The challenge remains to reach the working temperature of the catalyst as fast as possible, and nanotechnologic materials may have the answer to this problem, as demonstrated by our group of research with the development of a nanostructured catalyst exceptionally active in the catalytic oxidation of methane at low temperature (*8*), based on $Pd@CeO_2$ units supported on a high-surface area Al_2O_3-based support.

In Section 3 of the present work, we study the effect of poisoning compounds typically found in real applications on the performance of $Pd@MO_x$ (MO_x= CeO_2, ZrO_2 or Ce-Zr mixed oxides) nanostructured catalysts in the methane catalytic oxidation reaction. Detailed surface studies

allowed to propose deactivation mechanisms in the presence of H_2O, phosphates or SO_2, and to develop strategies aimed to improve catalysts resistance to deactivation.

1.2 Biofuels

World transportation fuel consumption is expected to double by 2035 under a business-as-usual scenario, with forecasted CO_2 emissions reaching 12 gigatonnes per year (Gt yr^{-1}) (*24*). In order to reduce the environmental impact of such a staggering growth, the energy efficiency of conventional fuels should be increased, and alternative fuels (*e.g.* biofuels, electricity) should be extensively used.

Currently, 95% of transportation fuels are being produced from crude oil. One of the most mature energy alternatives to fossil fuels are biofuels, *i.e.* fuels obtained by upgrading biomass feedstocks. Biofuels production processes are not without problems, but they are currently in practice around the world. For instance, in 2013 the US consumed more than 14.5 billion gallons of biofuels, reducing the need for gasoline and diesel fuels made from crude oil (*25*). Recent reports claim that cellulosic biofuels can reduce greenhouse gas emissions by more than 60% compared to petroleum-derived gasoline[4] (*26*). This means that the same amount of energy can be produced with significantly less climate-disrupting pollution.

Biofuels are generally classified as first, second or third generation biofuels, depending on the feedstock and the processing technology used (*27*). Most biofuels produced worldwide are first-generation, that is, derived from food crops by fermentation to bioethanol or by abstraction of oils for use in biodiesel (*26*). However, first-generation biofuels present serious limitations, such as the competition with food sources exploitation, so research and development is focused on second generation biofuels, *i.e.* derived from non-food, lignocellulosic sources, such as agricultural and forest wastes, energy crops, and even algae (third generation biofuels).

The main issues impeding widespread low-cost production of biofuels from lignocellulosic biomass are its recalcitrant nature and the diversity of chemico-physical properties of its components. These properties vary dramatically not only among feedstocks but even for a certain kind of feedstock, to the point that the US Department of Energy (DOE) has established a Bioenergy Feedstock Library, a database for physical, chemical and conversion performance characteristics of more than 50,000 biomass feedstocks[5]. This complex scenario is further worsen by the expensive pretreatments and upgrading processes required for both biochemical and thermal conversion of biomass to biofuels (*24*).

[4] To assess the life-cycle impacts of biofuels on greenhouse gas emissions, biofuels are credited with all the carbon dioxide captured and stored as the biomass grows, as well as any emissions created during harvest, conversion, distribution, and use.

[5] https://bioenergylibrary.inl.gov/Home/Home.aspx

In order to achieve economically and environmentally sustainable production of biofuels, advances in several fronts of plant science, biochemical and chemical engineering, catalysis and analytical chemistry are needed. Agronomic science advances could yield tailored energy crops characterized by enhanced plant productivity, efficient nutrient utilization, reduced water demand and higher resistance to pests and disease, while providing favorable life-cycle benefits. From a biochemical perspective, genome editing techniques can be used to manipulate plants components (such as lignin) on a molecular level, in order to enhance our ability to convert biomass to fuels, by making biomass easier to break down. For instance, research at the Bioenergy Science Center[6] proved that genetic modification of switchgrass can produce phenotypically normal plants having reduced thermal-chemical (≤180 °C), enzymatic, and microbial recalcitrance, showing the potential to lower biomass processing costs (*28*).

Progress in chemical engineering is also essential for improving biofuels processing technologies. There is a need for lower-cost, better performing catalysts for hydrodeoxygenation (HDO) reactions and hydro-treatment processes along with the ability to produce the hydrogen needed for upgrading in sustainable ways. Concurrently, engineering shall deliver advances in separation technologies, reactor design, sensors, process control and waste minimization and treatment (*24*). For biofuels to be competitive with fossil fuels, their production facilities should progress from a single-product the bio-refinery model, in which starting resources are fractionated and all molecular components are used to maximize value generation.

Section 4 of this work is focused on HDO, an important step of thermo-chemical biofuels production. HDO is a hydrogenolysis process for removing oxygen from oxygen-containing compounds, especially relevant to the upgrading of bio-oils and lignocellulosic-derived feedstocks (*29*). Despite the extensive literature on the subject, many aspects remain unclear, such as the influence of reaction conditions, reactant molecule and catalyst composition and nanostructure on the catalytic performance. Herein, we first investigate and compare the mechanism of reaction of two important model compounds (furfural and 5-hydroxymethylfurfural – HMF), usually studied separately and with different approaches, to show that they share a very similar reaction pathway (Section 4.2) (*30*). We then report the effect of alloying Pt with non-noble metals (Co, Cu, Ni, Zn), and of alloying two base metals (Ni-Cu) on the catalytic performances in HDO of HMF, showing that for certain optimal composition the alloyed materials achieve much improved selectivity and stability with respect to single metal catalysts (Section 4.3-4.5). The nanostructural control over the studied catalysts, coupled with advanced spectroscopic and imaging techniques, allowed for a rationalization of the observed performances in terms of catalysts structure and composition.

[6] Funded by the US DOE, http://bioenergycenter.org/besc/

1.3 Sustainable Hydrogen Production

H_2 is a pivotal chemical in the industry and energy sectors, with applications in petroleum refining, power generation in turbines and fuel cells, methanol and ammonia production, welding and heat-treatments, semiconductor manufacturing and hydrogenation of unsaturated fatty acids in vegetable oil, to name a few. More than 50 million metric tons of H_2 are produced annually worldwide[7], mainly by steam reforming of natural gas. Sustainable H_2 production from low-carbon or renewable energies remains challenging and will require large-scale changes to our energy systems (*24*).

The existing methods for the production of renewable hydrogen can be divided into two major categories: direct solar-to-H_2 conversion and electrolytic conversion methods (*31*). In electrolytic routes, the renewable energy source is converted to electricity, and H_2 is then produced via electrolysis of water. In solar-driven water-splitting systems, photons instead of electricity are used to convert water into hydrogen and oxygen with the use of photocatalysts. Further advances in materials chemistry, catalyst development and system engineering are required for these systems to be competitive with existing technologies. For instance, there is a need for low-cost materials exhibiting high energy-conversion efficiencies, and for a collection and distribution system for hydrogen, comparable to landfill gas collection and piping. Although a scalable system has yet to be shown, significant progress has been made on each of the necessary components of a demonstration system (*24*).

Section 5 of this work is focused on direct solar-to-H_2 conversion over dye-sensitized photocatalysts. Sensitization of TiO_2 with visible light-absorbing moieties such as colored dyes is a widely investigated strategy to enhance the photocatalytic efficiency of TiO_2 by extending its otherwise UV-limited light absorption to the visible (Vis) range (*32*). In this thesis, we report advances in the synthesis of stable and efficient dye-sensitized Pt/TiO_2 through the rational molecular design of sensitizers. State-of-the-art performances are achieved using the synthesized dyes coupled with benchmark materials, and strategies to further improve the process sustainability are outlined.

1.4 Aim of the Work and Choice of the Material

This work focuses on some major aspects of the energy problem: emissions control, biofuels production and H_2 renewable photocatalytic production. Well-defined nanostructured materials are developed, characterized and tested for catalytic reactions, with the aim of rationalizing catalytic performances in terms of structure, composition and surface chemistry.

[7] https://www.hydrogen.energy.gov/

Three main classes of materials are investigated: hierarchical materials based on $Pd@MO_x$ units for methane catalytic oxidation, Pt-based nano-alloys (of Co, Ni, Zn, Cu) and Ni-Cu nano-alloys for hydrodeoxygenation reactions, and dyes-sensitized Pt/TiO_2 for H_2 photocatalytic production under visible light.

$Pd@MO_x$-based (M=Ce, Zr, or Ce-Zr) catalysts supported on high surface area $Si\text{-}Al_2O_3$ are selected for methane oxidation studies because they show state-of-the-art activity at low temperature under ideal conditions and high thermal stability, as previously reported by our research group (*8*). The focus of this section is the study of $Pd@MO_x$-based catalysts performances under conditions approaching the ones of real applications, such as industrial and automotive exhausts. H_2O, phosphates and SO_2 are chosen to test the catalysts resistance because they are the most powerful poisoning and deactivating agents of Pd-based catalysts (*33*).

Model catalysts based on $Pd@MO_x$ units supported on conductive materials are prepared for advanced photoelectron spectroscopy (PES) investigations, in order to gain insights into the transformation occurring at the catalysts surface during deactivation and to develop strategies for the synthesis of more resistant second-generation catalysts. In the P-poisoning study, graphite is used as a support because of its high conductivity and the possibility to deliberately introduce P in the system during the catalyst preparation (*34–36*), rather than introducing it from the gas feed during aging treatments (*37*). In this way, H_2O is not introduced in the reaction mixture by decomposition of H_3PO_4 to P_2O_5 and the effect of water addition can be studied separately. For the SO_2 poisoning study, indium tin oxide (ITO) is used as a conductive support because of its conductivity and high thermal resistance under oxidative conditions. Atomic Layer Deposition (ALD) is then used to deposit thin Al_2O_3 films on the ITO surface, in order to produce a support having a surface chemistry similar to high-surface area Al_2O_3, while retaining the conductivity required for precise PES studies.

Pt-based and Ni-Cu nano-alloys are selected for HDO studies because of the considerable evidence that bimetallic catalysts can be more selective for HDO reactions (*38*). The aim of this work is to understand the reason for such enhanced selectivity and to investigate the nature of the catalytic active sites for HDO reactions. Solvothermal methods are used to synthesize the nanocrystalline alloys in this work in order to achieve nanocrystals having well-controlled and uniform shape, size and composition (*39*, *40*). Uniformity is critical to study the factors influencing selectivity, especially for alloys in which both the metals are able to catalyze the HDO reaction, such as Pt-Co and Pt-Ni. Conventional methods, such as impregnation, are not able to produce such uniformity, which is the reason we prepare the catalysts in this study by synthesizing uniform NCs in solution.

The HDO catalytic studies reported in this thesis are carried out in a high-pressure, three phase tubular-flow reactor, because such setup allows to easily change experimental parameters (*e.g.* space velocity) and investigate their effect on the performance of catalysts. Tubular-flow reactors are preferred to batch reactors, for which the contact between the solid catalyst, the liquid-phase reactant, and the gas-phase H_2 can be ineffective and activity can be limited by H_2 diffusion (*41*). Also, in batch reactors, reactions can occur during the heating and cooling periods, further complicating the interpretation of results. In the first part of the HDO study, the importance of reaction conditions is underlined in the case of furfural, which was studied for the first time under high-pressure liquid flow conditions and compared to the widely reported low-pressure, gas phase setup, in order to get new insights in the HDO reaction mechanism.

For dye-sensitized H_2 photocatalytic production studies, Pt/TiO_2 nanomaterials are used as a benchmark because of their well-known photocatalytic properties (*42*). The performance of the dyes as sensitizers is evaluated by studying the H_2 photocatalytic production over dye-stained Pt/TiO_2 under visible light irradiation ($\lambda > 420$ nm). The aim of this study is to enhance photocatalytic performances of dyes/Pt/TiO_2 systems through the rational molecular design of donor-acceptor dyes. In particular, the effect of peripheral functionalization (aimed to increase surface wettability) and heteroatom substitution in the D core and π-spacers are discussed for a series of dyes previously reported for dye-sensitized solar cells applications (*43*, *44*).

The reaction conditions are also carefully optimized in terms of dye loading and amount of catalyst in the reaction suspension, following recent guidelines for photocatalytic studies (*45*). Triethanolamine (TEOA) is used as sacrificial agent in most of the reactions because it is widely reported in the literature (*46*), even if it's not a very sustainable choice. As a future perspective, the H_2 sustainable photocatalytic production from EtOH/water mixtures will be finally presented.

2. Characterization Techniques

In the following section an overview of the experimental techniques used in the present study is reported. Different techniques were employed to characterize the prepared catalysts and photocatalysts in terms of textural, structural and morphological properties. Their catalytic activity was evaluated for various reactions, relevant in the general context of sustainable energy production and environmental protection, such as catalytic oxidation of methane, biomass upgrading to biofuels and photocatalytic hydrogen production. A brief summary of each technique is given, highlighting the main elements that will help evaluating the results obtained in this thesis.

2.1 Physisorption

The activity of heterogeneous catalysts is strictly related to the morphology and the extension of their surface area. Indeed, gas reactions catalyzed by solid materials take place on those active sites of the catalyst that are in contact with the reactants phase, *i.e.* that are located on the catalyst interior or exterior surfaces accessible to the reactants. If the pores are wide enough to permit the diffusion of reactants and products to and from the active sites, the activity is directly proportional to the number of active sites. This principle is valid for all heterogeneous catalytic reactions, allowing to study the reactions under kinetic control (*47*). Otherwise, if pores are too narrow, the reaction is limited by the mass transport of reactants from the gas phase to the active site, and it is said to be under diffusional control. In this case the activity could be independent of the surface area or proportional to its square root, depending on the mode of diffusion. It is deduced that the catalytic activity of a solid material is not only influenced by its surface area, but also by its pore structure (texture and dimensions of the pores). For example, a particular pore structure may induce a shape selectivity to a reaction, limiting the diffusion of one particular reactant or product (*47*).

The activity of heterogeneous photocatalysts is also strongly dependent on surface area, since photocatalytic reactions occur on the material surface. Large surface areas provide more active sites to react with absorbed water and hydroxyl species to form hydroxyl radicals and anchor organic molecules for photodegradation (*48*). However, performances is also limited by the surface area available for capture of solar light and by the distribution and density of surface localized trap states at grain boundaries, which cause recombination of electrons and holes and depend on the material crystallinity and morphology (*49*). To obtain highly active TiO_2 photocatalyst, therefore, it is important to simultaneously consider these properties.

Even in the same material, pores can vary in shape and dimension in a wide range. Pores can be divided into three groups on the basis of their dimensions:

- micropores are pores having diameters smaller than 2 nm;
- mesopores have diameters in the range 2 - 50 nm and are typical of non crystalline materials;
- macropores have diameters larger than 50 nm.

In the particular case of core-shell modular units supported on alumina, the pore size distribution of the support becomes very important because pores narrower than 20-30 nm are too small to be accessible to the core-shells, and so the associated fraction of surface area is not available for their deposition (*8*). The ability to measure the surface area of a catalyst and the dimension and distribution of its pores is therefore essential to any catalytic study.

2.1.1 Estimating Surface Area

Among the well-established methods that are used to determine the surface area of a porous solid, the most commonly employed is the volumetric method. This method is widely used for determining the surface area and pore size distribution of a variety of different solid materials, such as ceramic, industrial adsorbents and catalysts (*50*, *51*). The volumetric method consists in measuring the adsorption of an inert gas on the solid at a given constant temperature as a function of the partial pressure of the adsorbent. Notably, a fundamental requisite to apply this technique is that the interaction between the adsorbent molecules and the material surface has to be weak. Therefore, only a physical interaction must take place. This process allows to obtain a physisorption isotherm. On the basis of the isotherm shape, it is possible to determine the surface area and pore distribution of the sample, according to empirical equations and adsorption models (*47*).

Since physisorbed molecules are not restricted to specific sites but are free to completely cover the surface of the solid, the method allows to estimate the total surface area of the sample. Furthermore, since the interactions that lead to the adsorption are reversible and weak, the process doesn't modify the surface of the sample, so is not invasive. The process is also reversible, so both adsorption and desorption processes can be studied. Moreover, because many molecular layers of adsorbate can be formed, the pore volume may be measured if the amount of adsorbate needed to completely fill the pores can be extrapolated. According to the International Union of Pure and Applied Chemistry (IUPAC) recommendations (*50*), the majority of physisorption isotherms can be classified into six types, that are displayed in summarized in Figure 2.1.

Figure 2.1 Physisorption isotherm types and hysteresis classification according to the IUPAC recommendations (Adapted from (*50*))

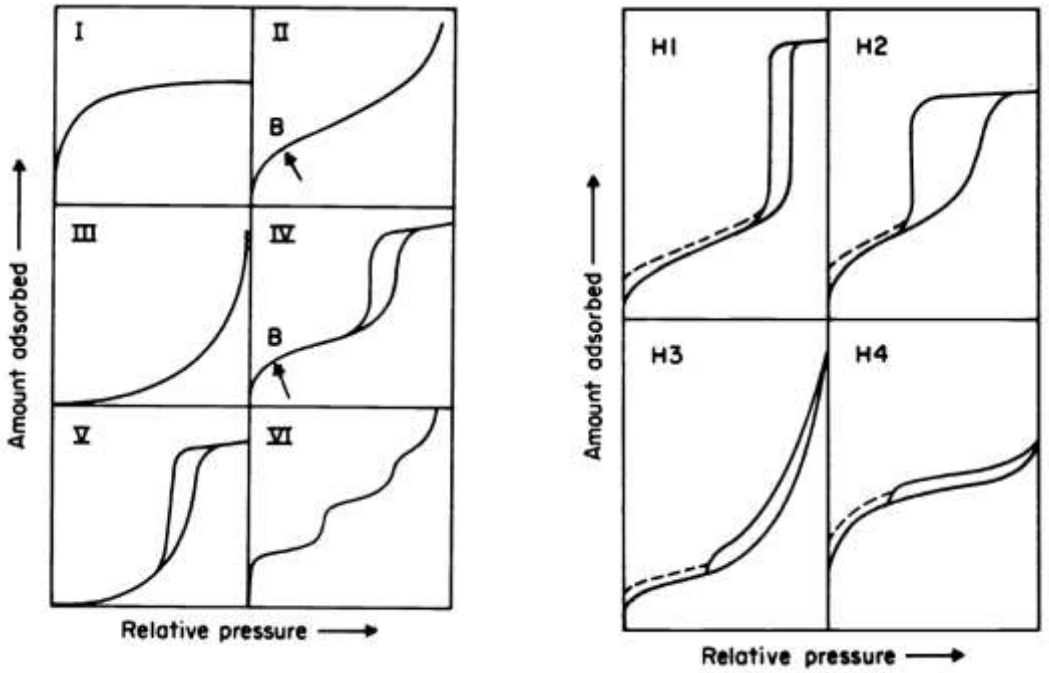

The standard physisorption isotherms can be described as follow:

- Type I isotherms are given by microporous solids having relatively small external surfaces, such as activated carbons and zeolitic molecular sieves.
- Type II isotherms are typical of non-porous or macroporous solids, on the surface of which unrestricted monolayer-multilayer adsorption takes place.
- Type III isotherms are not common. They are convex to the relative pressure axis over their entire range and, as we shall discuss later, are not useful to extrapolate the surface area of the solid. The adsorbate species may be replaced by another one in order to get another type of isotherm.
- Type IV isotherms are given by many industrial adsorbents. They present a hysteresis loop, which is associated with capillary condensation taking place in mesopores and can vary to a great extent depending on pores geometry. The hysteresis loop is also very important for determining the pore distribution of the material. According to the IUPAC recommendations, these are grouped in four types (H1-H4 in Figure 2.1), basing on their shape. H1 type is observed for compact agglomerates of spherical particles with rather uniform dimensions and disposition, while H4 type is observed for adsorbents made of agglomerates of bi-dimensional particles. H2 and H3 hysteresis types are observed for

intermediate situations. Hysteresis are often not easily classified, as most of the materials show heterogeneous distributions in shapes and dimensions of pores.

- Type V isotherms are uncommon and related to type III isotherms: the adsorbent-adsorbate interaction is weak.
- Type VI isotherms represent stepwise multilayer adsorption on a uniform non-porous surface.

In order to estimate the total surface area of a material using the volumetric method, the completion of an adsorbed monolayer has to be detected from the isotherm shape by some means. This is possible only for isotherm types I, II and IV. For isotherm type I, the adsorption is usually described adequately by the Langmuir equation.

$$\frac{V}{V_m} = \frac{\mathrm{bp}}{1 + \mathrm{bp}} \tag{2.1}$$

where p is the pressure of gas, b is a constant derived from kinetic principles that depends on temperature and adsorption heat, V is the volume of adsorbed gas and V_m is the volume of adsorbed gas forming a theoretical monolayer on the surface of the material. In order to determine the monolayer volume from empirical data, the Langmuir equation can be rearranged into:

$$\frac{p}{V} = \frac{\mathrm{p}}{\mathrm{V_m}} + \frac{1}{\mathrm{bV_m}} \tag{2.2}$$

Therefore, a plot of p/V *vs.* p will give a straight line, the slope of which is $1/V_m$, the inverse of the monolayer volume.

For isotherm types II and IV instead, the Langmuir equation doesn't hold through because multilayer coverage takes place. The monolayer coverage may be extrapolated roughly by referring to the ordinate value of the inflection of the isotherms, known as the point B (see Figure 2.1). The point B method may be used only if the beginning of the almost linear section of the isotherm is well defined, that is, if a sharp change of curvature is noted. Otherwise, a more sophisticated analysis of the isotherm is required and the surface area can be calculated by extrapolation of the monolayer volume applying the Brunauer-Emmett-Teller (BET) theory. The BET model starts from the assumption that adsorption is a reversible process consisting in the formation of a series of layers, where the most external one is formed by adsorbate molecule directly in equilibrium with the vapor phase. On the basis of these principles, the BET equation is derived:

$$\frac{p}{V(p^0 - p)} = \frac{1}{V_m C} + \frac{C - 1}{V_m C} \cdot \frac{p}{p^0} \quad (2.3)$$

where p is the gas pressure, p^0 the saturated vapor pressure of the liquid at the operating temperature, V is the volume of adsorbed gas, V_m is the volume of monolayer coverage and C is the BET constant (that depends on temperature and interactions between adsorbent and adsorbed species). Plotting $p/V(p^0-p)$ *vs.* p/p^0 usually gives a straight line in the range of $0.05 < p/p^0 < 0.35$, and from the slope and intercept the monolayer coverage volume is determined.

Once the monolayer coverage volume V_m is known, the available surface area is calculated from the equation:

$$S = \frac{V_m}{V_{mol}} N_A a_m \quad (2.4)$$

where V_{mol} is the molar volume of the adsorbate (at the same temperature and pressure of V_m), N_A is the Avogadro's number and a_m is the area of an adsorbed molecule ($a_m = 0.162$ nm^2 for N_2 at the liquid nitrogen temperature).

2.1.2 Estimating Pore Volume and Diameter

Many methods have been developed to estimate pores distribution of solid materials. In this study, the gas adsorption method will be employed. This method is based on the physisorption process, just like the volumetric method used to assess the surface area of solid materials (*47*). In this case, however, one wants to observe just one particular phenomenon of the physisorption process, that is the capillary condensation of the gas used as adsorbate. The capillary condensation takes place in narrow pores at a lower pressure than the saturation pressure of the adsorbate. The capillary condensation in cylindrical pores is described by the Kelvin equation:

$$\ln \frac{p^0}{p} = \frac{2V\gamma \cos \alpha}{rRT} \quad (2.5)$$

which is obtained by equating the work spent in enlarging a spherical drop of liquid to that done in adding molecules to the interior of the drop. In this case, p^0 is the vapor pressure at the operation temperature, p is the pressure of the gas, V is the molar volume of the gas, α is the contact angle of the liquid on the pore surface, γ is the surface tension of the liquid , r is the radius of the pore, R is the gas constant and T is the absolute temperature of operation. Basing on this

equation, a pore size distribution curve can be constructed, plotting the volume of adsorbed gas *vs.* the diameter of the pores calculated for each p/p^0.

From this simple equation, it is also possible to understand that the formation of the hysteresis loop in the physisorption isotherm is related to particular shapes of the pores. In fact, in the case of cylindrical pores, the capillary condensation takes place at the same partial pressure during both the adsorption and desorption processes. The hysteresis loop is originated by the fact that, during desorption, evaporation of the gas takes place at a lower p/p^0 with respect to the condensation during adsorption. Therefore, evaporation takes place on pores with a diameter smaller than that of pores in which capillary condensation occurs. This situation can be rationalized only assuming the formation of neck-bottle pores, in which the apertures have diameters smaller than the cavities (*47*).

The Kelvin equation is a powerful method for investigating the pore distribution of a sample, but is insufficient in order to interpret correctly the experimental results obtained via the gas adsorption method. A model of the porous structure of the material is needed. Many different pore models have been developed, some qualitative and some much more complicated based on mathematical simulations. One of the differences among them arises from the pores dimension range in which they can be applied. In the present work particular attention is given to mesopores, while micropores are not taken into account because of their scarce thermal stability (they collapse at typical operation temperatures considered in this study) and because they are too narrow in diameter to be accessible by core-shell nanostructures (*8*). The method commonly used to describe mesopores (and small macropores) distribution is that developed by Barret, Joyner and Halenda (BJH method) (*52*). Analyzing the physisorption isotherm in the $0.40 < p/p^0 < 0.98$ range (region comprised between the formation of the monolayer and the saturation of the system, equivalent to a complete filling of pores), it is possible to obtain the mesopore volume and pore distribution.

In the present work, N_2 physisorption experiments were carried out on a Micromeritics ASAP 2020C. The samples were first degassed in vacuum at 350 °C overnight prior to N_2 adsorption at liquid nitrogen temperature.

2.2 Chemisorption

Chemisorption is based on a specific interaction between a probe molecule and the metal surface that constitute the active phase of a catalyst (*47*). The probe molecule is able to chemically react with the metal, producing a single layer of chemisorbed molecules. The measure of the volume of gas consumed for the formation of the monolayer allows the calculation of the area of the active phase and consequently its dispersion. A typical chemisorption isotherm is shown in Figure 2.2.

Figure 2.2 Typical chemisorption isotherm.

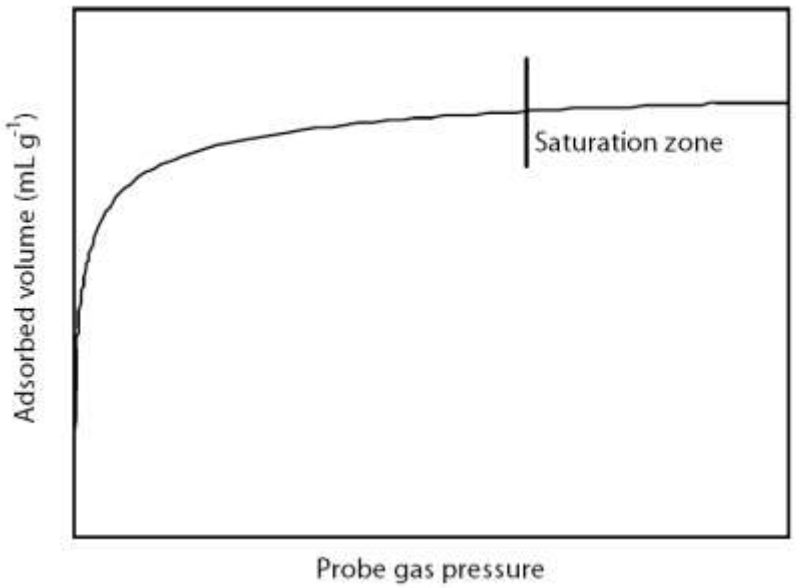

The number of surface metal atoms $N(s)_M$ and the active metal surface S_M can be obtained from the following equations:

$$N_{(S)M} = n\frac{V}{V_m}N_A \tag{2.6}$$

$$S_M = N_{(S)M}a_M \tag{2.7}$$

where V is the volume of adsorbed gas, V_m is the gas molar volume, N_A is the Avogadro's number, a_M is the cross sectional area of a single metal atom and n is the chemisorption reaction stoichiometry, that is the number of metallic atoms that are needed to bind a single molecule of adsorbate.

The most common gases used for chemisorption studies are hydrogen and carbon monoxide. Notably, many other gases can be used as probe for chemisorption. The best choice of the gas depends on the nature of the metal and of the support included in the formulation of the catalyst under analysis.

Generally, the chemisorption stoichiometry with hydrogen is assumed to be 2, because H_2 can be activated by the metal surface and subsequently dissociated, each hydrogen atom forming a bond with one metal atom. On the other hand, the stoichiometry of adsorption CO on metals (such as Pd and Pt) is assumed to be 1. These assumptions are not always true: actually, for very

small nanoparticles the stoichiometric coefficient of CO may vary, because of the formation of geminal di-carbonylic species on edge and vertex atoms (*53*). Similarly, in the case of H_2 the stoichiometric coefficient may vary for extremely dispersed particles (lower than 1nm), but also the formation of metals hydrides and spillover effects (especially in reducible oxides) can alter the measurement (*54*). These phenomena must be taken into account during planning of the measurements and evaluating the experimental results.

In the case of non-dissociative adsorption (as is the case of CO) the Langmuir isotherm equation can be applied, assuming a constant chemisorption energy:

$$n_{ads} = \frac{n_{ads}^{m} bp}{1 + bp} \tag{2.8}$$

where n_{ads} is the quantity of gas adsorbed at pressure p, n^{m}_{ads} is the quantity of gas needed for the formation of the monolayer and b is a constant. The saturation limit should correspond to a horizontal section of the isotherm in the high pressure region. However, as shown in Figure 2.2 this is not usual because, in most of the experiments, this region shows a straight positive trend due to the formation of subsequent layers due to the physical adsorption of the probe gas. The monolayer volume may be calculated by extrapolating the linear part of the isotherm to zero pressure, but a more elegant method exists. This is based on the subtraction of the physisorption contribute from the chemisorption isotherm: the total isotherm is measured, then the system is evacuated at the temperature of analysis for a short time, leading to desorption of the physisorbed gas, and finally another isotherm is measured. The difference between the two gives the irreversible adsorption, which is due solely to the contribution of chemisorbed species. The monolayer adsorption is then calculated extrapolating to zero the linear section of the subtracted isotherm.

From the chemisorbed volume it is possible to obtain the metal dispersion D_M and the average metal particle diameter d_M. To obtain these values, the geometry of the metal particles has to be assumed. Assuming a geometrical shape of the particles:

$$\mathrm{D_M} = \frac{\mathrm{N_{(S)M}}}{\mathrm{N_{(tot)M}}} \tag{2.9}$$

$$\bar{d}_M = 6\frac{V_M}{a_M}\frac{\mathrm{N_{(tot)M}}}{\mathrm{N_{(S)M}}} = 6\frac{V_M}{a_M}\frac{1}{\mathrm{D_M}} \tag{2.10}$$

where $N_{(s)M}$ is the number of surface metal atoms, $N_{(tot)M}$ is the total number of metal atoms, 6 is the geometrical factor for spherical particles and a_M is the area of a metal atom. V_M is the volume of a bulk metal atom. It can be calculated from the Equation 2.11:

$$V_M = \frac{MW}{\rho N_A} \quad (2.11)$$

where MW is the atomic weight of the metal and ρ is the density of the metal.

In the present thesis, chemisorption experiments were performed on a Micromeritics ASAP 2020C. The samples (~ 150mg), placed in an U-shaped quartz reactor, were subjected to preliminary thermo-chemical treatments in order to clean and reduce the sample and finally to fully eliminate the hydrogen gas from the surface of the catalyst. Usually, samples were cleaned by a treatment under flowing O_2(5%)/Ar at 500°C for 1h, reduced under H_2(5%)/Ar at 80°C for 1h and finally evacuated at 350°C for 4h.

For any Pd/CeO_2 system there are some particular elements that should be underlined. First, the support has the ability to spill-over the hydrogen. To obtain the chemisorption contribution of the active phase alone it is thus necessary to halt the spill-over phenomenon. It has been observed that it is possible to do so by measuring the chemisorption isotherm at low temperature (solid/liquid acetone cooling bath, -90°C) (*54*). At this temperature, the kinetic of hydrogen diffusion on the oxide surface is very slow, while the adsorption kinetic is almost the same (since the activation energy is almost zero). However, operating at low temperature results in a much greater physisorption contribution. The chemisorbed hydrogen can be obtained via extrapolation at p=0 of the linear part of the isotherm measured at 180 K. The isotherms measured at room temperature allow instead to compare the mobility of hydrogen on the oxide surface. Another aspect to be considered is that the palladium is known for its ability in absorb hydrogen, leading to the formation of hydrides. Therefore, chemisorption studies of the Pd/CeO_2 catalysts are usually performed at low temperature (about -90 °C) and low H_2 pressures (2 - 20 Torr) (*54*).

To avoid these complications, in this study CO chemisorption experiments were conducted. Whereas with some metals, such as nickel, the adsorbed CO molecule may thermally dissociate on the surface, with Pd and Pt only molecular adsorption is observed and this is completely reversible (*55*). The chemisorption pressure however must not be too high (2-20 Torr), in order to avoid the formation of carbonate species, that would alter the measurement results (*56*).

2.3 Powder X-Ray Diffraction

X-ray crystallography is a well established technique to explore the structure of a material. The method is based on the diffraction phenomena occurring when X-ray photons are scattered by the crystallographic planes of a lattice, and revolves in particular on the interference patterns given by the diffracted photons. The intensity of the diffracted beam is maximal when all the diffracted rays give constructive interference and is described by the Bragg's law:

$$n\lambda = 2dsen\theta \tag{2.12}$$

where n is the order of diffraction, λ is the wavelength of the incident X-ray, d is the interplanar spacing and θ is the angle of incidence of the beam.

X-ray diffractograms reveal several important properties of a material, namely the crystallinity of the sample or of a particular component of it, an estimate of the size of the microcrystallites that may be present, the atomic constituents of the unit cell and so on (*47*). Powder XRD was used in the current study to identify the composition of the phases and to estimate the average dimension of the crystallites. Most of the powder XRD patterns were recorded with a computer-controlled Philips X'Pert diffractometer using Cu Kα radiation (λ = 0.154 nm). The data were collected at 0.02 ° in the 2θ range from 10 ° to 100 °.

The experimental broadening of the XRD reflections is composed of many contributions, but it can be related to the size of the crystallites of the studied material, according to the Scherrer's equation:

$$\tau = \frac{K\lambda}{\beta cos\theta} \tag{2.13}$$

where τ is the crystallites mean size, K is a constant which to some degree depends on the shape of the peak, λ is the X-ray wavelength, β is the Full Width at Half Maximum (FWHM) of the peak and θ is the Bragg angle.

According to the Scherrer's equation, reflections having larger FWHM coincide with lower dimension of the crystallites. For the same principle, non-crystalline materials show no sharp diffraction reflections, but only broad features, because of the absence of a long-range order (*47*). However, it should be noticed that the Scherrer's equation only provides a lower bound on the particle size, because the reflections may be broadened by a variety of factors besides crystallite size. Some examples of reflection broadening sources may be dislocations, stacking faults, residual stresses, grain boundaries, impurities, *etc.* If all of these contributions were zero, then the peak

width would be determined solely by the crystallite size and the Scherrer formula would apply. However, if the other contributions to the peak width are non-zero, then the actual crystallite size is larger than that predicted by the Scherrer formula. Moreover, the value of β in the Scherrer's equation is affected also by instrumental effects.

2.4 Fourier Transform Infrared Spectroscopy

Fourier Transform Infrared Spectroscopy (FTIR) is a technique used to acquire absorption or emission infrared spectra of a sample, that relies on a Fourier transform mathematical process to convert the raw data (interferogram) into the actual spectrum. Contrary to dispersive spectroscopy techniques, in which a monochromatic light beam is used to measure how much of the light is absorbed at every wavelength, FTIR allows to simultaneously collect high spectral resolution data over a wide spectral range.

An FTIR spectrometer consists of a polychromatic IR source, a Michelson interferometer allowing to block or transmit a certain wavelength of light, a sample holder/chamber and a detector. The most common IR source for the mid-IR region, 2–25 μm (5000–400 cm^{-1}), is a silicon carbide element heated to about 1200 K, giving an output which is similar to a blackbody. The light coming from the source is collimated and directed to a beam splitter, usually made of KBr with a germanium-based coating that makes it semi-reflective. Here, some of the light is refracted towards a fixed mirror and some is transmitted towards a moving mirror. Light is reflected from the two mirrors back to the beam splitter and some fraction of the original light passes into the sample compartment. There, the light is focused on the sample and finally refocused on to the detector. The difference in optical path length between the two arms of the interferometer is known as the retardation, or optical path difference, OPD. The interferogram is obtained by varying the OPD and recording the signal from the detector for various values of OPD. Mid-IR spectrometers commonly use pyroelectric detectors that respond to changes in temperature due to IR radiation intensity variation (*e.g.* deuterated triglycine sulfate (DTGS) or lithium tantalate ($LiTaO_3$)). These detectors operate at ambient temperatures and provide adequate sensitivity for most routine applications.

The three principal advantages of FTIR compared to scanning dispersive IR are higher signal-to-noise ratio for a given scan time, higher wavelength accuracy and less sensitivity to stray light, which is radiation of one wavelength appearing at another wavelength in the spectrum. The higher signal-to-noise ratio arises from the fact that information from all wavelengths is collected simultaneously and that no slits are needed: the interferometer throughput is determined only by the diameter of the collimated beam coming from the source. The higher wavelength accuracy is due to the fact that the scale is calibrated by a laser beam of known wavelength that passes

through the interferometer. This is much more stable and accurate than in dispersive instruments where the scale depends on the mechanical movement of diffraction gratings.

In this study, DRIFTS spectra were acquired using a Mattson Galaxy 2020 FTIR spectrometer with a diffuse-reflectance attachment (Collector II) purchased from Spectra-Tech Inc., using a resolution of 16 cm^{-1}. Since the sample could not be heated to sufficiently high temperatures in the sample stage of the diffuse reflectance unit, the catalysts were first treated under different conditions in a separate flow reactor, cooled to room temperature in He, and then transferred to a sample holder for the spectroscopic measurements. In the diffused reflectance cell, the catalyst was degassed in dry flowing He at 200 °C before data collection. All spectra were recorded at room temperature in dry He.

2.5 Transmission Electron Microscopy Techniques

In the field of heterogeneous catalysis and photocatalysis, the design of more active and selective catalysts often relies on the precise identification of active sites. Sophisticated imaging methods that enable detailed characterization of a sample at the nanometer and atomic level are of pivotal importance (*57*). Among many characterization techniques, advanced electron microscopy techniques are the most powerful to get information on the individual components of an heterogeneous material. These techniques are essential to understand the properties of heterogeneous catalysts and to provide useful information for the development of nanostructured materials. Using modern electron microscopes it is possible to directly observe small particles, clusters or even single atoms of a sample, while all other techniques (*e.g.* X-ray techniques, IR spectroscopy, NMR spectroscopy) provide information averaged over millions to trillions of components, or they require stringent conditions on the samples to be examined (*e.g.* Scanning Probe Microscopy techniques) (*57*).

Transmission Electron Microscopy (TEM) techniques overcome the limitation of light microscopes for imaging very small objects, thanks to their higher resolution. The resolution of a microscope is the minimum distance between distinguishable objects in an image and it's limited by two different and unrelated aspects: aberration and diffraction. Aberration can be explained by geometrical optics and can (in principle) be solved by increasing the optical quality of the system. Diffraction is instead strictly related to the nature of the wave used for the observation.

The maximum theoretical resolution of a microscope, limited by diffraction alone, is related to the wavelength of the radiation used according to the Rayleigh criterion, that leads to the simplified statement that the limit of resolution of any imaging process is on the order of the wavelength of the wave used to image it. It follows that the maximum theoretical resolution of a

good light microscope (hundreds of nm) is not useful to characterize the typical nanocomponents of a heterogeneous catalyst. On the other hand, the maximum resolution for an electron microscope is adequate to get nanoscopic resolution, and can be calculated referring to de Broglie's wavelength of the particle:

$$\lambda = \frac{h}{p} \tag{2.14}$$

where p is the particle momentum, λ is the particle wavelength and *h* is the Planck's constant.

In the TEM apparatus the electrons are accelerated by a potential drop, V, acquiring a potential energy eV that is converted to kinetic energy of the electrons at the end of the accelerating section of the instrument. Equaling the two energies, an expression of momentum as a function of the potential is derived:

$$eV = \frac{1}{2}\mathrm{m_0 v^2} \tag{2.15}$$

$$p = \sqrt{2m_0 eV} \tag{2.16}$$

The value of λ can be obtained substituting Equation 2.16 in Equation 2.14. For example, an electron accelerated to 100 keV has a wavelength (which more or less corresponds to the maximum theoretical resolution of a microscope) of about 0.004 nm, which is 100 times smaller than the diameter of an atom. Moreover, by increasing the accelerating voltage the wavelength of the electrons would decrease. However, it must be pointed out that Equations 2.14 - 2.16 do not take into account relativistic effects, that cannot be ignored for energies above 100 keV. In addition to this intrinsic limitation, considerable practical limitations involved in the microscope construction must be taken into account, such as aberration limits and non homogeneity of the magnetic fields used as lenses. Nonetheless, atomic scale resolution is attainable using modern instruments. Using aberration correctors (usually referred to as C_s-TEM), it is possible to dramatically improve the spatial and spectral resolution of the electron microscope even when using lower accelerating voltages (Figure 2.3) (*57*). This is particularly advantageous since a lower accelerating voltage generally leads to less sample damage from the electron beam.

Figure 2.3 Spatial resolution versus year for optical microscopes and electron microscopes. Currently, best point-to-point spatial resolution is 0.5 Å. (Reproduced from (*57*))

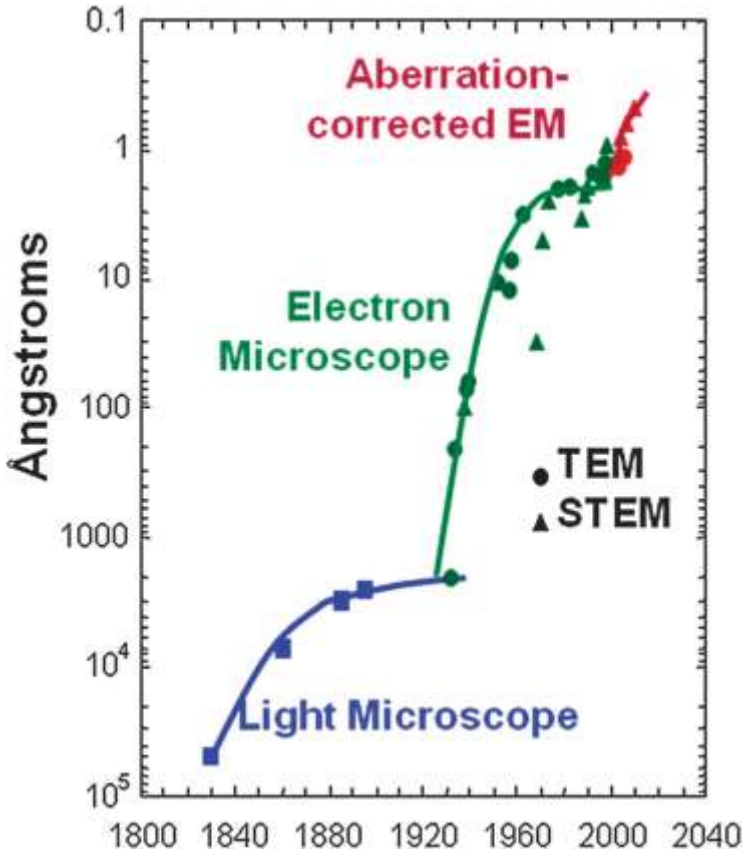

A typical Transmission Electron Microscope (TEM) consists of a vertical column in which the electron beam passes from an electron source at the top, through the specimen and down to the bottom of the column where the image is formed and revealed (Figure2.4). The column is held under ultra-high vacuum (UHV) conditions by a system of high performance pumps in order to reduce the scattering of the electron beam by gas atoms. Electromagnetic coils that function as lenses are positioned around the column along its length and work in an analogous way the optical lenses do in a light microscope. Apertures of different diameters can be inserted into the electron beam at several positions along the column. This is done to select part of the beam and exclude the contribution of the rest. There are two common types of electron sources, which are characterized by the way in which the electron beam is generated (thermionic emission source or field emission gun).

After electrons are produced, they are focused and accelerated by an electrostatic field and they enter into the TEM column. The strength of this field determines the kinetic energy of the

electron beam (Equation 2.14 and 2.16). In practice, an applied potential of at least 100 kV is advisable for HRTEM.

Figure 2.4 Schematic representation of the TEM column. Blue lines represent the electron beams.

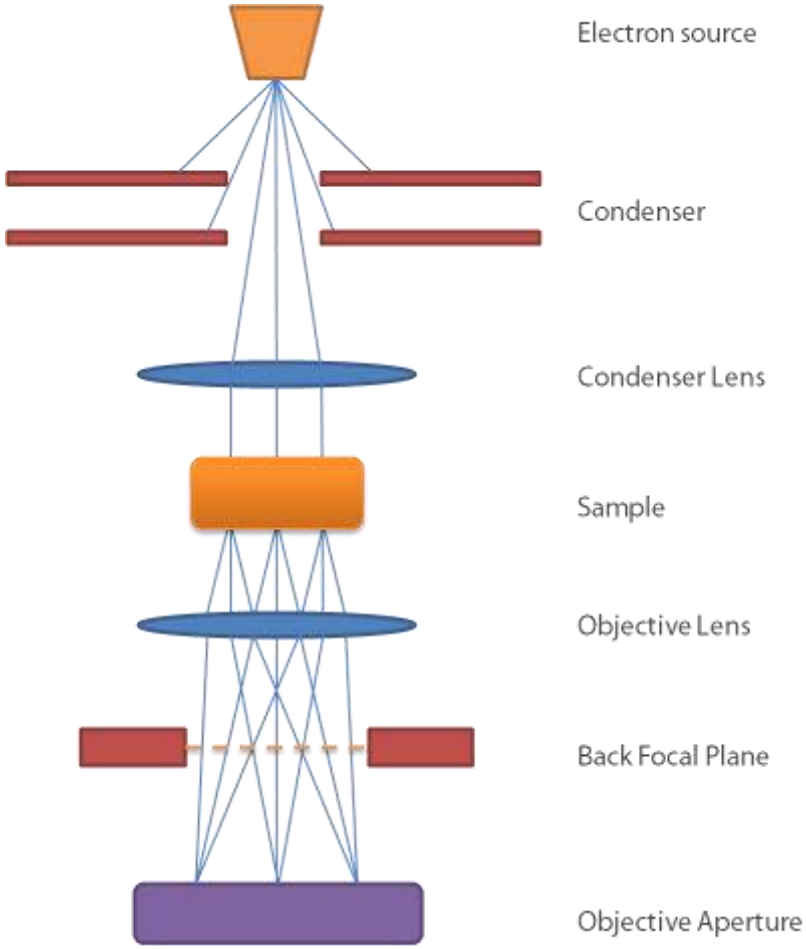

The condenser apertures and lens system select the electrons and focus them in a parallel beam, setting the beam diameter to a desired value. Then, the electron beam passes through the specimen, which is mounted on the specimen holder. The incident beam interact with the internal crystal structure of the sample and emerges as a set of diffracted and non-diffracted (transmitted) beams. These beams are again focused by the objective lens on the Back Focal Plane (BFP). In this plane, the diffraction pattern is formed.

Considering the rules for diffraction (similarly to single crystal X-ray diffraction) each spot is related to one family of crystal planes at one particular orientation. The objective lens performs a Fourier Transform on the exit wave to form the diffraction pattern, that is processed via inverse Fourier Transform to construct an image closely related to the internal structure of the sample.

Images and diffraction patterns are visualized on a fluorescent screen and may be digitally recorded using a camera positioned below the fluorescent screen (*58*).

The diffraction pattern contains electrons from the whole area of the specimen illuminated by the beam and is not very useful because the specimen will often be buckled and because the direct beam is often so intense that it will damage the camera. Therefore, there are basic TEM operations that allow both to select a specific area of the specimen to contribute to the diffraction pattern and to reduce the intensity of the diffraction pattern reaching the screen. There are two ways to perform this operation: either the beam is made smaller, or an aperture is inserted above the specimen so that only electrons passing through it may hit the specimen. Usually the second way is applied: this operation is called Selected-Area Diffraction (SAD).

After the diffraction pattern area is selected, it is possible to perform the two most basic imaging operations in the TEM. It is possible to form the image in the TEM by using the central spot or some of the scattered electrons. If the direct beam is selected, the resultant image is called bright field (BF) image, while if scattered electrons of any form are selected, the resultant image is called dark-field (DF) image. The BF detector is aligned to the transmitted beam in the TEM column while the DF detector is usually annular and surrounds the BF detector. An image obtained with the annular detector is called Annular Dark-Field (ADF) image. The DF detector will collect not just scattered electrons but also some Bragg electrons. To get an image formed only by scattered electrons another detector can be used, placed at very high angles, called High-Angle ADF (HAADF) detector. The images collected with this detector are sometimes called Z-contrast images because the signal strength of the high-angle scattered electrons is proportional to approximately Z^2 (in the limit of electron single scattering). This technique is particularly advantageous for detecting supported heavy-metal particles. The complete HAADF detector set-up for Z-contrast imaging in a STEM is depicted in Figure 2.5.

Figure 2.5 Schematic representation of the HAADF detector set-up for Z-contrast imaging in a STEM. The conventional range of electron scattering angles gathered by each detector is also reported.

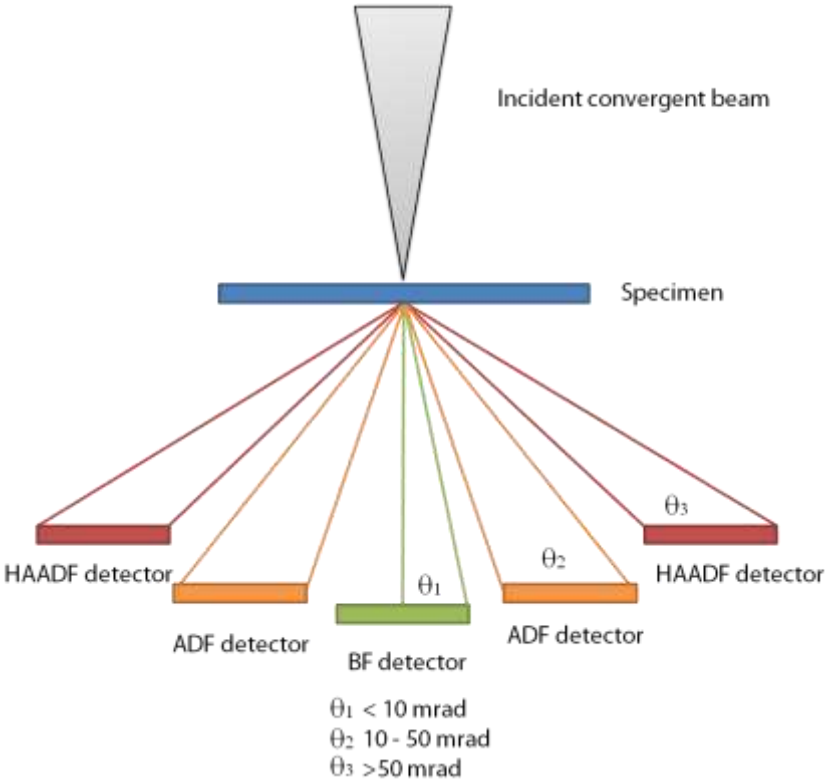

HRTEM is a very powerful technique for the characterization of crystallinity, defect structure, symmetry, morphology and facets of individual nanoparticles. However, it presents some limitations which must be remembered. Since it is a transmission technique, the samples must be electron transparent and, in addition, must be thin enough to minimize multiple diffraction of the electrons. Generally the specimens must have a thickness below 100 nm, or in some cases below 50 nm. Moreover, the high energy electron beam may alter and damage the specimen by heating it or by reducing susceptible materials such as some oxides. Nonetheless, it must be taken into account that HRTEM images are 2-D representation of a 3-D set of objects viewed by transmission rather than reflection, and sometimes the third dimension cannot be neglected. Recent developments in electron tomography (ET) and quantitative scanning TEM (STEM) have further expanded the abilities of TEM by allowing 3-dimensional (3D) reconstructions of nanomaterials instead of only 2-dimensional (2D) projections (*59*).

STEM operation mode is another way to perform the analysis of the specimen, consisting in scanning a focused convergent beam over the sample using a system of additional lenses, usually incorporated in the instrument. This operation mode has the advantage that the sample doesn't

have to be moved to get more than one image. Moreover, less noisy images than TEM DF can be obtained via the combination of the STEM mode with the ADF detector. The ability to quantify the size of individual nanostructures in the STEM is primarily determined by the size of the electron beam and the stability of the nanoclusters under the intense electron irradiation of the beam. The recent development of aberration correctors for STEM has largely improved the spatial resolution allowed by these instruments, taking the resolution to less than 0.1nm. However, this advance does not automatically improve sensitivity/accuracy when the size measurement is limited by electron irradiation effects such as chemical changes and the movement of the nanoclusters on the support surface.

Inelastic interactions of the beam electrons with the specimen, in which energy is transferred, also provide useful complimentary information and several analytical techniques have grown up around the TEM to exploit this. Energy transfer from an incoming high energy electron to one of the core electrons of an atom may result in ionization of the atom, forming a hole in the core. An electron in a higher energy level of the atom may then recombine with this hole, releasing its excess energy as an X-ray photon. The frequency of these photons is determined by the difference between the two electron energy levels and will therefore be characteristic of the nature of the atom from which it was emitted. In X-ray Energy Dispersive Spectroscopy (XEDS or EDX), these X-ray photons are collected and number of counts plotted against their energy to give a spectrum. This technique allows quantitative measurement of the elemental composition of the area of the sample illuminated by the beam and provides information which is not available from HRTEM itself. For this reason, XEDS spectrometer is commonly fitted to the modern TEM.

2.6 X-Ray Absorption Spectroscopy

X-ray Absorption Spectroscopy (XAS) is a well-established technique used for determining the local geometric and/or electronic structure of matter (*60*). XAS measures the energy-dependent fine structure of the X-ray absorption coefficient near the absorption edge of a particular element. According to Beer's Law, if X-rays of intensity I_0 are incident on a sample, the extent of absorption depends on the photon energy E and sample thickness t.

$$I_t(t) = I_0 \mathrm{e}^{-\mu(\mathrm{E})\mathrm{t}} \tag{2.17}$$

where I_t is the transmitted intensity and μ(E) is the energy-dependent X-ray absorption coefficient.

Over large energy regions, μ(E) varies approximately as:

$$\mu(E) \sim \frac{dZ^4}{\mathrm{m\ E}^3} \tag{2.18}$$

where *d* is the target density and Z and m are the atomic number and mass, respectively (*61*). Therefore, μ(E) decreases with increasing photon energy. However, if the photon energy equals or exceeds the binding energy of a core electron, another core electron can be excited and a sharp increase in absorption coefficient is observed. Above the absorption edge, the difference between the photon energy and the binding energy is converted into kinetic energy of the photoelectron and μ(E) continues to decrease with increasing photon energy. Core-hole states have a short lifetime (10^{-15} s), after which an electron from a higher energy state fills the hole, releasing the energy difference via fluorescence X-ray or Auger electron emission.

According to quantum mechanical perturbation theory, the transition rate between the core level and the final state is proportional to the product of the squared modulus of the matrix element M and the density of states ρ:

$$\mu \propto |M|^2 \rho \propto \left|\langle f|H_p|i\rangle\right|^2 \rho \tag{2.19}$$

where |i⟩ and |f⟩ are the initial and final state, respectively, and Hp is the electromagnetic field of the X-ray photon, the Hamiltonian that causes the transition (*60*). Both factors can cause a modulation of the absorption coefficient thus creating the X-ray absorption fine structure (XAFS). At the smallest X-ray energies for which the photon can be absorbed, the photoelectron will be excited to unoccupied bound states of the absorbing atom. This can lead to a strong increase of the absorption coefficient at particular X-ray energies corresponding to the energy difference between the core level and the unoccupied states (pre-edge absorption bands). For higher X-ray energies, the photoelectron is promoted to a free or continuum state. The wave thus created propagates outwards and is scattered at neighboring atoms. The outgoing and scattered waves interfere in a manner that depends on the geometry of the absorber environment and on the photoelectron wavelength, which is inversely proportional to the photoelectron momentum and therefore changes with photon energy. Thus, the final state is an energy-dependent superposition of outgoing and scattered waves. Because the initial state is highly localized at the absorbing atom, the matrix element M in (2.19) depends on the magnitude of the final state wave function at the site of the absorbing atom. Constructive or destructive interference of outgoing and scattered

waves thus increases or decreases the absorption probability, creating an energy-dependent fine structure of the absorption coefficient. Figure 2.6 schematically shows the absorption fine structure as a function of photon energy. Three regions are commonly distinguished: the pre-edge region, the X-ray absorption near edge structure (XANES) and the extended X-ray absorption fine structure (EXAFS)(*62*).

Figure 2.6 Example of XAS spectrum with the three regions of pre-edge, XANES and EXAFS highlighted.

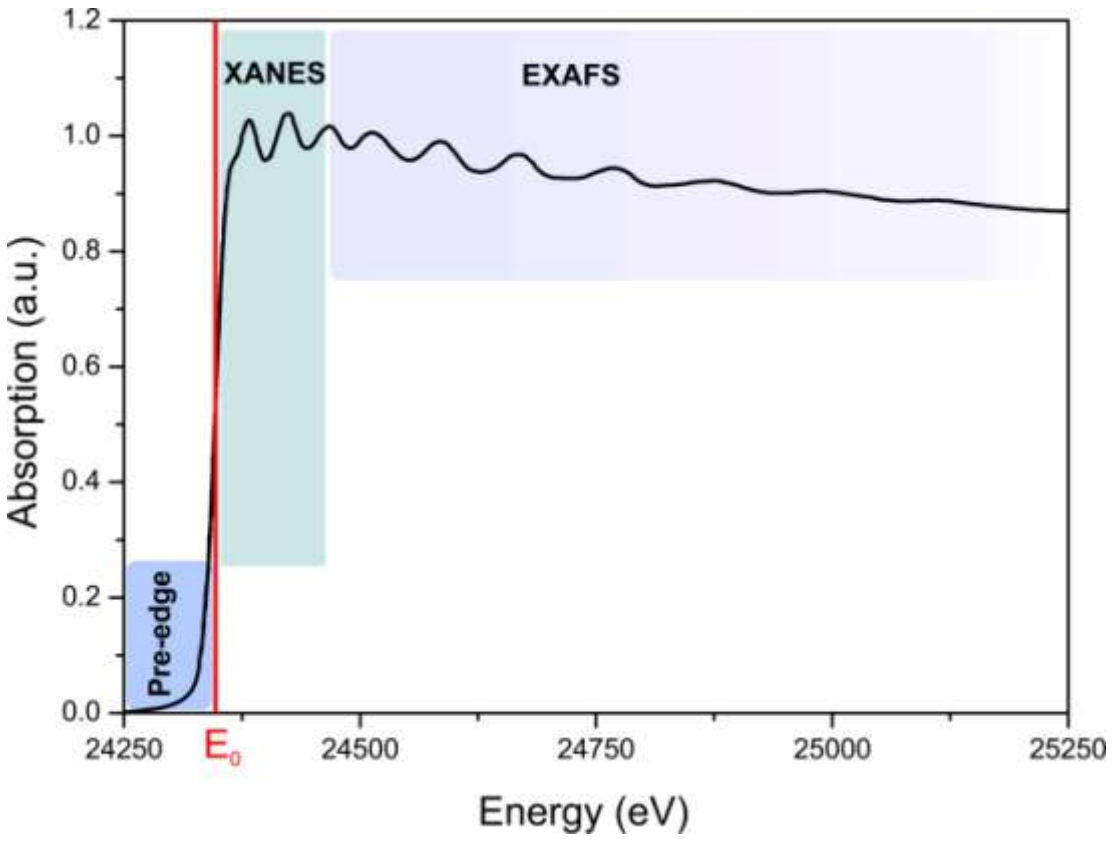

XANES is characterized by transitions of the photoelectron to unoccupied bound states and is therefore sensitive to the chemical bonding, exhibiting characteristic features for different oxidation states and compounds of the absorbing atom(*60*). The XANES features are also influenced by strong multiple scattering effects which depend on the three-dimensional geometry of the local structure around the absorbing atom. This provides a means of distinguishing between different crystal phases. Although significant progress has been made over recent years, theoretical calculations of the fine structure in this region are complex and the accuracy of such simulations is still limited. Therefore, the measured spectra are usually compared to those of known standards

and the ratios in which the standards are present in the sample are calculated using linear combination fitting.

In the EXAFS region (photon energies higher than ~30 eV above the edge), the photoelectron is promoted to a free or continuum state, and the signal depends on the atomic arrangement around the absorber (*60*). EXAFS contains information about the coordination number, interatomic distances and structural and thermal disorder around a particular atomic species. An advantage of EXAFS with respect to XRD is that it does not require long-range order and is applicable to a wide range of ordered and disordered materials. Theoretical calculations of the fine structure in the EXAFS region have also improved enormously during the last two decades and simulations with sufficient accuracy are now available. Nevertheless, the measurement of suitable standards still constitutes an important part of the experimental procedure.

Most XAS experiments are performed at synchrotron sources due to the requirement of high X-ray intensities and a continuous energy spectrum. In a typical XAS beamline, mirrors are used to collimate and focus the beam while apertures and slits define its size. In a classical XAFS beamline, a double crystal monochromator is used to select X-rays of a very narrow energy band using the criterion for Bragg diffraction. Harmonic energies (that satisfy the Bragg condition with $n \geq 2$) are removed from the beam by slightly detuning the monochromator, which decreases the transmission of harmonics significantly more than that of the primary energy. Alternatively, X-ray mirrors can be used that only reflect energies below a critical value. With such an experimental arrangement, the absorption coefficient can be measured as a function of X-ray energy.

In general, the absorption coefficient can be detected either directly by measuring the intensities of incoming and transmitted beam (transmission mode) or indirectly by measuring the intensity of the incoming beam and of the decay products, such as fluorescent X-rays or Auger electrons (fluorescence or electron yield mode). The experimental setups for the various acquisition modes during XAS experiments are shown schematically in Figure 2.7.

Figure 2.7 Schematic representation of the experimental setup for the different XAS detection modes

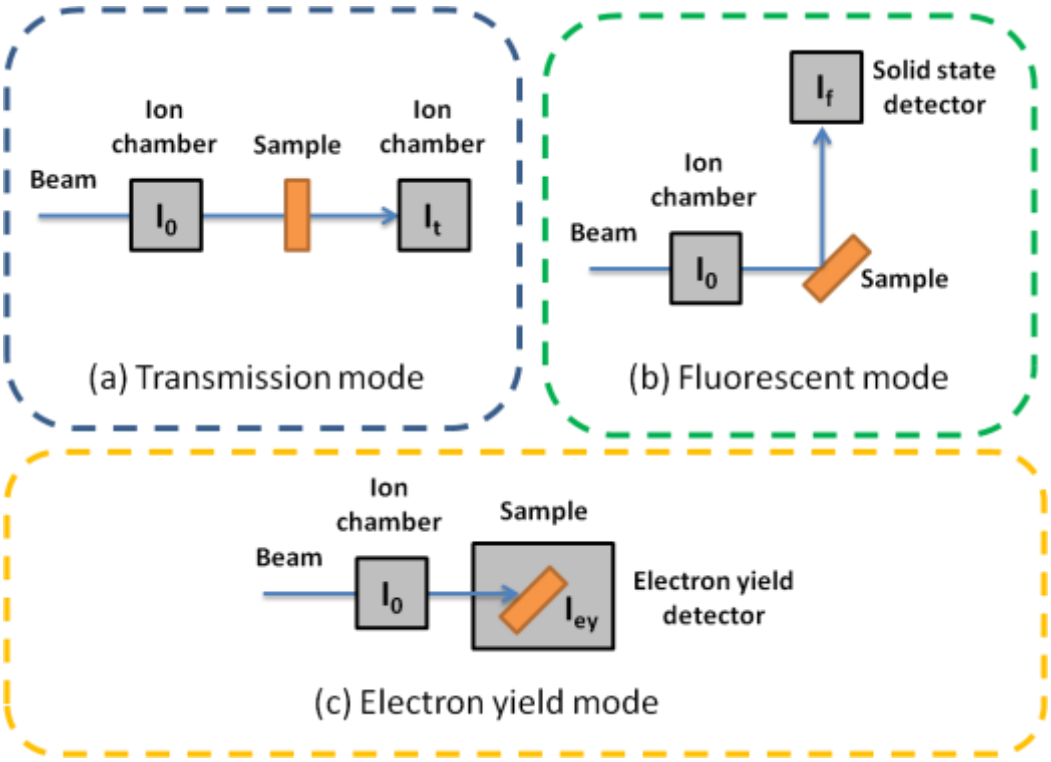

Once the signal is recorded, XAS data require some mathematical analysis in order to be meaningful. There exists a variety of ways to analyze XAS data and a large number of codes and programs are available. In general, data from the XANES and EXAFS region are analyzed separately. This is due to the different information contained in both spectral regions and to the fact that theoretical modeling for XANES is not yet as advanced as it is for EXAFS. The calibration of the energy scale and the alignment of different spectra is very important in both cases: in the XANES for the determination of edge shifts and in the EXAFS for accurate bond length determination. For each absorption edge, the beamline monochromator has to be calibrated with a known reference, often a thin metal foil, measured simultaneously with each sample of interest.

The first step in XANES analysis is the normalization of the spectrum: this removes effects of sample thickness and concentration and allows the direct comparison of different samples and measurements. The spectrum in the energy region before the absorption edge is fitted by a linear pre-edge line, while the spectrum well above the absorption edge is typically approximated by a quadratic post-edge line. The edge step $\Delta\mu_0$ is obtained as the difference between pre-edge and post-edge lines at the absorption threshold E_0. A normalized XANES spectrum is finally obtained by subtracting the pre-edge line from the measured spectra over the whole energy range and dividing by $\Delta\mu_0$, therefore flattening the spectrum after the threshold. The normalized spectrum

can be compared with spectra of standard compounds. The relative amount of the most important components of the sample can be determined by fitting the experimental normalized spectrum with a linear combination of the spectra of standard compounds, the so-called Principal Component Analysis (PCA).

EXAFS analysis requires more steps: first, the fine structure χ(E) is isolated from the absorption background, fitting the pre- and post-edge lines. The pre-edge line is subtracted from the spectrum over the whole energy range and the absorption background $\mu_0(E)$ is typically approximated by a spline function that approaches the post-edge line at energies well beyond the absorption edge. The difference between the absorption coefficient μ(E) and the background $\mu_0(E)$ is normalized with respect to the step height $\Delta\mu_0$, yielding the fine structure χ(E). In order to calculate χ(k), the threshold energy E_0 is needed: this is typically taken as the maximum of the derivative of μ(E) with respect to E or as the energy corresponding to the half of the step height. The second step is a Fourier transform of the data into R-space. Fourier transformation (FT) of the EXAFS provides a means to visualize different scattering contributions and is often used during analysis. When Fourier transformed, different scattering contributions with a large difference in Rj will produce well separated peaks with amplitudes approximately proportional to Nj /σj . However, one should remember that the FT is a complex function and both magnitude and phase (or alternatively, real and imaginary part) have to be considered for the full information content.

A back-transformation can be used to isolate different scattering contributions if their signals are well separated in R-space. However, this procedure usually fails for higher coordination shells due to the overlap of different scattering contributions. To overcome this problem, the path fitting approach can be used. Path-fitting is a model-dependent approach based on the cumulant expansion of the different single and multiple scattering paths and requires some pre-existing knowledge about the system under investigation. The analysis starts with a model structure that specifies the absorbing atom and the position and type of the surrounding atoms that are to be considered in the fitting procedure. The biggest advantage of the path fitting approach is the ability to analyze the structural parameters beyond the first coordination shell which often contain crucial information not available from the first nearest neighbor environment.

EXAFS experiments on Pd@CeO_2-based catalysts for methane oxidation (Chapter 3) were performed at the SAMBA beamline of Synchrotron SOLEIL (France) with a Si 220 double crystal monochromator. The monochromator was kept fully tuned and harmonics were rejected by a pair of Pd-coated, Si mirrors. Spectra were measured in transmission mode using ionization chambers as detectors. One chamber was used as the baseline monitor and two other chambers were used to continuously check the stability of the energy scale by placing one after the sample and the other

after a reference foil. Because we used Pd mirrors to reject harmonics, the baseline was checked to ensure the absence of a residual Pd signal due to nonlinearity in the detectors. The experiments were conducted using the transmission and fluorescence cell fully described in (*63*). 8 mg of catalyst, diluted 1 : 10 by weight with BN, and a total gas flow rate of 12 mL min^{-1} (0.5 % CH_4, 2.0 % O_2 , 15% water if needed, and N_2 balance) were used for Ce L(III) edge experiments. 95 mg of catalyst and a total gas flow rate of 130 mL min^{-1} (0.5 % CH_4, 2.0 % O_2 , 15% water if needed, and N_2 balance) were used for Pd K edge experiments. Products analysis systems was a Cirrus - MKS mass spectrometer, and activity comparable to that observed during catalytic test were observed. The fractions of Ce(III) and Pd(0) in the samples were determined by fitting the XANES (X-Ray Absorption Near Edge Spectroscopy) part of the spectrum using a linear combination of spectra for $CeAlO_3$ and CeO_2 to fit data for Ce and a combination of spectra for PdO and a Pd foil to fit data for Pd. All measurements were performed during the same beam session. EXAFS data were fit with Feff8.4 (*64*) and Horae (*65*) software packages. Fits were performed in r-space and a Hanning window was applied in k-space from 3 to 13 A^{-1} (the window was zero outside these values).

EXAFS experiments on Pt-Co based catalysts for hydrodeoxygenation of biomass-derived feedstock (Chapter 4.3) were performed at the beamline 5BM-D at the Advanced Photon Source, Argonne National Laboratory. Catalyst samples were diluted with boron nitride and pressed into pellets in a six-well sample holder. The catalysts were reduced at 250 ^oC (pre-treatment temperature) and 400 ^oC (higher than the pretreatment temperature) for 1 h (ramp rate 5 ^oC min^{-1}) under atmospheric pressure in a 40 ml min^{-1} hydrogen flow prior to measurement at ambient temperature under hydrogen. Data processing was done using the program Athena of the Demeter suite. Fitting of the EXAFS oscillations was done using the Artemis program of the same suite. For the Pt L3 edge, oscillations were fitted using the Fourier transform (FT) from wavenumbers k = 3 $Å^{-1}$ to k = 12 $Å^{-1}$ and R = 1.6 Å to 3.3 Å while for the Co K edge, oscillations were fitted using a FT from wavenumbers k = 3 $Å^{-1}$ to k = 12 $Å^{-1}$, and R = 1.4 Å to R = 3.2 Å. Amplitude reduction factors were calculated using the EXAFS spectrum of the Pt or Co foils and assuming a coordination number (CN) equal to 12. A single Debye-Waller factor was used for all scattering paths.

2.7 X-Ray Photoemission Spectroscopies

Photoemission spectroscopy (PES) refers to the measurement of the kinetic energy and number of photoelectrons, *i.e.* electron emitted from a sample by the photoelectric effect, in order to determine the oxidation state of the chemical species (through the binding energies of electrons) and their relative amount in the sample under investigation. Since photoelectrons have a short inelastic mean free path in matter, PES techniques are very sensitive to the composition of the sample surface (in the order of 1-10 nanometers), and are thus very relevant for studying

catalytic materials (*66*). PES is a general term indicating various techniques, depending, among others, on the photon energy (Ultraviolet Photoemission Spectroscopy – UPS; X-Ray Photoemission Spectroscopy – XPS), on the source of photon (Synchrotron Radiation Photoelectron Spectroscopy – SRPES) and the pressure in the sample chamber (Near-Ambient Pressure and Ambient Pressure XPS – NAP-XPS and AP-XPS).

The power of XPS for chemical analysis derives from the fact that electron core levels have small chemical shifts depending on the chemical environment of the atom that is ionized. XPS allows to determine the formal oxidation state of the atom, the identity of its nearest-neighbors and its bonding hybridization to that nearest-neighbor atoms. XPS is routinely used to analyze inorganic compounds, metal alloys, semiconductors, catalysts, ceramics and many others. It is a powerful tool to detect and quantify impurities, since the detection limits for most of the elements (on a modern instrument) are in the parts per thousand range. One limit of XPS is that it requires high vacuum (P ~ 10^{-8} millibar) or ultra-high vacuum (UHV; P < 10^{-9} millibar) conditions, strongly limiting XPS use for insightful *in-situ* analysis of catalysts. However, a current area of development is adopting differential pumping in order to expose the sample to higher pressure (tens of millibar for NAP-XPS) and overcoming this obstacle. Another intrinsic drawback of XPS is that some materials can be sensitive to X-rays or vacuum degradation, causing a modification of the sample upon analysis.

XPS can be performed using a common XPS system equipped with an Al Kα or Mg Kα X-rays source, or using a synchrotron-based light source combined with a custom-designed electron energy analyzer (SRPES). Since the energy of an X-ray with particular wavelength is known (1486.7 eV for Al Kα source) and the emitted electrons' kinetic energies are measured, the electron binding energy of each of the emitted electrons can be determined by using the energy conservation equation:

$$BE = E_p - (E_k + \Phi) \tag{2.20}$$

where BE is the binding energy of the electron, E_p is the energy of the X-ray photons, E_k is the kinetic energy of the photoelectron as measured by the instrument and Φ is the work function, an adjustable instrumental correction factor, dependent on both the spectrometer and the sample. It accounts for the few eV of kinetic energy given up by the photoelectron as it becomes absorbed by the instrument's detector. In practice, it is a constant parameter that rarely needs to be adjusted.

A typical XPS spectrum is a plot of the number of electrons detected versus their BE. Each element produces a characteristic set of XPS peaks at characteristic BE values, corresponding to the

electron configuration of the electrons within the atoms. The number of detected electrons for a certain signal is directly related to the amount of atoms of element within the XPS sampling volume, so atomic percentages can be determined, upon correction by a relative sensitivity factor and normalization. The quantitative accuracy depends on several factors, such as signal-to-noise ratio, peak intensity, surface volume homogeneity, correction for energy dependence of electron mean free path and degree of sample degradation due to analysis.

The main components of a XPS system (Figure 2.8) include a source of X-rays, an ultra-high vacuum (UHV) stainless steel chamber with UHV pumps, an electron collection lens, an electron energy analyzer, magnetic field shielding, an electron detector system (electron multiplier), a moderate vacuum chamber for sample introduction, sample mounts and stage, and a set of stage manipulators.

Figure 2.8 Graphical representation of a XPS system.

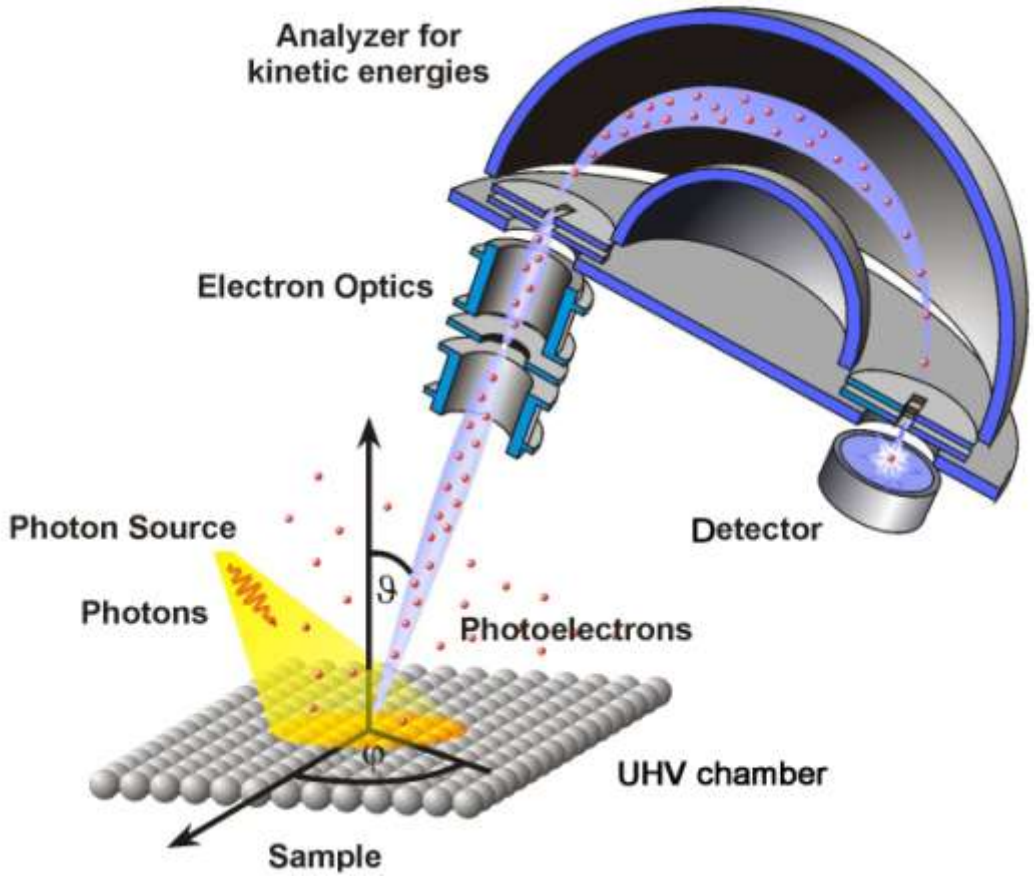

The development of the near ambient pressure XPS (NAP-XPS) in the past decades made it possible to investigate surfaces under reactive environments. The main experimental problem is

the electron mean free path in the gas phase (*e.g.* 0.04 cm at 1 mbar for 50 eV electrons or 0.4 cm at 1000 eV), which is much shorter than the classic sample-analyzer distance (15 mm), making the probability to detect photoelectrons extremely low. This problem has been overcome by placing the sample surface very near the electron energy analyzer entrance and by differentially pumping the analyzer. To do so, the analyzer entrance diameter has to be small, which results in a small sampled area. A small focal spot of X-rays (~100 μm) impinging on the sample is also indispensable.

In the present work, NAP-XPS experiments were carried out in a custom-built system (SPECS Surface Nano Analysis, GmbH Germany) equipped with a PHOIBOS 150 Hemispherical Energy Analyzer, coupled with a differentially pumped electrostatic pre-lens system. The reaction NAP cell was installed in an analysis chamber that had a base pressure of ~10^{-10} mbar and allowed *in situ* XPS studies at pressures up to 20 mbar. A high-intensity, monochromatized Al Kα X-ray source (1486.6 eV) was used to record the spectra of Cu 2p, Ni 2p, O 1s, P 2p, N 1s and C 1s core levels. Binding energies are reported after correction for charging, using metallic Cu $2p_{3/2}$ signal (932.4 eV) as a reference.

2.8 Atomic Force Microscopy

Atomic Force Microscopy (AFM) is a type of scanning probe microscopy, with demonstrated resolution on the order of fractions of a nanometer. The AFM has three major abilities: force measurement, imaging, and manipulation. For imaging, a mechanical probe (tip) attached to a cantilever is scanned on the specimen surface, so that interatomic forces between the tip and the specimen surface lead to a deflection of the cantilever, according to Hooke's law (Figure 2.9). Forces that are measured in AFM include mechanical contact force, van der Waals forces, capillary forces, chemical bonding, electrostatic forces, magnetic forces, *etc*. The deflection of the cantilever is detected (*e.g.* by interferometry, piezoresistive methods) and converted to an electrical signal of intensity proportional to the deflection, so that a trace of the sample surface is outlined during a scan. In practice, several different imaging modes can be used: either the value of the deflection (contact mode), or the amplitude of an imposed oscillation of the cantilever (tapping mode), or the shift in resonance frequency of the cantilever (non-contact mode) can be monitored. Raster scanning of the sample gives a tridimensional map of the surface, commonly displayed as a pseudo-color plot.

Figure 2.9 Graphical representation of an AFM system.

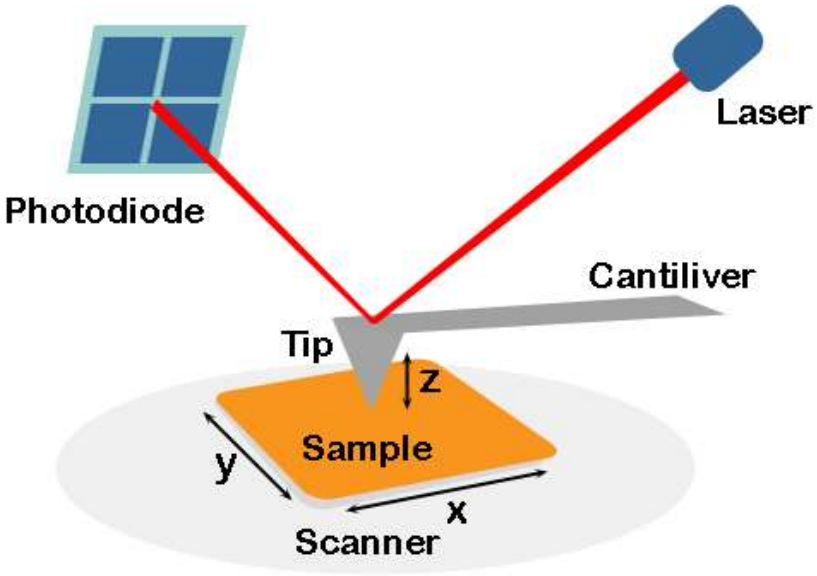

Compared to competitive technologies such as optical microscopy and electron microscopy, the AFM does not require lenses or beam irradiation, avoids loss of space resolution due to diffraction limit and aberration, and does not require vacuum to operate. Unlike the SEM electron microscope, which provides a two-dimensional image of a sample, the AFM gives a three-dimensional surface profile. In addition, AFM does not require special sample treatments such as metal/carbon coating, usually employed in SEM for insulating materials.

Disadvantages of AFM are the single scan image size and the scanning speed. In one pass, AFM can only image an area up to 150×150 μm, so a typical scan requires several minutes, while SEM can image an area up to square millimeters, allowing to scan at near real-time, although at relatively low quality. Parallel probes may be used to improve the size of the scanned area in AFM, but this is not always feasible. AFM images can also be affected by nonlinearity, hysteresis, creep of the piezoelectric material and image artifacts. Some artifacts are unavoidable, and could be induced by an unsuitable tip, a poor operating environment, or even by the sample itself (presence of steep walls or high-curvature features).

2.9 Scanning Electron Microscopy

Scanning electron microscopy (SEM) is a type of electron microscopy that produces images of a sample by scanning it with a focused beam of electrons. The beam interaction with the sample produces a variety of signals containing information about the sample's surface topography and

composition. Secondary electrons emitted by atoms excited by the electron beam are most commonly analyzed (Figure 2.10). The number of secondary electrons that can be detected depends, among other things, on specimen topography. Resolution better than 1 nanometer can be achieved. Since the electron beam is very narrow, SEM micrographs have a large depth of field, yielding a three-dimensional appearance useful for understanding the surface structure of a sample. Specimens are usually observed in high vacuum, but modern applications allow low vacuum and wet conditions (in environmental SEM – ESEM) operations.

Figure 2.10 The types of signals produced by an SEM and the information they contain. Secondary electron detectors are standard equipment in all SEMs, but it is rare that a single machine would have detectors for all other possible signals. Interaction volume is depicted by a blue drop.

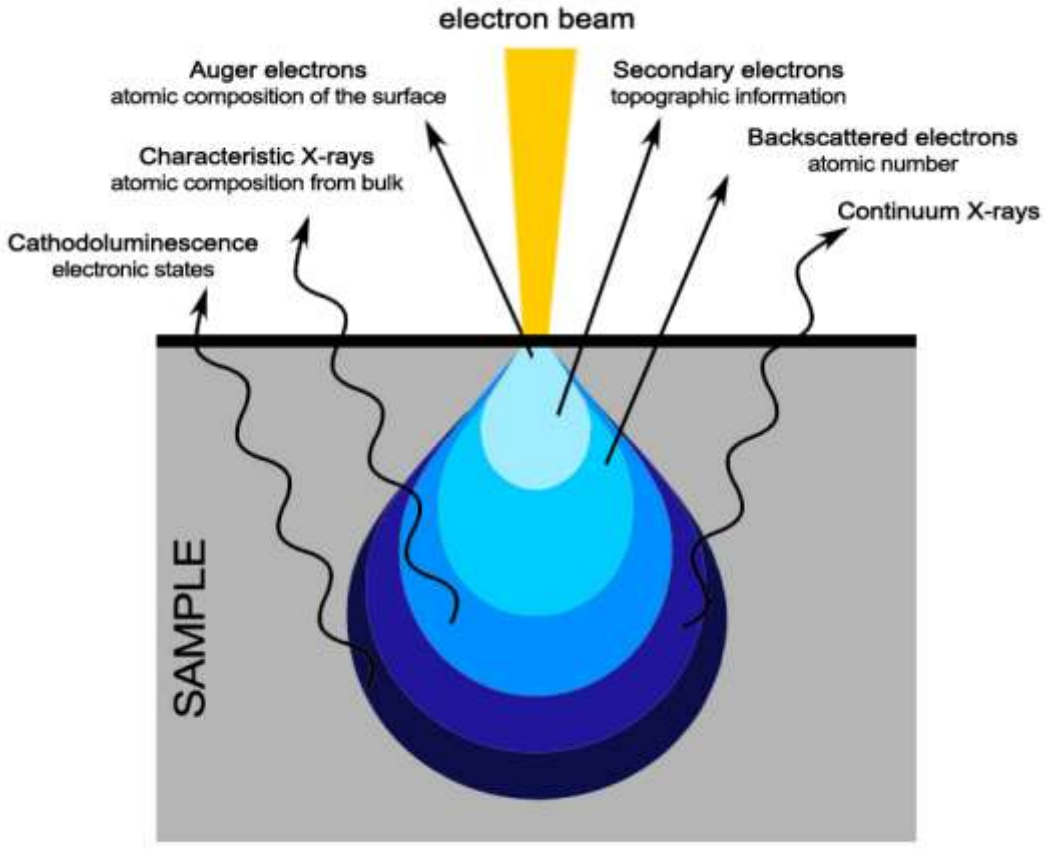

The different signals result from interactions of the electron beam with atoms at various depths within the sample. The primary electrons (of the beam) lose energy by repeated random scattering and absorption within a teardrop-shaped volume of the specimen known as the interaction volume. The interaction volume extends from less than 100 nm to 5 µm into the surface, depending on the electron's landing energy, the atomic number of the specimen and the

specimen's density. The secondary electrons are emitted from very close to the specimen surface, while back-scattered electrons (BSE) and characteristic X-rays (EDX) emerge from deeper locations within the specimen. BSE and EDX are used in analytical SEM, because they are dependent on the atomic number (Z) of the specimen, providing information about the distribution of different elements in the sample.

For conventional imaging in the SEM, specimens must be electrically conductive, at least at the surface, and electrically grounded to prevent the accumulation of electrostatic charge at the surface, scanning faults and image artifacts. Insulators are therefore usually coated with an ultrathin coating of electrically conducting material (such as Au, Pt, Ir, W, Cr or graphite), deposited on the sample either by low-vacuum sputter coating or by high-vacuum evaporation. Otherwise, low-voltage mode SEM operation or ESEM can be employed to reduce charging problems. In low-voltage SEM operating conditions must be adjusted such that the incoming beam current is equal to sum of secondary and backscattered electrons currents. In ESEM instruments the specimen is placed in a relatively high-pressure chamber and differential pumping is used to keep vacuum adequately low at the electron gun. The high-pressure region around the sample in the ESEM helps neutralizing charges.

In a typical SEM, an electron beam (0.2 – 40 keV energy) is emitted from an electron gun (a heated tungsten filament or a field emission gun). The electron beam is focused by condenser lenses to a spot about 0.4 – 5 nm in diameter, and finally deflected by scanning coils or deflector plates, in order to raster scan the sample surface. Magnification in an SEM can be controlled over a range of about 6 orders of magnitude from about 10 to 500'000 times. Magnification results from the ratio of the dimensions of the raster on the specimen and the raster on the display device. It is therefore controlled by the scanning coils, the deflector plates, and not by objective lens power as in optical and transmission electron microscopes. Depending on the instrument, the resolution can fall somewhere between less than 1 nm and 20 nm. The spatial resolution in SEM is limited by the size of the interaction volume and by the size of the electron spot, which in turn depends on the wavelength of the electrons and the optical system. The spot size and the interaction volume are both large compared to the distances between atoms, so the resolution of the SEM is not high enough to image individual atoms, as is possible transmission electron microscope (TEM). The advantages of SEM include large area imaging, bulk materials imaging (not possible with TEM), and the ability to measure the composition and properties of the specimen in a variety of analytical modes.

2.10 Catalytic Activity Measurements

The catalytic tests reported in this thesis were performed on three types of reactivity lines, that are schematically represented in Figure 2.11-Figure 2.13.

2.10.1 Low Pressure, Gas Flow Reactor Line

For methane catalytic oxidation experiments, the system depicted in Figure 2.11 was used.

Figure 2.11 Schematic representation of the reactivity line used for testing the activity of catalysts in methane catalytic oxidation.

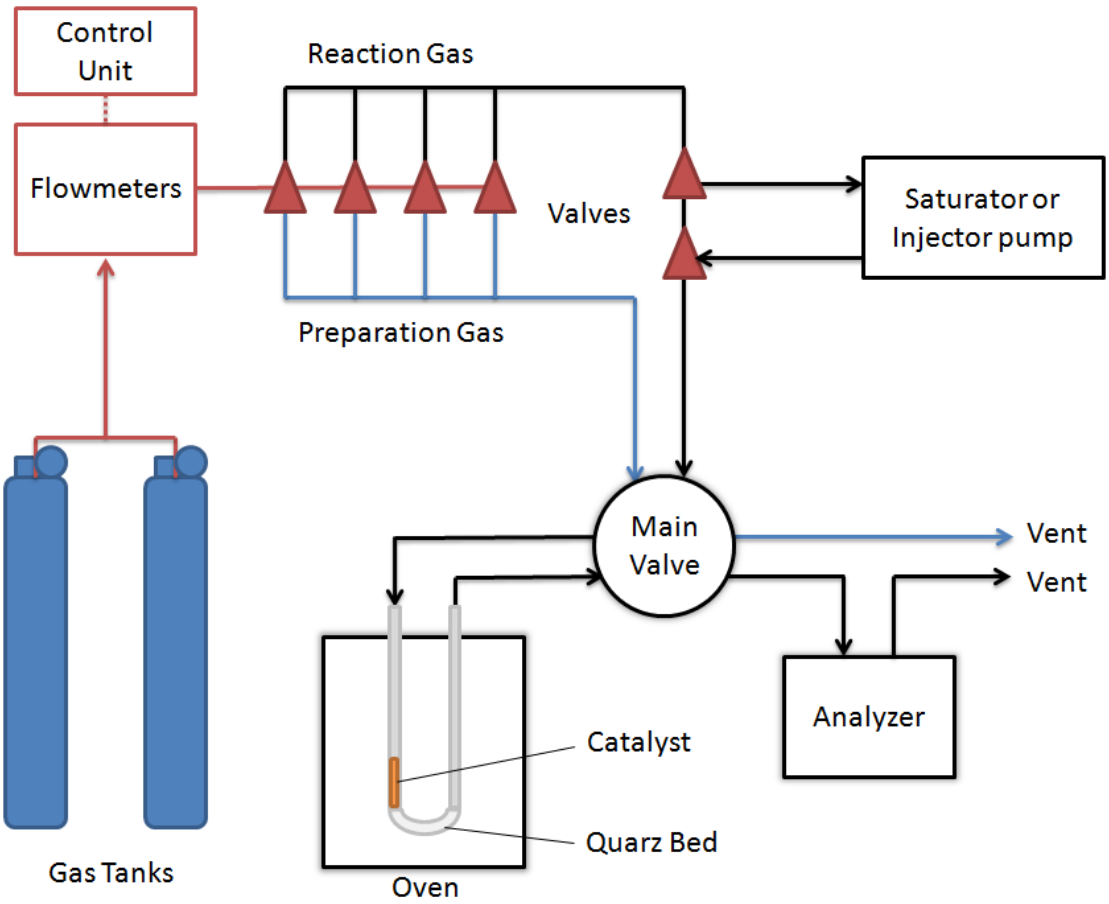

The gas mixing system allows to pre-treat the catalyst (*e.g.* reduction or oxidation) and to simultaneously acquire information on the composition of the reaction mixture, bypassing the reactor. The mixing system is composed of four flow meters controlled by a central control unit (Brooks Instruments). A system of valves before the flow meters allows the selection of the desired gases. A second system of valves positioned after the flow meters diverts each gas to one of the two following branches: the reaction line or the preparation line. The preparation line is not

connected to the analyzer and is therefore usually employed for the pre-treatment of the catalyst. The reaction line, connected to the analyzer, is used to perform the catalytic tests. A 10 way valve allows to select which one of the two gas streams passes through the reactor. A saturator is connected to the reaction line by two switching valves and is used to introduce water vapor in the reaction gas mixture. All the lines are heated at 125 °C in order to avoid condensation of vapor.

A U-shaped quartz reactor with a 4 mm internal diameter was used for testing powdered catalysts. The sample was located between two layers of granular quartz in order to sustain the catalyst powder and preheat the reagents. The reactor was heated by a oven (Micromeritics) equipped with a PID controller (Eurotherm 847) and the temperature of the catalyst was measured with a K-type thermocouple[8] inserted inside the reactor catalytic bed. In case of model, flat catalysts, a U-shaped quartz reactor of 1.5 cm internal diameter was used.

The catalytic system was connected to a mass spectrometer Hiden Analytical HPR20, equipped with a ionization chamber and a quadrupole to separate the ions basing on their mass, plus two detectors: a Faraday detector and a Secondary Electron Multiplier (SEM) detector. The catalytic activity were calculated on the basis of the parental ions of the species of interest, after correction for the cracking pattern of other signals.

2.10.2 High Pressure, Three Phases Reactor Line

For most of the catalytic hydrodeoxygenation reactions, the flow system was designed to work at high pressures (Figure 2.12). The chosen setup allows to feed H_2 gas and a liquid two desired and independent flow rates. H_2 (UHP grade, Airgas) flow rate was controlled by adjusting the length (corresponding to a certain pressure drop) of a 0.002-inch ID capillary tubing (Valco Instruments, Inc.). The liquid was injected by a High-Pressure Liquid Chromatography (HPLC) pump (Series I+, Scientific Systems Inc.), which was also used to measure the total pressure in the reactor. The pressure within the reactor was controlled by a backpressure regulator (KPB series, Swagelok) placed at the reactor exit. The liquid flow rates were varied from 0.02 to 0.2 mL min^{-1}, while the H_2 flow rates were 2 to 20 mL min^{-1}. The reactor gaseous and liquid effluents were examined separately by injection into a GC/MS.

Figure 2.12 Schematic representation of the reactivity line used for testing the activity of catalysts in catalytic hydrodeoxygenation reactions.

[8] K-type: non-expensive thermocouple composed of chromel (90% nickel and 10% chromium)- alumel (95% nickel, 2% manganese, 2% aluminium and 1% silicon)

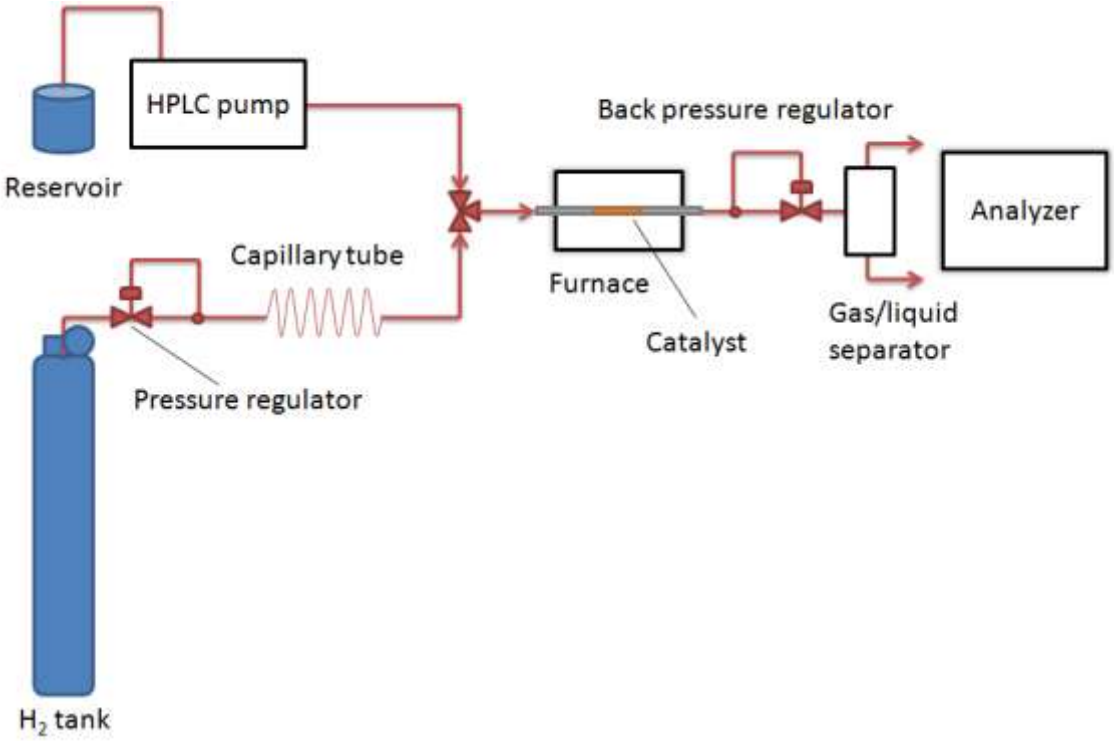

A GC-MS (QP-5000, Shimadzu) equipped with a capillary column (HP-Innowax, Agilent Technologies) was used to measure the products composition. For furfural experiments, the calibration of liquid samples was accomplished using standard solutions with known concentrations of furfural, 2-methylfuran (MF), 2-methyltetrahydrofuran (MTHF), furfuryl alcohol (FA), tetrahydrofurfuryl alcohol (THFA), furfuryl-dipropyl acetal (FAct), furfuryl-propyl ether (FEther), 2-pentanone, 2-pentanol, and pentane. Calibration of the gas-phase samples was verified for furan, furfural, FA, and MF using the known vapor pressures of the pure compounds. For quantification of FEther, the GC sensitivity was assumed to be the same as that for FAct. For open-ring pentanedione and ether products, the GC sensitivity was assumed to be the same as 2-pentanone. Since the quantities of most of these side products were relatively small, these assumptions will not have a major impact on the conclusions of the study. Selected HDO experiments were performed in a gas mixing system similar to the one described in Figure 2.11, saturating the gas feed with furfural vapor.

For 5-hydroxymethylfurfural (HMF) experiments, the selectivity for each product was quantified using standard solutions with known concentrations of HMF, dimethylfuran (DMF), dimethyltetrahydrofuran (DMTHF), 2-hexanone, 2-hexanol, and 2,5-hexandione (all purchased from Sigma Aldrich). For quantification of other furan-based, intermediate products, the GC

sensitivity was assumed to be the same as that for HMF. For open-ring, ether products, the GC sensitivity was assumed to be the same as 2-hexanone or 2,5-hexandione.

2.10.3 Photocatalytic Reactor Line

The photocatalytic activity of dyes-sensitized Pt/TiO_2 was studied under simulated solar light irradiation in the visible-IR range using a Solar Simulator LOT-Oriel, equipped with a 150 W Xe lamp, an Atmospheric Edge Filter and a cut-off filter at 420 nm. Irradiance was ~ 6 x 10^{-3} W m^{-2} in the UV-A range and ~ 180 W m^{-2} in the visible range (400 – 1000 nm). The photocatalytic system setup is schematically represented in Figure 2.13.

Figure 2.13 Schematic representation of the photocatalytic reactor used for testing the activity of dyes-sensitized TiO_2.

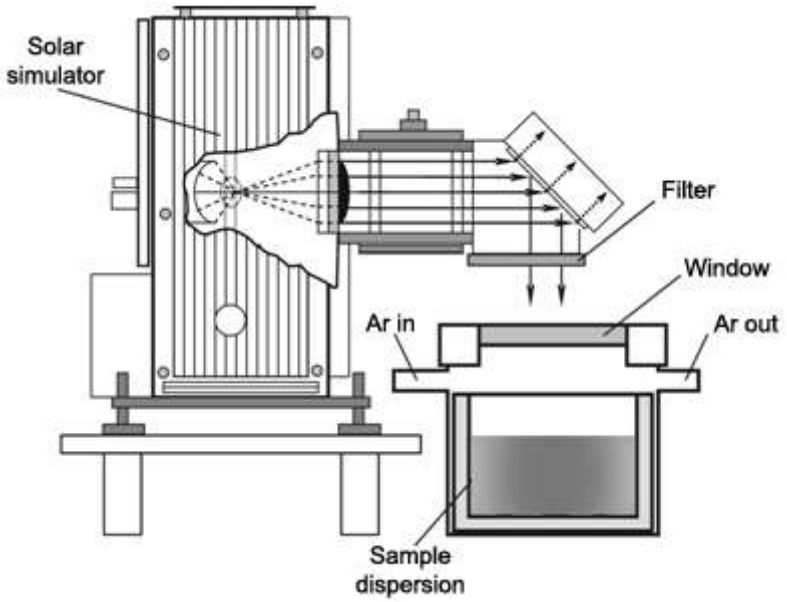

The reactor is comprised of a cylindrical Teflon-lined stainless steel container connected to the gas carrier line and hermetically sealed with a quartz window. The catalyst is dispersed with a magnetic stirrer within the aqueous solution containing the sacrificial agent employed. The reactor is thermostated at 25 °C. The produced H_2 was stripped from the reactor by an Ar flow (15 mL min^{-1}) and the concentration of H_2 in gas stream was quantified using a Agilent 7890 gas chromatograph equipped with a TCD detector, connected to a Carboxen 1010 column (Supelco, 30 m x 0.53 mm ID, 30 μm film) using Ar as carrier.

In order to evaluate and compare the performance of photocatalytic systems, some specific parameters are used. The Turnover Number (TON) is the number of electrons which react to produce H_2, per active site, before the catalyst becomes inactive. A stable, ideal catalyst would have an infinite TON. In the specific case of dye-sensitized photocatalytic evolution of H_2, the number of

electrons that react is equal to 2 times the molecules of produced H_2, and the catalytic active sites may be considered equal to the number of sensitizer molecules, so that the simplified Equation 2.21 is used in practical experiments:

$$TON = \frac{2n_{H_2}}{n_{dye}} \quad (2.21)$$

Since TONs are dependent on the irradiation period, their values should be always referred to the timescale [*e.g.*, TON(5 h)]. The Turnover Frequency (TOF), that is rate of H_2 production per active site, can also be used to compare photocatalytic activities. It should be noted that TON and TOF are dependent on many parameters, such as temperature, intensity and wavelength range of light irradiation.

Apparent Quantum Yield (AQY) and Internal Quantum Yield (IQY) are other parameters that can be used to compare different catalytic systems. For AQY calculation, the number of catalytic sites is replaced by the number of incident photons in the TON equation (Equation 2.22). It is called *apparent* QY because not all the incident photons are effectively absorbed and/or reach the reaction center.

$$AQY = \frac{2n_{H_2}}{n_{incident\ photons}} \quad (2.22)$$

For AQY calculation, the number of incident photons is typically measured as a function of the wavelength by using a monochromatic light source or band-pass filters. In comparative studies, AQY is usually reported at the same wavelength, even if a more indicative value should be taken at the maximum of the Vis absorption of the dye-sensitized photocatalyst, which depends on the specific dye sensitizer.

In the Intrinsic or Internal Quantum Yield (IQY) (Equation 2.23), the absorbed photons actually reaching the active site are considered. It should be noted that, by definition, AQY ≤ IQY. However, IQY is rarely used since the real number of absorbed photons is hard to determine for a dye/Pt/TiO_2 suspension in water, because of light scattering.

$$IQY = \frac{2n_{H_2}}{n_{absorbed\ photons}} \quad (2.23)$$

Solar-to-Hydrogen (STH) energy conversion efficiency is the efficiency of the system in terms of the amount of incoming solar energy converted into chemical energy in the hydrogen product (Equation 2.24), where F_{H_2} is the flow of H_2 produced (expressed in mol s^{-1}), $\Delta G^0_{H_2}$ is the enthalpy associated with H_2 combustion (237×10^3 J mol^{-1}), S is the total incident light irradiance (expressed in W cm^{-2}), and A_{irr} is the irradiated area (expressed in cm^2).

$$STH = \frac{F_{H_2} \Delta G^0{}_{H_2}}{S\, A_{irr}} \tag{2.24}$$

An alternative way to describe the conversion efficiency is the Light-to-Fuel Efficiency (LFE) (Equation 2.25), in which $\Delta H^0_{H_2}$ is the enthalpy associated with H_2 combustion (285.8×10^3 J mol^{-1}).

$$LFE = \frac{F_{H_2} \Delta H^0{}_{H_2}}{S\, A_{irr}} \tag{2.25}$$

Both STH and LFE are dependent on the experimental conditions and the irradiation time, so comparison of STH and LFE values among different studies should be taken carefully. Typical reported values of STH and LFE are below (in most cases much below) 1%, comparable to the low efficiency of the natural photosynthesis (*67*).

3. Methane Catalytic Oxidation

3.1 Introduction

Methane is an abundant and available energy source, widely employed for power generation by thermal combustion and as a fuel in Natural Gas Vehicles (NGVs). However, methane is a potent greenhouse gas, 20 times as powerful as CO_2, so its release in the atmosphere due to incomplete burning should be mitigated. Catalytic oxidation is widely employed in industrial and vehicles exhaust after treatments because it drastically reduces the temperature required for hydrocarbons abatement. Nevertheless, CH_4 is the most stable alkane and its activation at low temperature (<500 °C) is problematic. This represents a serious challenge for environmental protection and for complying with upcoming emissions regulations. Therefore, better methane-oxidation catalysts, with high activities at low temperatures and better stability, are needed.

Pd-supported catalysts are the most active materials for methane catalytic oxidation at low temperature (*8*, *21*, *68–71*). Both metallic Pd and PdO are active for methane oxidation, but PdO has a higher specific activity (*8*, *72*). PdO forms between 300 and 400 °C, and decomposes to metallic Pd above 800 °C (in air, atmospheric pressure). The decomposition is not a reversible process, so when PdO is decomposed, its reformation can require a temperature well below 700°C, and this results in a sharp transient deactivation during cooling of the catalyst. The transition temperatures depend on O_2 pressure and on the interactions between Pd and the support (*73*). It should be recognized that the above discussion is a greatly simplified picture of the reaction on working catalysts because Pd and PdO can co-exist under non-steady conditions and the nature of C-H bond cleavage changes with the Pd oxidation state (*72*, *74*).

Reducible supports such as CeO_2 can act as promoters for Pd oxidation, enhancing stability and activity of Pd-based catalysts in methane oxidation (*75*, *76*). CeO_2 is known to have two beneficial functions: it provides oxygen for the catalytic oxidation at low temperature by transferring oxygen to Pd (*73*, *77*, *78*) and it can improve the stability of the active PdO phase at high temperatures (*79–81*). However, pure ceria has limited thermal stability (*82*), and direct contact between the ceria and Pd is required for oxygen transfer.(*39*, *75*) Indeed, recent work has shown that the activity of ceria-supported Pd catalysts increases with the interfacial contact between the Pd phase and ceria (*39*). To maximize this contact, self-assembly methods can be used to synthesize Pd@CeO_2 hierarchical catalysts, which consist of Pd nanoparticles (NPs) surrounded by a thin porous shell of ceria (*8*). These catalysts have shown exceptional activity for methane

oxidation under dry conditions and increased thermal stability of the catalyst(*83*). Complete methane conversion was achieved on a Pd@CeO2/Si-Al2O3 catalyst at temperatures below 400 °C and at high space velocities. Significantly, the deactivation associated with the classical PdO-Pd transition observed in conventional Pd-based catalysts was not observed in temperature ramping experiments, even at very high GHSV (*8*).

Despite their high intrinsic activity for methane oxidation, Pd-based catalysts suffer from deactivation under realistic conditions, mainly because of sintering of the metal or support and because of the presence of poisons in the gas feed, including water vapor, sulfur oxides and phosphorous compounds (*84–91*). The aim of this chapter is to report the effect of these common deactivating agents on the novel Pd-based hierarchical catalysts previously developed by our research group. Some possible deactivation mechanisms and strategies for enhancing resistance to poisoning are proposed.

3.2 Hierarchical Pd@MO_x-based Catalysts Synthesis

The hierarchical catalysts investigated in this chapter are based on core-shell units: nanocomposites consisted of a noble metal nanoparticle core surrounded by an outer porous oxide shell, encapsulating it (Figure 3.1). This configuration differs greatly from traditional supported metal catalysts, that are comprised of small metal particles dispersed on the internal surface of an oxide support.

Figure 3.1 Schematic representation of core-shell synthesis procedure, starting from MUA protected metal nanoparticles (Adapted from (*92*)).

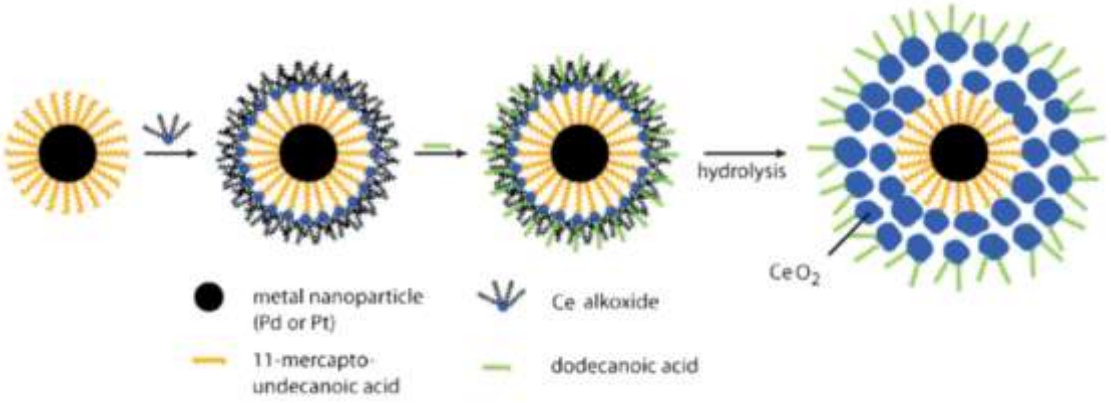

Dispersible core-shell nanostructures having a Pd or Pt core and a TiO_2, ZiO_2 or CeO_2 shell can be prepared exploiting the versatile self-assembly synthesis previously reported by our group (*92*). Here, the supramolecular approach in which single units composed of a Pd core and a CeO_2, ZrO_2 or ceria-zirconia (CZ) mixed oxide shell are prepared in solution and then homogeneously deposited onto hydrophobic supports will be reported. The catalyst preparation requires five steps, which will be outlined in the following sections.

3.2.1 Synthesis of Functionalized Pd NPs

Materials: Potassium tetrachloropalladate(II) (32.04 % as Pd) was purchased from ChemPur, 11-mercaptoundecanoic acid (MUA, 95 %) from Sigma-Aldrich, Sodium borohydride (98+%) from Acros Organics, H_3PO_4 (85% min) from Rectapur and NaOH pellets (>97%) from Carlo Erba Reagenti. Solvents (reagent grade), were purchased from Sigma- Aldrich and used as received.

The first step in the synthesis of the catalysts studied in the present chapter is the preparation of Pd NPs functionalized with terminal carboxylic group, which are required for the reaction with the metal oxide precursor. Briefly, the Pd precursor is reduced in the presence of 11-

mercaptoundecanoic acid (MUA), which binds to the growing metal nanoparticle (NP) forming a three dimensional SAM (Figure 3.2).

Figure 3.2 Schematic representation of MUA-Pd NPs synthesis procedure.

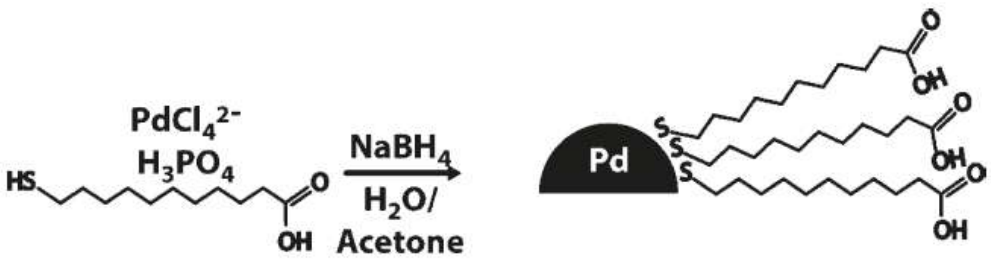

In a typical synthesis, K_2PdCl_4 (93.63 mg, to get 30 mg of Pd) was dissolved in 10 mL water, obtaining an orange solution. 50 mL acetone were added and the solution turned red. H_3PO_4 (1.17 mL, 60 mol *vs.* Pd) was added, followed by 11-mercaptoundecanoic acid (MUA, 32.40 mg, 0.5 mol *vs.* Pd). The solution was stirred for 5 min, then a freshly prepared aqueous solution (4.60 mL) of $NaBH_4$ (106.64 mg, 10 mol *vs.* Pd) was rapidly added, causing the solution to turn black immediately. Stirring was continued for 10 min, and then solvents were evaporated under vacuum and the particles washed three times with water (20 mL portions) and two times with dichloromethane (10 mL portions), with sonication and centrifugation (4500 rpm, 15 min) after each washing cycle. Particles were then recovered by dissolution in THF. The final dispersion was stable for several weeks.

3.2.2 Cerium (IV) Tetrakis(decyloxide) Synthesis

Materials: cerium ammonium nitrate ($(NH_4)_2Ce(NO_3)_6$, CAN, 99.99%) and sodium methoxide (ca. 25 wt % in methanol) were purchased from Sigma-Aldrich. 1-Decanol (98+%) was purchased from Alfa Aesar. The solvents used in the preparation of this compound were stored over activated 3 Å molecular sieves overnight prior to use.

The preparation of cerium(IV) tetrakis(decyloxide) [$Ce(C_{10}H_{21}O)_4$, $Ce(ODe)_4$] followed previously reported procedures (*93*, *94*). Cerium ammonium nitrate (CAN) (5.00 g, 9.12 mmol) was dissolved in 50 mL MeOH, after which 1-decanol (6.97 mL, 4 mol *vs.* Ce) was added. Next, a 25 wt % solution of MeONa in MeOH (12.51 mL, 6 mol *vs.* Ce) was introduced drop-wise, causing formation of gaseous NH_3 and precipitation of a bright yellow solid (cerium(IV) methoxide) and a white solid ($NaNO_3$). The mixture was stirred for 1 h. Then, the solvent was evaporated to yield an orange-colored oil and $NaNO_3$ precipitate. The oil was dissolved into 25 mL dichloromethane, and the

solvent was evaporated again. This procedure was repeated several times, until the precipitate re-crystallized in bigger grains. Then, the oil was dissolved in DCM and the $NaNO_3$ was filtered out. Finally, the solvent was removed by evaporation, and the orange-oil product was used without further purification.

3.2.3 Pd@MO_x Core-Shell Units Synthesis

Materials: Zirconium butoxide (80% in 1-butanol), dodecanoic acid (99% minimum) and THF were purchased from Sigma-Aldrich and used as received.

The hierarchical Pd@MO_x(CeO_2, ZrO_2 and $Ce_xZr_{1-x}O_2$) units were prepared by modifying published procedures(*92*). The Pd NPs dispersed in THF were added to a THF solution of cerium(IV)tetrakis(decyloxide) and/or zirconium butoxide, followed by the addition of a THF solution of dodecanoic acid. Typically, 10 mL of the THF solution of MUA-Pd nanoparticles (0.5 mg/mL as Pd) were slowly added to 5 mL THF solution of pre-mixed metal alkoxides, keeping constant the Pd:MO_x molar ratio (1:5.5), followed by the addition of dodecanoic acid (1 mol vs. Ce + Zr) dissolved in 10 mL of THF. The hydrolysis of the metal alkoxide in the Pd–Ce/Zr solution was carried out by slowly adding up to 1.2 mL H_2O dissolved in 10 mL THF over 4 h (up to 120 mol vs. Ce + Zr).

3.2.4 Al_2O_3-based Supports Preparation and Hydrophobization

Materials: Triethoxyoctylsilane (TEOOS, ≥97.5 %) and toluene were purchased by Sigma-Aldrich and used as received. High-surface area Al_2O_3 was purchased by Puralox and calcined at 950°C for 12 hours before use. For model catalysts support preparation, trimethylaluminum (TMA) was supplied by Cambridge Nanotech, together with the ALD system, while ITO/quartz slides were purchased from Präzisions Glas & Optik (PGS).

On pristine hydrophilic alumina, hydrophobic core-shell structures agglomerate with one another rather than adhering to the support (Figure 3.3, part A) (*8*). The presence of agglomerates causes loss of accessible active phase surface area, so it was crucial to develop a synthetic way to modify the support, allowing homogeneous dispersion of the active phase on it. This has been achieved by reacting alumina with an organosilane, triethoxyoctylsilane (TEOOS): this silane has three alkoxy groups that are prone to hydrolysis and one alkyl chain that is not, so TEOOS binds to the support exposing the alkyl chain to the external environment, making alumina surface hydrophobic. Hydrophobic Al_2O_3 (Si-Al_2O_3) exhibits much greater capacity for the adsorption of the Pd@MO_x structures compared to the pristine Al_2O_3 (Figure 3.3, part B). In the present work, two different supports were reacted with TEOOS: High-Surface Area (HSA) Al_2O_3 and Al_2O_3-modified ITO/quartz slides, used for model catalysts preparation.

Figure 3.3 Schematic representation of hydrophobic alumina preparation, and comparison of loading of core-shells on pristine and hydrophobic alumina. (Reproduced from (*8*)

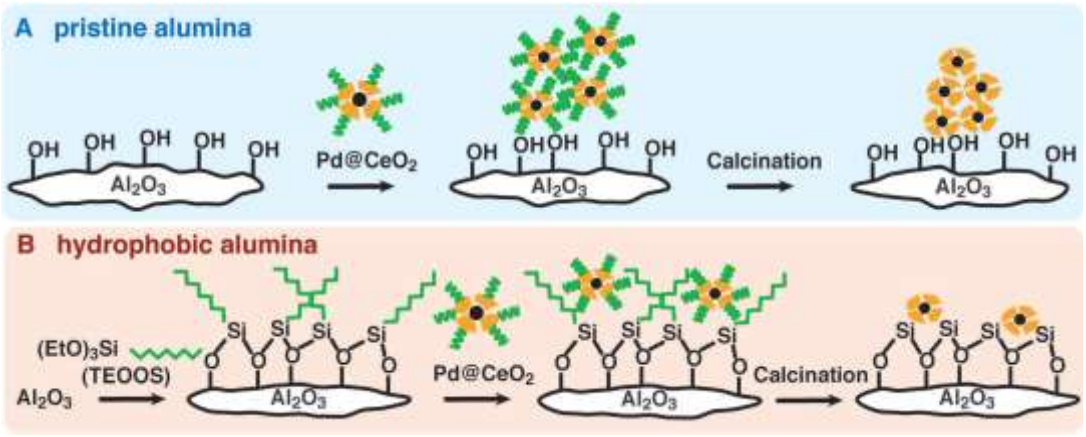

For HSA Al_2O_3, 1 g of powder was sonicated in 20 mL of toluene, followed by addition of TEOOS (0.55 mL). The resulting solution was refluxed for 3 hours and the precipitate powder was recovered by centrifugation (4500 rpm). The powder was subsequently washed twice with toluene to remove unreacted TEOOS and byproducts and was dried overnight at 120 °C.

The supports for the model catalysts were prepared by ALD of Al_2O_3 overlayers of various thicknesses (2, 5 and 10 nm) on an ITO/quartz support (flat, low-surface-area material). Both TMA and water precursors were kept at room temperature, resulting in vapor pressures of about 20 Torr and 11 Torr, respectively. The deposition chamber was maintained at 250°C and a base pressure of 0.1 Torr, with N_2 flow of 20 mL min^{-1}. The deposition steps were as follows: 1) pulse water for 0.015 s, 2) hold 5 s, 3) pulse TMA for 0.015 s, and 4) hold 5 s. The thickness of the Al_2O_3 film increased by approximately 1 Å/cycle, so that 50 cycles were used to make a 5 nm film. The Al_2O_3/ITO/quartz slides were then cut into 9 × 9 mm pieces with a glass cutter and treated in freshly prepared piranha solution (concentrated $H_2SO_4$and 30% H_2O_2 solution in a 3:1 ratio) in order to clean the surface from any impurity and increase the hydroxyl group population. The slides were washed many times with water and acetone prior to being functionalized by reaction in a diluted solution of TEOOS (0.5 mL) in toluene (20 mL) for 2 days at room temperature.

3.2.5 Impregnation of the Core-Shell Structures on Hydrophobic Supports

For HSA catalysts preparation, the Pd@MO_x nanostructures dissolved in THF (50 mL) were added to the appropriate mass of degassed support to achieve the nominal loading for Pd of 1.0 % wt. After the mixture was stirred overnight, the solid residue was recovered by centrifugation (4500

rpm for 15 minutes) and washed twice with THF. Finally, the powder was dried at 120 °C overnight, ground to a particle size below 150 m and calcined at 850°C for 5 h, using a heating rate of 3 °C min^{-1}.

$Pd@MO_x$ units were deposited on $Si\text{-}Al_2O_3$/ITO/quartz model catalysts following a previously reported procedure (*95*). Briefly, 0.1 mL of $Pd@MO_x$ solution was deposited onto the support and rinsed with THF after 2 min to remove weakly adsorbed particles. The model catalysts were finally calcined at 850◦C in air for 5 h, using a heating rate of 3 °C min^{-1}.

3.3 Effect of Water

3.3.1 Introduction

Gasoline and lean-burn vehicles exhausts contain large amounts of water vapor (5-15%), which is detrimental for after treatment catalysts performance (*21*, *96*). It has been reported that water and methane competitively adsorb on PdO active sites and that water reacts with PdO to form $Pd(OH)_2$, which is much less reactive with methane (*87*, *97*). There is some disagreement over whether this deactivation is reversible or irreversible (*84*, *98*, *99*), but the inhibition effect of water is known to be more important at lower temperatures. Burch *et al.* reported methane-oxidation reaction rates on Pd/Al_2O_3 were inhibited by water up to approximately 450 °C (*97*). The importance of water inhibition on Pd catalysts also depends on the support, with reducible oxides showing improved resistance to water inhibition (*85*). The accumulation of hydroxyl/water on the oxide support was also suggested to hinder oxygen mobility from the support and lead to deactivation (*100*). In this section, the effect of water on $Pd@CeO_2$-based catalysts for methane catalytic oxidation will be discussed.

3.3.2 Results

The catalytic performance of Pd(1 wt%)@CeO_2(9 wt%)/Si-Al_2O_3 catalysts for CH_4 oxidation under dry and wet conditions was characterized using light-off curves with a heating and cooling rate of 10 °C min^{-1}. As shown in Figure 3.4, under dry conditions CH_4 conversion began at approximately 300 °C with increasing temperature and was shifted by approximately 50 degrees to lower temperatures during the cooling cycle. Subsequent light-off measurements on the same catalyst were identical to that shown here, demonstrating complete reversibility of the catalyst. As reported in earlier work (*8*), no dip in conversion was observed during heating or cooling cycles for space velocities below 1000 000 mL g^{-1} h^{-1}. The addition of 15.0 % water to the feed had a dramatic effect on the light-off curves. Methane conversion was shifted to higher temperature by approximately 200 °C, and transient deactivations were observed during both heating and cooling cycles. The decrease in CH_4 conversion was small during the upward temperature ramp, down to 98 % of conversion at about 750 °C; but the dip in conversion was very noticeable during cooling, going down to 60 % conversion at 650 °C.

Figure 3.4

Effect of water on methane oxidation light-off curves over Pd(1 wt%)@CeO_2(9 wt%)/Si-Al_2O_3 . Dry conditions (circles): 0.5 % CH_4, 2.0 % O_2, Ar balance, $O_2/O_{2(stoich)}$=2, GHSV=200 000 mL g^{-1} h^{-1}, heating and cooling rates 10 °C min^{-1}. Wet conditions (squares): same conditions as above, with the addition of 15.0 % H_2O.

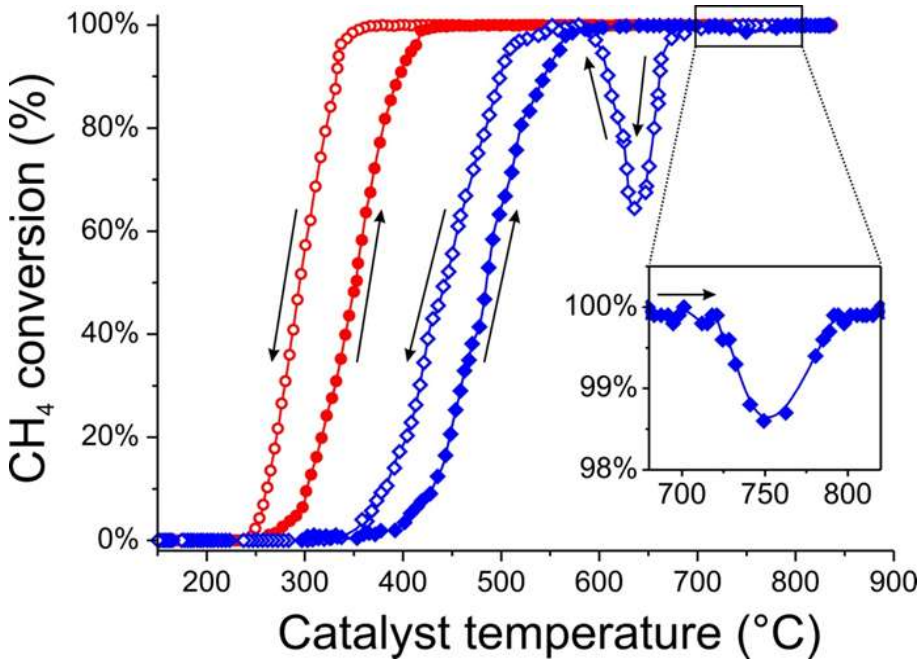

As previously discussed, transient deactivation for CH_4 oxidation is associated with a PdO → Pd phase transition (*69*). When the temperature is ramped upward, conversions can decrease with increasing temperature, owing to decomposition of PdO, then return to 100 % conversion as temperature is further increased. The transient deactivation is more evident during the cooling cycle because the re-oxidation of Pd to the more active PdO is kinetically controlled (*101*), with Pd reoxidation occurring through a nucleation mechanism that is favored when some PdO is still present (*72*). The transition temperatures depend on the O_2 pressure and can be influenced by the support. The absence of transient deactivations with Pd(1 wt%)@CeO_2(9 wt%)/Si-Al_2O_3 under dry conditions is likely caused by the close contact between Pd and ceria in the core-shell structures. The presence of these transients upon the addition of water to the feed suggests water suppresses reoxidation of Pd.

Further evidence that the detrimental effect of H_2O is due to suppressed oxidation of Pd is demonstrated in Figure 3.5, which shows light-off curves as a function of the O_2 partial pressure. The magnitude of the dip in the conversion during the cooling cycles decreased steadily with increasing O_2 concentration, while the temperature at which the minimum occurred increased,

from 640 °C for 2.0 % O_2 to ≈710 °C for 14.0 % O_2. The explanation for both of these observations is that the higher O_2 partial pressures help to maintain the Pd as PdO.

Figure 3.5 Effect of oxygen concentration on methane oxidation light-off curves over Pd(1 wt%)@CeO_2(9 wt%)/Si-Al_2O_3 under wet reaction conditions: a) 2.0, b) 4.0, c) 10.0, and d) 14.0 %. Conditions: 0.5 % CH_4, different concentrations of O_2, 15.0 % H_2O, Ar balance, GHSV=200 000 mL g^{-1} h^{-1}, heating and cooling rates 10 °C min^{-1}.

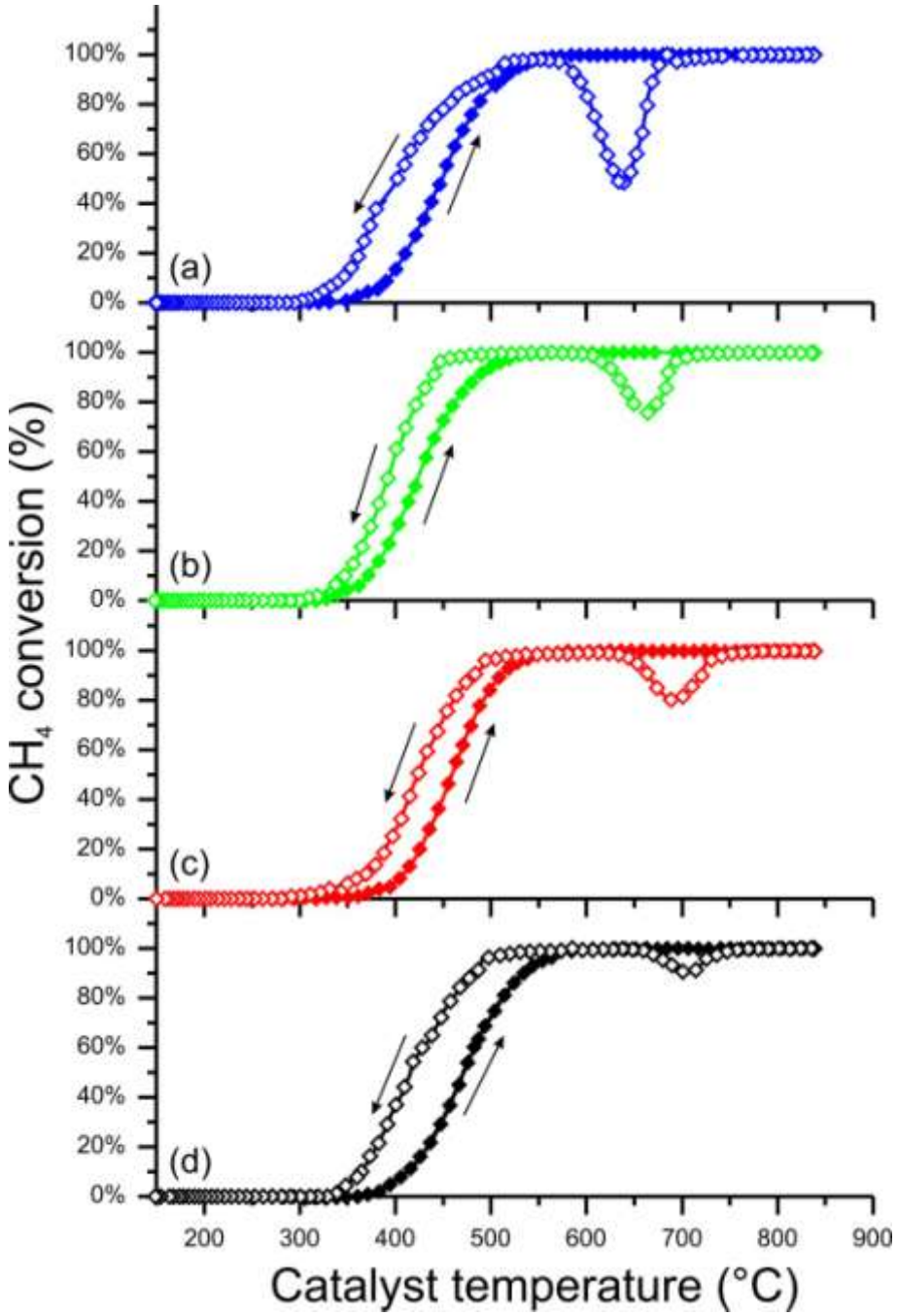

Steady-state measurements of CH_4 oxidation over Pd(1 wt%)@CeO_2(9 wt%)/Si-Al_2O_3 in the presence of water at 500 and 600 °C were especially revealing. In these experiments, the catalyst temperature was ramped to the desired temperature in 0.5 % CH_4, 2.0 % O_2 and 15.0 % H_2O and held at that temperature for a period of time. Then water was removed from the reaction mixture while monitoring the CH_4conversion. Results for experiments performed at 500 °C are shown in Figure 3.6. After the catalyst temperature reached 500 °C, methane conversion decreased slowly from an initial value of 90 % to ~60 % after 4 h. When water was removed from the reaction mixture, the activity was completely restored after less than 10 min. When the sample was cooled to room temperature at 10 °C min^{-1}, the conversion followed the cool-down curve for dry methane oxidation reported in Figure 3.4. These results imply that H_2O at 500 °C does not modify the structural properties of the Pd(1 wt%)@CeO_2(9 wt%)/Si-Al_2O_3 catalyst.

Figure 3.6

Steady state aging test under wet reaction conditions at 500 °C, followed by activity recovery under dry reaction conditions. Dry conditions (circles): 0.5 % CH_4, 2.0 % O_2, Ar balance, $O_2/O_{2(stoich)}$=2, GHSV=200 000 mL g^{-1} h^{-1}, heating and cooling rates 10 °C min^{-1}. Wet conditions (squares): same conditions as above, with the addition of 15.0 % H_2O.

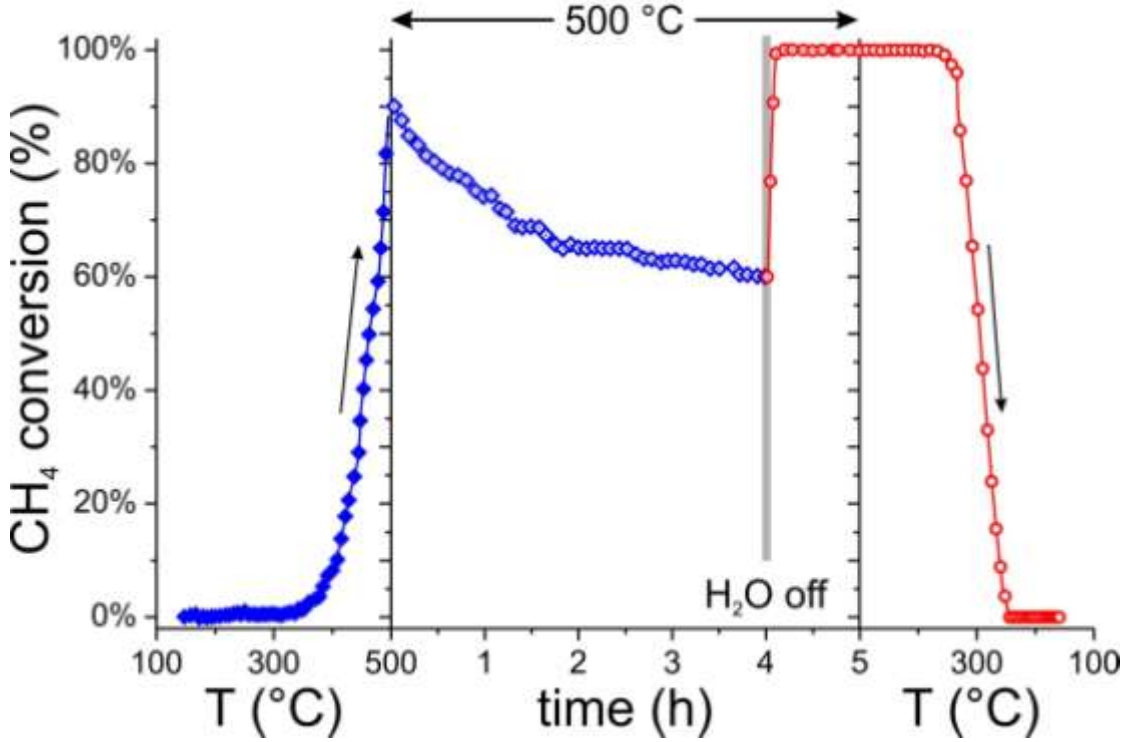

The results from the analogous experiment at 600 °C (Figure 3.7) were very different. The CH_4 conversion decreased much more sharply during isothermal aging, reaching only 10 % after 4 h. Removing water from the reaction mixture at 600 °C did not completely restore the conversion, even after 10 h. Finally, when the sample was cooled to room temperature at 10 °C min^{-1}, the conversion did *not* follow the cool-down curve for dry methane oxidation reported in Figure 3.4; but, rather, the conversions were shifted to high temperatures.

Figure 3.7 Steady state aging test under wet reaction conditions at 600 °C, followed by activity recovery under dry reaction conditions. Dry conditions (circles): 0.5 % CH_4, 2.0 % O_2, Ar balance, $O_2/O_{2(stoich)}$=2, GHSV=200 000 mL g^{-1} h^{-1}, heating and cooling rates 10 °C min^{-1}. Wet conditions (squares): same conditions as above, with the addition of 15.0 % H_2O.

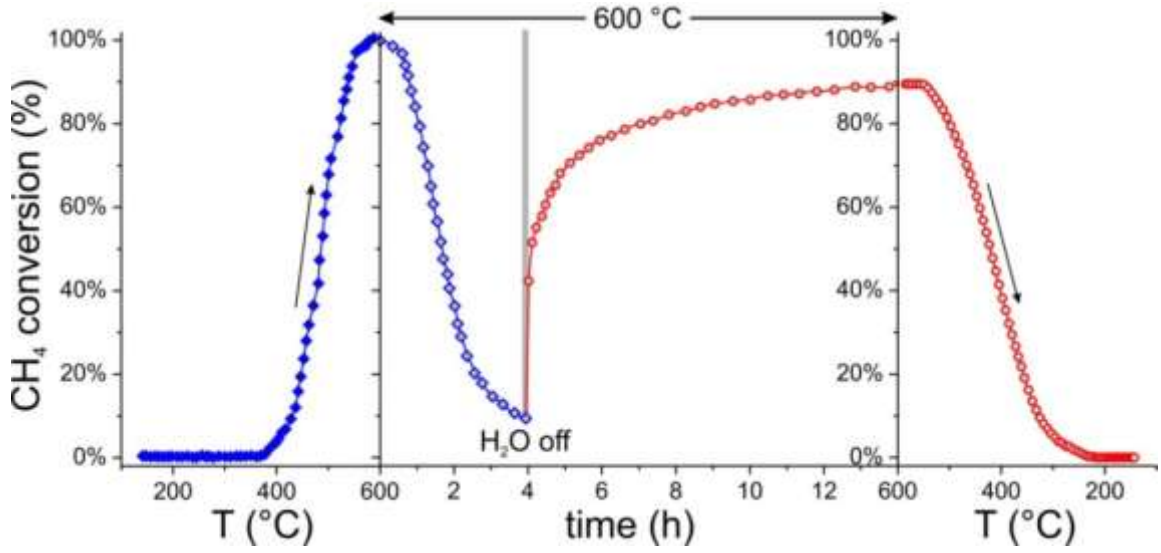

The catalyst deactivation observed in Figure 3.7 was not caused by a permanent destruction of the catalyst, as demonstrated by the data in Figure 3.8a. In this experiment, the Pd(1 wt%)@CeO_2(9 wt%)/Si-Al_2O_3 catalyst was again aged in 0.5 % CH_4, 2.0 % O_2, and 15.0 % H_2O for 4 h, then the sample was purged under Ar and cooled to room temperature. Next, the sample temperature was ramped to 850 °C at 10 °C min^{-1}. The conversions during this initial temperature ramp were shifted to significantly higher temperatures than that observed even with wet feed in Figure 3.4. On the aged catalyst, 100 % conversion of CH_4 was not reached until above 650 °C. However, the cool-down curve followed the conversion data observed for dry CH_4 oxidation on the fresh catalyst and subsequent light-off curves for dry CH_4 oxidation were identical to that observed on the fresh catalyst.

Figure 3.8

Methane oxidation light off experiment over a) Pd(1 wt%)@CeO_2(9 wt%)/Si-Al_2O_3 catalyst and b) reference impregnated Pd(1 wt%)-CeO_2(9 wt%)/Si-Al_2O_3 catalyst, both aged at 600 °C for 4 h under wet reaction conditions and cooled to 150 °C under Ar. Squares represent first cycles and circles second cycle. Conditions: 0.5 % CH_4, 2.0 % O_2, Ar balance, $O_2/O_{2(stoich)}$=2, GHSV=200 000 mL g^{-1} h^{-1}, heating and cooling rates 10 °C min^{-1}.

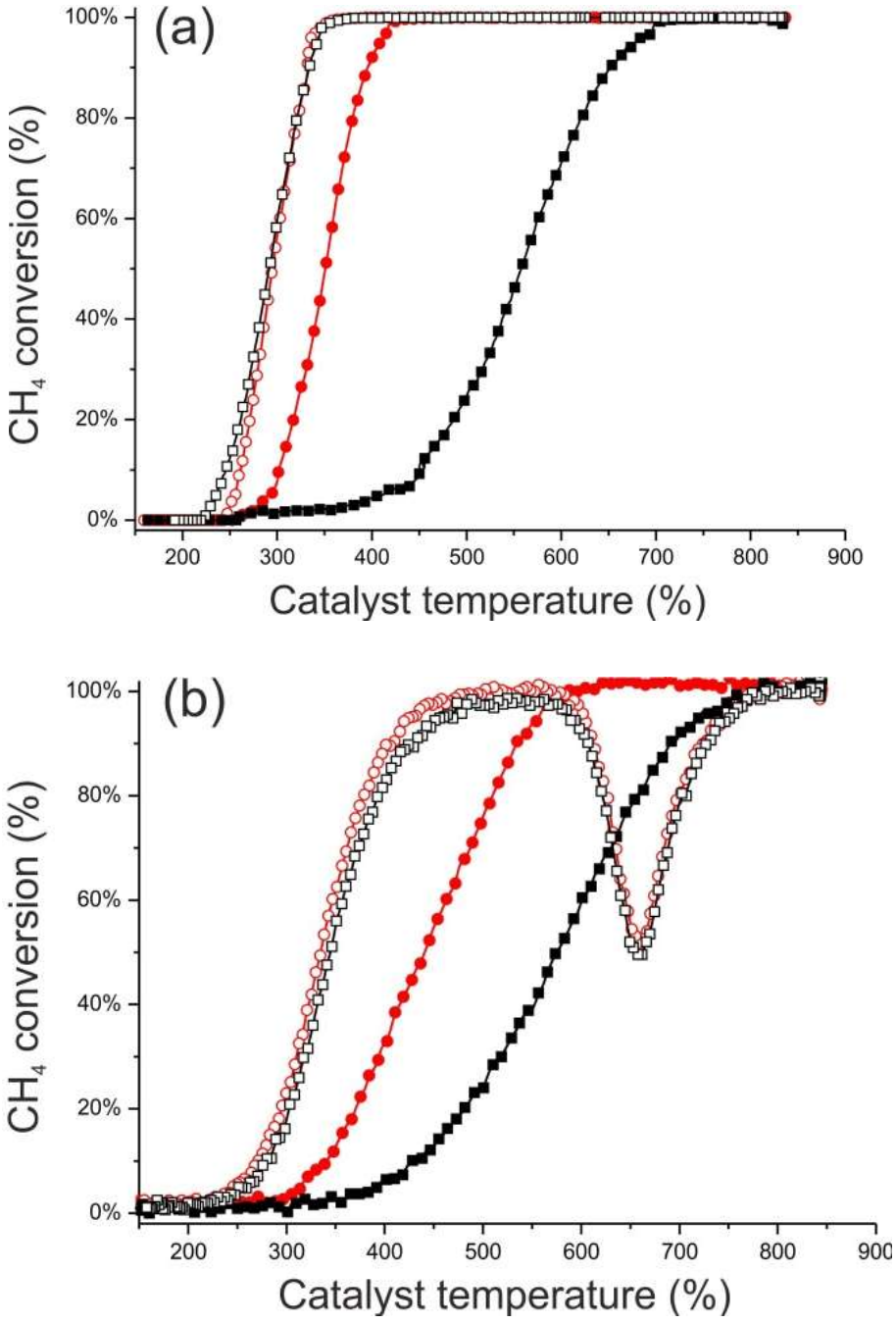

It is interesting to note that something similar occurs on the reference impregnated sample. However, aging at 600 °C under wet conditions for 4 hr leads to a deactivation of the catalyst that is less marked with respect to that of the hierarchical catalyst under the same experimental conditions (residual conversion ~32 % vs. ~8 %). Upon removing water, a sharp increase in activity is obtained and complete restoration of the initial activity is achieved after high temperature treatment. Interestingly, the light-off curve measured under dry conditions for this aged impregnated catalyst (Figure 3.8b) is once again shifted to higher temperature and the cooling cycles resembles that of the fresh sample as the following activity.

Simultaneously with the conversion measurements in Figure 3.8a, water evolution was also monitored over the Pd(1 wt%)@CeO_2(9 wt%)/Si-Al_2O_3 sample, with results shown in Figure 3.9.

Figure 3.9

Water evolution (signal *m*/*z*=18) recorded for the experiments presented in Figure 3.8. The horizontal bars correspond to the period during which complete conversion of methane was observed. Shadow area highlights the additional water evolution with respect to that formed by methane oxidation. Squares represent first cycles and circles second cycle. Solid line represents the catalyst temperature (on the right axis).

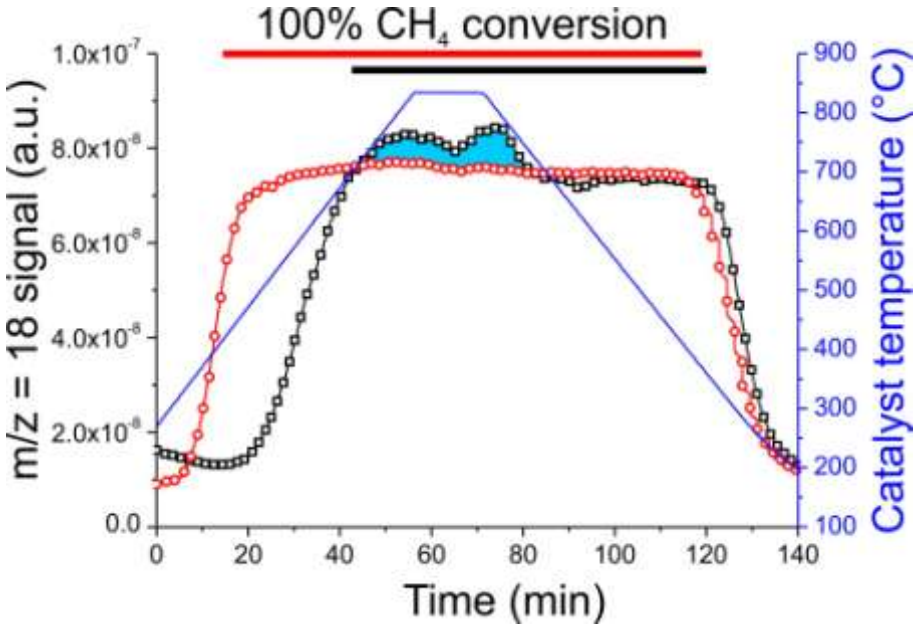

For the active catalyst, the water production increases with temperature as CH_4 conversion increases. When the temperature is sufficient to completely oxidize the CH_4, the water production is constant. However, with the catalyst deactivated by treatment under wet CH_4 oxidation conditions, a significant excess of water, above that produced by the steady-state oxidation of CH_4, is released from the sample when the temperature is above 700 °C. Although an accurate estimate

of this amount is difficult, owing to the steady-state reaction in the background, we monitored an amount of water from the deactivated catalyst that is slightly higher than the moles of cerium in the sample. This could suggest that, besides significant formation of cerium hydroxyls on CeO_2, some hydroxyls are also formed on the alumina.

To determine whether other pretreatment conditions could cause the deactivation observed in Figure 3.7, the CH_4 conversion was monitored under dry conditions for longer times and after high-temperature reduction, with results shown in Figure 3.10. First, the conversion in a dry mixture of 0.5 % CH_4 and 2.0 % O_2 at 600 °C showed no decrease from 100 %, even after 14 h. Neither the high temperatures nor exposure to CH_4 and O_2, in the absence of H_2O, are responsible for the catastrophic loss in conversion. Next, the catalyst was reduced at 600 °C in 5.0 % H_2/Ar. When the catalyst was again exposed to the dry reaction mixture, 100 % conversion was achieved after 6 min.

Figure 3.10 Catalytic oxidation of methane. Aging test under dry reaction conditions at 600 °C, followed by reduction in 5.0 % H_2/Ar at 600 °C and subsequent purge in Ar. Conditions: 0.5 % CH_4, 2.0 % O_2, Ar balance, $O_2/O_{2(stoich)}$=2, GHSV=200 000 mL g^{-1} h^{-1}.

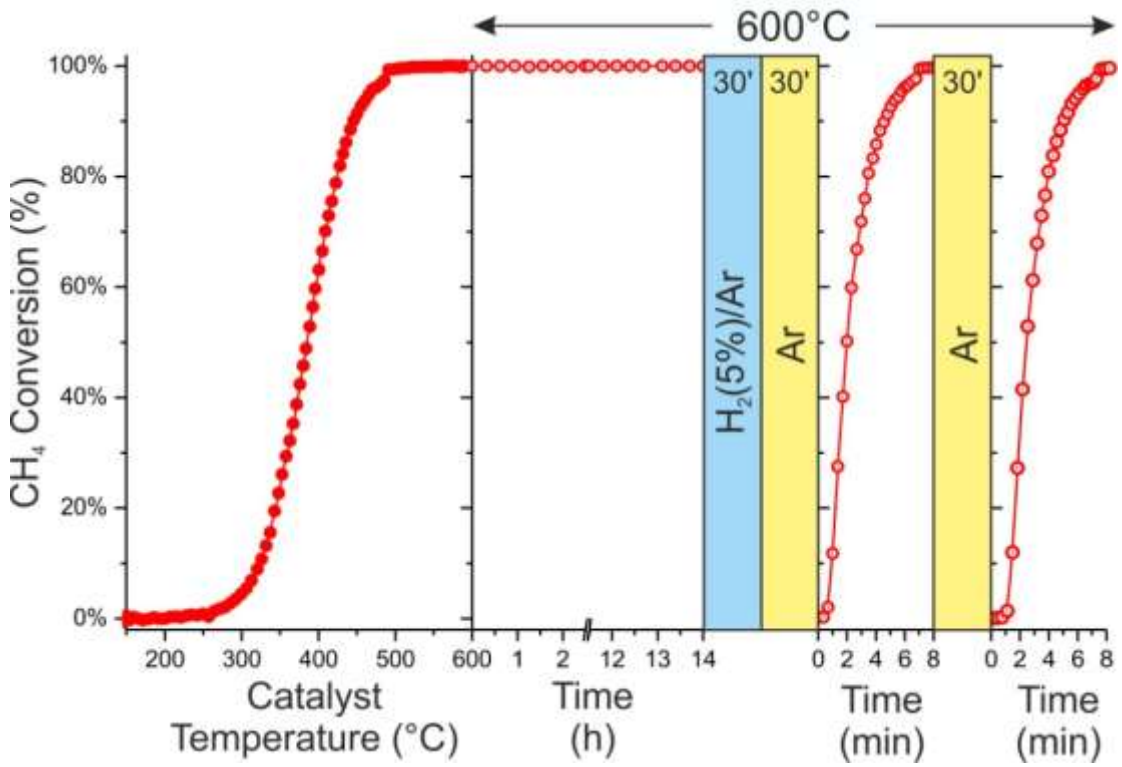

Flowing Ar over the catalyst at 600 °C for 30 min also had no effect on the subsequent activity. The effect of catalyst pre-reduction was also examined by means of *operando* XAFS experiments demonstrated that Pd is almost completely reduced under 5.0 % H_2/N_2 already at 150 °C. In addition, the data indicate the presence of 20 % Ce^{III} in the fresh catalyst, in accordance with the nanometric dimensions of the ceria crystallites (*102*). This contribution was determined to be constant during all operando X-ray absorption near edge spectroscopy (XANES) experiments, either under dry or wet conditions. Upon reduction at 600 °C under 5.0 % H_2/N_2, the Ce^{III} content increases up to 45 %. Excellent fitting of the Pd EXAFS data was achieved by considering only the contribution of Pd fcc phase with a distance of 0.273 nm (0.271 in bulk Pd) in accordance with a similar study for Pd/PdO on γ-Al_2O_3(0.274 nm) (*103*). In the absence of oxygen (N_2 atmosphere), operando XANES experiments demonstrated that PdO almost fully decomposes to Pd at 600 °C, even if in close contact with CeO_2 (Figure 3.11b). The equilibrium is reversed under dry conditions leading to the almost immediate reoxidation of 25 % Pd to PdO followed by a further slow increase during the following reaction time (Figure 3.11c). Only the use of 5.0 % O_2/N_2 leads to a steep increase in the Pd to PdO oxidation (Figure 3.11d). Notably the catalytic activity of the pre-reduced catalyst (Figure 3.10) is fully recovered after a comparable time (7–8 min) indicating that partial reoxidation of the Pd is sufficient to guarantee high catalytic activities (*101*).

Figure 3.11 Fraction of PdO obtained from XANES spectra during subsequent treatments at 600 °C under a) dry reaction conditions (0.5 % CH_4, 2.0 % O_2, N_2 balance), b) pure N_2, c) dry reaction conditions, and d) 5.0 % O_2/N_2.

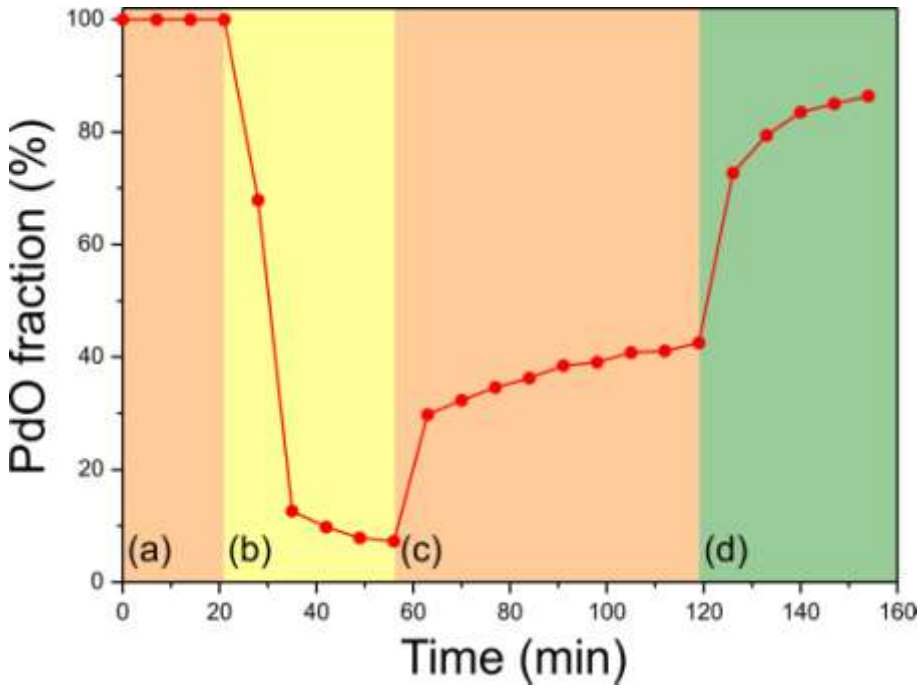

To understand the changes that occur in the catalyst following CH_4 oxidation under wet conditions, we examined the effect of catalyst pretreatment conditions using FTIR and XANES measurements, with results from ex situ FTIR shown in Figure 3.12. The spectrum in Figure 3.12a was obtained on the catalyst that had simply been calcined to 850 °C. After exposure to air and mild heating in dry He, a rather broad ν(OH) stretching band is observed in the region of 3700 cm^{-1}. Aging the catalyst under dry CH_4-oxidation conditions (Figure 3.12b), does not lead to significant modification of the spectrum. However, following treatment of the catalyst in wet CH_4-oxidation conditions (Figure 3.12c), the ν(OH) hydroxyl band becomes much more intense and centered near 3720 cm^{-1}, a frequency that has been assigned to mono-coordinated and doubly bridged OH groups bound to ceria. A small shoulder at 3565 cm^{-1} may be attributable to triply bridging OH species (*104*). Exposing the catalyst to dry CH_4-oxidation conditions for 1 h (Figure 3.12d) caused minimal changes; however, heating the sample to 800 °C (Figure 3.12e) greatly reduced the intensity of the ν(OH) stretching band.

The fact that this feature is significantly less evident in the case of Pd/Si-Al_2O_3 (Figure 3.12e-f) aged under wet conditions suggests that the stable hydroxyls are somehow linked to the defective - nanostructured ceria. Nevertheless, since the Al_2O_3 support presents various ν(OH) band in the same region (Figure 3.12f), the intense ν(OH) band in Figure 3.12c and 3.12d cannot be definitely assigned to cerium hydroxide. The formation of these stable hydroxyls under conditions where catalyst deactivation occurs and their removal by conditions that reactivate the catalyst strongly suggest that they are associated with deactivation. The IR spectra of the reference impregnated Pd-CeO_2/Si-Al_2O_3 samples are different, indicating the influence of the preparation method on nature of the surface hydroxyls. Remarkably, the wet aging at 600 °C leads to less marked changes in the population of hydroxyls.

Figure 3.12

FTIR spectra of Pd(1 wt%)@CeO_2(9 wt%)/Si-Al_2O_3 a) fresh sample and after different treatments: b) dry reaction condition at 600 °C for 4 h, c) wet reaction condition at 600 °C for 4 h, d) wet reaction condition at 600 °C for 4 h, followed by dry condition at 600 °C for 1 h, e) wet reaction condition at 600 °C for 4 h, followed by dry condition at 800 °C for 1 h, f) Pd/Si-Al_2O_3 and conventional impregnated Pd(1 wt%)-CeO_2(9 wt%)/Si-Al_2O_3 after different treatments g) dry reaction condition at 600 °C for 4 h, h) wet reaction condition at 600 °C for 4 h.

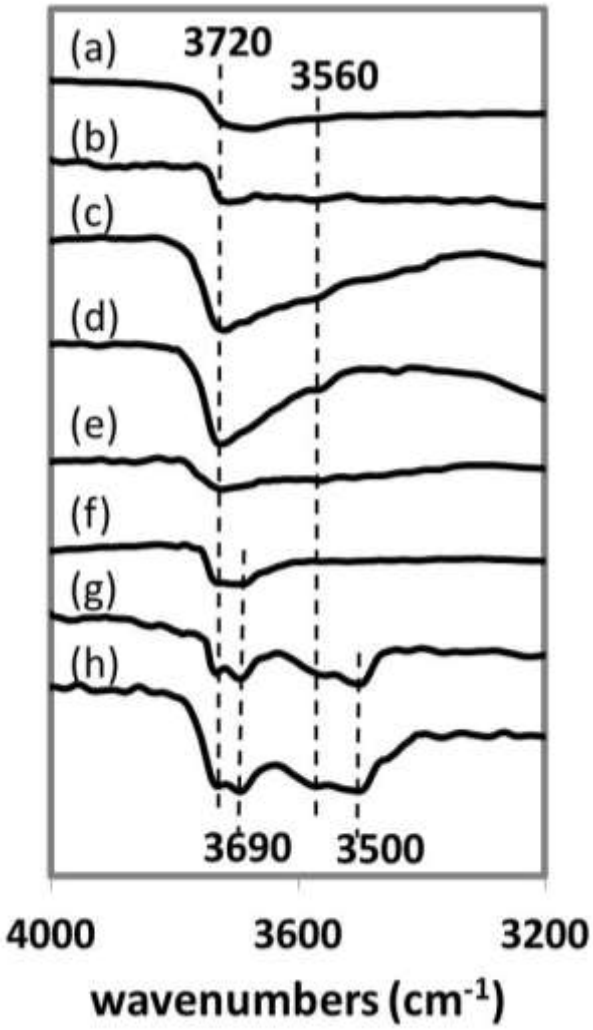

Results from the operando XANES experiments on Pd(1 wt%)@CeO_2(9 wt%)/Si-Al_2O_3 are reported in Figure 3.13. Figure 3.13a shows XANES spectra of the Pd edge as a function of time as the catalyst is exposed to dry CH_4oxidation conditions at 600 °C. The spectra remain unchanged over a period of 79 min; from measurements on reference samples (shown in the inset of Figure 3.13a), it is apparent that the Pd is present as PdO. Upon the introduction of 15.0 % H_2O to the

reaction mixture (Figure 3.13b), the spectra evolve with time to form a mixture of both PdO and the less active metallic Pd. As shown in the inset, approximately 60 % of the PdO is converted to Pd after 80 min under these conditions.

Figure 3.13

Normalized XANES spectra obtained during operando methane oxidation under a) dry and b) wet reaction conditions at 600 °C. Conditions: 0.5 % CH_4, 2.0 % O_2, 15.0 % H_2O (if present), N_2 balance. The insets report XANES of reference Pd and PdO and PdO percentage during wet reaction conditions at 600 °C, respectively.

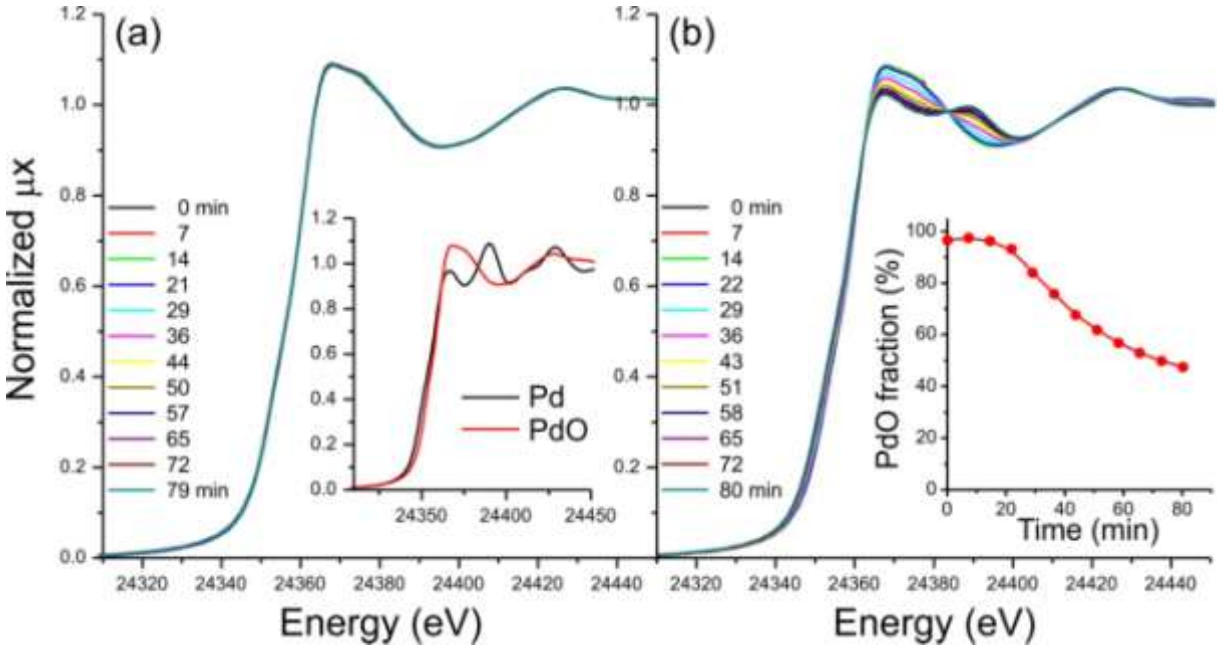

CO chemisorption data on fresh, dry, and wet aged samples, as well as the corresponding high temperature regenerated ones are reported in Table 3.1. The data clearly indicate that, consistently with the stable catalytic activity, the relatively high accessible Pd surface area of the fresh Pd@CeO_2/Si-Al_2O_3sample is not altered by the dry aging. Vice versa, the wet aging at 600 °C leads to an appreciable decrease of the capability to chemisorb CO. Although significant, the observed decrease of exposed metal surface area (Table 3.1) cannot alone explain the observed dramatic deactivation of the catalytic activity. Remarkably, the initial Pd accessibility is fully recovered after the high temperature treatment, which eliminates the hydroxyls groups and restores the catalytic activity. The results for the conventional impregnated Pd-CeO_2/Si-Al_2O_3 were different and the initial accessible Pd surface area is only marginally reduced by either dry or wet aging (Table 3.1). Only minor sintering occurs with a few hours of aging under the adopted

conditions and there is no significant coverage of the catalytic active phase by reduced cerium oxide or by hydroxyls. However, the initial metal-support contact area, as indirectly indicated by the metal dispersion, is decreased, partially accounting for the lower activity.

Table 3.1 Accessible Pd surface area, CO/Pd ratio and apparent particle size obtained from low temperature CO chemisorption on $Pd@CeO_2/Si\text{-}Al_2O_3$ and conventional impregnated $Pd\text{-}CeO_2/Si\text{-}Al_2O_3$.

Sample	Accessible Pd surface area ($m^2\ g^{-1}$)	CO/Pd ratio (%)	Apparent particle size (nm)[a]
$Pd@CeO_2/Si\text{-}Al_2O_3$			
fresh	3.0	67	1.7
dry aged	2.8	64	1.8
reactivated after dry aging[b]	3.3	74	1.5
wet aged	1.1	27	4.2
reactivated after wet aging[b]	3.2	72	1.6
$Pd\text{-}CeO_2/Si\text{-}Al_2O_3$			
fresh	2.4	53	2.1
dry aged	2.2	50	2.2
wet aged	2.1	48	2.3

[a] Apparent particle size was estimated assuming a spherical geometry.
[b] Sample reactivated by thermal treatment at 850 °C under 5.0 % O_2/Ar.

3.3.3 Discussion

$Pd\text{-}CeO_2$ based catalysts show very good low-temperature activity for methane oxidation (*69*), especially when prepared in a hierarchical structure that maximizes the contact between the PdO core the surrounding porous ceria (*8*). The reactivity of these systems strongly depends on the oxidation state of Pd, with PdO showing much higher activity than Pd, so that the O_2 partial pressure in the reaction feed plays a major role in affecting rates. The intimate contact between the Pd phase and CeO_2 obtained in our $Pd@CeO_2/Si\text{-}Al_2O_3$ catalysts not only stabilizes Pd particle size but also facilitates oxygen spillover, reducing the extent of PdO decomposition at high temperatures and the subsequent decrease in activity associated with the transition of PdO to Pd (*8*).

At lower temperatures, the presence of water is known to significantly alter the activity of all Pd catalysts due to formation of hydroxyls on the Pd surfaces (*84*, *87*, *97–99*). In conventional impregnated catalysts, such as Pd/Al_2O_3, the extent of this deactivation significantly decreases with increasing temperature, owing to the thermal instability of surface hydroxyls. However, the presence of water at high temperature can promote Pd sintering (*105*). Notably, on those catalysts, the high temperature PdO-Pd phase transition leads also to a significant decrease of catalytic activity even under dry conditions. What we have observed in the present study is that there is an additional deactivation process occurring on the $Pd@CeO_2/Si\text{-}Al_2O_3$ core-shell catalysts during oxidation of methane in the presence of water vapor at high temperatures. After exposure to these conditions, the exceptional activity observed for $Pd@CeO_2/Si\text{-}Al_2O_3$ was lost. The presence of water induces 1) a shift of the light off curve to higher temperature and 2) the appearance of the transient deactivation generally observed in the 600–750 °C range.

The influence of water on catalytic activity can be understood by considering the reaction mechanism that is generally accepted for palladium supported on CeO_2. In the presence of PdO, a Mars-van Krevelen mechanism is operative, in which PdO lattice oxygen atoms are consumed by CH_4 to produce CO_2 and water (*106*). Re-oxidation of palladium can occur by reaction with O_2 from the gas phase or by spillover of O atoms from CeO_2 (*85*). For each oxygen vacancy formed by oxygen spillover, two reduced Ce^{III} ions are generated (*107*) and these in turn must be re-oxidized by molecular O_2. Therefore, the excellent catalytic properties of the core-shell $Pd@CeO_2$ catalyst can be associated with intimate contact between the PdO phase and the CeO_2 nanocrystallites which leads to efficient O spillover, resulting from the peculiar core-shell structure.

Consistent with previous results (*21*), the presence of water at medium-low temperature results in a moderate catalyst deactivation. The effect of water in the reaction media at high temperature is more remarkable and less reversible (Figure 3.7). IR data shows that, in the presence of a large amount of water, the oxygen vacancies present on the nanoceria can react with H_2O, forming OH groups on the surface of the ceria nanoparticles (Figure 3.12).

Results from density functional theory (DFT) simulations performed on reduced CeO_2 (1 1 1) indicate that water can dissociate into an OH group, which fills the oxygen vacancy, and an H atom which bonds to a surface O atom(*108*, *109*). Therefore, the reaction of a vacancy, caused by reduction of ceria, with one water molecule results in the formation of two hydroxyl groups, without affecting the oxidation state of Ce^{III} ions close to the original oxygen vacancy site. The hydroxyl groups formed by the dissociation of water on the oxygen vacancies can in turn inhibit the oxygen diffusion on the surface of the CeO_2nanoparticles and stabilize Ce^{III} (*100*). Since the oxygen vacancies originate from the O back spillover from ceria to the metal, a process that

involves short range interactions (*110*), it is reasonable to expect that the hydroxyls resulting from the reoxidation by water are mostly located in the proximity of the Pd. In this way, an efficient Pd re-oxidation is hindered and a deactivation of the catalyst occurs (Scheme 3.1), owing to the PdO transformation to Pd as observed by operando XANES experiments (Figure 3.13).

Scheme 3.1 A representation of the proposed evolution of the $Pd@CeO_2/Si\text{-}Al_2O_3$ catalyst accounting for the deactivation observed in the presence of water.

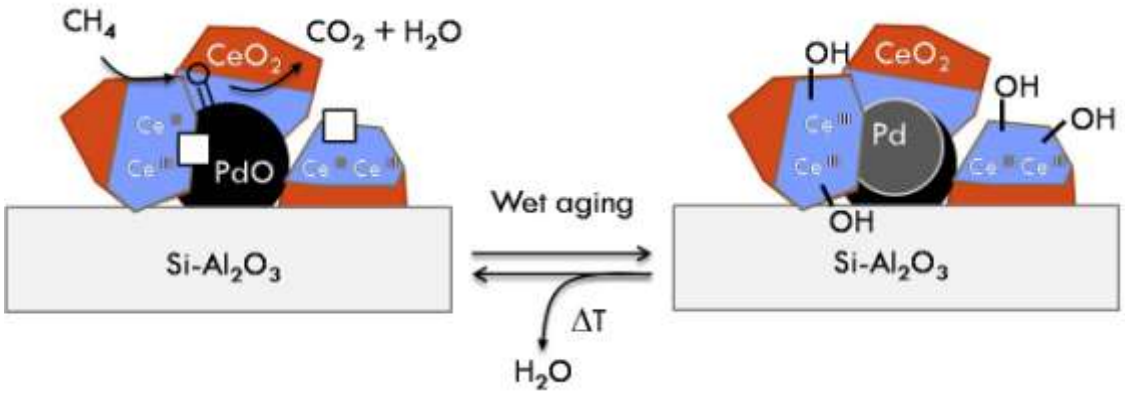

The proposed reaction scheme is fully consistent with both the transient and steady state catalytic data. Under transient conditions (Figure 3.4), the rapid increase in temperature does not allow a significant buildup of hydroxyl groups, the stability of which decreases with temperature. In steady-state experiments at 500 °C (Figure 3.6), the weak and fully reversible deactivation is still consistent with the competitive adsorption of water and methane. At this temperature, the occurrence of ceria back spillover is not a key requirement for having high activity. The catalytically active PdO is thermally stable at 500 °C and Pd can be easily oxidized by gas-phase molecular oxygen. On the other hand, aging at 600 °C under wet reaction conditions (Figure 3.7) induces a deeper deactivation and a reduction of PdO observed by EXAFS (Figure 3.13), along the formation of hydroxyl groups (Figure 3.12). The activity recovery observed when switching from wet to dry reaction conditions at 600 °C (Figure 3.7) is a slow process that involves the recovery of active phase accessibility and hydroxyl removal, which can be outlined in the following steps:

1. the recombination of OH groups to form a chemisorbed water molecule;
2. the desorption of water leaving an oxygen vacancy on the CeO_2 surface;
3. the reaction of O_2 from the gas phase with surface O vacancies on CeO_{2-x};
4. the migration of O species to Pd forming PdO.

Since steps 3 and 4 are also involved in the fast regeneration of the catalyst after reduction in H_2/Ar at 600 °C (Figure 3.10), the slow recovery observed after aging under wet reaction conditions should be limited by step 1 and/or step 2 (Scheme 3.2). Notably, the same steps are involved in the reduction of CeO_2-based materials in H_2 (*111*, *112*) and are recognized as the rate determining steps for the processes operative above 550 °C (*113*, *114*).

Scheme 3.2 A representation of OH groups recombination to chemisorbed H_2O (step 1) and of water desorption, with an oxygen vacancy formation (step 2).

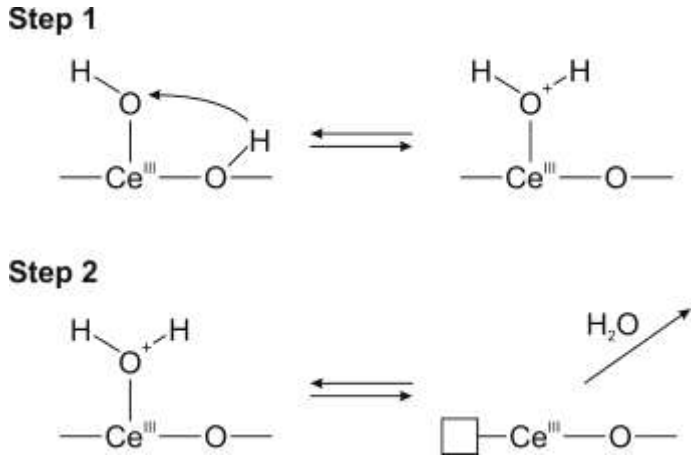

Investigations of the catalyst that was deactivated under wet conditions at 600 °C (Figure 3.8) further corroborate the proposed mechanism of high temperature deactivation. Under dry conditions, the light-off curves for the aged sample are shifted significantly towards higher temperatures (Figure 3.8). In addition to the water generated by methane oxidation, the additional water evolved from the deactivated catalysts in the temperature range from 700 to 850 °C (Figure 3.9) confirms the high temperature stability of the hydroxyls groups on Ce^{III} and their role in the deactivation phenomenon. The catalyst deactivated under wet condition is, therefore, composed of a mixture of PdO and metallic palladium (EXAFS data of Figure 3.13) surrounded by a shell of hydroxylated (IR data of Figure 3.12) and partially reduced ceria. In addition to the specific lower activity of Pd with respect to PdO, the presence of thermally stable OH may also hinder gaseous reactants from reaching the surface and limit the active sites accessibility, as observed by the decrease of CO chemisorption capability (Table 3.1). Finally, the exceptional high activity observed under dry condition on the fresh sample is fully recovered on the wet aged sample after complete removal of the hydroxyls on CeO_2 (Figure 3.8).

3.3.4 Strategies to Improve Catalytic Stability and Conclusions

The amount of Ce in the Pd@CeO_2 synthesis can be varied by changing the ratio in which the two pre-formed building blocks are mixed (functionalized Pd NPs and Ce alkoxide). A Pd (1

wt%)@CeO_2(6 wt%)/Si-Al_2O_3 catalyst was prepared and tested in methane oxidation under wet conditions at 600°C (Figure 3.14). The catalyst was not only very active, but also remarkably more stable than the Pd@CeO_2(1:9 wt), retaining 70% of conversion after 16 hours of wet conditions operation. This was due to a much higher active phase accessibility after wet aging (2.7 m^2 g^{-1} versus 1.1 m^2 g^{-1} for the wet aged 1:9 catalyst). For comparison, impregnated catalysts having comparable formulation, *i.e.* Pd(1 wt%)-CeO_2(6 wt%)/Si-Al_2O_3 and Pd(1 wt%)-CeO_2(9 wt%)/Si-Al_2O_3 were tested under the same conditions. As expected, the Pd(1 wt%)-CeO_2(6 wt%)/Si-Al_2O_3 was less active than the Pd(1 wt%)-CeO_2(9 wt%)/Si-Al_2O_3 catalyst, since the contact between the promoter and the active phase is statistically less probable. Both the impregnated catalysts were quite stable under the reaction conditions, in accordance with the chemisorption results, indicating that the active phase is still accessible even after wet aging (Table 3.1). These results show that hierarchical catalysts are deactivated by water in a different way with respect to impregnated catalysts, and that the strategies to enhance the catalytic performance of nanostructured catalysts may be different.

Figure 3.14

Steady state aging test under wet reaction conditions at 600 °C for Pd(1 wt%)@CeO_2(9 wt%)/Si-Al_2O_3 (solid squares); Pd(1 wt%)@CeO_2(6 wt%)/Si-Al_2O_3 (empty squares); Pd(1 wt%)-CeO_2(9 wt%)/Si-Al_2O_3 (solid line); Pd(1 wt%)-CeO_2(6 wt%)/Si-Al_2O_3 (dashed line). Conditions: 0.5 % CH_4, 2.0 % O_2, 15.0 % H_2O, Ar balance, $O_2/O_{2(stoich)}$=2, GHSV=200 000 mL g^{-1} h^{-1}.

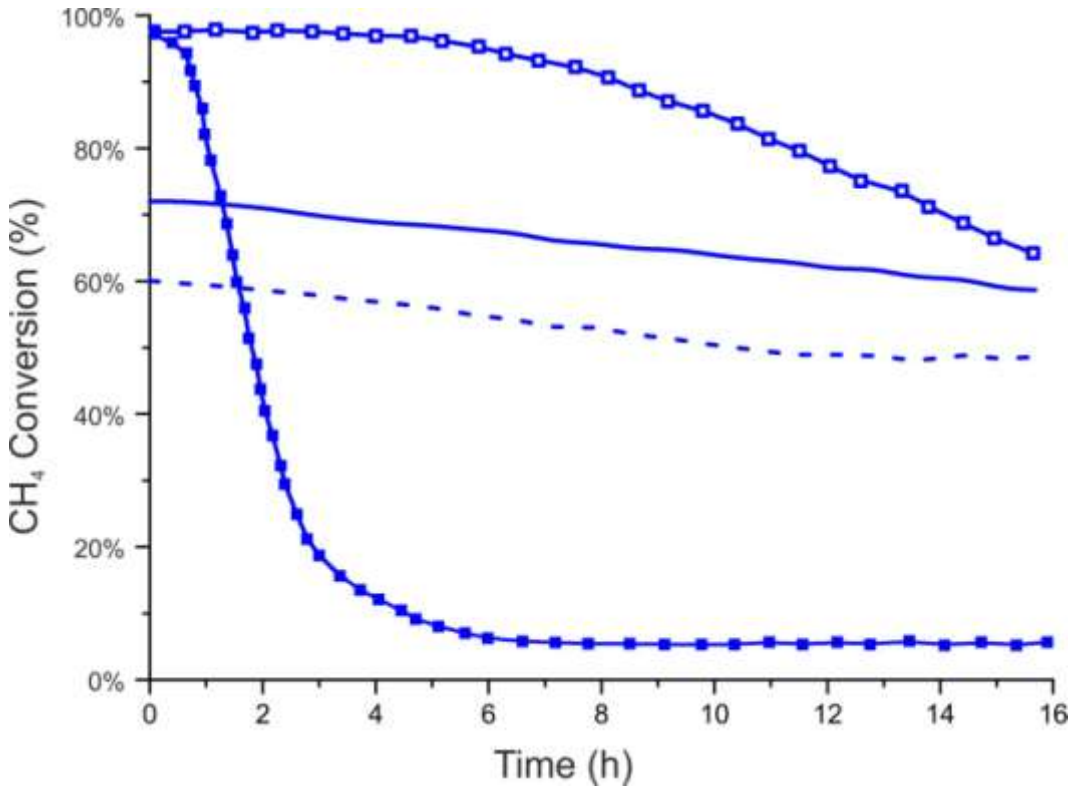

In conclusion, methane oxidation on $Pd@CeO_2/Si\text{-}Al_2O_3$ is strongly influenced by the presence of water during methane oxidation at higher temperatures. Although the catalyst is thermally stable under both run-up experiments and steady-state experiments at both 500 and 600 °C under dry conditions, the addition of water progressively deactivates the system. While at temperatures below 500 °C deactivation is easily reversed by removing the water, at higher temperatures an irreversible deactivation process is observed. This is attributable to lower active phase accessibility and to the formation of stable hydroxides, which are decomposed only by high-temperature treatment. Lowering the amount of CeO_2 in hierarchical catalysts leads to enhanced stability thanks to the retention of more accessible active phase. The results show that design of catalysts for methane oxidation must maximize metal-support interactions to favor oxygen transfer from a reducible promoter, while keeping the active phase accessible to gas phase reactants. It has also been demonstrated that hierarchical $Pd@ZrO_2/Si\text{-}Al_2O_3$catalyst can both guarantee high activity thanks to the nanostructural design and also good hydrothermal stability (*115*).

3.4 Phosphorus Poisoning

3.4.1 Introduction

Phosphorus is a particularly serious poison for CeO_2-promoted catalysts and is a primary agent for irreversible deactivation of automotive catalytic converters under real operating conditions (*116–118*). The presence of phosphorus compounds (P_2O_5 or H_3PO_4) in vehicle exhaust is due to decomposition/volatilization of motor oil anti-wear additives, such as zinc dialkyldithiophosphate (ZDDP) (*35*, *119*). These additives are present in most available motor oils in concentration up to 1-2% (although this can vary depending on the final application) and their effect on catalytic converters is well documented (*116–118*). Based on studies of model systems (CeO_2 and $Ce_xZr_{1-x}O_2$) (*34–37*, *119–122*), it is known that mixed phosphates (Zn, Ca and Mg) form glassy overlayers on the washcoat surface and also react with the catalyst to form $CePO_4$ and $AlPO_4$ (*122*).

$CePO_4$ formation is irreversible and detrimental to the catalytic activity due to loss of oxygen storage capacity (OSC), which is caused by locking of the Ce^{3+}/Ce^{4+} pair in the 3+ state (*121*, *122*). Both the direct reaction of CeO_2 with phosphorus compounds in the gas phase and the reaction of CeO_2 with P-containing species on the catalyst (*e.g.* aluminum phosphate) can lead to the formation of $CePO_4$ (*37*). Based on evidence from total reflection X-ray florescence (TXRF), XPS and ^{31}P NMR data on P-poisoned CeO_2, phosphates species formed on the surface and sub-surface region dramatically decrease OSC. Cerium phosphate is also very stable and cannot be removed from either pure CeO_2 or $Ce_xZr_{1-x}O_2$ by calcination treatments to 1000 °C (*34*, *123*). A few studies indicated partial removal of phosphate species by washing the spent catalyst with oxalic acid (*119*) or chlorine containing species (*124*). However, $CePO_4$ persists even after these treatments (*119*), implying that alternative methods need to be developed to address the problem of P-poisoning.

Despite previous work on regenerating P-poisoned catalysts, relatively little is known about the conditions in which $CePO_4$ is formed. In studies regarding commercial catalysts, the effect of P-aging is evaluated by comparing fresh samples and samples aged for 30, 000 - 160,000 km in conventional automobiles (*116–118*). In model systems studies the aging treatment is typically simulated by depositing phosphates by impregnation of the catalyst with $NH_4H_2PO_4$ solutions followed by calcination to get a final P content of 0.04-4.5 wt% (*34–36*). In one study, CeO_2 aging was performed for only 10 hours by introducing 85 ppm H_3PO_4 through the gas feed (*37*). Notably, aging effects were similar in model systems and real catalysts, even if the chosen conditions, the materials studied and method of P addition were different. This suggests that model systems studies are relevant to real applications, and also that aging can be very fast as soon as phosphates reach the catalytic bed at a certain temperature of formation. Despite this, to our best knowledge,

time-on-stream deactivation studies on commercial or model systems are still too limited. Also, the temperature threshold at which $CePO_4$ is formed was only reported by Xu *et al.* (*37*) for pure CeO_2 under lean conditions (600°C). However, in their study, gas-phase P_2O_5 was introduced by thermal decomposition of aqueous H_3PO_4, resulting in 5% H_2O in the reaction atmosphere. In this section, we show that the introduction of H_2O in methane oxidation reaction mixture enhances the effect of phosphorus poisoning, leading to deactivation. This is particularly relevant to lean-burn engines converters and other real applications, in which water is typically present in 5-15% vol. concentration (*89*, *91*).

3.4.2 Results

In this study, model catalysts based on $Pd@CeO_2$ units deposited on graphite foils were prepared, in order to have conductive supports suitable for PES analysis. A $Pd:CeO_2$ ratio of 1:6 in weight was chosen, accordingly to previous results (see Figure 3.14, chapter above). Two types of graphite foils were used: one pure (99.8% purity, phosphorus-free graphite), and one containing phosphorus (99% purity). The foils were cut into 9x9 mm slides and analyzed by EDS to determine their P content. As expected, no P was observed on the pure graphite support, while the P-graphite samples contained 1000 ± 100 ppm of P. The P signal did not change appreciably upon deposition of $Pd@CeO_2$ units, nor was it affected by any of the aging treatments performed in this study.

Complementary XPS/SRPES analysis was performed on the as-received graphitic supports to determine the chemical state of phosphorus and the surface/bulk distribution. Prior to calcination, there was no P signal on either the P-graphite or the pure graphite. A phosphorus signal, at a Binding Energy (BE) corresponding to that of PO_4^{3-} (133 eV) was only observed on the P-graphite after thermal treatment to 450 °C in air (see Figure 3.15). Similar treatment of the pure graphite did not cause the appearance of a P signal. This suggests that P is initially present only in the bulk of the P-graphite support and is released during the thermal treatment. An O 1s signal at 530.5 eV appeared together with the P signal, indicating the presence of PO_4^{3-} species. This fingerprint of PO_4^{3-} was present on all $Pd@CeO_2$/P-graphite samples, independent of aging conditions and with a similar intensity as was observed following calcination at 450 °C. In accordance to these observations, phosphates can be present as intercalating compounds of graphite foils manufactured by squeezing exfoliated graphite (*125*).

Figure 3.15 P 2p XPS spectra of P-graphite samples: fresh support (A), 450°C calcined support (B), Pd@CeO_2/P-graphite samples fresh and aged (C).

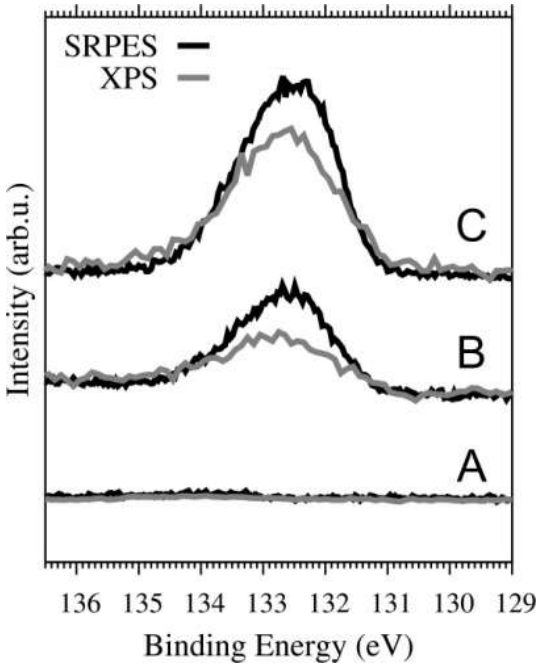

SEM images of the fresh Pd@CeO_2/graphite and Pd@CeO_2/P-graphite catalysts are shown in Figure 3.16 and exhibit very similar surfaces, displaying large, smooth domains of a continuous film, separated by small, shallow cracks. The distributions of Pd, Ce and O signals over the samples were homogeneous, demonstrating that the Pd@CeO_2 particles were well-dispersed and exposed to the gas phase for both supports, an important prerequisite for model catalytic systems.

Figure 3.16 20 µm viewfield SEM images and EDS mapping of Pd, Ce and O signals of fresh Pd@CeO_2/graphite (top row) and Pd@CeO_2/P-graphite (bottom row) samples.

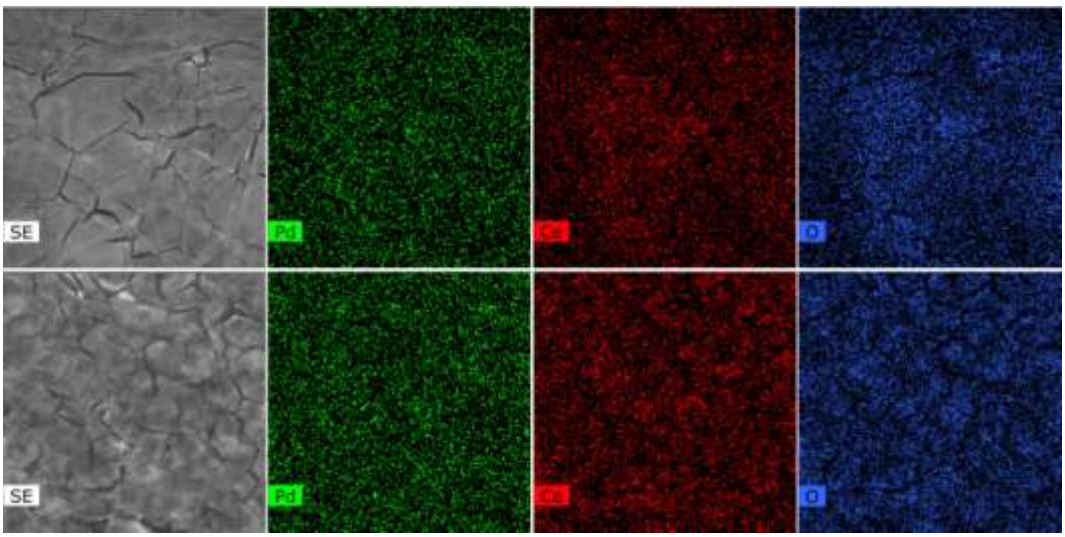

The "fresh" catalysts were then aged for 0 min, 30 min, 1 h, or 9 h at catalytic reaction conditions, at 500 °C and 600 °C, in dry and wet conditions. In all experiments, the catalyst was ramped to the desired temperature in 0.5% CH_4, 2.0% O_2 and 15.0% H_2O (for wet conditions) and held at that temperature for the chosen time span. After aging, the gas flow was switched to pure Ar and the samples cooled to room temperature before being transferred to either the SRPES/XPS line or to the SEM.

As shown in Figure 3.17A, the fresh model Pd@CeO_2/graphite catalyst showed significant and constant evolution of CO_2 as result of CH_4 oxidation at both 500 and 600 °C. While rates were stable under dry conditions, they decreased with time at both temperatures when water was added. The Pd@CeO_2/P-graphite samples were less active for methane oxidation (Figure 3.17B). Most notably, there was a fast and irreversible deactivation during wet aging at 600 °C. After 1 h of isothermal treatment under these conditions, the sample was almost completely inactive.

Figure 3.17 CO_2 evolution over time. A: Pd@CeO_2/graphite; B: Pd@CeO_2/P-graphite. Circles: 600 °C aging; squares: 500 °C aging; filled symbols: dry conditions (CH_4 0.5%, O_2 2%, GHSV: 10^6 mL g^{-1} h^{-1}) ; open symbols: wet conditions (15% H_2O vapor added to reaction atmosphere).

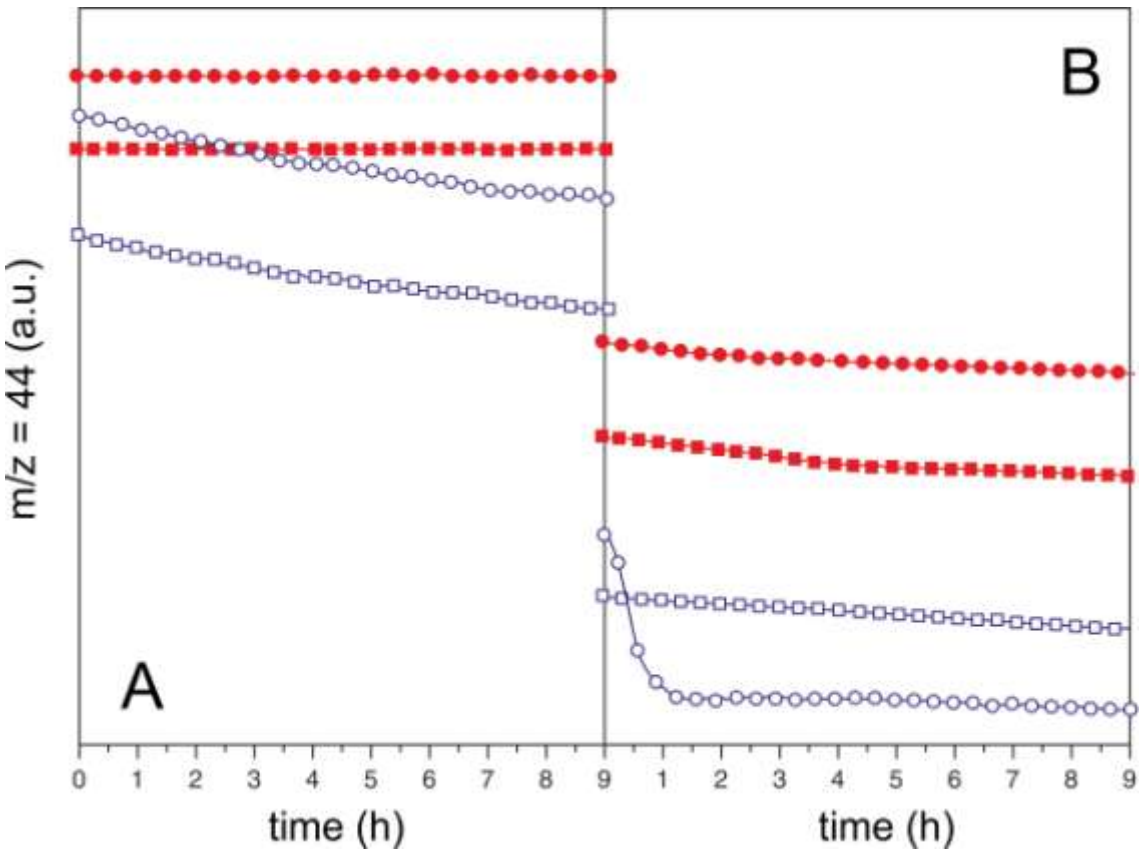

SEM images of the aged samples in Figure 3.18 show differences between the catalysts supported on graphite and P-containing graphite. The surfaces of the $Pd@CeO_2$/graphite samples were not appreciably altered by any of the aging treatments. However, images of the $Pd@CeO_2$/P-graphite samples show features having diameters of 10-30 nm, with sizes that are slightly bigger for 600 °C aging treatments. These spots are partially sintered $Pd@CeO_2$ particles. The SEM analysis suggests that the presence of phosphorus causes partial aggregation of the $Pd@CeO_2$ units and growth of crystallite sizes that does not occur in the absence of P.

Figure 3.18

SEM of $Pd@CeO_2$/graphite (A-E) and $Pd@CeO_2$/P-graphite samples (A'-E'). The samples were fresh (A, A') or treated for 9 h under the following conditions: dry reaction conditions at 500 °C (B, B') or 600 °C (D, D'); wet reaction conditions at 500 °C (C, C') and 600 °C (E, E').

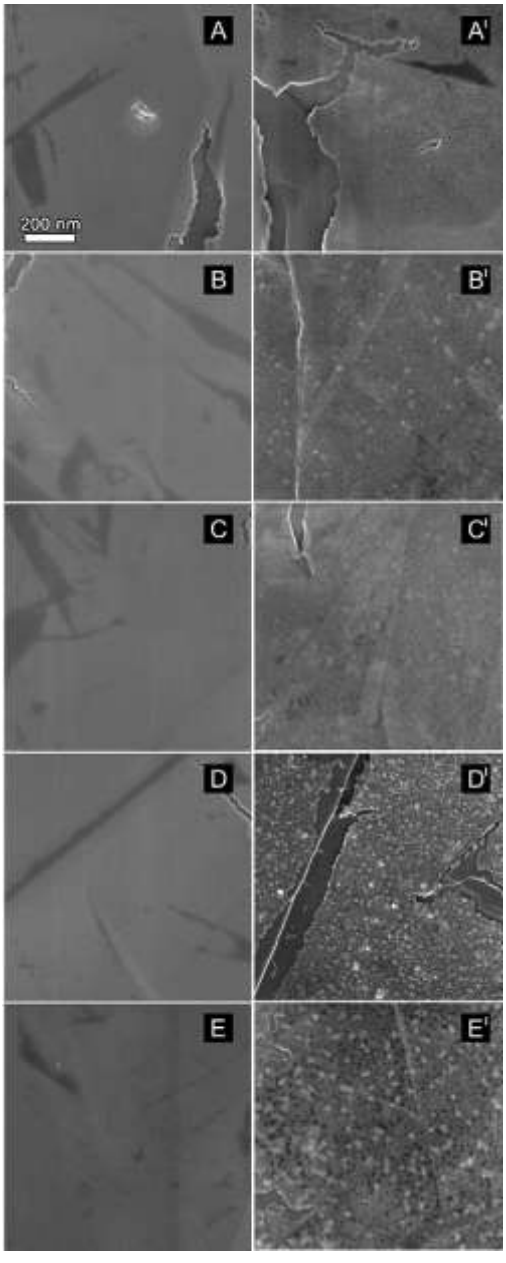

Figure 3.19 indicates that the Ce 3d region of the XPS spectra is very different for the Pd@CeO_2/graphite and Pd@CeO_2/P-graphite samples. Spectra on the Pd@CeO_2/graphite samples were all similar, with features typical of pure CeO_2. Initially, the apparent O:Ce stoichiometry is 1.94 (12% Ce^{3+}) but it increases to 2.0 with aging time. Apparently, a small fraction of the cerium is in the Ce^{3+} state in the initial particles but all of the Ce atoms are converted to Ce^{4+} under the aging conditions used in this study. This behavior differs from that observed for Pd@CeO_2/Si-Al_2O_3 catalysts, which showed a low but constant Ce^{3+} fraction for all the treatments (*89*). Various factors could contribute to this, including the different surface sensitivity of the techniques used (XPS-XAS) and the different Pd:Ce ratio, but the different calcination temperatures used here (450 °C vs. 850 °C) and the different supports (Al_2O_3 vs. graphite) are likely the primary causes.

Figure 3.19

Representative Ce 3d XPS spectra of: (A) the fresh Pd@CeO_2/graphite sample; (B) fresh Pd@CeO_2/P-graphite; (C) Pd@CeO_2/P-graphite aged at 500 °C; (D) Pd@CeO_2/P-graphite aged at 600 °C. Dry conditions are shown by red lines and wet conditions by the blue lines. The areas of the presented spectra have been normalized after subtraction of Shirley background and the curves have been offset for clarity. The positions of the most prominent peaks in Ce^{4+} and Ce^{3+} spectra are marked by grey lines.

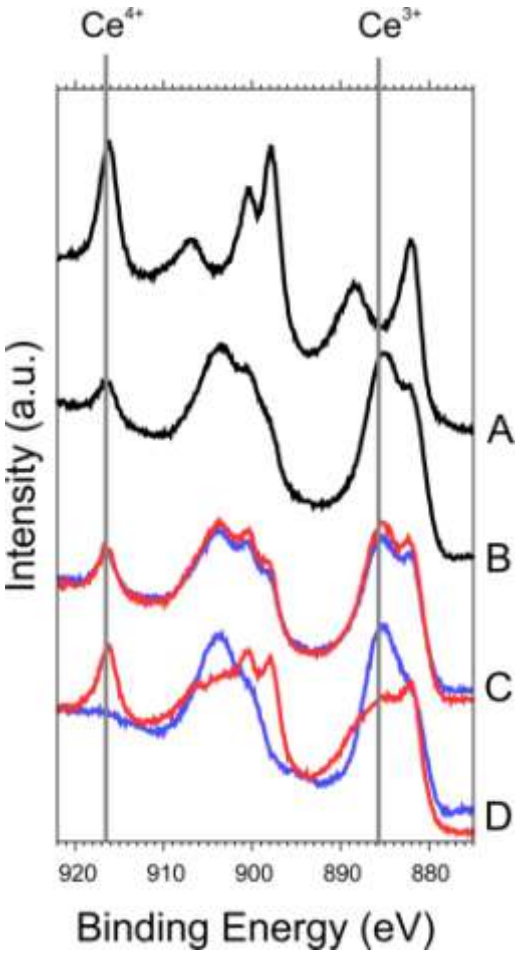

On the Pd@CeO_2/P-graphite sample, in contrast, the XPS spectra show mainly features of $CePO_4$ (*35*, *126*), even on the fresh sample, for which Ce^{4+} is also still observed. Spectra taken after heating to 500 °C under dry and wet aging were similar to each other and showed only small changes compared to the fresh sample. On the other hand, aging treatments at 600 °C resulted in dramatic changes. After 30 min of wet aging at this temperature, the Ce^{4+} signal completely disappeared. Spectra obtained after prolonged dry aging (9 h) showed partial oxidation to Ce^{4+} with respect to the fresh sample.

Figure 3.20 shows the percentage of Ce^{3+} on the Pd@CeO_2/P-graphite sample for the different aging conditions. Since, in the absence of P, the Ce in the Pd@CeO_2 particles is almost completely oxidized to Ce^{4+} after the initial calcination and after all aging treatments, the trends observed for the Ce^{3+} percentage in this case are indicative of $CePO_4$ formation on the surface of the particles sampled by XPS. The fresh sample contains 75% Ce^{3+}, demonstrating that the particles are extensively covered by $CePO_4$ already after calcination. For aging at 500 °C, the percentage of Ce^{3+} does not change appreciably, regardless of the aging conditions (dry or wet). However, aging at 600 °C changed the sample dramatically. Wet aging caused an increase in Ce^{3+} percentage to 100% after 30 min, while dry aging decreased the Ce^{3+} content, to 40% Ce^{3+} after 9 h. These results indicate a crucial role for water in the formation, accumulation, and stabilization of phosphates on ceria.

Figure 3.20

Calculated Ce^{3+} percentage for Pd@CeO_2/P-graphite samples, determined by fitting of Ce XPS spectra. Fresh samples: star. Squares: aged at 500 °C (filled: dry conditions, empty: wet conditions). Circles: aged at 600 °C (filled: dry conditions, empty: wet conditions). The solid lines are guides to the eye.

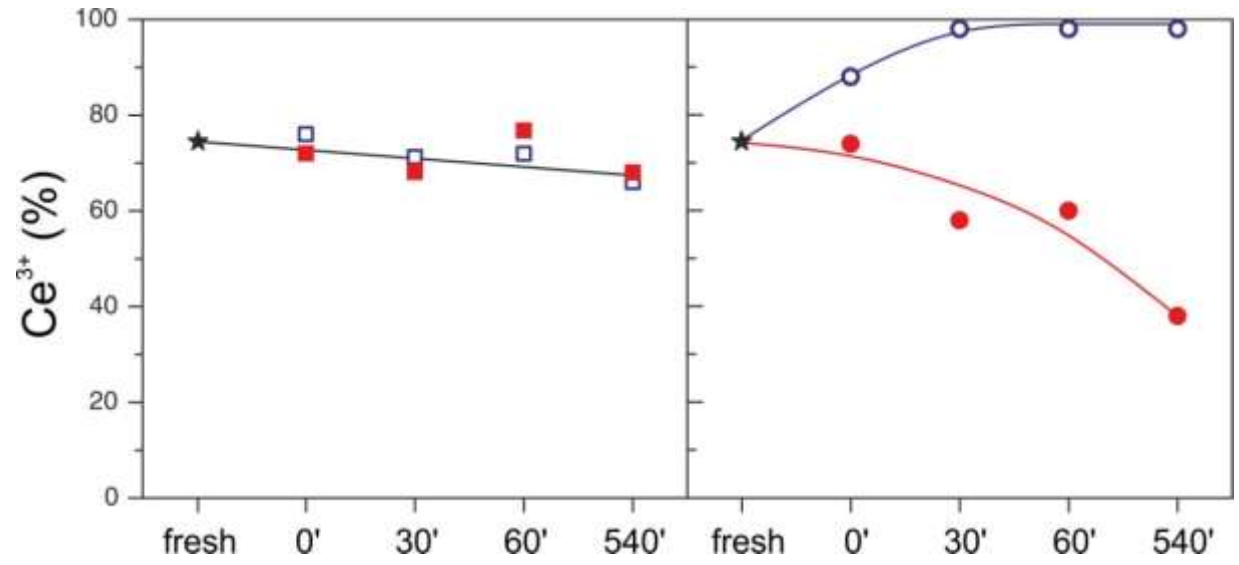

To gain further insights into the extent of $CePO_4$ formation and the extent of cerium reduction, *operando* and *ex-situ* XANES measurements were performed on the $Pd@CeO_2$/P-graphite catalysts, with representative results shown in Figure 3.21. In all cases, only minor differences were observed between fresh, dry-aged and wet-aged samples, at both 500 °C and 600 °C. In contrast to the XPS results, the Ce^{3+} percentage did not evolve during aging treatments and ranged from 15% to 18% in all the samples studied. Indeed, these results are similar to recent *in-situ* EXAFS data on a $Pd@CeO_2/Si\text{-}Al_2O_3$ powder having a similar $Pd@CeO_2$ composition with no P poisoning. That study also indicated the presence of 20% Ce^{3+} in the fresh catalyst (*89*).

Figure 3.21 *Operando* XANES spectra of $Pd@CeO_2$/P-graphite sample at Ce L_{III} edge: (A) fresh; (B) during dry aging at 600 °C; (C) during wet aging at 600 °C. Reference spectra: CeO_2 (D), $CePO_4$ (E).

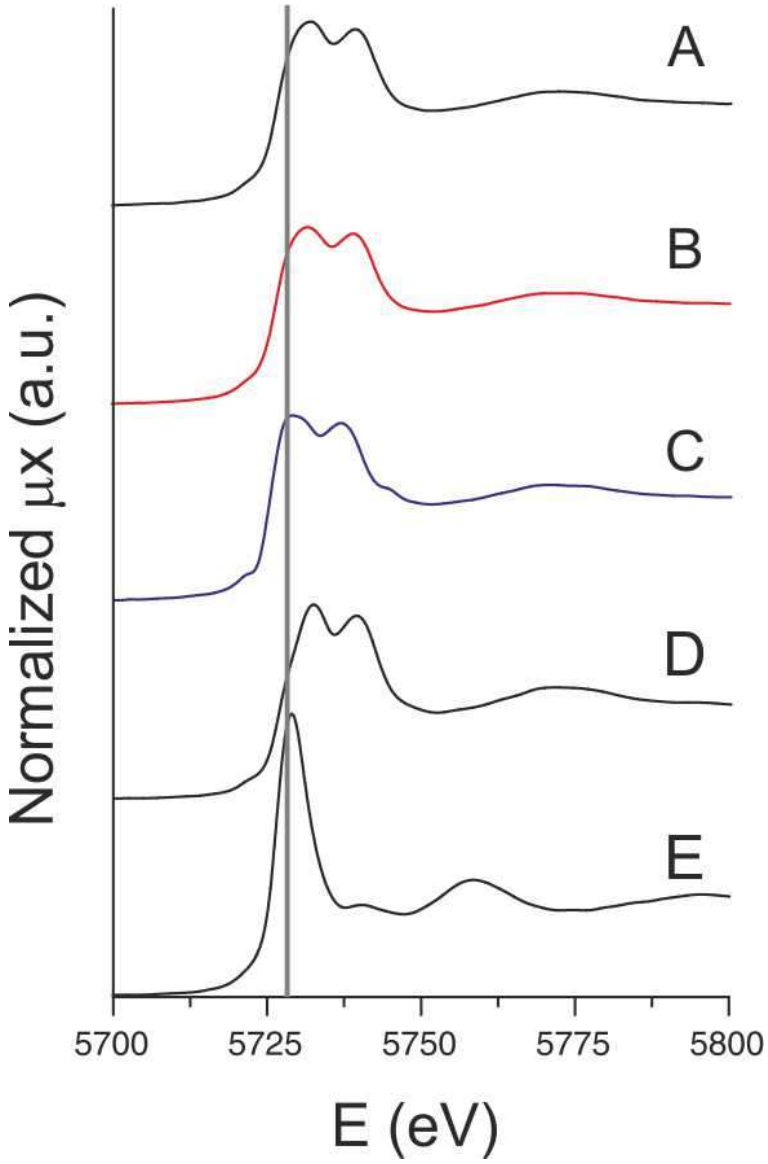

The dramatic difference in the valence ratios calculated from XPS and XANES implies that the surface and bulk concentrations can be very different on these samples. Since the inelastic mean free path in CeO_2 of the photoelectrons originating from Ce 3d level in the XPS study is approximately 1.2 nm and the expected dimensions of the CeO_2 crystallites in the Pd@CeO_2 particles is 3 to 4 nm (*8*), the large difference between surface and bulk concentrations cannot be explained by the presence of $CePO_4$ at the surface of the initial Pd@CeO_2 core-shell particles. Rather, the data indicate that thermal sintering or partial aggregation of ceria crystallites must occur under wet aging at 600 °C.

To further investigate the evolution of the Pd@CeO_2 particles dimensions during aging, the Pd@CeO_2/graphite and Pd@CeO_2/P-graphite samples were characterized by AFM topographic analysis. Figure 3.22 shows images and height profiles for the Pd@CeO_2/P-graphite sample, both fresh and after 9-h aging at 600 °C. Results for the Pd@CeO_2/graphite sample are not shown but were essentially identical to that observed for fresh Pd@CeO_2/P-graphite, even with various aging treatments. For both Pd@CeO_2/graphite and Pd@CeO_2/P-graphite, the fresh and dry aged samples showed small features, approximately 10 nm in height, similar to what was observed for Pd@CeO_2 particles deposited onto YSZ(100) single crystals (*95*) (Figure 3.22A and B). Wet aging did not appreciably change the Pd@CeO_2/graphite sample at either 500 °C or 600 °C. However, wet aging at 600 °C caused dramatic sintering on the Pd@CeO_2/P-graphite sample, leading to the appearance of features that were 50-60 nm high and 50-70 nm wide, distributed over a corrugated surface (Figure 3.22C). The changes in particle size help explain how the bulk and surface compositions can be so different.

Figure 3.22 AFM topography images with representative line scans for $Pd@CeO_2$/P-graphite: (A) fresh; (B) aged at 600 °C under dry conditions for 9 h; (C) aged under wet conditions at 600 °C for 9 h. Please note the different scales in part C.

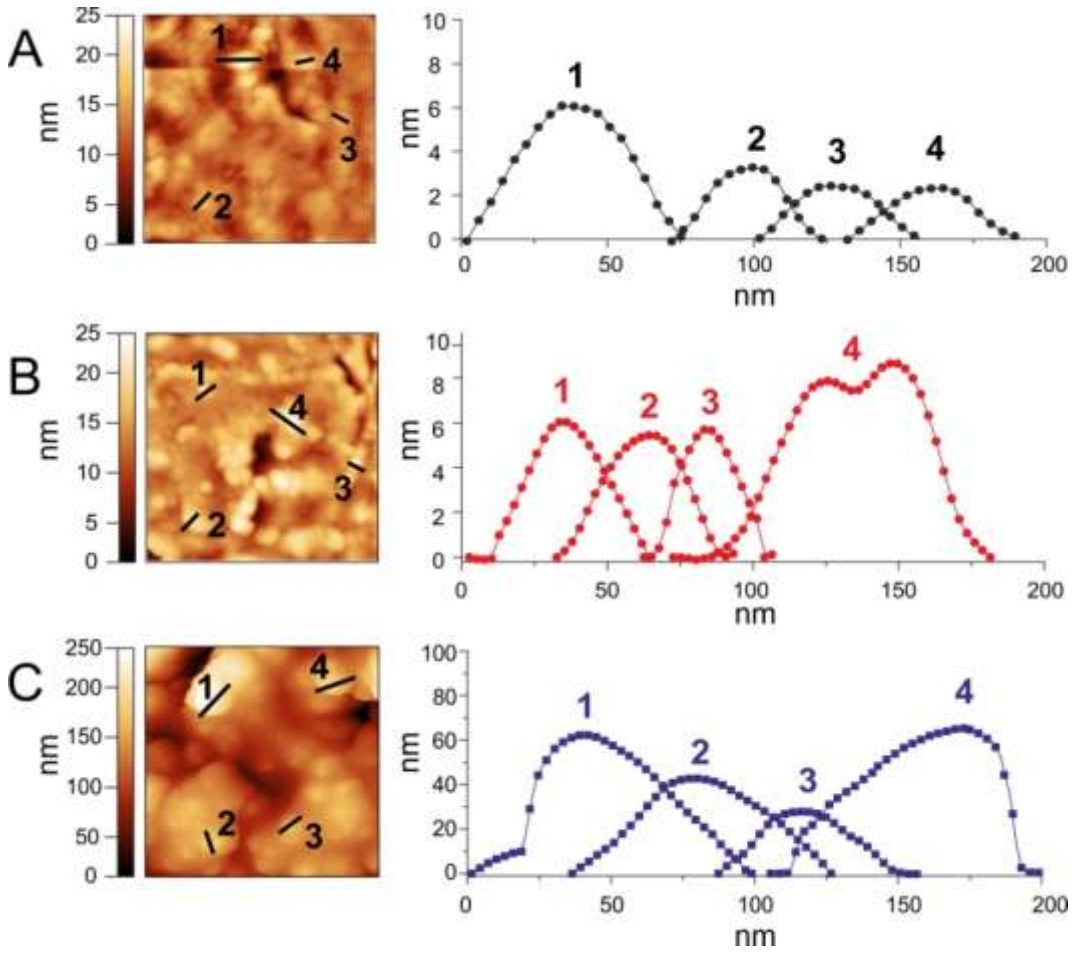

Figure 3.23 shows XPS/SRPES spectra for the O 1s region of the $Pd@CeO_2$/graphite and $Pd@CeO_2$/P-graphite samples and the results support the conclusions reached from the Ce 3d core level. The spectrum of the fresh $Pd@CeO_2$/graphite sample, Figure 3.23A, shows two peaks at 529.2 eV and 531.6 eV. The peak at lower BE can be assigned to bulk CeO_2, while higher BE peak is likely due to hydroxyl species (*127*). However, the presence of other species having similar BE cannot be entirely ruled out. Carbonates arising from reaction with the graphite supports are not expected to form during the thermal treatments performed here; also, similar O 1s spectra were observed for $Pd@CeO_2$ on Au (not reported here). When the $Pd@CeO_2$/graphite sample was aged under wet conditions, Figure 3.23B-C, the intensity of the peak at 532 eV was enhanced and a slight shift to higher binding energies was observed, further supporting the assignment of the signal to hydroxyl species (*85*, *89*, *127*). With $Pd@CeO_2$/P-graphite, the spectrum of the fresh sample, Figure 3.23B', again showed a peak near 529 eV due to bulk CeO_2 but the largest peak was centered at 530.4 eV,

which can be assigned to $CePO_4$ basing on the preliminary analysis performed on the P-containing graphite. There was very little change in the spectrum of samples aged under dry conditions at either 500 °C or 600 °C, but wet aging at either temperature gave increased intensity in the region assigned to hydroxyls. After wet aging at 600 °C, the peak associated with bulk CeO_2 essentially disappeared. This is consistent with the disappearance of the Ce^{4+} signal in the Ce 3d region of the 600 °C wet-aged samples.

Figure 3.23

Left: representative O 1s XPS spectra of Pd@CeO_2/graphite samples: fresh (A), 500°C aged 9h (B), 600°C aged 9h (C); Right: representative O 1s XPS spectra of : (A') fresh Pd@CeO_2/graphite; (B') fresh Pd@CeO_2/P-graphite; (C') Pd@CeO_2/P-graphite aged at 500 °C; (D') Pd@CeO_2/P-graphite aged at 600 °C. The red lines were obtained after aging under dry conditions and the blue lines under wet conditions. The areas of the presented spectra have been normalized to the $CePO_4$ contribution (B,C and D) and the P free samples have been adjusted to comparable intensity. The curves have been offset for clarity. The positions of assigned O 1s contributions are marked with grey lines.

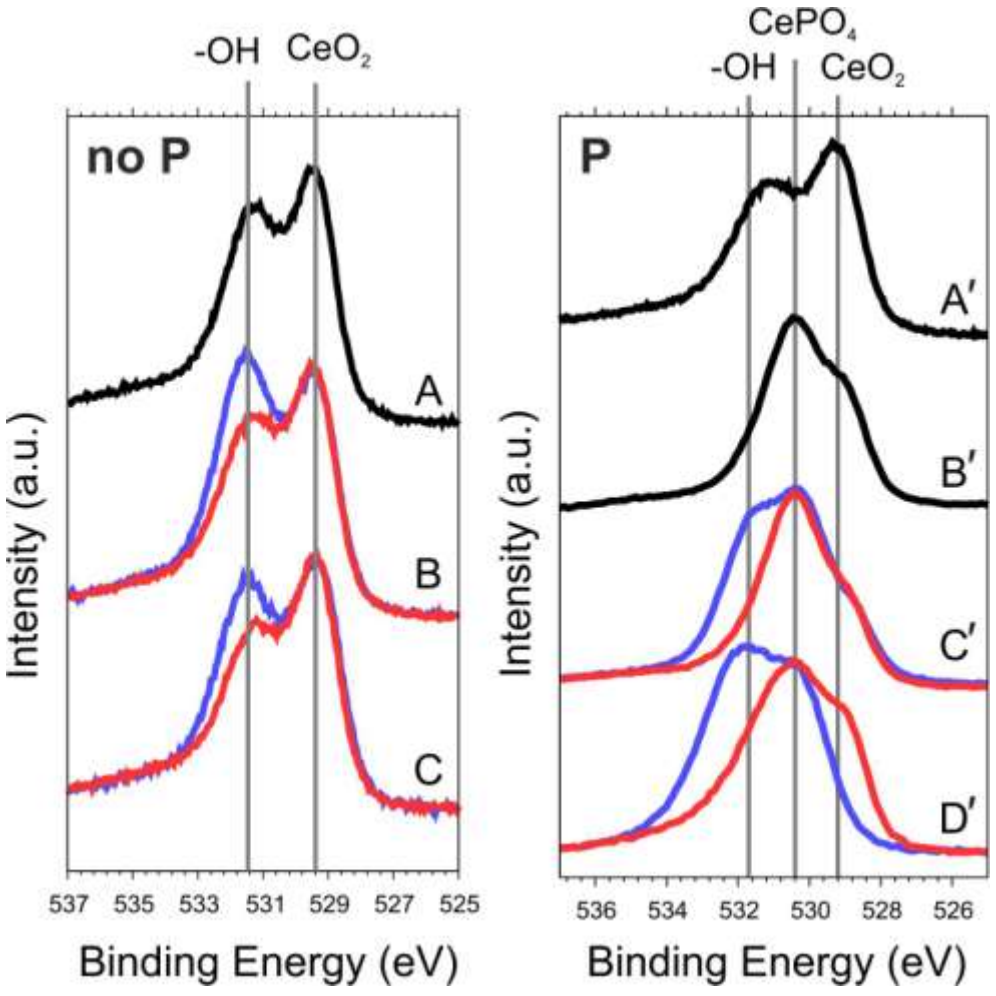

XPS spectra of Pd 3d region on representative samples are shown in Figure 3.24. For both $Pd@CeO_2$/graphite and $Pd@CeO_2$/P-graphite, the fresh samples show two peaks at 337.2 eV and 342.4 eV, which are almost certainly due to PdO. The two peaks are due to the Pd spin-orbit split doublet (Pd $3d_{5/2}$ and Pd $3d_{3/2}$). The BE of the doublet is actually close to the BE expected for PdO_2 (*128*); however, a shift to higher binding energy is often observed for metal and metal-oxide nanoparticles, including Pd and PdO (*129–135*). For example, the $3d_{5/2}$ signals of both PdO and Pd nanoparticles have previously been reported to shift to approximately 1.0 eV higher BE due final-state effects (*129*, *133*).

Figure 3.24

Representative Pd 3d XPS spectra: (A) $Pd@CeO_2$/graphite; (B) fresh $Pd@CeO_2$/P-graphite; (C) $Pd@CeO_2$/P-graphite aged at 500 °C; (D) $Pd@CeO_2$/P-graphite aged at 600 °C. Aging under dry conditions is indicated by the red lines while wet aging is indicated in blue. The curves have been offset for clarity.

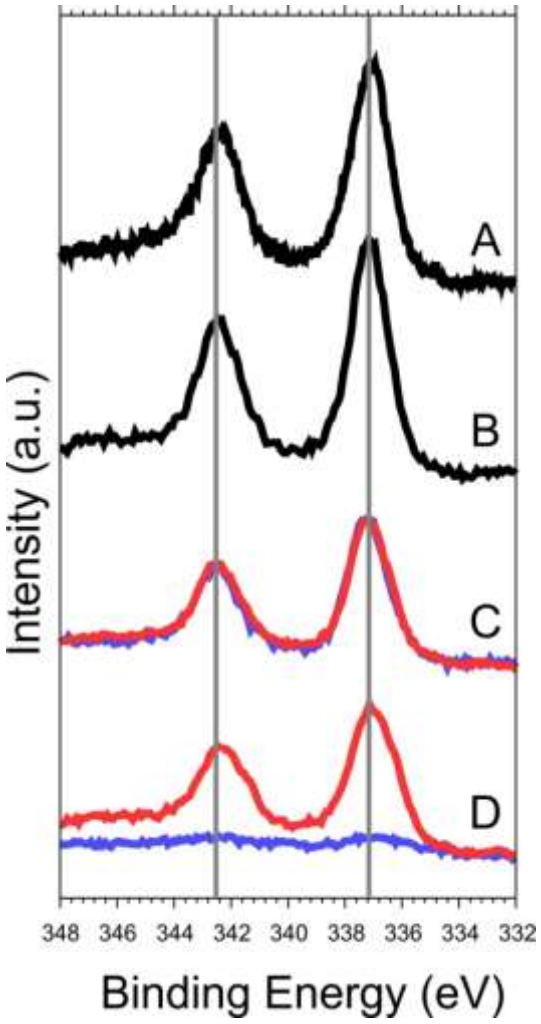

The fact that our samples contained PdO was confirmed by *operando* and *ex-situ* XANES measurements on both the graphite and P-graphite supported catalysts (Figure 3.25). Neither wet nor dry aging had any effect on the XPS spectrum for Pd on the Pd@CeO_2/graphite sample; however, the same was not true for Pd@CeO_2/P-graphite. While dry aging did not affect the spectrum, wet aging of the P-containing sample at 600 °C resulted in the complete disappearance of the Pd signal. Since EDS and XANES results demonstrate that Pd is not lost under these conditions (Figure 3.25), the loss of Pd signal in XPS must be due to burial of Pd under the $CePO_4$. This agrees with the SEM results, showing that the Pd@CeO_2 particles undergo severe sintering during wet aging when P is present.

Figure 3.25 Pd K edge XAS spectra of: (A) fresh (black line), 600°C dry aged 9h and 600°C wet aged 9h Pd@CeO_2/P-graphite samples, not normalized; (B) normalized PdO reference.

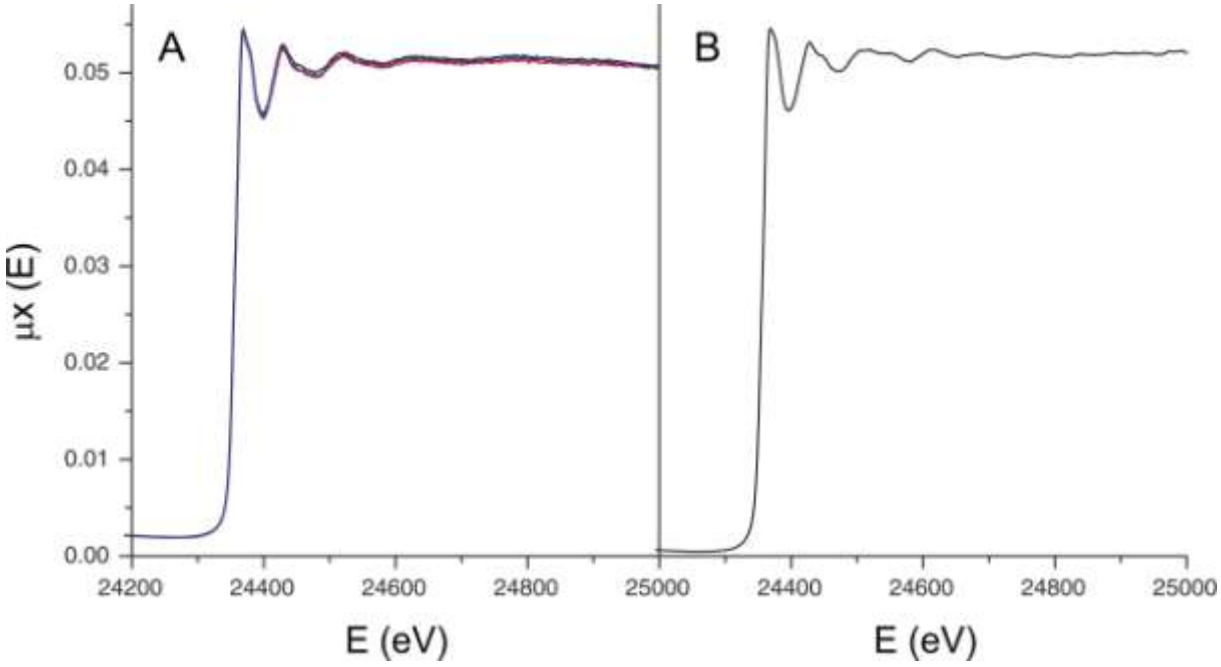

3.4.3 Discussion

One of the main objectives of this work was to study the effect of P poisoning on the catalytic performance of Pd-CeO_2 catalysts. Similarly to other P-poisoning studies, phosphorus was deliberately introduced in the system during the catalyst preparation (*34–36*), rather than introducing it from the gas feed during aging treatments (*37*). In this way, H_2O is not introduced in the reaction mixture by decomposition of H_3PO_4 to P_2O_5 and the effect of water addition can be studied separately. The combined results in this study demonstrate that the presence of phosphorus in the vicinity of a Pd/ceria catalyst results in the rapid formation of $CePO_4$ at

temperature as low as 450 °C. Since vapor pressure of phosphates is negligible under these conditions, the formation of $CePO_4$ indicates that there is a high affinity of Ce and P. This agrees with previous results from Xu *et al*., who observed formation of $CePO_4$ from the reaction of CeO_2 with $AlPO_4$ (*37*). Notably, the distribution of $CePO_4$ in the surface and subsurface of CeO_2 particles is in agreement with other observations from the literature (*35–37*, *121*, *122*), even if the source of phosphorus and aging conditions were different.

Interestingly, the phosphorous-poisoned catalysts maintain a relatively high activity under dry conditions, despite being extensively covered by phosphates. Indeed, the XPS spectra even indicate that cerium phosphate can be partially removed from the surface of ceria particles at 600 °C under dry conditions. In agreement with this, López Granados *et al.* reported that, on P-poisoning of CeO_2 by addition of $(NH_4)_2HPO_4$, followed by calcination to 600 °C (*35*) some of the CeO_2 surface was not converted to $CePO_4$ and was still available for oxygen exchange with gas-phase oxygen, even for samples having a high P:Ce ratio.

The presence of water changes things completely, and a rapid, irreversible deactivation is observed at temperatures above 600 °C. At these temperatures, $CePO_4$ becomes highly mobile and causes severe aggregation of ceria particles and Pd encapsulation. The results of this study indicate that water and phosphorus have a cooperative effect and take part in a deactivation mechanism activated by high temperature. For the first time, the deactivation of Pd-CeO_2 catalysts in the presence of P was studied in steady-state experiments, revealing that poisoning occurs in very short time under conditions relevant for real applications (*36*, *37*, *122*). Although surface blockage by $CePO_4$ is reported in the literature as the main effect of P-poisoning on ceria-based catalysts, our work reveals that phosphorus can also cause deep morphological transformations of the catalyst and dramatic loss of activity, especially in the presence of water.

3.4.4 Conclusions

In conclusion, the effect of phosphorus poisoning on the catalytic oxidation of methane over Pd@CeO_2/graphite catalysts was found to be dramatically influenced by temperature and presence of H_2O. When P was not introduced in the catalyst formulation, the catalysts were active and stable under all studied conditions (500-600 °C; dry and wet conditions). On the other hand, P-poisoned catalysts were less active and stable because of partial thermal sintering. Water vapor causes rapid and complete deactivation at higher temperatures by inducing severe aggregation of ceria nanoparticles, incorporation of Pd active phase in the bulk of the crystallites and exposure of $CePO_4$ to the catalyst surface. The combination of XPS/SRPES, *operando* XANES measurements, SEM/EDS and AFM techniques provide evidence of a temperature dependent, water-driven P-poisoning of Pd and CeO_2-based oxidation catalysts.

3.5 SO_2 Poisoning

3.5.1 Introduction

SO_2 is a particularly serious poison of catalytic converters, produced by the oxidation of sulfur compounds present in fuels and in lubricating additives (*23*, *136*). Despite the continuing reduction of sulfur in fuels (The Ultra-Low Sulfur Diesel (ULSD) regulation established a 15 ppm sulfur content for diesel fuel in 2006(*137*)), long-term exposure to low concentrations of SO_2 is still detrimental to the catalytic activity of the exhaust after-treatment catalysts (*21*, *136*, *138*). Under lean conditions and at temperatures above 200 °C, the presence of SO_2 in the exhaust leads to formation of sulfate species on both the support and the active phase (*71*, *139*). One of the possible pathways for the formation of sulfates involves SO_2 oxidation to SO_3 by O_2 (Reaction 3.1) and subsequent adsorption of SO_3 on the metal-oxide surface (Reaction 3.2).

$$2SO_2 + O_2 \rightarrow 2SO_3 \quad (3.1)$$

$$SO_3 + M - O \rightarrow M - SO_4 \quad (3.2)$$

Alternatively, SO_2 may be oxidized by oxygen from the support or disproportionate to SO and SO_3 (*140*). Formation of sulfates on supports such as alumina can also deactivate the catalyst by acting as a buffer of SO_x that prevents adsorption of SO_2 onto the active phase during exposure to gas-phase SO_2 but prolongs the poisoning effect after SO_2 removal due to a slow decomposition of the accumulated sulfates(*23*, *136*). With a non-sulfating support, such as SiO_2, the active phase will not be protected from poisoning, leading to faster deactivation, but also to faster recovery (*23*).

SO_2 poisoning on reducible supports, CeO_2 and $Ce_xZr_{1-x}O_2$, has been widely investigated because of the importance of these oxides in catalytic converters (*141–144*). It is known that ceria forms sulfates that are stable to relatively high temperatures (600 °C - 700 °C) (*142*, *145*). ZrO_2 forms fewer sulfates when exposed to the same conditions, and these are mostly confined to its surface (*142*). However, conflicting observations have been made regarding the resistance of Ce-Zr (CZ) mixed oxides to SO_2 in comparison to CeO_2 and ZrO_2. Luo *et al.* reported that CeO_2 and CZ catalysts were affected in a similar manner by SO_2 poisoning for both the water-gas-shift (WGS) and CO-oxidation reactions (*142*), while Deshmukh *et al.* reported enhanced resistance to poisoning for the mixed oxides (*144*).

In this chapter, we report the effect of SO_2 poisoning on methane oxidation over hierarchical Pd@$Ce_xZr_{1-x}O_2$ catalysts supported on modified alumina. The previously reported synthesis (*92*) was modified in order to achieve a range of shell compositions, from pure CeO_2 to

pure ZrO_2. We investigate the effect of SO_2 on these core-shell catalysts using XPS on model catalysts designed to closely resemble the high-surface-area (HSA) materials in both surface composition and temperature treatments, while avoiding charging and low resolution problems often experienced with powdered materials (*146*).

3.5.2 High-Surface-Area Materials

The synthesis of $Pd@CeO_2$ and $Pd@ZrO_2$ particles reported in previous works (*8*, *92*) was modified in this study to allow the preparation of $Pd@Ce_xZr_{1-x}O_2$ particles. Ce and Zr alkoxides were mixed together before slowly adding the dispersed Pd-MUA nanoparticles to allow the reaction of both alkoxides with the carboxylic group of MUA. The Pd:(Ce+Zr) molar ratio was kept constant and the following Ce:Zr molar ratios were selected to investigate the generality of the synthetic method: (80:20), (60:40), (40:60), (20:80). Pure $Pd@CeO_2$ and $Pd@ZrO_2$ units were also prepared as references. After controlled hydrolysis, the particles were deposited on hydrophobic, silanized alumina and the materials were calcined at 850 °C for 5 h. The final $Pd@MO_x/Si\text{-}Al_2O_3$ catalysts were characterized by XRD to check for the formation of mixed or segregated CZ oxide phases (Figure 3.26 and Figure 3.27).

Figure 3.26 XRD patterns of the $Si\text{-}Al_2O_3$ calcined at 850 °C for 5 h (grey line) and $Pd@MO_x/Si\text{-}Al_2O_3$ samples calcined at 850 °C for 5 h (orange: CeO_2; green: CZ 80:20; red: CZ 60:40; magenta: CZ 40:60; purple: CZ 20:80; blue: ZrO_2).

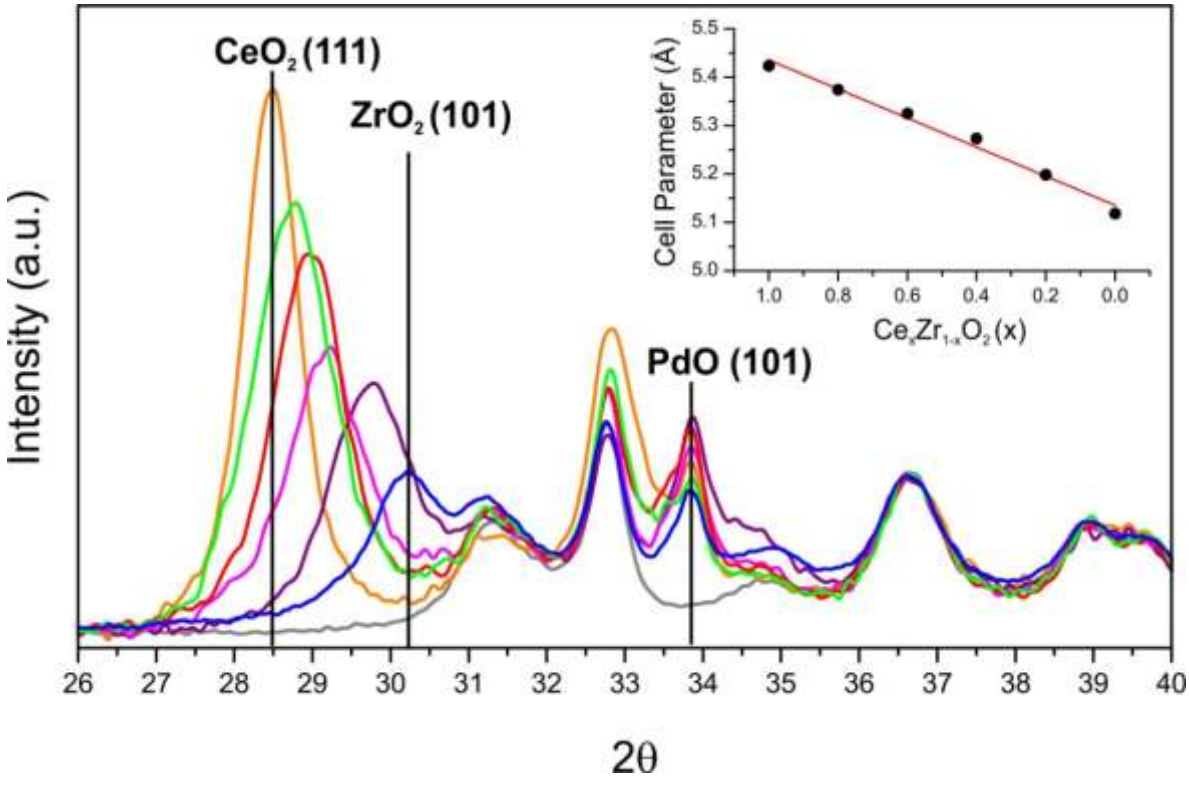

Figure 3.27 XRD patterns of hydrophobic the Si-Al_2O_3 calcined at 850 °C for 5h (a) and Pd@MO_x/Si-Al_2O_3 samples calcined at 850 °C for 5h: ZrO_2 (b), CZ 20:80 (c), CZ 40:60 (d), CZ 60:40 (e), CZ 80:20 (f), CeO_2 (g).

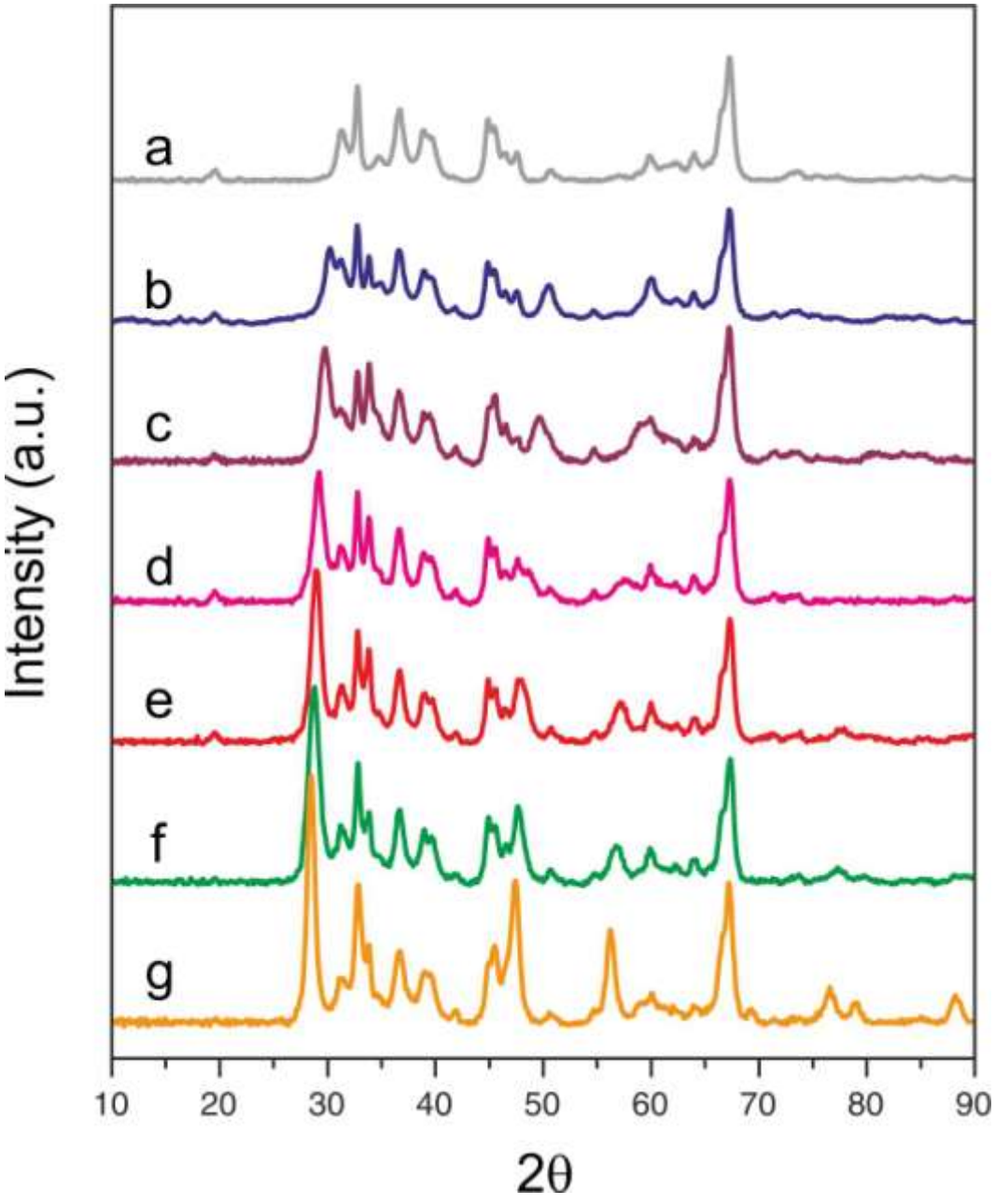

A complete Rietveld analysis of the CZ XRD pattern was not possible due to overlap with the signal from the Al_2O_3 support, which was more than 90 wt% of the studied materials and consisted of a mixture of metastable γ- and θ-Al_2O_3 after thermal pre-treatment (*147*). Nonetheless, the partial XRD spectrum reported in Figure 3.26 clearly showed the first and most intense reflection of the CZ mixed oxides, which varied between 28.5° (for CeO_2) to 30.2° (for ZrO_2). Therefore, only pseudo-cubic cell parameters were calculated in the present case, despite the fact

that a transition from cubic to tetragonal crystal structure is expected in the oxide promoter with high ZrO_2 content (*148*). The linear dependence of the cell parameter for the pseudo-cubic cells with the CZ composition is consistent with the formation of solid solutions between CeO_2 and ZrO_2 (inset of Figure 3.26) (*149*). Only in the case of CZ 40:60 did a shoulder appear at lower diffraction angles, suggesting that segregation of a small amount of a CeO_2-rich phase occurred for that sample. Phase separation has been observed previously for CZ mixed oxides with 40:60 Ce:Zr ratios, because this composition is thermodynamically unstable(*148*). The decreased intensity of the main reflection with increasing ZrO_2 content is due to the lower weight loading and scattering factor of Zr.

The mean crystallite sizes of the CZ mixed oxides were calculated to be in the range of 7-11 nm (Table 3.2), which is in good agreement with TEM results (5-10 nm apparent particles size). Notably, the apparent size of CZ mixed-oxide crystallites is smaller than that of CeO_2, as expected in view of the stabilizing effect of Zr(*149*). The most intense reflection for PdO, the (101) plane, can be observed at 34°. The fitting of this line is complicated by the overlapping of other reflections, so that the mean crystallite size calculated by the Scherrer equation (15-18 nm, see Table 3.2) is not very indicative of the actual size distribution of the PdO active phase in the samples, as discussed further in the section on TEM analysis.

Table 3.2 Cell parameter and apparent crystal size of CZ mixed oxides and apparent crystal size of PdO.

Sample	CZ Cell Parameter (Å)[a]	CZ Apparent Crystal Size (nm)[b]	PdO Apparent Crystal Size (nm)[c]
$Pd(1\%)@CeO_2(9\%)/Si\text{-}Al_2O_3$	5.424	11	18.4
$Pd(1\%)@Ce_{0.8}Zr_{0.2}O_2(8.5\%)/Si\text{-}Al_2O_3$	5.374	7.2	18.4
$Pd(1\%)@Ce_{0.6}Zr_{0.4}O_2(8.0\%)/Si\text{-}Al_2O_3$	5.325	8.4	14.4
$Pd(1\%)@Ce_{0.4}Zr_{0.6}O_2(7.4\%)/Si\text{-}Al_2O_3$	5.273	13.3 (7.7)[d]	15.2
$Pd(1\%)@Ce_{0.2}Zr_{0.8}O_2(6.9\%)/Si\text{-}Al_2O_3$	5.199	7.4	16.4
$Pd(1\%)@ZrO_2(6.4\%)/Si\text{-}Al_2O_3$	5.119	8.5	17.8

[a] Calculated from the Bragg's law and assuming cubic or pseudo-cubic crystal structure
[b] Calculated by Scherrer's equation on the (111) reflection of the CZ oxides
[c] Calculated by Scherrer's equation on the (101) reflection of PdO
[d] apparent crystal size of the segregated Ce-rich phase

Physisorption and chemisorption experiments on $Pd@MO_x/Si\text{-}Al_2O_3$ catalysts revealed that all the samples had similar surface areas, pore-size distributions, and Pd accessibility, as detailed in Table 3.3.

Table 3.3 Results of N_2 physisorption and CO chemisorption analysis of the investigated samples.

Sample	BET surface area ($m^2\ g^{-1}$)	Pore dimensions (nm)	Pd Accessible Surface Area ($m^2\ g^{-1}$)
$Si\text{-}Al_2O_3$	100	10-50	-
$Pd(1\%)@CeO_2(9\%)/Si\text{-}Al_2O_3$	98	10-50	2.8
$Pd(1\%)@Ce_{0.8}Zr_{0.2}O_2(8.5\%)/Si\text{-}Al_2O_3$	97	10-50	2.7
$Pd(1\%)@Ce_{0.6}Zr_{0.4}O_2(8.0\%)/Si\text{-}Al_2O_3$	98	10-50	3.0
$Pd(1\%)@Ce_{0.4}Zr_{0.6}O_2(7.4\%)/Si\text{-}Al_2O_3$	96	10-50	2.8
$Pd(1\%)@Ce_{0.2}Zr_{0.8}O_2(6.9\%)/Si\text{-}Al_2O_3$	98	10-50	2.8
$Pd(1\%)@ZrO_2(6.4\%)/Si\text{-}Al_2O_3$	97	10-50	2.9
$Pd(1\%)/Si\text{-}Al_2O_3$	99	10-50	2.0

The results are comparable with those reported in previous studies on $Pd@CeO_x/Si\text{-}Al_2O_3$ and $Pd@ZrO_x/Si\text{-}Al_2O_3$ (*89*, *115*). On the other hand, the Pd dispersion for the $Pd/Si\text{-}Al_2O_3$ was significantly lower due to severe sintering of Pd nanoparticles. The pore-size distributions were also consistent with previous results: $Pd/Si\text{-}Al_2O_3$ and the $Si\text{-}Al_2O_3$ support have similar pore structures, with pore sizes in the range from 10 to 50 nm in diameter, while the $Pd@MO_x/Si\text{-}Al_2O_3$ catalysts exhibited fewer large pores due to partial filling with the nanostructured units, along with the formation of small pores (around 10 nm in diameter) associated with the units themselves (Figure 3.28).

Figure 3.28 BJH pore size distribution taken from the desorption branch of: Si-Al_2O_3 (grey), Pd/Si-Al_2O_3 (black) and Pd@MOx/Si-Al_2O_3 (orange: CeO_2; red: CZ 60:40; blue: ZrO_2).

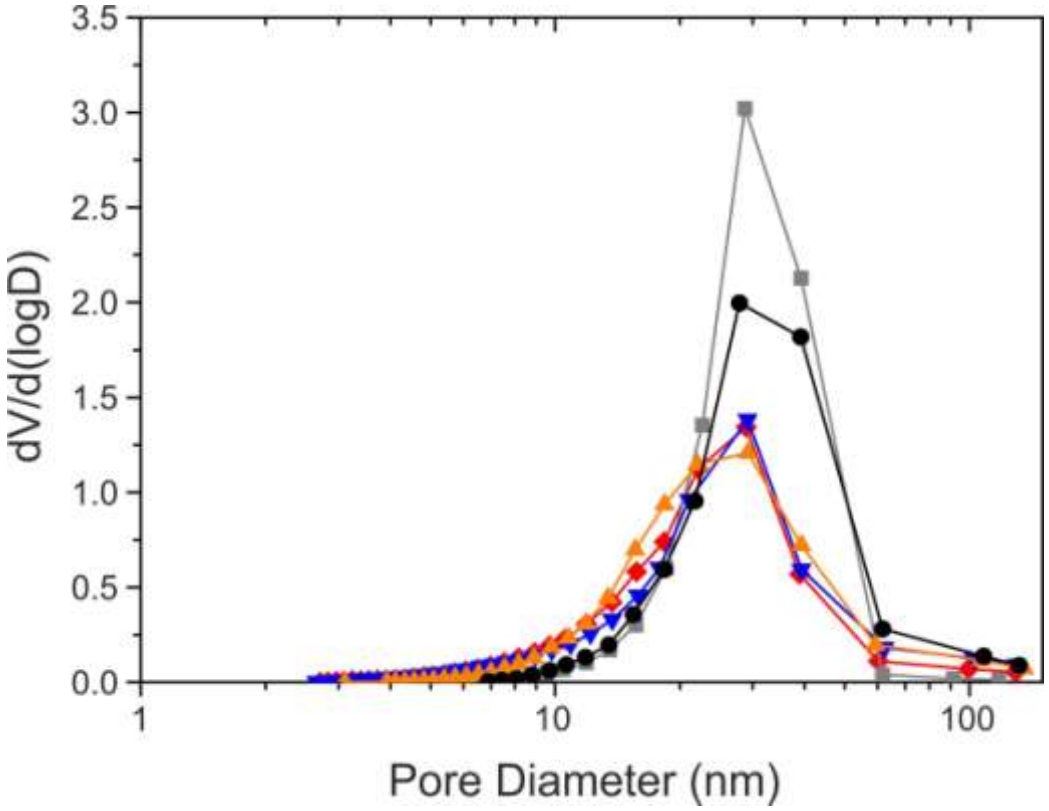

Representative TEM-EDS results (Figure 3.29) demonstrated that all Pd@MO_x-based catalysts have similar morphologies: the CZ particles, identified by EDS spectra and lattice fringes, are 5–10 nm in diameter and are sometimes aggregated. For Pd@CZ 60:40, the signals of Ce and Zr observed in EDS mapping mode are always associated and the signal analysis in spot mode revealed a good agreement with the desired Ce:Zr stoichiometric ratio. The Pd signal in EDS is typically low and diffuse, though some large palladium particles were observed, similar to what was reported by Zhang *et al.* for similar catalysts (*150*). Such a bimodal particle distribution is not detected by XRD, since the very small PdO nanoparticles will give a broad reflection that is hard to distinguish in the presence of overlapping XRD patterns from the Al_2O_3 support. The Pd/Si-Al_2O_3 catalyst showed only very large Pd particles (up to 100 nm in diameter) due to severe sintering after calcination at 850 °C for 5 h. In all cases, no apparent changes in morphology were observed after any SO_2 aging treatments, discussed in the following section (Figure 3.30).

Figure 3.29 Representative High-Angle Annular Dark-Field (HAADF) images (left column) and EDS mapping (right column) of samples Pd@CeO_2/Si-Al_2O_3 (Pd@CeO_2), Pd@$Ce_{0.6}Zr_{0.4}O_2$/Si-Al_2O_3 (Pd@CZ), Pd@ZrO_2/Si-Al_2O_3 (Pd@ZrO_2) and Pd/Si-Al_2O_3. EDS mapping colors: blue = Al, red = Pd, yellow = Ce, green = Zr.

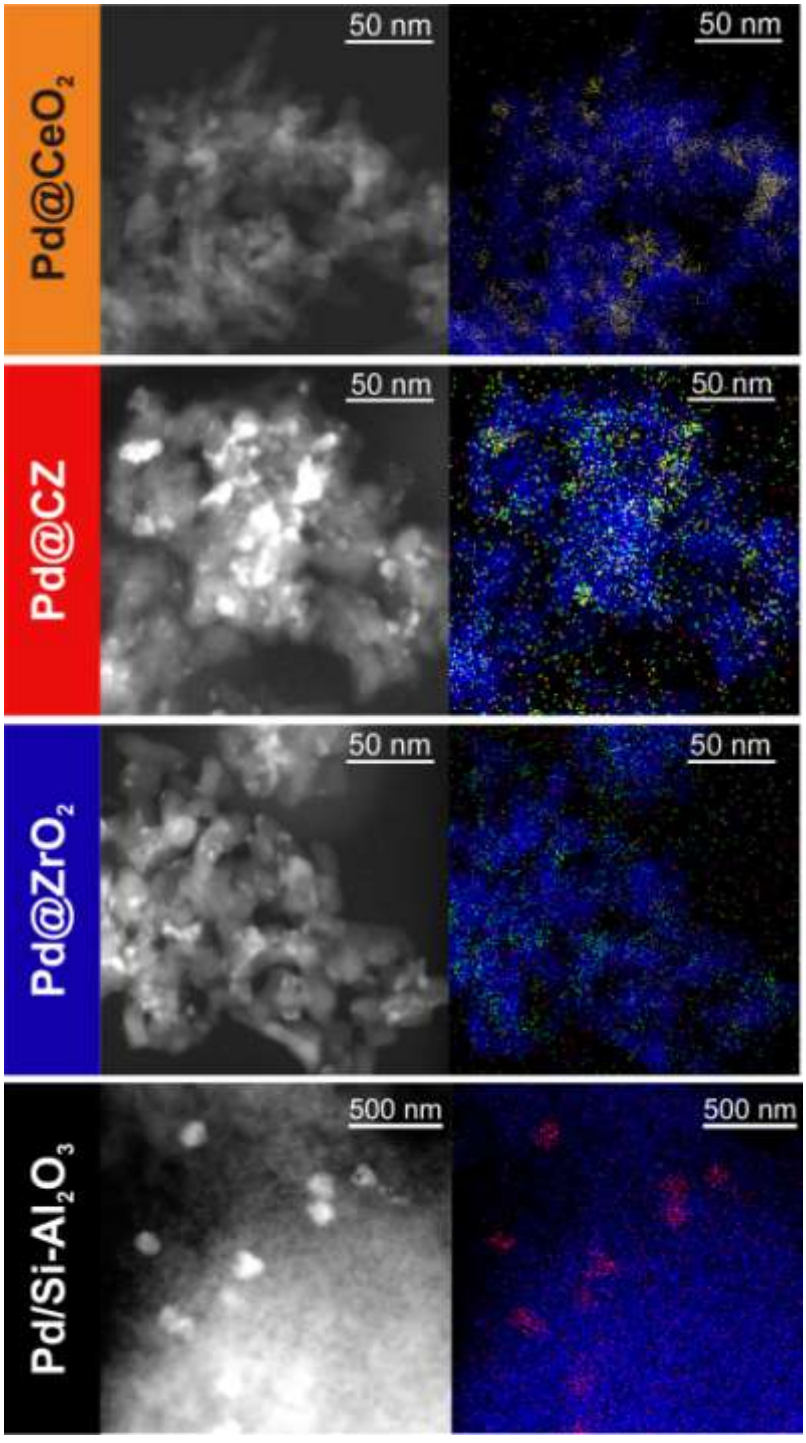

Figure 3.30

Representative High-Angle Annular Dark-Field (HAADF) images of samples: $Pd@CeO_2/Si\text{-}Al_2O_3$ ($Pd@CeO_2$), $Pd@Ce_{0.6}Zr_{0.4}O_2/Si\text{-}Al_2O_3$ (Pd@CZ), $Pd@ZrO_2/Si\text{-}Al_2O_3$ ($Pd@ZrO_2$) and $Pd/Si\text{-}Al_2O_3$. Left column: samples calcined at 850 °C; right column: samples aged at 600 °C for 2h in SO_2 + dry conditions (2% O_2, 0.5% CH_4, 50 ppm SO_2, balance Ar).

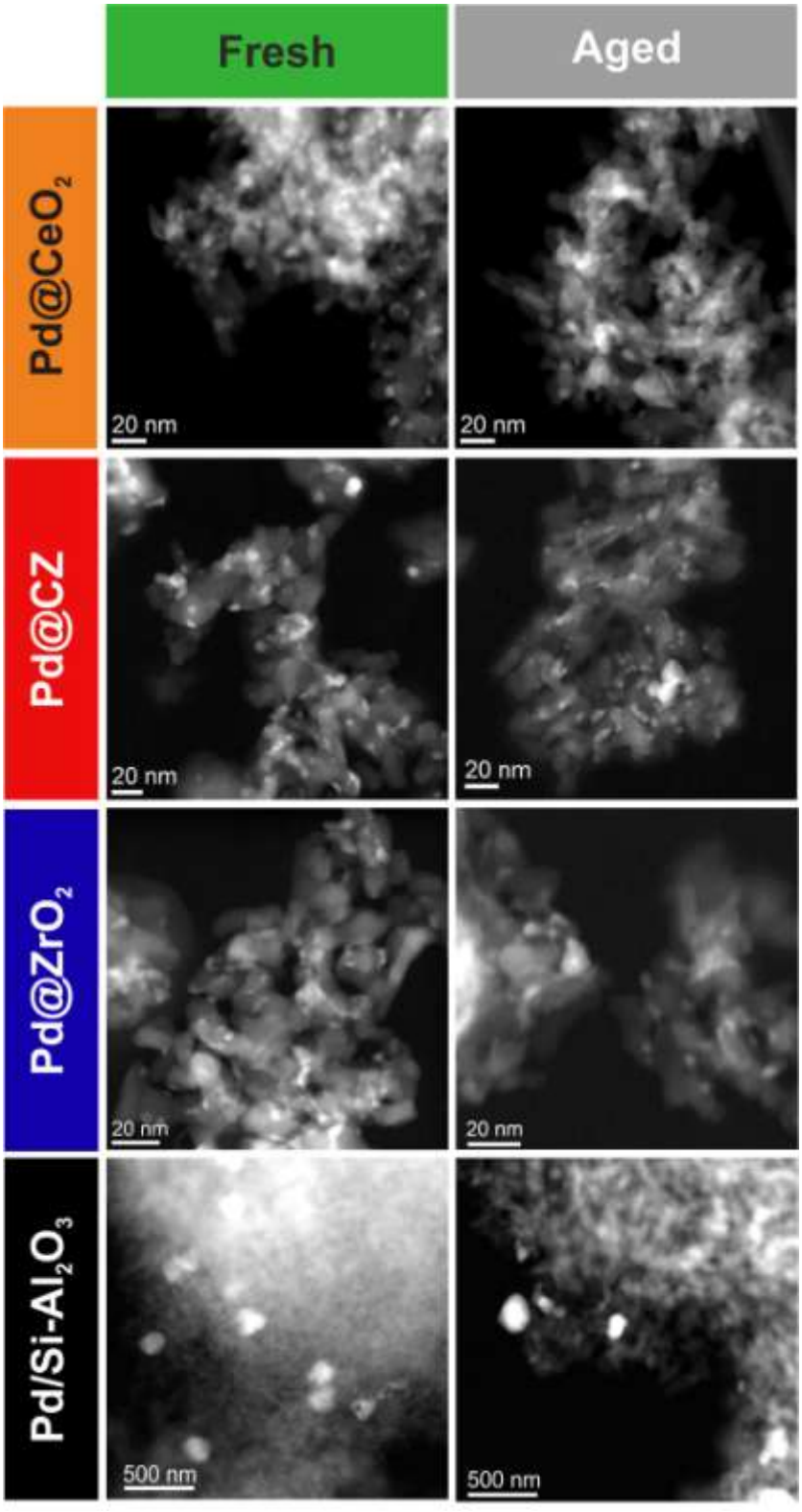

Methane-oxidation, light-off experiments performed on each of the $Pd@MO_x$-based catalysts showed comparable results that were similar to those previously reported for the single-oxide catalysts (Figure 3.31) (*8*, *92*). By comparison, the $Pd/Si\text{-}Al_2O_3$ catalyst showed a higher light off temperature and the usual conversion hysteresis after heating to high temperature (Figure 3.31).

Figure 3.31 Methane oxidation light-off curves over $Pd@MO_x/Si\text{-}Al_2O_3$ (red curve) and $Pd/Si\text{-}Al_2O_3$ (black curve). Conditions: 0.5% CH_4, 2.0% O_2, Ar balance, GHSV=200000 $mL g^{-1} h^{-1}$, heating and cooling rates 10 °C min^{-1}.

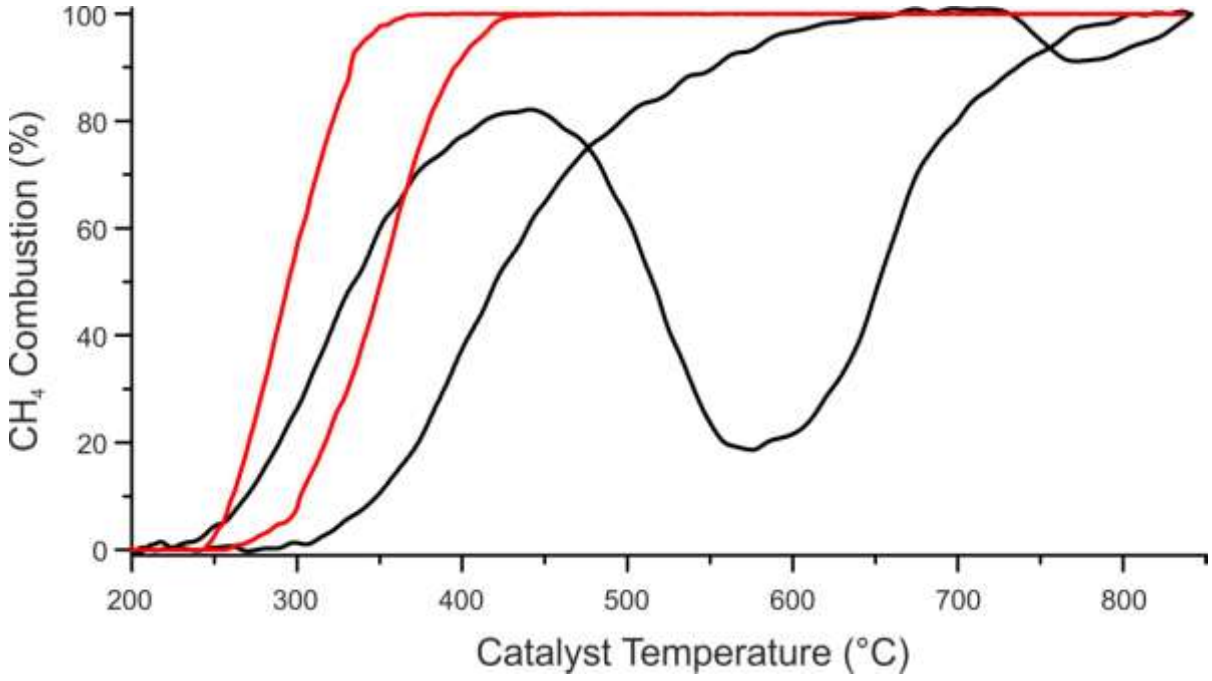

While light-off curves were comparable for all $Pd@MO_x$ catalysts, sulfur tolerance was expected to vary more strongly with composition. In order to study SO_2-poisoning resistance, aging tests were performed in which the catalysts were exposed to specified concentrations of SO_2 (typically 50 ppm) at different temperatures (from 300 to 600 °C). Introducing 50 ppm of SO_2 into the feed under dry conditions (0.5% CH_4; 2% O_2; Ar balance) caused complete and irreversible deactivation of all the studied catalysts between 300 °C and 400 °C (Figure 3.32). At 450 °C, each of the hierarchical, core-shell catalysts was partially regenerated under dry conditions, recovering 50 to 60 % of their initial conversion. The final conversion trend was $Pd@ZrO_2/Al_2O_3$ > $Pd@Ce_{0.6}Zr_{0.4}O_2/Al_2O_3$ > $Pd@CeO_2/Al_2O_3$. Although less active, the $Pd/Si\text{-}Al_2O_3$ catalyst was almost completely regenerated under dry conditions. This observation suggests that the promoting effect

of the metal oxides in the hierarchical catalysts is largely suppressed by SO_2 at 450 °C, while the active phase can be largely regenerated.

Figure 3.32 Methane Catalytic oxidation: Effect of 50 ppm SO_2 dry aging for 30 min at different temperatures on the catalytic activity of $Pd@CeO_2$ (orange line), $Pd@ZrO_2$ (blue line), Pd@CZ (red line) and $Pd/Si\text{-}Al_2O_3$ (black line). Conditions: 0.5% CH_4; 2% O_2; 50 ppm SO_2 (if present) Ar balance, GHSV=200000 $mLg^{-1}h^{-1}$.

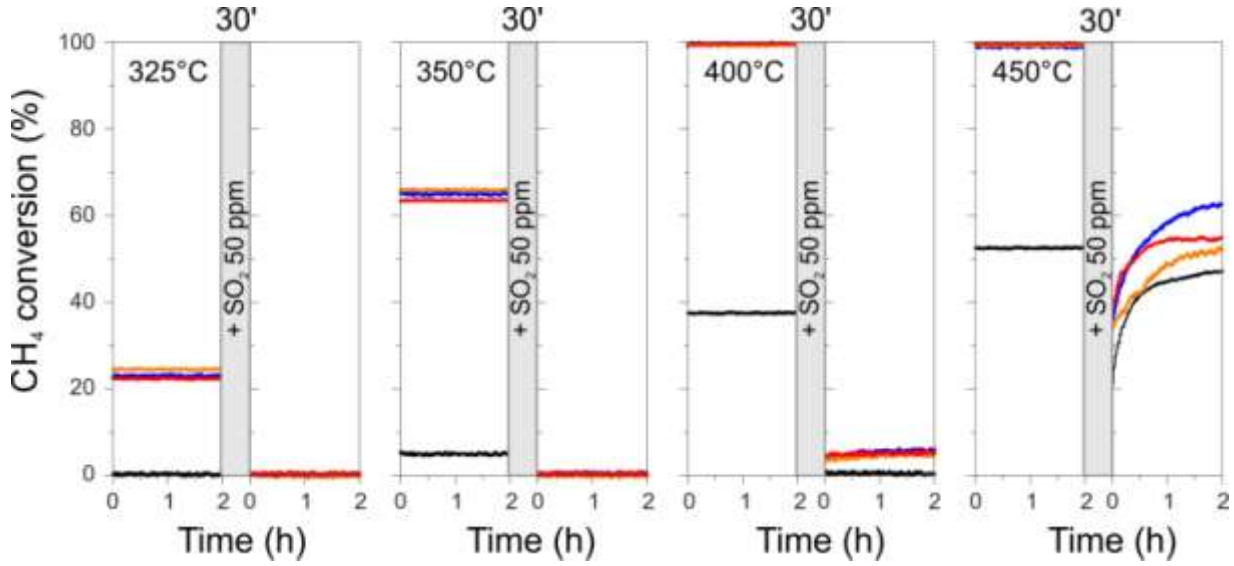

To look for longer-term effects, the methane conversions under dry conditions at 500 °C were monitored over each of the catalysts for 2 h during SO_2 exposure (Figure 3.33). The hierarchical catalysts deactivated sharply during the first hour of treatment, reaching a plateau at around 60 % of the initial conversion. The $Pd@ZrO_2$ and Pd@CZ catalysts showed similar deactivation trends and were partially reactivated over time after reaching that plateau. The $Pd@CeO_2$ underwent a slightly slower deactivation but was not reactivated after reaching the plateau.

Figure 3.33 Methane Catalytic oxidation: SO_2 dry aging at 500 °C. $Pd@CeO_2$ (orange line), $Pd@ZrO_2$ (blue line), Pd@CZ (red line) and $Pd/Si\text{-}Al_2O_3$ (black line) Conditions: 0.5% CH_4; 2% O_2; 50 ppm SO_2, Ar balance, GHSV=200000 $mLg^{-1}h^{-1}$.

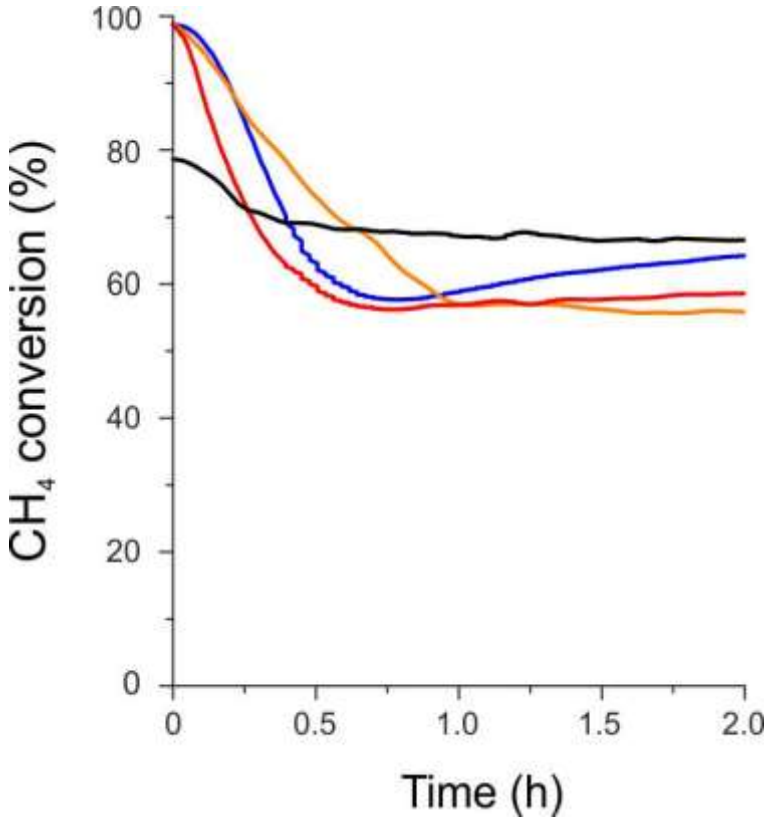

Aging at 500 °C using different SO_2 concentrations resulted in different deactivation rates but did not significantly change the plateau conversion (not shown). The residual conversion is likely associated with the partially poisoned Pd phase, unpromoted by the metal oxide. Indeed, the $Pd/Si\text{-}Al_2O_3$ sample was very stable under SO_2 aging at 500 °C, indicating that the SO_2 effect on Pd is largely inhibited at this temperature. Moreover, $MO_x/Si\text{-}Al_2O_3$ catalysts without Pd in their formulation, prepared following a similar procedure as that used to synthesize the hierarchical catalysts, did not exhibit any methane conversion at 500 °C and conversions on these materials did not light-off until above 550 °C (Figure 3.34).

Figure 3.34 Methane oxidation light-off curves over CeO_2/Si-Al_2O_3 (orange) and $Ce_{0.6}Zr_{0.4}O_2$/Si-Al_2O_3 (red curve). Conditions: 0.5% CH_4, 2.0% O_2, Ar balance, GHSV=200000 $mL g^{-1} h^{-1}$, heating and cooling rates 10 °C min^{-1}.

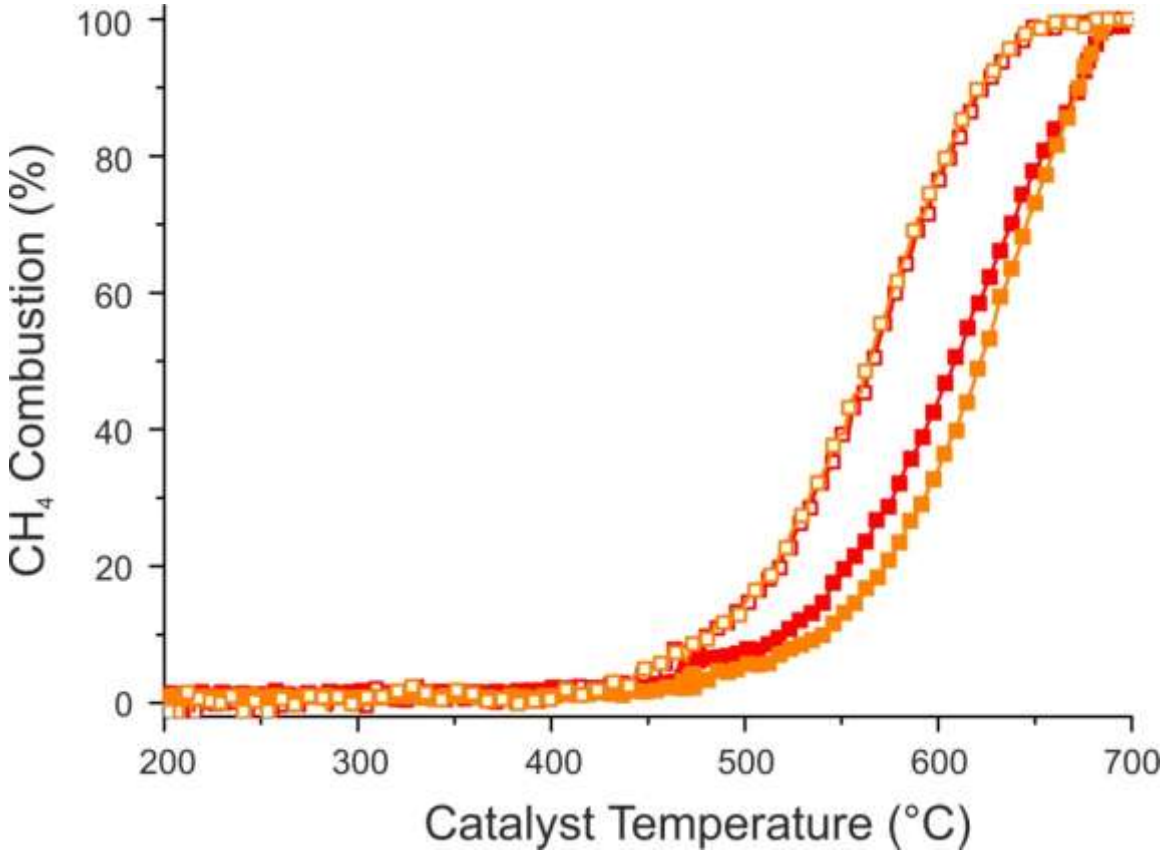

In parallel experiments, consecutive 50 ppm SO_2-aging treatments for periods of 30, 60 or 120 min at 500 °C caused partial but irreversible deactivation of the Pd@CeO_2 and Pd@CZ samples (Figure 3.35). Conversely, the poisoning effect of SO_2 on Pd@ZrO_2 and Pd/Si-Al_2O_3 catalysts was reversible at this temperature (Figure 3.35), even after 12 h aging (data not shown). Heating the Pd@ZrO_2 catalysts that had been aged at temperatures below 500 °C in dry conditions also resulted in complete reactivation of the materials. Finally, it should be noted that the conversion trends reported in Figure 3.32 and Figure 3.35 were affected by chromatographic effects due to the time required for the entire catalyst bed to be exposed to SO_2 at these low concentrations. Therefore, the conversion at the beginning of reactivation can only be extrapolated.

Figure 3.35 Methane Catalytic oxidation: reactivation trends following consecutive SO_2 dry aging treatments at 500 °C. $Pd@CeO_2$ (orange line), $Pd@ZrO_2$ (blue line), Pd@CZ (red line) and $Pd/Si\text{-}Al_2O_3$ (black line). Conditions: 0.5% CH_4; 2% O_2; 50 ppm SO_2 (if present) Ar balance, GHSV=200000 $mLg^{-1}h^{-1}$.

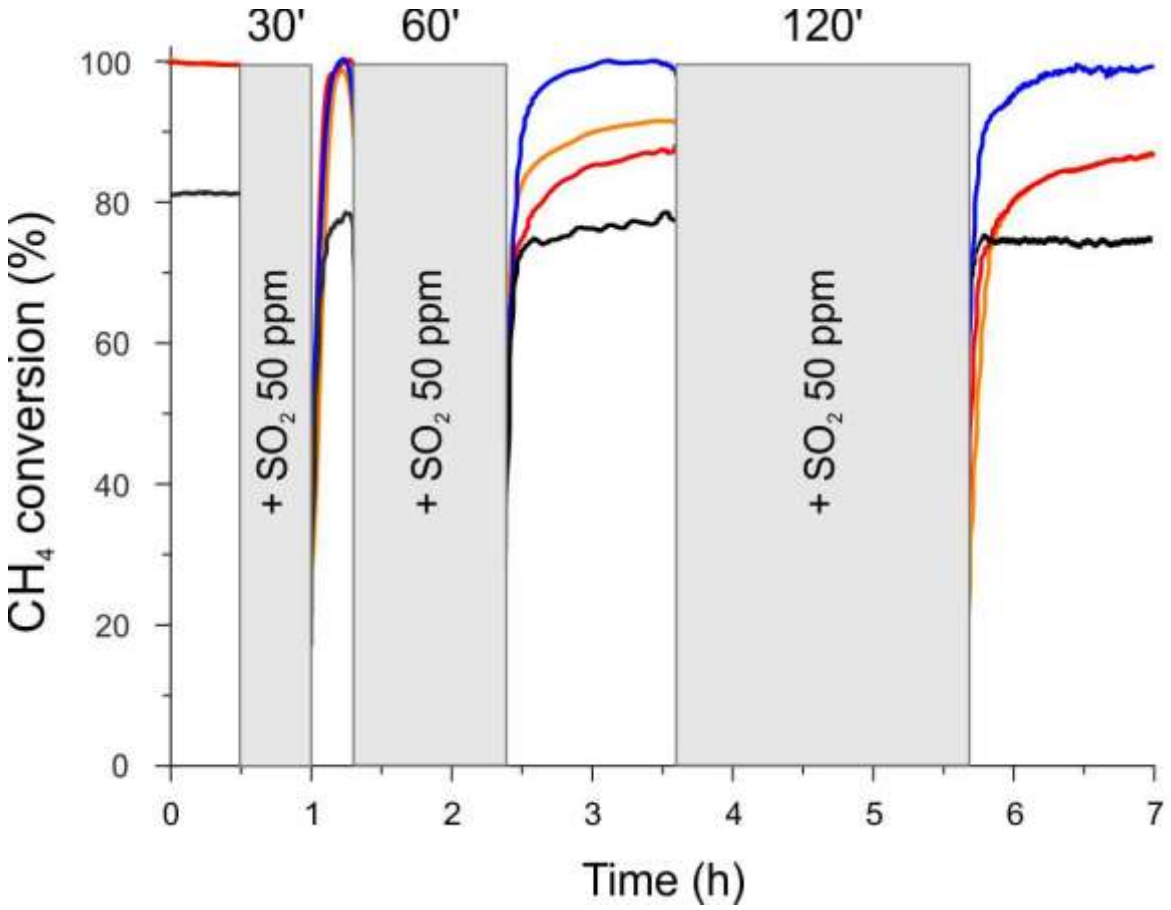

At 600 °C, under dry conditions, methane was completely converted to CO_2 over all the catalysts and there was no loss of conversion during SO_2 exposure. To increase the sensitivity of the experiment, the catalysts were diluted by addition of Al_2O_3 in a ratio of 1:3 and aged using the same conditions as those employed for the pure catalysts (Figure 3.36). The diluted $Pd@MO_x$ catalysts all achieved complete conversion at 600 °C prior to SO_2 exposure, but the diluted $Pd/Si\text{-}Al_2O_3$ catalyst showed only 80% conversion under these conditions. Exposure of the $Pd@CeO_2$ and Pd@CZ samples to SO_2 at this temperature caused the conversion to decrease continuously with time; however, for the $Pd@ZrO_2$ and $Pd/Si\text{-}Al_2O_3$ samples, after displaying an initially sharp decline in conversion, conversions partially recovered and reached a plateau value. This behavior was reproducible and was never observed for CeO_2-containing catalysts. A possible explanation for the transient behavior on $Pd@ZrO_2$ and $Pd/Si\text{-}Al_2O_3$ is that SO_2 initially deactivates the PdO active

phase, competing with CH_4 for oxidation. Later, SO_3 and sulfate species formed by oxidation migrate to the promoter/support. It has been previously reported that the activity of Pd/ZrO_2 catalysts can increase after SO_2 aging due to formation of a composite site between PdO and sulfates at the PdO-support interface(*151*). It is noteworthy that there was also an increase in conversion with SO_2 exposure time at 500 °C for $Pd@ZrO_2$ and Pd@CZ catalysts (Figure 3.33), although the time scale for increasing conversion was much larger and the initial dip was not as sharp.

Figure 3.36 Methane Catalytic Oxidation: SO_2 dry aging at 600 °C and reactivation trends. $Pd@CeO_2$ (orange line), $Pd@ZrO_2$ (blue line), Pd@CZ (red line) and $Pd/Si\text{-}Al_2O_3$ (black line). Conditions: 0.5% CH_4; 2% O_2; 50 ppm SO_2 (if present) Ar balance, GHSV=200000 $mLg^{-1}h^{-1}$.

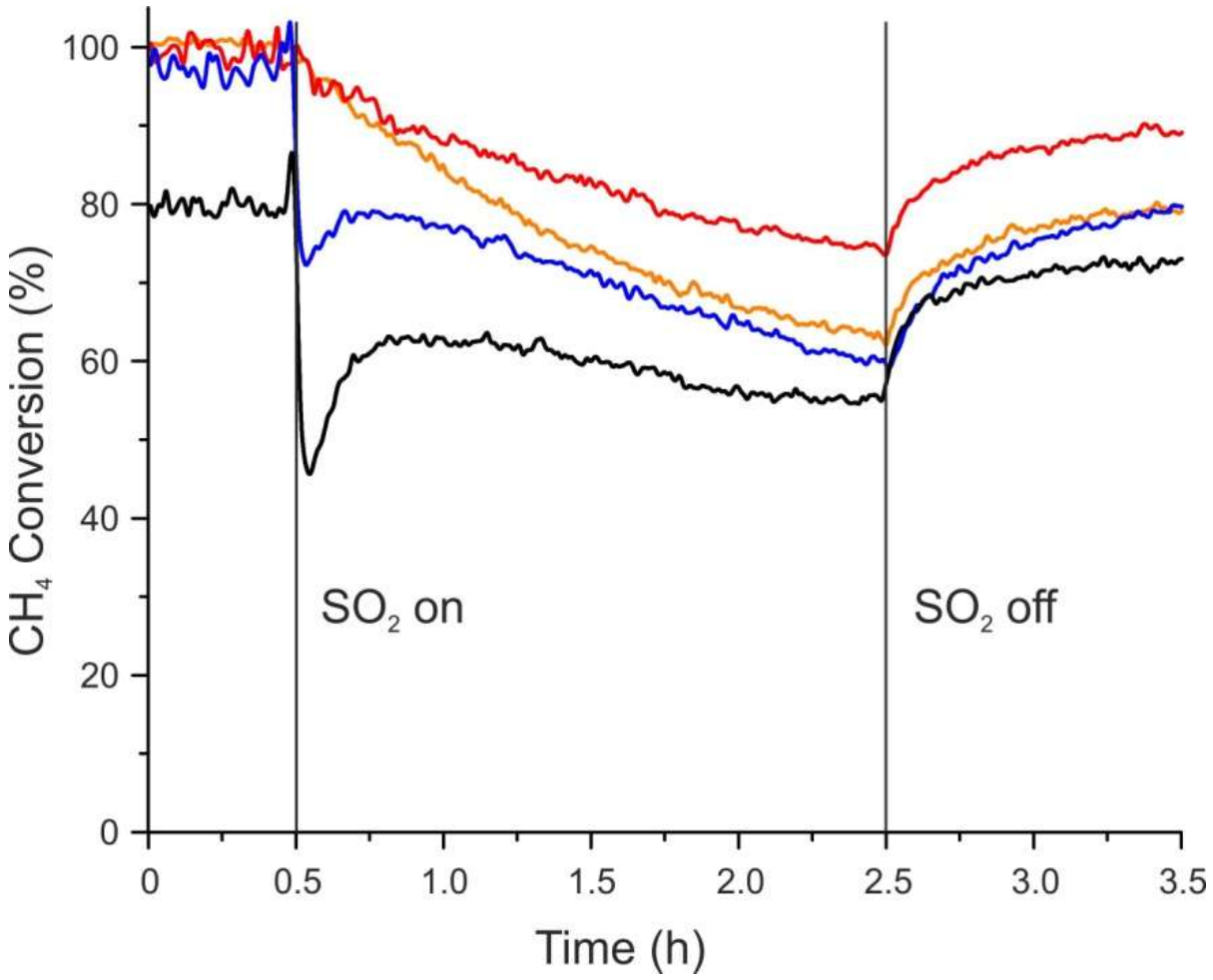

3.5.3 Model Catalysts

Photoelectron spectroscopy (PES) is a very useful technique to investigate the surface chemistry of materials, in terms of chemical species accumulation/desorption, change in chemical state of atoms, and surface/bulk distribution of species. However, insulating materials such as the high surface area catalysts studied in this work are not suited for PES analysis, because of dramatic charging effects that cause inhomogeneous shifts in the spectrum signals. For this reason we developed model catalysts suitable for photoelectron spectroscopy analysis (*i.e.* having a conductive support) designed to resemble the real catalysts in terms of surface composition and resistance to high temperature oxidizing treatments (calcination/aging).

The choice of a proper support was a rather difficult task: aluminum and Al-alloys were tested in the first place, but were discarded due to the low melting points and uncontrolled growth of thick Al_2O_3 layer (leading to loss of surface conductivity). Stainless steel supports covered with thin Al_2O_3 layers deposited by ALD were also tested, but the difference in thermal expansion coefficients of steel (12-16x10^{-6} °C^{-1}) and alumina (8.1x10^{-6} °C^{-1}) resulted in cracking and leaching of Al_2O_3 and even its incorporation in thermally grown Fe, Mn and Cr mixed oxides. Thermal oxidation and expansion problems were finally bypassed by the choice of a conductive oxide, *i.e.* Indium-Tin Oxide (ITO), supported on quartz for mechanical stability. ITO is stable in air over 900 °C without experiencing loss of conductivity and has a thermal expansion coefficient very similar to that of Al_2O_3 (8.1-8.6x10^{-6} °C^{-1}).

On the basis of these preliminary observations, the supports for the model catalysts were prepared by ALD of Al_2O_3 overlayers of various thicknesses (2, 5 and 10 nm) on an ITO/quartz support (flat, low-surface-area material). The Al_2O_3 layer deposition was also carefully optimized, because it caused a drop in surface conductivity as the thickness of the layer increased. 10 nm thick layers were discarded because heavy charging was observed during preliminary XPS analysis. On the other hand, ITO exposure after calcination had an opposite trend, increasing with decreasing layer thickness. As revealed by Ion Scattering Spectroscopy (ISS), a 2 nm layer Al_2O_3 was not enough to completely cover ITO, exposing it to the environment (Figure 3.37). 5 nm Al_2O_3 slides were selected for further investigation because of minimized ITO exposure and negligible charging during SRPES/XPS analysis.

Figure 3.37 ISS results for slides calcined at 850 °C for 5h: ITO/Quartz slides (black line), 2 nm ALD-Al_2O_3/ITO/quartz (red line), 5 nm ALD-Al_2O_3/ITO/quartz (green line).

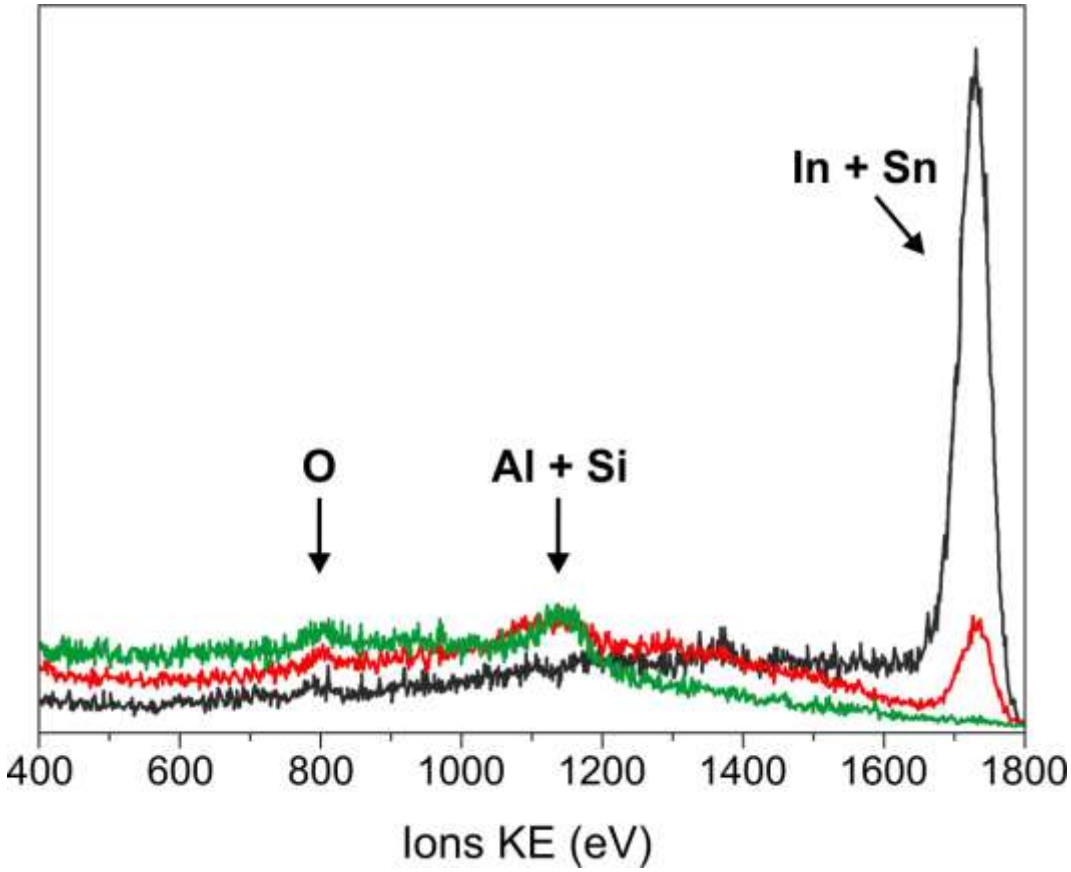

The structure of the model catalysts used in this study is depicted graphically in Figure 3.38. A 1-mm thick quartz slide was used to support a 500-nm thick conductive layer of ITO, over which a 5 nm Al_2O_3 layer was grown by ALD. To obtain a silanized, hydrophobic Si-Al_2O_3 comparable to that of the HSA Si-Al_2O_3, the slides were allowed to react with TEOOS by soaking them in TEOOS solutions, diluted with toluene, for 2 days. Finally, the slides were loaded with Pd@CeO_2, Pd@ZrO_2 or Pd@$Ce_{0.6}Zr_{0.4}O_2$ (Pd@CZ) particles and calcined at 850 °C for 5 h. The catalysts are labeled Pd@CeO_2-m (m for model), Pd@ZrO_2-m and Pd@CZ-m, respectively.

Figure 3.38 Graphical representation of Pd@MO_x/Si-Al_2O_3/ITO/quartz model (A, not to scale); AFM 3D image and mapping of ITO/quartz (B1), ALD-Al_2O_3/ITO/quartz (B2), Pd@CZ-m calcined at 850 °C for 5 h (B3). EDS wide spectrum of calcined Pd@CZ-m (C) and SEM image of Pd@CZ-m with 1 µm view field (D1) and 10 µm view field (D2).

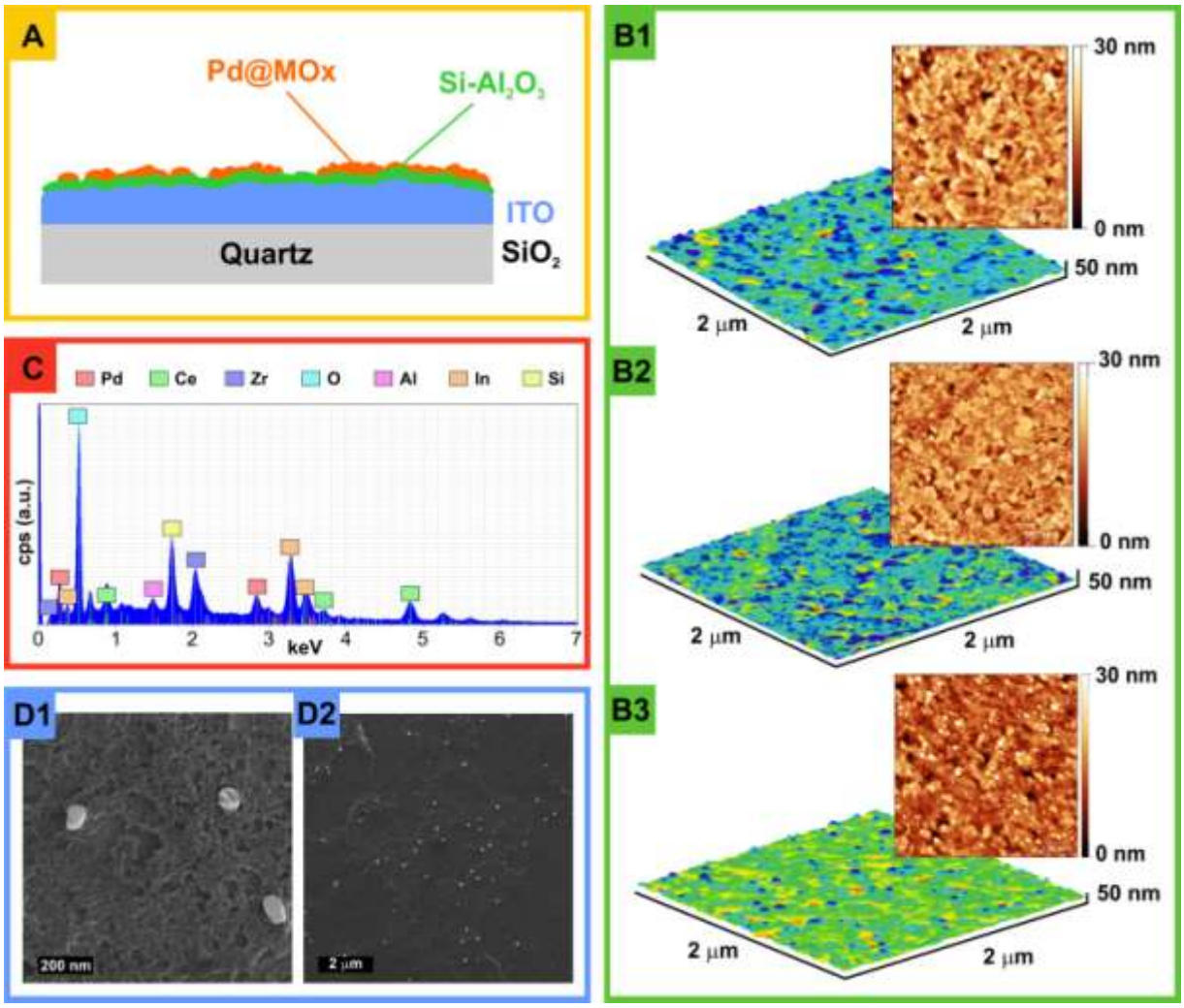

AFM analysis of the model catalysts was performed at different stages in the preparation procedure (Figure 3.38B). The bare ITO surface shows characteristic worm-like structures (Figure 3.38B1) which become slightly more defined in shape after Al_2O_3 deposition (Figure 3.38B2). The final structure obtained after depositing Pd@MO_x, followed by calcination at 850 °C, shows a similar morphology, but with some aggregates on the surface (In Figure 3.38B3, see the white spots in the 2D image, blue in the 3D image). Similar to the results reported in a recent paper by Zhang *et al.* (*150*), SEM/EDS analysis revealed aggregates composed of Pd with CeO_2, ZrO_2 or CZ on top of small features that covered the Al_2O_3 layer (Figure 3.38D). A representative EDS spectrum of Pd@CZ-m is reported in Figure 3.38C. The spectra obtained from different spots on the model catalysts revealed

a uniform composition with the expected Pd:(Ce+Zr) and Ce:Zr molar ratio (1:5.5 and 6:4 respectively). CeO_2- and ZrO_2-based catalysts also showed the expected Pd:MO_x molar ratio. No differences in surface morphology were observed for CeO_2, ZrO_2 or CZ-containing samples.

Since the SRPES signals for Pd 3d and Zr 3p overlap ($3p_{1/2}$: 343eV, $3p_{3/2}$: 330 eV), only Pd 3d spectra of Pd@CeO_2-m samples are reported in Figure 3.39. Calcination temperature had a significant effect on the Pd 3d region. Reference Pd@CeO_2-m samples calcined at 500 °C showed the Pd spin-orbit split doublet (Pd $3d_{5/2}$ and Pd $3d_{3/2}$) at 337.2 eV and 342.2 eV (Figure 3.39, A1), which can be assigned to PdO, based on previous XPS and X-ray Absorption Near Edge Structure (XANES) analysis of similar materials (*152*). A shift of the PdO signal to higher BE (almost 1 eV) with respect to a bulk value is likely due to a size effect (*129–135*). Calcination of the Pd@CeO_2-m samples to 850 °C causes partial agglomeration of some of the nanostructures to form Pd and CeO_2 particles in the range of 50 to 100 nm (Figure 3.39, B2) (*150*); and this agglomeration gives rise to an additional contribution in the Pd 3d spectra, more typical for bulk PdO (366.5 eV) (Figure 3.39, B2).

Figure 3.39 Left: Pd 3d SRPES spectra at different excitation energies for Pd@CeO_2-m calcined at 500 °C (A1) and 850 °C (B1). 500 eV: red line, 640 eV: green line, 880 eV: blue line. Grey lines are guidelines to the eye. Right: representative SEM images of Pd@CeO_2-m samples calcined at 500 °C (A2) and 850 °C (B2); bars: 200 nm.

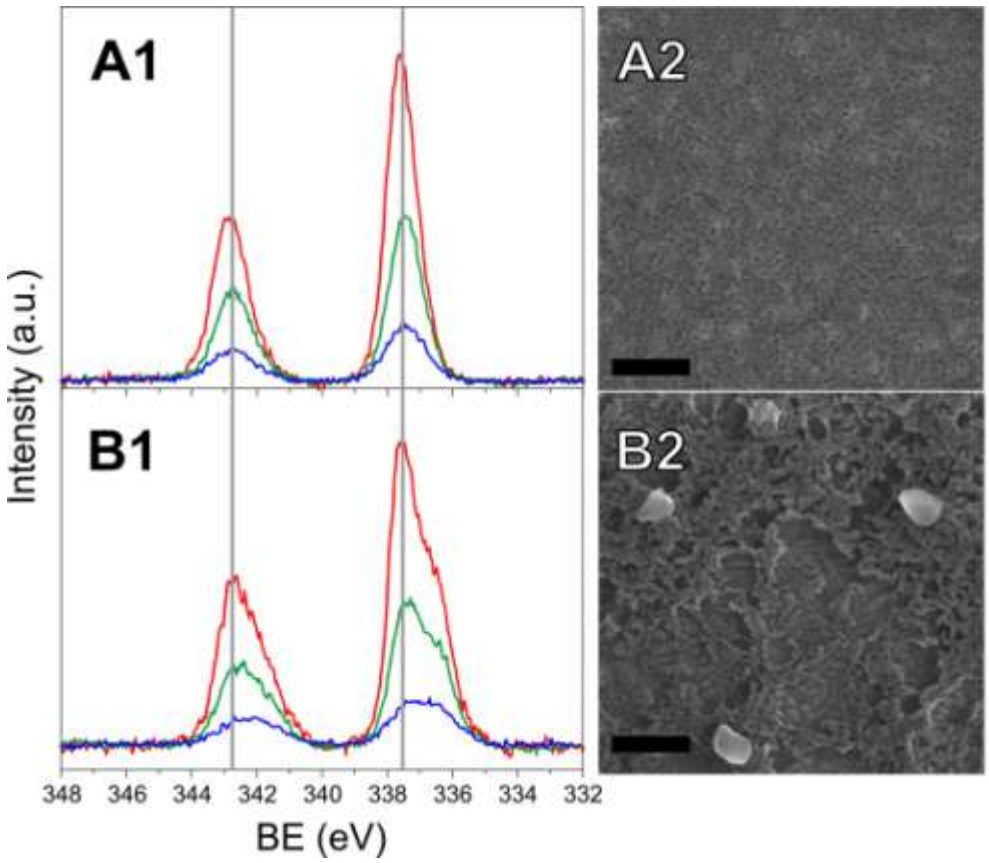

Because the relative contribution of the larger agglomerates in photoemission is expected to increase with excitation energy, we examined the surface:bulk signal contribution by tuning the SRPES excitation energy. In agreement with this, the signal at higher BE, tentatively assigned to PdO NPs, was relatively more intense at lower excitation energies, implying that this feature is associated with a considerably smaller structures. An alternative explanation is that the two contributions to the SRPES signal could be due to a Pd-Ce mixed oxide and a bulk PdO. For example, the Pd 3d signal of Pd–Ce mixed oxides has been reported to have BE of 338 eV BE (*153*). Since the mixed oxides would likely segregate at higher temperatures, resulting in bulk PdO formation, this could also explain the two features in the spectra (*154*). However, we regard this explanation as less probable since the synthesis of the core-shell materials starts with pre-formed Pd nanoparticles and complete disruption of the PdO and incorporation into CeO_2 seems unlikely to occur at 500 °C. Also, this latter explanation does not agree with the observation of a PdO (101) reflection in the HSA catalysts calcined at 850 °C (Figure 3.26) or with previous EXAFS studies on similar systems (*89*, *152*). Due to the lower resolution, only one contribution averaging the signals associated to PdO NPs and aggregates was observed in XPS (Figure 3.40).

In order to study the effect of SO_2 aging at different temperatures, the model catalysts were treated under similar conditions to those used with the HSA catalysts (except for higher GHSV) and then transferred under inert atmosphere to the analysis chamber for analysis by XPS/SRPES. First, the catalysts were aged for 2 h under dry methane-oxidation (0.5% CH_4, 2.0% O_2) conditions with 50 ppm SO_2 at 350, 500 or 600 °C. Then, after XPS analysis, the aged catalysts were regenerated under dry methane-oxidation conditions, without SO_2, for 2 h at the same temperature at which they were aged. After SO_2 aging at 350 °C, the XPS spectrum showed a peak at 335.2 eV, which can be assigned to metallic Pd (Figure 3.40) (*71*, *155*, *156*). Partial reduction of PdO could result from SO_2 oxidation to SO_3 by PdO lattice oxygen. The complete re-oxidation of the then formed metallic Pd would not be possible under the conditions of this study at 350 °C, as previous XANES results on HSA Pd@CeO_2/Si-Al_2O_3 suggest, because of the low temperature and oxygen pressure involved (*89*). A similar effect has been reported by Venezia *et al.* after aging Pd-based catalysts on TiO_2 or SiO_2 at the same temperature overnight (*71*, *155*) and by Liotta *et al.* for Pd/CeO_2 catalysts operated under lean conditions and 10 ppm of SO_2 (*156*).

Along with the reduction of the Pd, there was a slight increase of the XPS signal at higher BE following SO_2 aging at 350 °C. The shift of the signal is less than that expected for Pd in the form of $PdSO_4$ and we suggest that this might be indicative of some interaction with sulfates groups, in agreement with the literature (*23*, *84*). After 2h under dry methane-oxidation conditions at 350 °C,

the XPS spectra did not change appreciably from those of the SO_2 aged catalyst. An irreversible poisoning of the PdO active phase would explain the similar behavior observed for HSA catalysts, regardless of the presence and composition of the promoter (Figure 3.32). At higher temperature (500 °C to 600 °C) SRPES spectra of the Pd 3d region did not change after SO_2 aging or regeneration, suggesting that the interaction of PdO with sulfates is weaker and reversible. Accordingly, the Pd/Si-Al_2O_3 catalyst was very stable during dry SO_2 aging at 500 °C (Figure 3.33) and a sharp transient deactivation at 600 °C could only be observed on the diluted catalyst (Figure 3.36). These observations are in accordance with thermodynamic calculations on $PdSO_4$ formation from mixtures of O_2 and SO_3, predicting $PdSO_4$ decomposition below 400 °C (*157*).

Figure 3.40 XPS spectra of Pd 3d region of Pd@CeO_2-m, fresh (black line) and 350 °C SO_2 aged (red line).

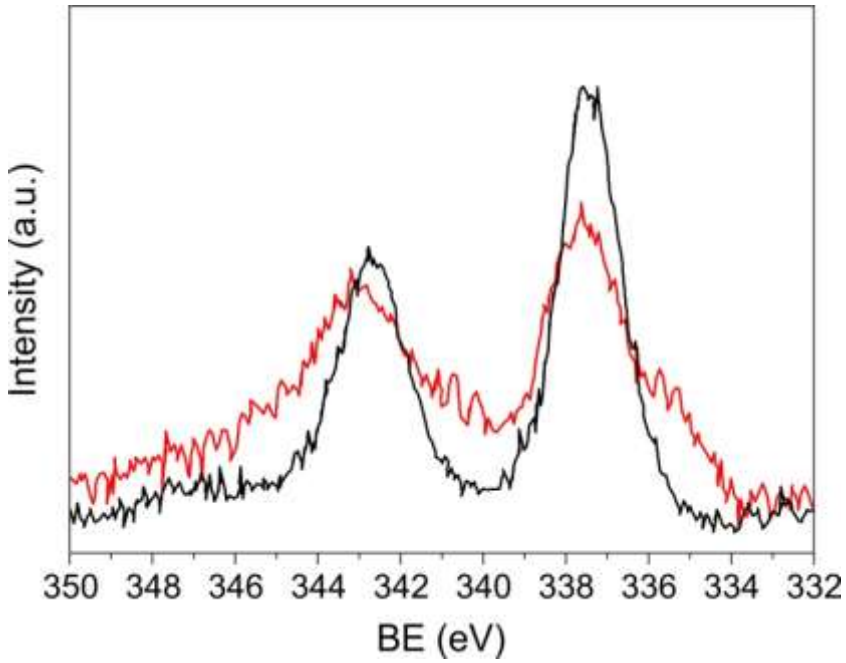

Independent of the SO_2 aging temperature, the S 2p region of the SRPES/XPS spectra showed only a signal corresponding to sulfate species (168-172 eV BE). The use of SRPES was crucial in order to observe an intense and resolved S 2p signal, thanks to the much higher photoionization cross-section (0.83 Mbarn at 425 eV; 0.022 Mbarn at 1486.6 eV) (*158*) and shorter information length, which favors signal from surface species. Indeed, after 500 °C aging, sulfates were only observed in SRPES spectra and not in XPS spectra (Figure 3.41A,C), which also showed an overlapping Zr 3d signal due to Al $K_{\alpha 3}$ (1476.8 eV) and $K_{\alpha 4}$ (1474.8 eV) lines. After 2 h of regeneration at 500 °C, sulfates were partially removed from Pd@ZrO_2-m, while the sulfates remained on the Pd@CeO_2-m and Pd@CZ-m samples, a finding consistent with the regeneration trends observed with the HSA catalysts (Figure 3.34).

During regeneration of the catalyst, only a small fraction of sulfur species desorbed, suggesting that a rearrangement of sulfates on the surface could lead to reactivation and that TPD studies may give misleading results for evaluation of SO_2 poisoning resistance. At 600 °C, more sulfates are formed (even if a decrease in conversion was observed only in diluted samples) and these could be observed both in SRPES and XPS spectra (Figure 3.41B,C). Based on the cross section corrected photoemission signal of S and Ce (and/or Zr) in XPS, we estimate a MO_x:S molar ratio of 5:1 for CeO_2 and CZ and 7:1 for ZrO_2. These ratios are consistent with about 1 monolayer (ML) of sulfate being formed on the surface of the oxide nanoparticles, considering that the XPS information depth is around 2 nm, which corresponds to about 6 ML of CeO_2 in the close-packed (111) direction. Regeneration under dry conditions at 600 °C resulted in desorption of sulfates from the surface/subsurface of all the samples (Figure 3.41B), consistent with similar trends observed in the recovery of conversion (Figure 3.36).

Figure 3.41 S 2p region of SRPES spectra of SO_2 aged and regenerated samples at (A) 500 °C and (B) 600 °C (orange: Pd@CeO_2-m; red: Pd@CZ-m; blue: Pd@ZrO_2-m; thick line: aged; thin line: regenerated); (C) S 2p region of XPS spectra of SO_2 aged samples at 500 °C (red line) and 600 °C (green line) (top: Pd@CeO_2-m; middle: Pd@CZ-m; bottom: Pd@ZrO_2-m).

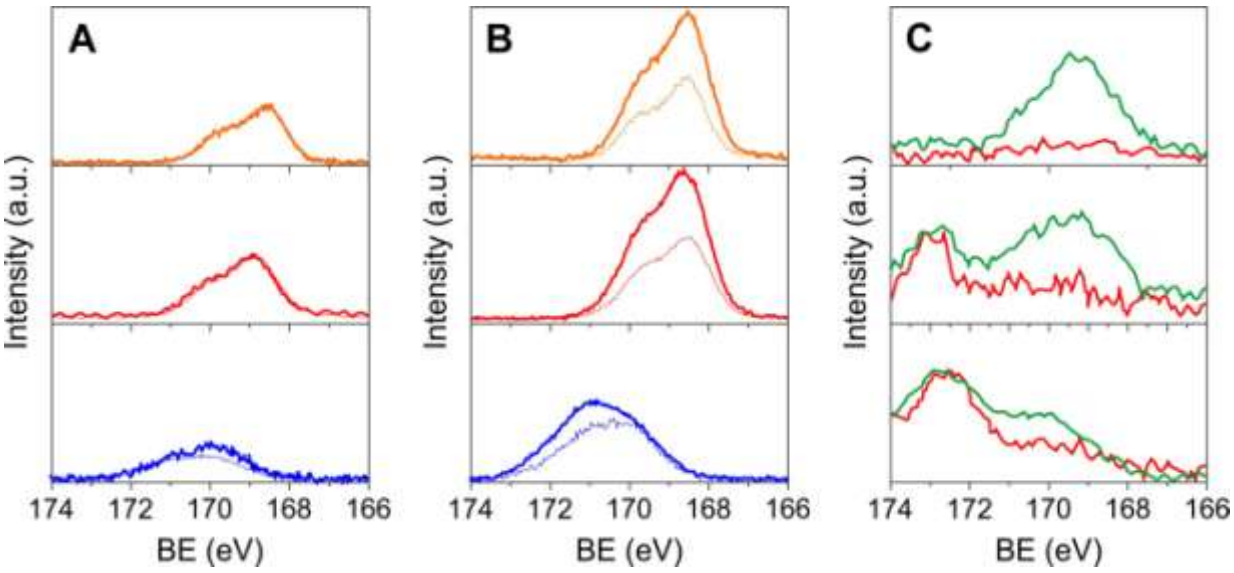

Previous FTIR (*145*), TPD (*142*) and XPS (*159*) studies reported sulfate desorption from $Ce_1Zr_{1-x}O_2$ in the range of 600 °C to 700 °C. The desorption of sulfate species from pure ZrO_2-based materials is much less investigated, with TPD results showing higher desorption temperatures than for CeO_2 sulfates (800 °C) (*142*). We suggest that the surface sensitivity of SRPES/XPS analysis

allowed us to observe a partial desorption of sulfates from ZrO_2, occurring at lower temperature, which could not be detected by TPD. The difference of observed sulfate stability could also be due to the atmosphere in which desorption was performed, which can affect decomposition of S-species (*138*). Indeed, Colussi *et al.* observed different TPD profiles on SO_2-aged $Pd/CeO_2/Al_2O_3$ samples when the desorption was carried out in reaction conditions or inert atmosphere (*138*), suggesting a role of *in-situ* produced water in the SO_2 desorption mechanism.

Interestingly, the BE for the S 2p features in Figure 3.41 was different for the $Pd@CeO_2$-m and $Pd@ZrO_2$-m samples, implying that sulfates bonded to Zr or Ce cations are distinguishable. Since the spectra of Pd@CZ-m are very similar to that of $Pd@CeO_2$ both in shape and formation/desorption trends, it appears that primarily Ce sulfates are formed on Pd@CZ-m samples and that these are similar to sulfates formed on CeO_2. In agreement with this, the Ce 3d and Zr 3d XPS spectral regions show modifications after SO_2 aging that depend on the MO_x composition (Figure 3.42).

Figure 3.42 XPS spectra of pristine samples (black line) and SO_2 aged samples at 500 °C (red line) and 600 °C (green line). (A) Ce 3d region of $Pd@CeO_2$-m; (B) Zr 3d region of $Pd@ZrO_2$-m; (C1) Ce 3d region and (C2) Zr 3d region of Pd@CZ-m.

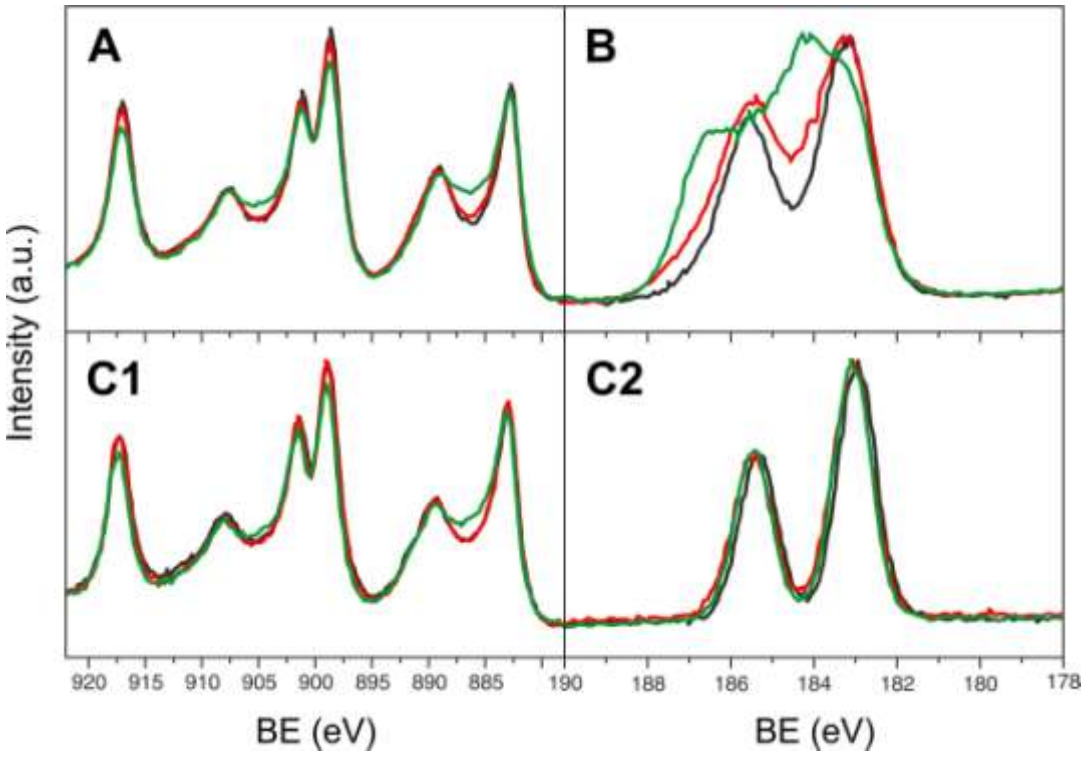

In particular, Ce 3d spectra of Pd@CeO_2-m (Figure 3.42A) and Pd@CZ-m (Figure 3.42C1) aged at 600 °C are similar and exhibit more intense Ce(III) contributions than what is observed on the fresh catalyst, probably due to reduction of CeO_2 by SO_2 with consequent formation of cerium sulfate. By contrast, Zr 3d spectra for Pd@ZrO_2-m (Figure 3.42B) are different from spectra for Pd@CZ-m (Figure 3.42C2), revealing sulfate formation on Pd@ZrO_2-m after aging at 500 °C and 600 °C, while the Pd@CZ-m spectra do not change. This is consistent with the formation of sulfates only on Ce cations in CZ materials, which leaves the chemical environment of Zr cations unaffected.

Figure 3.43 shows the O 1s spectra of the fresh samples, exhibiting peaks typical of bulk oxygen (529 eV for CeO_2 and 531 eV for ZrO_2) and hydroxyl species (532 eV) (*127*). SO_2 aging leads to an increase in the intensity of the higher BE contribution (532 eV) associated with OH groups (Figure 3.43). These results, taken together with the trends observed in S 2p spectra, suggest that the variation of O 1s signals is mostly due to oxygen from sulfate species.

Figure 3.43 O 1s region of SRPES spectra of SO_2 aged and regenerated samples at (A) 500 °C and (B) 600 °C (orange: Pd@CeO_2-m; red: Pd@CZ-m; blue: Pd@ZrO_2-m; thick line: aged; thin line: regenerated); (C) O 1s region of XPS spectra of SO_2 aged samples at 500 °C (red line) and 600 °C (green line) (top: Pd@CeO_2-m; middle: Pd@CZ-m; bottom: Pd@ZrO_2-m). SRPES and XPS spectra of fresh samples are reported for reference (black lines).

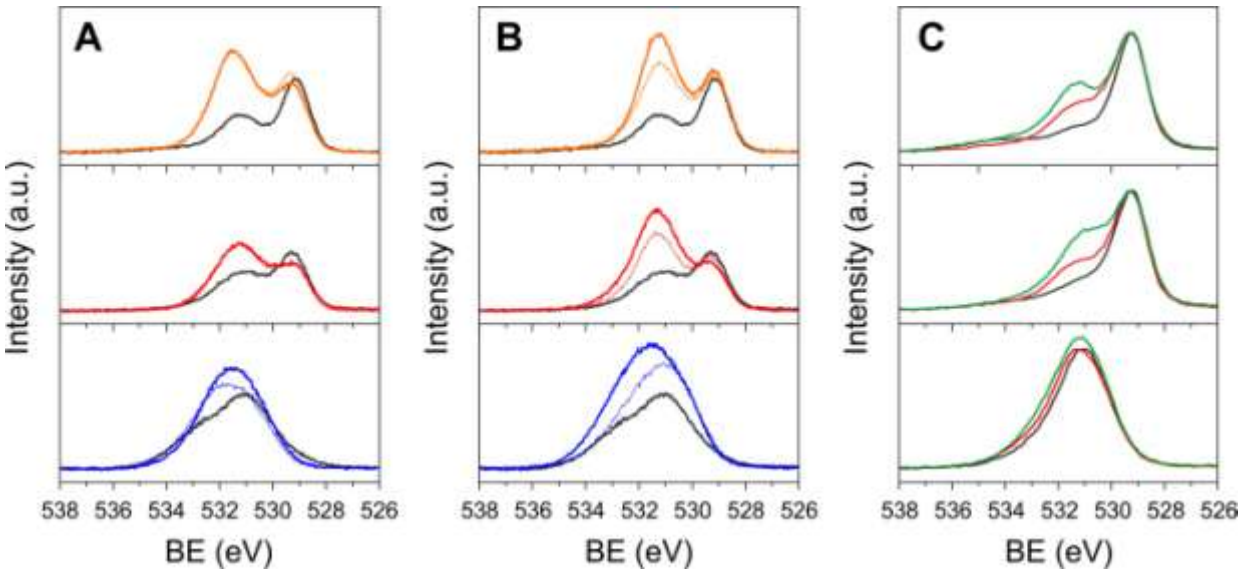

3.5.4 Discussion

First, the observations here demonstrate that the previously reported synthesis of Pd@CeO_2 and Pd@ZrO_2 particles by self-assembly can be extended to form materials with mixed-oxide shells, Pd@$Ce_xZr_{1-x}O_2$. The pre-formed core-shell particles can be deposited on both high-surface-area (HSA), functionalized alumina or on model Si-Al_2O_3 surfaces to achieve a similar, controlled morphology. In all of the materials, the oxide shell was found to promote catalytic activity for methane oxidation. The series of hierarchically structured catalysts supported on Si-Al_2O_3 also had comparable surface areas and active-phase accessibilities. These properties make them good candidates to study the effect of the oxide promoter composition on SO_2 poisoning.

The methods used in preparing the model catalysts in this study are also of general interest for investigating the effects of temperature and operating conditions. The approach is based on the ability of ALD to form uniform, thin films having precise thicknesses and a wide range of possible final compositions. Indeed, model supports could be prepared from almost any metal oxide by varying the ALD precursors(*160*). This allows support composition to be varied systematically in order to study the effect of metal-support interactions on the catalyst performance, morphology (by SEM) and chemical state (by XPS/XANES). Also, model catalysts prepared in this way can be tested and analyzed repeatedly, making it possible to study the effect of aging and regeneration treatments together with properties for adsorption, desorption or redistribution of surface species. The lower surface area of model catalysts, that affects the range of achievable GHSV, is the only drawback of this powerful method of investigation.

SO_2 poisoning of Pd-based catalysts in lean catalytic oxidation of methane proceeds via two distinct mechanisms, depending on the aging temperature. At lower temperature (<450 °C), SO_2 irreversibly poisons PdO, causing a partial reduction to Pd and the formation of sulfates in close proximity to the active phase. The temperature is not high enough to allow the spillover of sulfate species from the active phase to the support/promoter and to promote a complete re-oxidation of the poisoned catalyst (*89*, *161*). At higher temperatures, PdO is more resistant to poisoning, thanks to the spillover of sulfates from the active phase and/or the direct reaction of SO_2 with the promoter. However, since the promoting effect of the metal oxide is turned off by sulfate poisoning, the catalysts deactivate until a plateau is reached, corresponding to the active phase residual activity.

The effect of the oxide promoter composition on SO_2 poisoning is also temperature dependent. At 500 °C, Pd@ZrO_2 catalysts showed the best sulfur resistance among the samples, being only reversibly deactivated thanks to partial sulfate desorption. The performance of Pd@CZ catalysts is intermediate between that of the two pure oxides, suggesting that no cooperative

effect of Ce and Zr takes place. On the other hand, at 600 °C, Pd@CeO_2 and Pd@CZ can stabilize the catalyst against transient deactivation, acting as a sink for SO_2, while Pd@ZrO_2 deactivates in a similar way as Pd/Si-Al_2O_3. However, the poisoning effect of SO_2 is less relevant than at 500 °C, since the deactivation is observed only for very high GHSV. These results make Pd@ZrO_2 catalysts a more suitable candidate for real application, taking into account the better stability in the presence of H_2O with respect to Pd@CeO_2 catalysts.

The chemical-state and surface sensitivity of photoelectron spectroscopy also allowed for the observation of preferential sulfation of Ce over Zr in CZ mixed oxides. The chemical environment of Zr cations only changed after sulfation of ZrO_2, while in the case of CZ no evident differences were observed. These results strongly suggest that sulfate species are associated with individual metal cations, producing a first evidence of what was tentatively proposed by Luo *et al.* based on TPD and pulse-reactor experiments (*142*).

3.5.5 Conclusions

The self-assembly methodology described previously (*162*) was modified in order to synthesize nanostructured Pd@$Ce_xZr_{1-x}O_2$ (Pd@MO_x) units in the whole compositional range ($0<x<1$). The synthesis of dispersed Pd@MO_x allowed the preparation of a series of high-surface-area Si-Al_2O_3 supported catalysts and model catalysts having similar nanostructure and surface chemistry. Comparison of results on the two types of catalysts allowed the SO_2 poisoning of methane oxidation on Pd-based catalysts to be systematically studied to elucidate the role of the MO_x promoter and the aging conditions. At lower temperatures (<450 °C), the PdO active phase is irreversibly poisoned by SO_2 due to interaction with sulfates which are not able to spillover to the support/promoter. At higher temperatures (>500 °C), poisoning is slowed by formation of sulfate species on the oxide promoter. Due to partial decomposition of sulfates at 500 °C, Pd@ZrO_2-based catalysts showed the best sulfur-poisoning resistance, attaining complete regeneration even after prolonged aging, and thus they are the best candidates for real application. Pd@$Ce_{0.6}Zr_{0.4}O_2$ catalysts showed intermediate sulfur tolerance compared to Pd@CeO_2 and Pd@ZrO_2, in agreement with previously reported results (*142*). The high chemical sensitivity of PES techniques provided direct evidence for previously suggested formation of sulfate species on individual metal cations in $Ce_xZr_{1-x}O_2$ mixed oxides (*142*). Finally, the model-catalyst approaches developed here should allow the study of metal-support interactions in other catalytically relevant systems by simply varying the ALD-deposited thin film composition.

4. Biomass to Biofuels: Hydrodeoxygenation Reaction

4.1 Introduction

Biomass is organic matter derived from living organisms, and it has been harnessed as an energy source since the discovery of fire. Nowadays, it can either be used directly via combustion to produce heat, or indirectly via thermal, chemical, or biochemical conversion to various biofuels and chemicals. Depending on the origin and production technology of biofuels, they are generally classified as first, second or third generation biofuels (*27*). First-generation biofuels are produced directly from food crops by fermentation to bioethanol or by abstraction of oils for use in biodiesel. However, such feedstock provide only limited biofuel yields and have a negative impact on food availability and security. To overcome the limitations of first-generation biofuels, second-generation biofuels have been developed. These are produced from feedstock of lignocellulosic, non-food materials that include straw, forest residues and purposely grown energy crops on marginal lands. The term third generation biofuels has only recently been introduced and it refers to biofuels based on algal biomass production. Algae are capable of much higher yields than other feedstock and can be genetically manipulated to produce a particular feedstock. Most notably, it has been suggested that algae might be tied directly to carbon emitting sources (power plants, industry, etc.) where they could convert emissions into usable fuel, thus dramatically improving the plants sustainability.

A wide range of chemical processes may be used to convert lignocellulosic biomass into more conveniently used, transported or stored biofuels (Figure 4.1). Gasification, pyrolysis, hydrolysis and biochemical routes are the main strategies to transform lignocellulosic biomass in intermediate products that can be further processed to produce valuable chemicals or fuels. Gasification produces syngas ($CO + H_2$), containing traces of methane, also called a *producer gas*, suitable for internal combustion engines or further processing to produce methanol, alkanes (via Fischer-Tropsch synthesis) or hydrogen (*163*). Pyrolysis and liquefaction of lignocellulosic biomass yields bio-oils that can be upgraded to yield liquid fuels. Conversion of biomass to biofuels can also be achieved via selective conversion of individual components of biomass. For example, cellulose and hemicellulose can be converted over solid acid catalysts via hydrolysis to intermediate platform chemicals such as sorbitol (*164*), glucose, xylose, levulinic acid (*165*, *166*), 5-

hydroxymethylfurfural (HMF) (*167*), and furfural (*168*), to name a few. Among the many upgrading processes of lignocellulosic feedstock, hydrodeoxygenation (HDO) is a pivotal reaction to produce liquid fuels (*163*, *169*).

Figure 4.1 Main strategies for fuel production from lignocellulosic biomass.

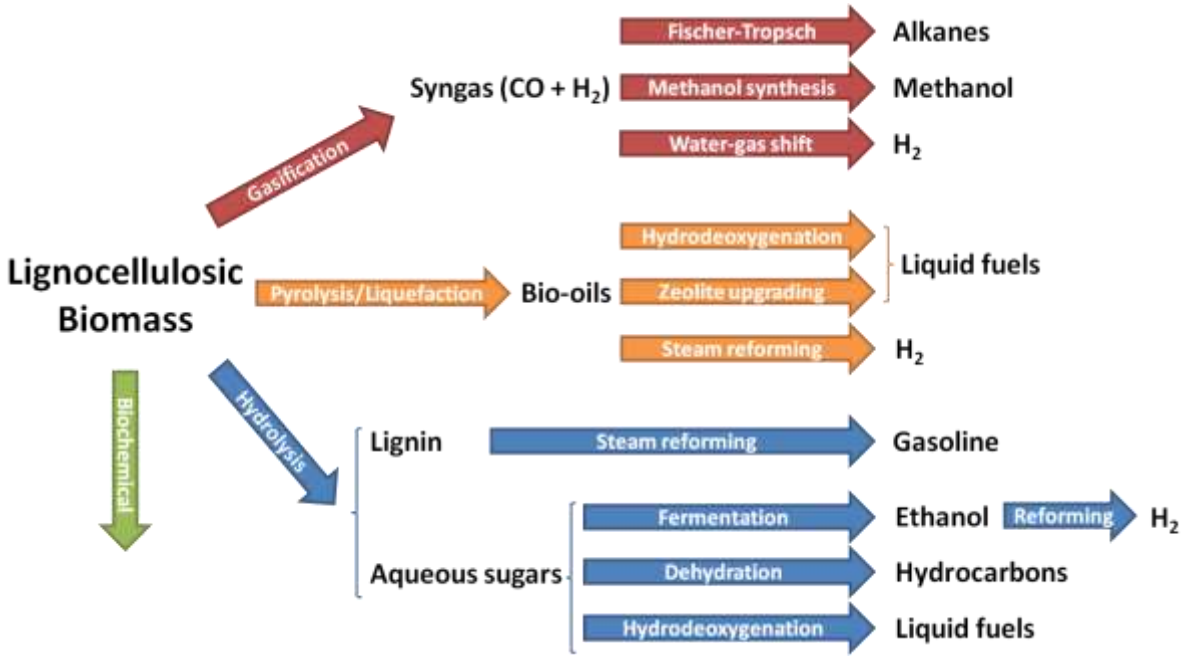

HDO is a hydrogenolysis process for removing oxygen from oxygen-containing compounds. It is a very attractive process due to high carbon efficiency (100% theoretical) and technology compatibility with existing petroleum hydrotreating technology. HDO requires relatively high H_2 pressure (7-40 bar), but in principle H_2 can be sustainably produced from biomass by sugar aqueous reforming, alcohol steam reforming, syngas steam reforming or using solar or wind power. In general, biomass-derived molecules contain many different functional groups, which are hydrogenated at different temperatures and may or may not be selectively activated by a catalyst (*29*). Moreover, the composition and oxygen content of bio-oils and hydrolyzed cellulosic feedstock varies dramatically depending on the source, and this results in different HDO reactivity. Therefore, the main strategy to study the performance of a certain catalyst in HDO reaction is to study model compounds activation. By understanding the chemistry and the reaction mechanisms of a certain model compound, one can study the selectivity to certain products and get insights for upgrading real feedstock to desired fuels and chemicals. In the present work, we study HDO of two very important model molecules: furfural and HMF.

Furfural is formed during pyrolysis of biomass (*170*, *171*) and can be obtained in high yields from dehydration of C-5 sugars, such as xylose and arabinose (*172*, *173*). By selective HDO, furfural produces 2-methylfuran (MF) (*174*), which can be used as gasoline additive due to its high octane rating and low solubility in water. HMF is another key platform chemical in biomass conversion, readily obtained by the acid-catalyzed dehydration of C-6 sugars (*174–178*). The selective HDO reaction of HMF leads to 2,5-dimethylfuran (DMF), which has a high energy density and an octane rating of 119 and can be used as fuel additive (*179*). Moreover, both MF and DMF can be reacted with ethylene via Diels-Alder reaction to yield toluene (*180*, *181*) and p-xylene, respectively (*181*).

Despite the recent advances in catalytic HDO reaction of HMF and furfural, some critical issues remain to be addressed, among which the understanding of the factors influencing high selectivity to MF and DMF and catalytic stability. In the present chapter, we aim to discuss the mechanism of HDO of furfural and HMF in pressurized flow reactors and to rationalize the influence of H_2 pressure and bimetallic catalysts nanostructure on the catalytic HDO reaction.

4.2 H_2 Pressure Dependence of HDO Selectivity for Furfural over Pt/C Catalysts

4.2.1 Introduction

Furfural has a relatively high vapor pressure at low temperature, so that HDO reaction of furfural can be performed in simple, vapor-phase reactors, and much of the published work in this area has been performed in this way (*38*, *182*, *183*). Decarbonylation to form furan is the major side reaction for essentially all metal catalysts and significant effort has gone into finding materials that show higher selectivity to MF, rather than producing furan (*38*, *182–184*). Interestingly, decarbonylation is not reported to be a major side reaction in HDO studies of 5-hydroxymethylfurfural (HMF) (*41*, *185*), which has a very similar structure to furfural. A major difference between HMF and furfural is that HMF has a much lower vapor pressure, so that reaction studies of HMF are commonly performed at high H_2 pressures with most of the HMF in the liquid phase, usually in the presence of a solvent (*186–188*). Recent theoretical studies have indicated that the furfural adsorption energy and conformation on metal catalysts can be profoundly changed by the hydrogen surface coverage, which in turn can affect the relative rates of hydrogenation and decarbonylation (*189*). Therefore, the fact that decarbonylation is observed in HDO of furfural, but not in HDO of HMF, may be due to differences in the reaction conditions.

In the present section, we examine the effect of reaction conditions on HDO of furfural over a Pt/C catalyst. The high-pressure, three-phase HDO reaction of furfural was performed in a tubular flow reactor described in detail in Section 2.10. Low-pressure reactions were carried out in the same temperature range but at one atmosphere total pressure, with variable H_2 partial pressures. At high pressures, HDO of furfural was found to be very similar to HDO of HMF: decarbonylation was negligible and the reaction was sequential, with all of the reactants proceeding through MF, which in turn reacted to over-hydrogenated products. At lower H_2 pressures, decarbonylation occurred in parallel with HDO, and was monotonically suppressed with increasing H_2 pressures.

4.2.2 Catalyst Synthesis and Characterization

A 10 wt % Pt/C catalyst was prepared by impregnation of carbon black (Vulcan XC-72R) with a water/ethanol (5:1) solution of tetraammineplatinum(II) nitrate ($Pt(NH_3)_4(NO_3)_2$, 99.99%, Alfa Aesar). The dried powders were heated in He flow at 500 °C for 6 h using a heating ramp of 3 °C min^{-1} and then used directly in the reactor without further pretreatment. After reduction in H_2 at 400 °C, the Pt dispersion was determined to be 12% by CO chemisorption and the Pt particle sizes observed by TEM varied between 4 and 10 nm (Figure 4.2).

Figure 4.2 Representative TEM image of 10 wt% Pt/C

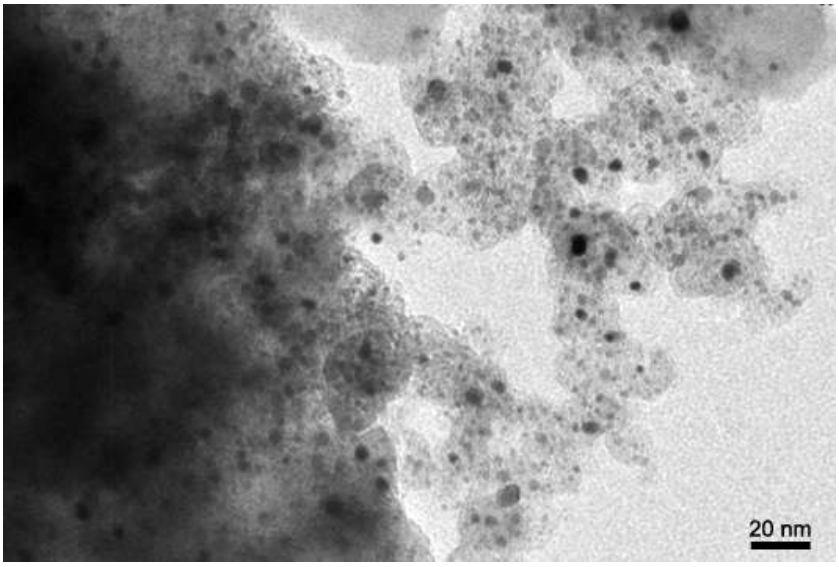

4.2.3 High Pressure HDO of Furfural

For work at high pressures, the reactor was part of the continuous flow system described in Section 2.10. The liquid feed (1-wt% furfural in 1-propanol) flow rates were varied from 0.02 to 0.2 ml min^{-1}, while the H_2 flow rates were 2 to 20 mL min^{-1} (STP). The reactor was held at 180 °C and 33 bar total pressure in all measurements, varying only the flow rates of reactants while maintaining a constant ratio of gas and liquid flow rates. The environment in this system is similar to that of a trickle-bed reactor and mass transfer processes, including diffusion of furfural, H_2, and products within the liquid phase and within the solid catalyst, are complex. Quantitative analysis of the reaction rates for such system is difficult, since the rates are dependent on catalyst wetting and mass transfer. The carbon balance (based on furfural) was always better than 90% in both high- and low-pressure measurements.

Figure 4.3 shows the furfural conversion and the product yields as a function of the reactor space time, W/F, defined here as the weight of the catalyst divided by the volumetric flow rate of the liquid. A guide to the products that are formed is shown in Scheme 4.1.

Figure 4.3

Conversion and product distribution for the liquid-phase HDO reaction of furfural over a 10 wt% Pt/C catalyst as a function of reactor space time. (A) the overall product distribution; (B) over-hydrogenated products in detail (product group D). Reaction conditions: 33 bar and 180 °C. (▼) furfural conversion, (▲) product group B, (●)MF, (■) product group D, (□) MTHF, (▷) 2-pentanol, (×) pentanedione, (◁)2-propoxypentane.

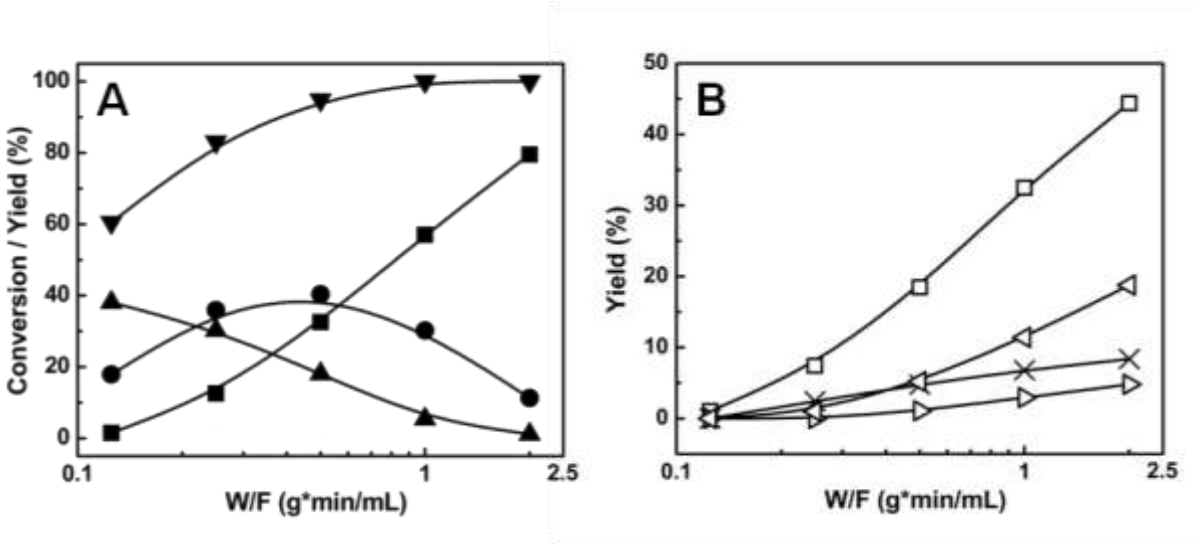

Scheme 4.1

Reaction network for liquid-phase hydrodeoxygenation of furfural in alcohol solvent.

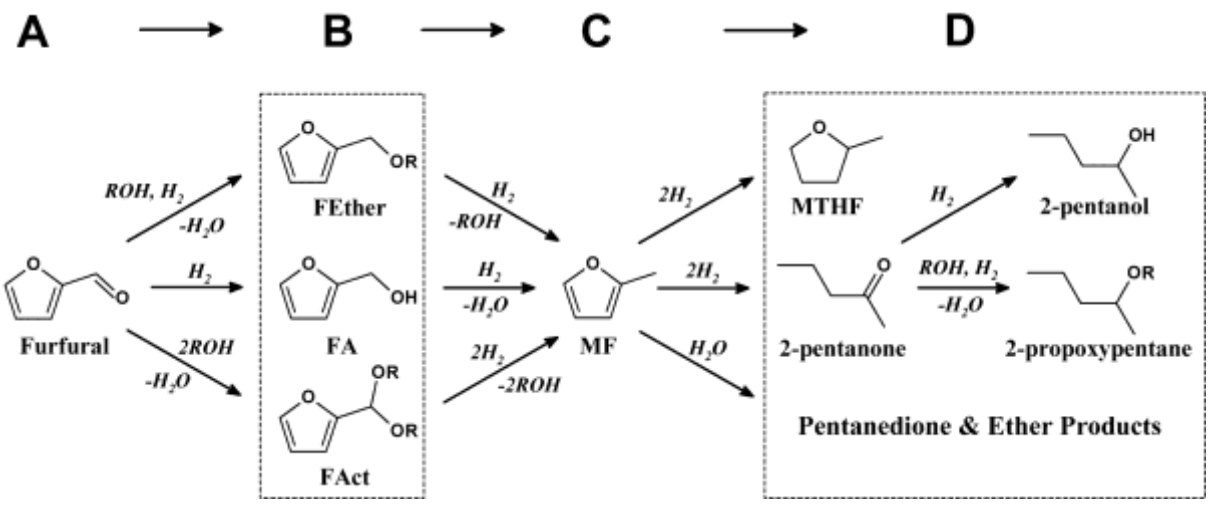

The results in Figure 4.3A correspond very closely to what was reported earlier for HDO of HMF for the same catalyst and reaction conditions (*185*). The furfural conversion increased with residence time, reaching 100% conversion for the highest W/F values. At the shortest residence times, the main products were 2-methylfuran (MF) and several partially hydrogenated products designated as B (furfuryl alcohol – FA, furfuryldipropyl acetal – FAct, and furfurylpropyl ether – FEther). At such short residence time, there was no evidence for over-hydrogenated products, listed as D in Scheme 4.1. With increasing residence time, the yield of B products decreased steadily while the yields of MF and D products increased (Figure 4.3B). With still longer residence times, the MF yield reached a maximum and began to decrease, while the D products continued to increase.

Several important observation can be made about the results presented in Figure 4.3. First, there was no evidence for decarbonylation products. No furan was formed and there were no C-4 products in the final D products. Second, as previously reported for HDO of HMF, the evolution of products indicates that HDO of furfural at high pressure is a series reaction, as shown in Scheme 4.1. This is demonstrated by the following facts: 1) The partially hydrogenated, B products form first and decrease continually with residence time. 2) The MF yield goes through a maximum, indicating it is formed from B, then declines. 3) The over-hydrogenated D products are absent at short residence times and increase continually.

As shown in Figure 4.3B, the major over-hydrogenated product is 2-methyltetrahydrofuran (MTHF). The fact that MTHF is formed only after MF has formed implies that ring hydrogenation can only occur after reduction of the carbonyl group of the furfural. Other products that formed in parallel with MTHF were 2-pentanol, pentanedione, and 2-propoxypentane (a reductive-etherification product formed by reaction of 1-propanol with 2-pentanone).

As a further test of the sequential reaction network proposed in Scheme 4.1, experiments were carried out in which the intermediate reactants were fed to the reactor. Figure 4.4 shows the MF conversion and final product distribution as a function of space time, at 180 °C and 33 bar, when 0.8 wt% MF in 1-propanol was fed to the reactor. The molar concentration of MF in these experiments was the same as that of furfural in Figure 4.3. The data in Figure 4.4 support the proposed sequential reaction scheme. The conversion of MF increases with residence time and the final product distribution is similar to that shown in Figure 4.3B. The slightly lower yields of pentanedione, along with its etherification products, may be due to the fact that water is formed in the reaction of furfural to MF and will therefore be present in lower amounts when MF is fed directly to the reactor.

Figure 4.4 Conversion and product distributions for the reaction of MF in 1-propanol over a 10 wt% Pt/C catalyst as a function of reactor space time. Reaction condition: 33 bar and 180 °C. (●) MF conversion, (□) MTHF, (▷) 2-pentanol, (×) pentanedione, (◁)2-propoxypentane.

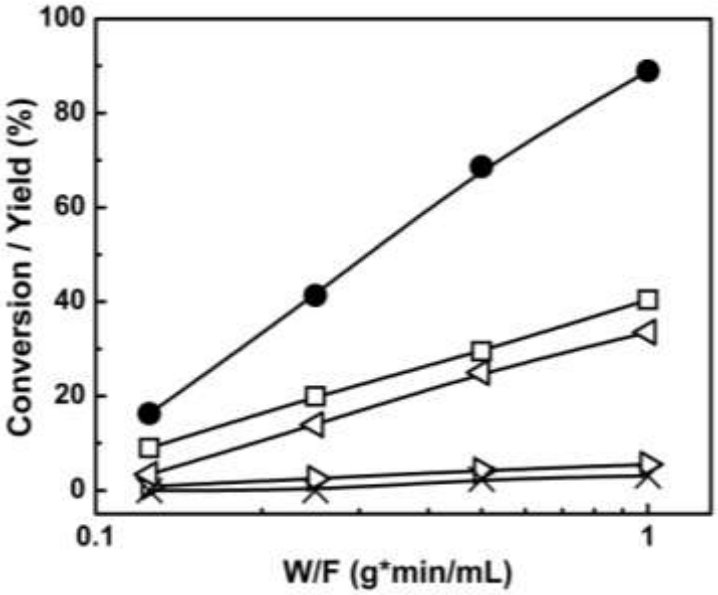

The reactivity of FA, MTHF, tetrahydrofurfuryl alcohol (THFA) and 2-pentanone were also examined in less detail, with results shown in Table 4.1. For these experiments, the reactants were diluted in 1-propanol to the same molar concentrations as furfural and their reactivity studied at 180 °C and 33 bar at a single reaction space time of 1 g min mL^{-1}. In agreement with the data in Figure 4.3 and Scheme 4.1, the conversion of FA under these conditions was 96% and the products were similar to those observed from furfural, with the exception that FEther and FAct were not observed. MTHF and THFA were completely unreactive under these conditions.

The low reactivity of MTHF indicates that ring-opening is difficult after the ring has been saturated, in agreement with a previous report by Bradley *et al.* (*190*), who argued that the strong adsorption of the aromatic ring on Group VIII metals can weaken the C-O bond in furan. The fact that the hydroxyl group on THFA is also not reactive, whereas the hydroxyl group on FA is very reactive, implies that the aromatic ring strongly affects the reactivity of that group. Finally, 2-pentanone was completely converted at the investigated space time, with a 90% yield to the reductive-etherification product, 2-propoxypentane. Only a small amount of 2-pentanol was formed under these conditions. This result is consistent with the observations from the reactions of furfural, explaining the presence of 2-propoxypentane as one of the major by-products.

Table 4.1 Product distributions of reaction from varied reactant over 10 wt% Pt/C, at 180 °C, 33 bar and space time of 1 g min mL^{-1}.

Reactant	Conversion (%)	MF	MTHF	THFA	2-Propoxypentane	2-Pentanone	2-Pentanol	Pentanedione
FA	96.1	16.3	41.2	<1	19.8	2.8	3.8	4.5
MTHF	0	-	-	-	0	0	0	0
THFA	0	-	0	-	-	0	0	0
2-Pentanone	100	-	-	-	90.0	-	6.8	-

4.2.4 Low Pressure HDO of Furfural

For the low-pressure measurements, furfural was introduced to the reactor by flowing a carrier gas through a heated bubbler. In most cases, the partial pressure of furfural was maintained at 0.02 bar. The total gas flow rate to the bubbler was fixed at 60 mL min^{-1}, while the H_2 partial pressure was adjusted by mixing He with the H_2. A bubble meter at the reactor exit was used to continuously check the gas flow rates. The effluent from the reactor was diluted with 120 mL min^{-1} He to decrease the final concentration of furfural and avoid condensation problems. The product analysis was carried out using a gas-tight syringe to inject the effluent from the reactor into the GC-MS. Notably, in the high-pressure experiments, the conversion and selectivity were measured as a function of the total flow rates in order to map out the product distribution as a function of residence time. Since the reaction pathway was qualitatively different at the lower H_2 pressures, most of the low-pressure measurements were performed under differential conditions, with furfural conversions less than 15%. Although the conversions increased from approximately 5 to 15% with increasing H_2 partial pressure for these fixed flow rates, the selectivity did not change significantly when the flow rates were adjusted to vary the conversions between 10 and 40%.

The selectivity for furfural HDO at low H_2 pressures are shown as a function of H_2 partial pressure in Figure 4.5. Since furan, FA, and MF accounted for more than 95% of the products under these conditions, only the selectivity to these products is shown, which is qualitatively different from what observed at higher pressures. Consistent with observations from a large number of literature studies on various metal catalysts, decarbonylation of furfural to furan was a major reaction pathway in all cases in these low-pressure experiments (*38*, *182–184*). At lower H_2 pressures, the decarbonylation product, furan, was clearly the dominant product, with a selectivity to furan of more than 70% at 0.1 bar H_2. With increasing H_2 pressure, the selectivity to furan decreased and the selectivity to FA increased. At 1 bar H_2, FA was the largest product.

Figure 4.5 Products selectivity for the vapor-phase HDO reaction of furfural over a 10 wt% Pt/C catalyst as a function hydrogen pressure by varying H_2: He ratio. Reaction conditions: total flow rate 60 mL min^{-1}, furfural partial pressure 0.02 bar, total pressure 1 bar and 180 °C. (□) furan, (△) FA, (▽) MF.

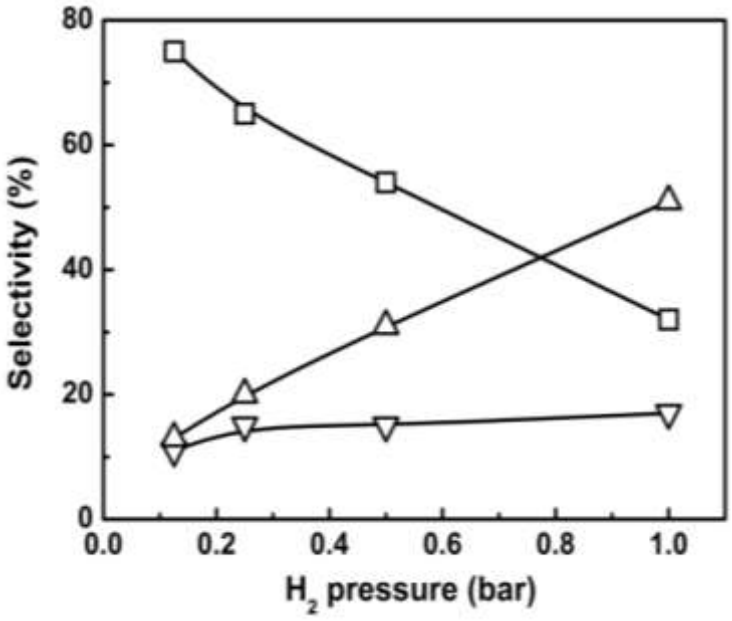

To rule out furan production from FA, experiments were conducted in which FA was fed to the reactor. For these conditions, no furan was produced from FA and the major product was MF (>60% selectivity). Additional products formed from FA were MTHF, THFA, and 2-pentanone. Since all of these are 5-carbon molecules, there is no additional decarbonylation once FA is produced. Therefore, the relative importance of decarbonylation and HDO in the reaction of furfural can be determined from the furan selectivity in Figure 4.5.

The results in Figure 4.5 demonstrate the importance of H_2 pressure in determining decarbonylation selectivity over Pt/C catalysts. For the 33 bar experiment, we estimate that the H_2 partial pressure was approximately 22 bar and the furfural pressure 0.14 bar, with the balance being 1-propanol. Although the presence of 1-propanol may also affect the selectivity, an extrapolation of the data in Figure 4.5 to higher pressures suggests that the higher H_2 pressure is the most likely reason for the absence of decarbonylation at 33 bar.

4.2.5 Discussion

The present results demonstrate the importance of H_2 pressure in the reaction network for furfural. For a typical Pt/C catalyst, decarbonylation to furan dominates at the lower H_2 pressures that are often used in laboratory testing of furfural HDO; however, a sequential reaction network, in which all the furfural proceeds through MF, dominates at higher pressures. This may help unify the literature for HDO of furfural and 2-hydroxymethyl furfural (HMF). Decarbonylation is not a major pathway in most studies with HMF. Because of the low vapor pressure of HMF, catalyst testing for HDO of HMF is usually performed in an autoclave at high pressures, where decarbonylation would also not be important for the reaction of furfural.

The fact that decarbonylation is unimportant at higher H_2 pressures agrees with previous papers where HDO of furfural was studied in an autoclave at higher pressures (*191*, *192*). What the present work demonstrates is that the absence of decarbonylation in previous high-pressure studies is probably not due to the catalysts that were studied but rather the conditions used to study the reaction. In other words, the selectivity of a catalyst can be changed by simply varying the H_2 pressure.

The reason for the strong H_2 pressure dependence on the reaction products is likely due to changes in the hydrogen surface coverage. DFT calculations of furfural adsorption and reaction on Pd(111) (*189*) have shown that the presence of co-adsorbed hydrogen changes the conformation of adsorbed furfural. Furfural prefers to lie flat on Pd surface in the absence of adsorbed hydrogen but the ring becomes perpendicular to the surface when hydrogen is present. Moreover, kinetic modeling indicates that the selectivity of the hydrogenation product (FA) increases relative to the decarbonylation (furan) with increasing hydrogen coverage. These calculations are in very good agreement with the trends observed in the present low-pressure HDO study.

At high H_2 pressures, the product distributions for the reactions of furfural and HMF are very similar. In both cases, the reactions are sequential, proceeding through either MF or DMF. For HDO of HMF, this was shown to be true for carbon-supported Pt, Pd, Ir, Co, Ni, and Ru (*185*). The final products formed from the reaction of MF and DMF are also similar. In earlier work with HMF, it was shown that Pt gives a mixture of products consisting of primarily open-ring ketones and alcohols, with some of the ring-saturated dimethyltetrahydrofuran (*185*). With furfural, the ring-saturated product, MTHF, is slightly favored but the product slate is similar. In both cases, the production of open-ring products occurs only after reduction of the carbonyl group to a methyl group.

The similarities in the reaction networks for furfural and HMF imply that the strategies for developing improved catalysts should also be similar. This leads to the important question of whether catalysts developed to minimize decarbonylation in the reaction of furfural will also be the most selective for producing DMF from HMF. Based on earlier theoretical studies, it seems likely that there will indeed be a strong relationship between minimizing decarbonylation at low pressures and selectivity towards DMF at high pressures but a careful examination of the relationship is needed. In both cases, bimetallic catalysts have been shown to exhibit improved selectivity than their single-component analogues (*38*, *188*, *193–195*).

Most high-pressure HDO studies employ a solvent, which can affect the product distribution. In addition to the fact that the solvent may also be a reactant (*e.g.* 2-propoxypentane is a product of a reaction between 1-propanol and 2-pentanone in the present study), adsorbed solvent molecules can also change the conformation of the adsorbed reactants in a manner similar to that with adsorbed hydrogen. Because the chemistry in earlier studies with HMF performed under the same conditions appeared to be similar for different solvents (*41*), we do not believe the presence of the solvent can explain the differences observed in the high-pressure and low-pressure results of the present study.

4.2.6 Conclusions

H_2 pressure plays an important role in determining the product distribution in HDO of furfural. Decarbonylation is a major reaction pathway only at lower H_2 pressures. At higher H_2 pressures, HDO of furfural follows a sequential reaction network, with MF formed as an intermediate. Great progress is being made in our understanding of HDO catalysis for furfural and HMF. The development of unifying concepts for different reactants and reaction conditions further helps our understanding of these reactions.

4.3 Mechanisms for High Selectivity in HDO of HMF over Pt-Co Nanocrystals

4.3.1 Introduction

The reaction of HMF to DMF has been extensively studied over various metal and metal-alloy catalysts (*196–198*), but selectivity to DMF over ring-opened (*e.g.* 2-hexanone, 2,5-hexanedione) and ring-hydrogenated (*e.g.* 2,5-dimethyltetrahydrofuran – DMF) products is often poor. Understanding what is required for a good catalyst is made more difficult by the different yields that have been reported by different groups for materials of similar composition (*186*, *187*). Some of these variations appear to be due the sensitivity of results to the type of reactor that is used in the rate measurements (*41*). Even so, bimetallic catalysts appear to be more selective than their pure-metal analogs (*38*, *194*, *195*). For example, Schüth and co-workers (*188*) reported DMF yields as high as 98% on Pt-Co nanoparticles which were encapsulated in hollow carbon spheres.

As already mentioned in the previous section, the reaction of HMF to DMF is sequential on Pt and many other metals(*185*), with HMF reacting selectively to DMF, but DMF then going on to form secondary products over the same catalysts. Based on these considerations, the yield of DMF is determined by the relative rates of formation and consumption of DMF, and the most selective catalysts should show low activity for reaction of DMF. An implication of this picture is that selective catalysts cannot consist of a mixture of selective and nonselective components, since even a relatively small fraction of nonselective material could convert DMF to other products. For the case in which two metals are nonselective (*e.g.* Pt and Co)(*185*), but their alloy is selective, this means that the composition of the metal particles must be uniform.

The synthesis of highly uniform Pt and Pt-Co nanocrystals (NCs) have been demonstrated via solvothermal methods (*39*, *199*). Solvothermal synthesis refers to a method which involves the use of a solvent under moderate to high pressure (typically between 1 bar and 10,000 bar) and temperature (typically between 100 °C and 1000 °C). The process can be used to prepare many geometries including thin films, bulk powders, single crystals, and NCs. If properly optimized, solvothermal synthesis can yield NCs having controlled and uniform size, morphology, and composition, parameters that are strongly correlated to the NCs catalytic properties (*39*, *200*). Therefore, this synthetic approach allows to prepare and test catalysts whose properties are well controlled, allowing us to understand the effect of various parameters on catalytic activities.

In this section we report the HDO of HMF into DMF catalyzed by Pt, Pt_3Co, and Pt_3Co_2 NCs-based catalysts using a continuous flow reactor. DMF yields as high as 98% were achieved with Pt_3Co_2 alloys due to very low reactivity of DMF towards over-hydrogenated products. Furthermore, the bimetallic catalysts synthesized using the solvothermal method are stable and superior to alloy

catalysts prepared by traditional wet impregnation. Characterization of the Pt-Co NCs revealed that they have a special structure consisting of a monolayer of surface oxide on a metallic core. Calculations using Density functional theory (DFT) rationalize the stability of this structure and indicate that the oxide prevents side reactions while providing catalytic sites for effective conversion of HMF to DMF. Computations reveal a radical-mediated reaction mechanism, which was found to be critical for selective HDO on oxides. Structural characterization and DFT calculations confirm that controlling the bimetallic composition is essential for preparing a good catalyst.

4.3.2 Synthesis and Characterization of Pt- and Pt-Co-based Catalysts

Nearly monodisperse Pt, Pt_3Co, and Pt_3Co_2 NCs were synthesized by using or modifying reported methods (*39*, *199*). The experimental setup used for the synthesis of NCs in this work is schematically depicted in Figure 4.6. A Schlenk line connected to a vacuum pump was used to operate under N_2 inert atmosphere (1 bar, flow).

Figure 4.6 Schematic representation of the solvothermal synthesis setup used in this work.

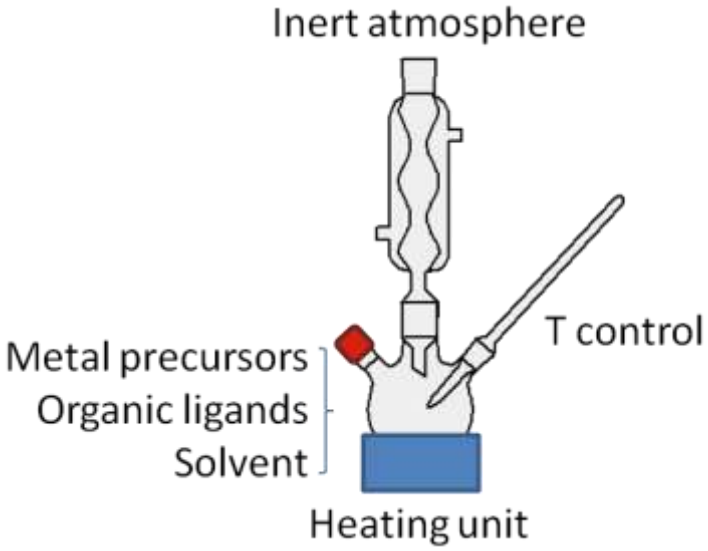

To prepare Pt NCs, 314 mg of platinum (II) acetylacetonate ($Pt(acac)_2$, Acros, 98%) was dissolved in 40 mL trioctylamine (TOA, Sigma-Aldrich, 97 %), 10.9 mL oleylamine (OAm, SigmaAldrich, 70 %), 2.6 mL oleic acid (OAc, Sigma-Aldrich, 90 %), and 0.9 mL trioctylphosphine (TOP, Acros Organics, 97 %). The reaction mixture was kept under vacuum at 80 °C for 30 minutes and then heated up to 300 °C at a rate of 10 °C min^{-1}. After 30 minutes, the reaction mixture was cooled down to room temperature. Then 40 mL toluene were added. The mixture was divided into

6 centrifuge tubes (50 mL) and 30 mL isopropanol and 5 mL ethanol were added. After 2 minutes of centrifugation at 6000 rpm, the supernatant was removed and the precipitate was re-dispersed in hexane or toluene. After washing the excess amount of OAc, OAm, and TOA by isopropanol, the NCs were dispersed in toluene.

To synthesize Pt_3Co NCs, a method reported by Shevchenko *et al*. was scaled up(*199*). 264 mg of $Pt(acac)_2$ was dissolved in 32 g hexadecylamine (Acros Organics, 90 %) and 16 mL diphenyl ether (Sigma-Aldrich, 99 %) in the presence of 672 mg 1- adamantane carboxylic acid (Acros, 99 %) and 1.04 g 1,2-hexadecanediol (HDD, Sigma Aldrich). The reaction mixture was put under vacuum at 80 °C for 30 minutes and then heated at a rate of 10 °C min^{-1}. When the temperature reached 170 °C, 334 mg $Co_2(CO)_8$ (Acros, 95 %) , dissolved in 3.2 mL 1,2-dichlorobenzene, were injected. The reaction mixture was further heated to 230 °C for 40 minutes. Then, the reaction mixture was allowed to cool down and 50 mL toluene were injected at 200 °C. When the system was cooled down to 90 °C, the reaction mixture was divided into 6 centrifuge tubes (50 mL) and 30 mL of warm isopropanol (~50 C°) were added to each centrifuge tube. After 2 minutes of centrifugation at 6000 rpm, the supernatant was removed and the precipitate was dispersible in non-polar solvent such as hexane and toluene. After washing the colloid with isopropanol 3 times, the NCs were kept in hexane.

For the synthesis of Pt_3Co_2 NCs, the method employed for Pt_3Co NCs synthesis was modified. Hexadecylamine was replaced by OAm (41 mL), diphenyl ether was replaced by 1-octadecene (Acros, 90 %,16 mL), and HDD was not added. After evacuation at 80 °C for 30 minutes, the reaction mixture was heated to 300 °C. At 170 °C, the solution of $Co_2(CO)_8$/1,2-dichlorobenzene was injected in the same amount as the Pt_3Co synthesis. After 30 minutes at 300 °C, the reaction mixture was cooled down to room temperature and 50 mL hexane were added. The work up was the same as for the synthesis of Pt_3Co NCs. Notably, in the case of Pt_3Co, HDD was used to reduce Pt, which is called "polyol process"(*201*). On the other hand, for the synthesis of Pt_3Co_2, hexadecylamine was replaced by oleylamine and HDD was not added. As oleylamine is a relatively milder reducing agent than HDD (*202*), this reaction resulted in NCs relatively richer in cobalt compared to the reaction done by the polyol process.

From the TEM images of NCs in Figure 4.7a-c, the average diameters of NCs were 2.4 nm, 3.2 nm, and 3.7 nm with less than 8% of size distribution for Pt, Pt_3Co, and Pt_3Co_2 NCs, respectively. A superlattice structure for each composition of NCs was observed, indicating that the NCs were highly monodisperse. Wide angle x-ray scattering data show that all the NCs possess face-centered cubic (fcc) crystal structure as displayed in Figure 4.7d. The compositions of the NCs were confirmed by Inductively Coupled Plasma Optical Emission Spectrometry (ICP-OES).

Figure 4.7 TEM images of a) Pt NCs, b) Pt_3Co NCs, and c) Pt_3Co_2 NCs, after removing the solvent. The scale bars in the insets represent 2 nm. d) Wide angle X-ray scattering data of Pt (red), Pt_3Co (green), and Pt_3Co_2 (blue).

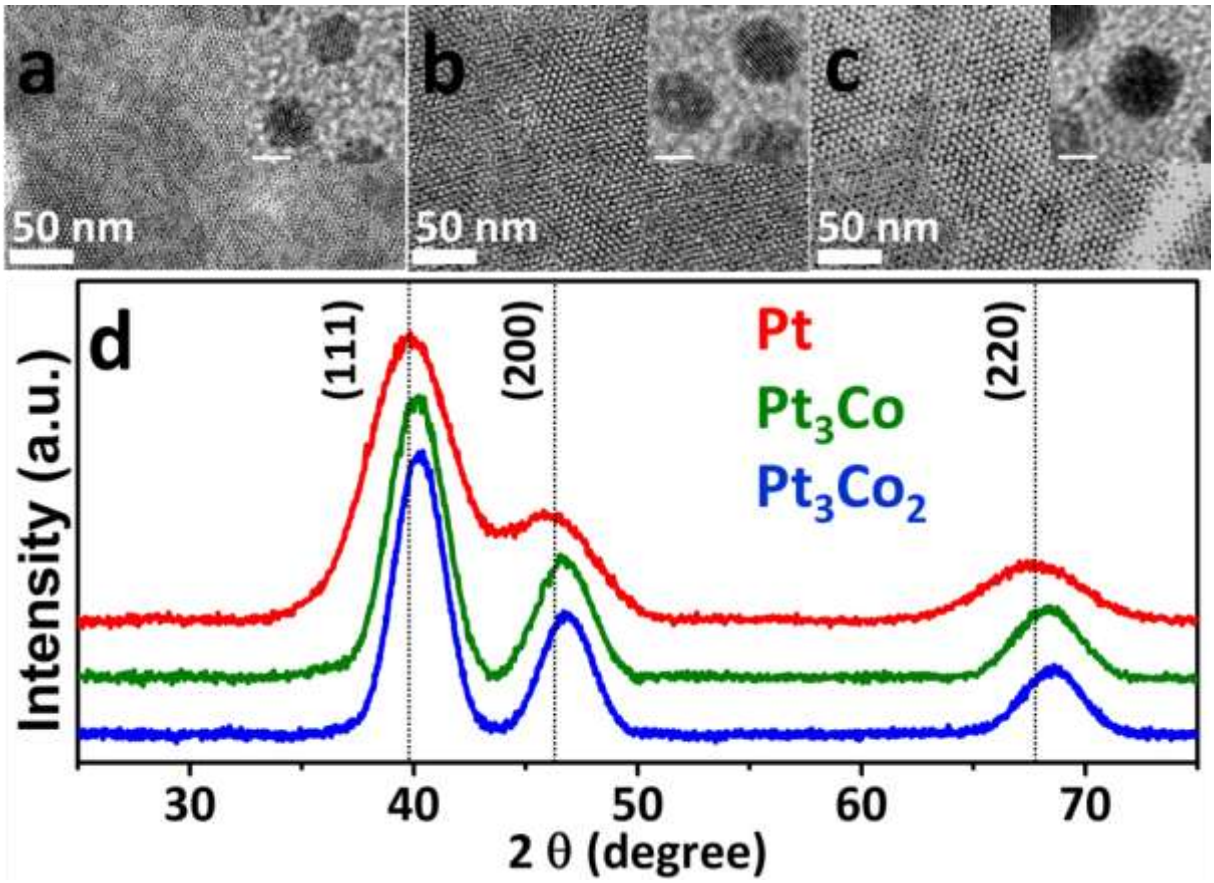

To prepare the final, 10 wt% carbon supported NC catalyst, the NCs suspended in 20 mL hexane were mixed with carbon powder (Cabot, Vulcan XC72R) in a 50 mL centrifuge tube under sonication. After 15 minutes of sonication, the solution was centrifuged at 6000 rpm for 1 minute. The transparent supernatant was removed and the powder was washed with 20 mL isopropanol and centrifuged again. Then, the powder was dried in vacuum at 50 °C.

The organic ligands covering the NCs surface for colloidal stability have the drawback that they inhibit catalytic reactions due to limited access of reactants to the binding sites on the NC. Therefore, the surface ligands should be removed in order to maximize NCs available surface area. The surface cleaning procedure consists of two steps. First, 300 mg of 10 wt% NCs/C catalysts were exposed to O_2 plasma for 15 min. After the plasma treatment, the catalyst was put into a furnace at 500 °C and taken out after 1 minute (Rapid Thermal Annealing – RTA) (*40*). Figure 4.8 shows TEM images of as-deposited and surface treated NCs on carbon support. After the plasma and thermal

treatment, no significant change in size and morphology is observed in all cases, which proves the reliability of the surface treatment technique.

Figure 4.8 TEM images of (A) as-synthesized NC catalyst on carbon support and (B) after surface treatment.

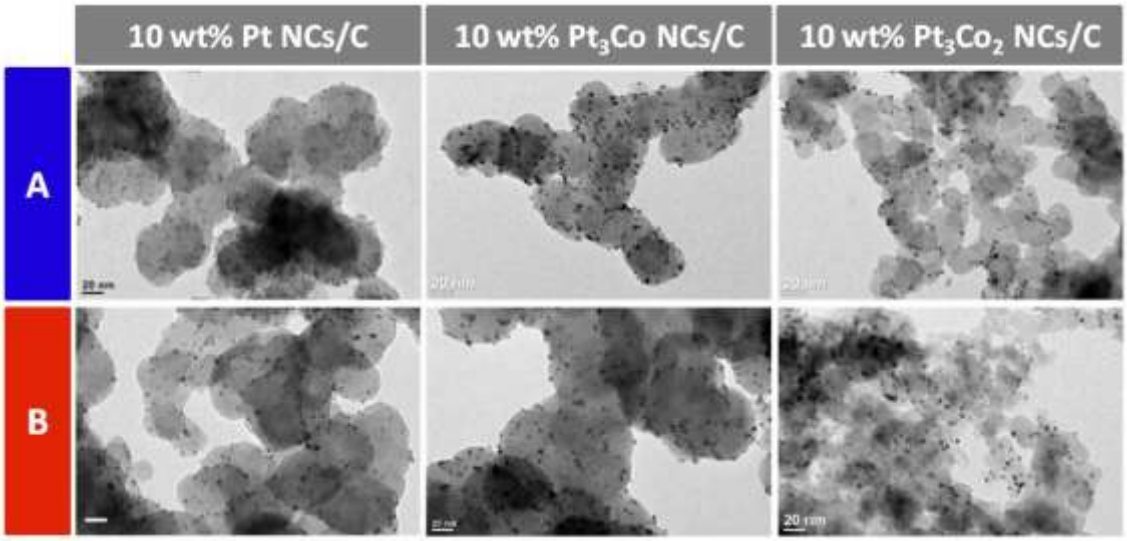

Also, from wide angle x-ray scattering measurements (Figure 4.9), it is confirmed that the phase of Pt_3Co and Pt_3Co_2 is not transformed from disordered fcc to ordered fct structure. Therefore, the potential effects of crystal structure ordering on the catalytic activity can be excluded and any difference in activity can be attributed to compositional effects (*203*).

Figure 4.9 Wide angle x-ray scattering data of as-synthesized (red) and surface cleaned (blue) Pt_3Co_2 NCs.

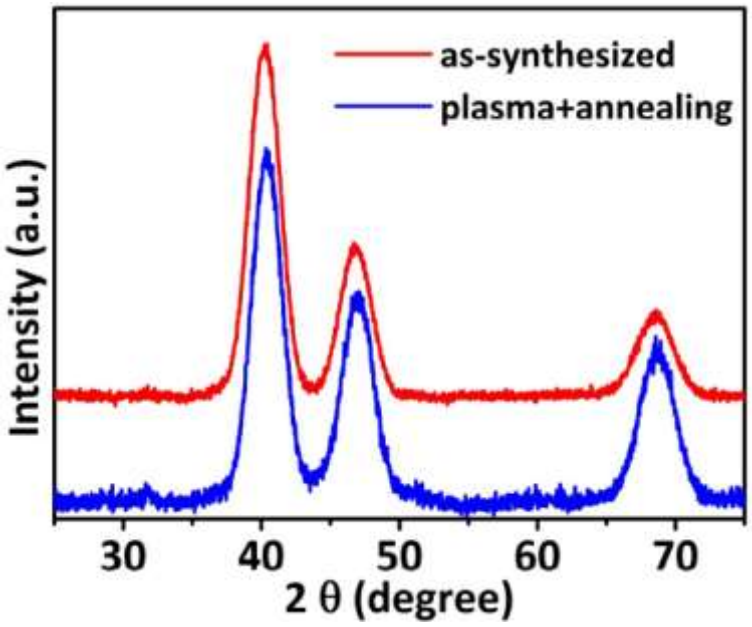

4.3.3 HDO studies

Previous studies on carbon-supported Pt and Co catalysts have shown that hydrodeoxygenation of HMF to DMF is a series reaction (*185*), proceeding as indicated in Scheme 4.2. The HMF (A) first reacts to a group of partially hydrogenated intermediate compounds (B), including 2-propoxymethyl-5-furanmethanol (ether-furfuryl alcohol, or EFA), 2-propoxymethyl-5-methylfuran (ether-methyl furan, or EMF), 5-methyl furfural (MFu), 2-hydroxylmethyl-5-methyl furan (HMMF), 2,5-bis(hydroxymethyl)furan (BHMF), and 2,5-bis(propoxymethyl)furan (BEF). These intermediate compounds can all be converted to DMF (C), which in turn reacts to over-hydrogenated products (D), dimethyltetrahydrofuran (DMTHF), 2-hexanone, 2-hexanol, 2,5-hexanedione, and their etherification derivatives, 1-propoxy-1-methyl-pentane (2-propoxyhexane) and 1,4-dipropoxy-1,4-dimethyl-butane (2,5-dipropoxyhexane).

Scheme 4.2 Reaction network for liquid-phase hydrodeoxygenation of HMF in alcohol solvent.

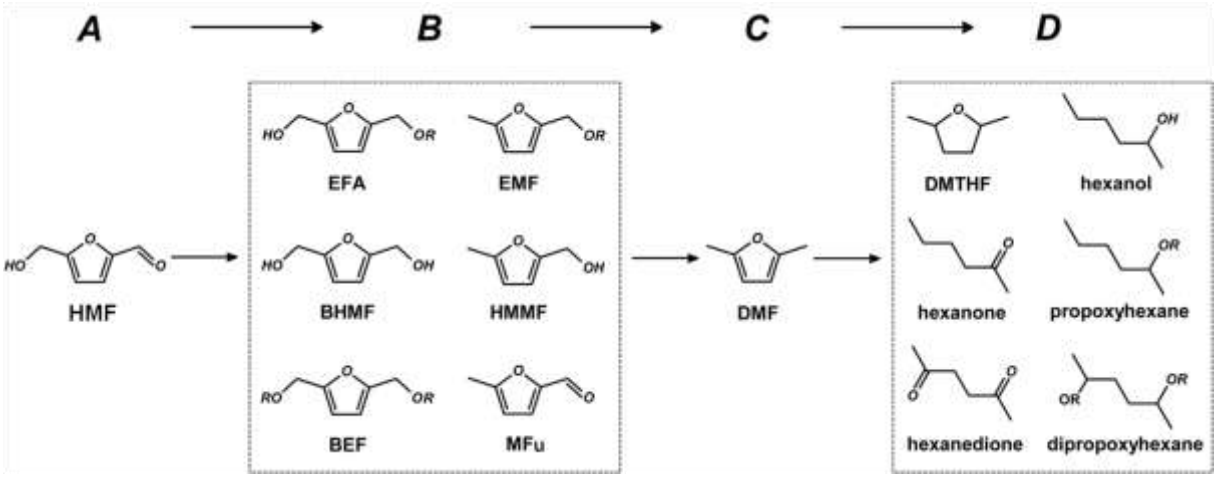

Figure 4.10 reports the conversion and products yield as a function of space time on the NCs-based catalyst prepared in this study. 10 wt% Pt NCs/C catalysts (Figure 4.10a) were much active: even for the shortest space time and at low temperature (120°C), the HMF conversion was greater than 65%. Scheme 4.2 also applies to the reaction of HMF in this case. Initially, partially hydrogenated products, B, were formed in the highest yields, but these declined steadily with increasing space time. DMF yield initially increased, then decreased, providing strong evidence that DMF is an intermediate product in a series reaction. The maximum yield was approximately 41%. Over-hydrogenated compounds, D, only formed at higher space times, indicating that they are not primary products. The fact that their formation follows the consumption of DMF strongly

suggests they are formed from DMF. The HDO of HMF over a traditionally prepared Co/C catalyst has been reported in a previous study(*185*). The products formed as a function of space time were similar to that formed over Pt catalysts. Co itself is not selective to DMF, due to the formation of the over-hydrogenated product 2,5-hexanedione at high space times.

Figure 4.10 Conversion and product distribution for the HDO reaction of HMF over (a) 10 wt% Pt NCs/C, (b) 10 wt% Pt_3Co NCs/C, (c) 10 wt% Pt_3Co_2 NCs/C, as a function of reactor space time. Reaction conditions: 33 bar and 120 ºC. (▼) HMF conversion, (▲) product group B, (●) DMF, (■) product group D.

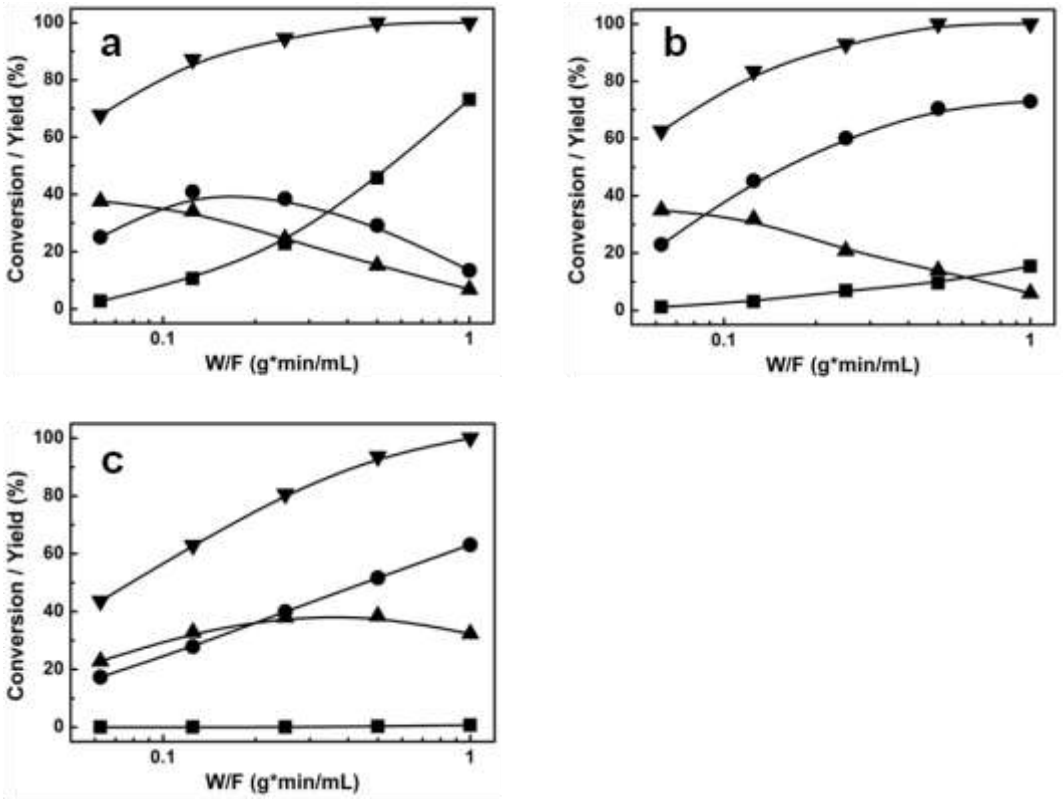

Similar experiments were performed on 10 wt% Pt_3Co NCs/C and 10 wt% Pt_3Co_2 NCs/C catalysts. Data at 120°C and 33 bar are shown in Figure 4.10b and 4.10c. For a given space time, the HMF conversions over the Pt_3Co in Figure 10.4b were slightly lower than that obtained on the pure Pt NCs. However, the initial products were the same partially hydrogenated compounds, B (see Table 4.2), with these again being converted to DMF at a similar rate. However, on the Pt_3Co catalyst, the DMF yield continued to increase, to a value of 75%; and only relatively small quantities of over-hydrogenated compounds, D, were formed at the largest space times. The activity of the Pt_3Co_2 catalyst was noticeably lower than that of the other two samples, and 100% conversion of HMF was achieved only at the highest space time. Because of the lower activity, the DMF yield was

still increasing at the highest space time and the production of D-group compounds was negligible.

A detailed analysis of the partially hydrogenated (B) and over-hydrogenated (D) compounds formed during HDO of HMF over the NCs-based catalysts is given in Table 4.2 and Figure 4.11.

Table 4.2 Yields of partially hydrogenated compounds (group B) for HDO of HMF at 120 °C and 33 bar.

Catalyst	W/F (g min mL^{-1})	MFu	HMMF	BHMF	EMF	EFA	BEF
Pt	0.0625	1.3	0	3.7	3.8	25.4	3.4
	0.25	0	0	2.1	2.7	17.0	2.7
	1	0	0	0	0	6.8	0
Pt_3Co	0.0625	0.8	0	4.8	3.2	23.5	2.6
	0.25	0	1.6	2.1	2.3	11.9	2.9
	1	0	0.8	0	0	5.2	0
Pt_3Co_2	0.0625	3.0	0	2.6	4.0	10.1	3.1
	0.25	2.3	2.4	11.5	3.7	14.2	4.0
	1	1.7	6.3	11.4	3.6	9.2	0

Figure 4.11

Yields of over-hydrogenated compounds (group D) as a function of space time at 33 bar. At 120°C: (a) 10 wt% Pt NCs/C, (b) 10 wt% Pt_3Co NCs/C and (c) 10 wt% Pt_3Co_2 NCs/C. At 160°C: (d) 10 wt% Pt_3Co NCs/C and (e) 10 wt% Pt_3Co_2 NCs/C. (□) DMTHF, (▽) 2-hexanone, 2-hexanol and 2-propoxyhexane, (△) 2,5-hexandione, 2,5-dipropoxyhexane, (◯) hexane, (◁) unidentified.

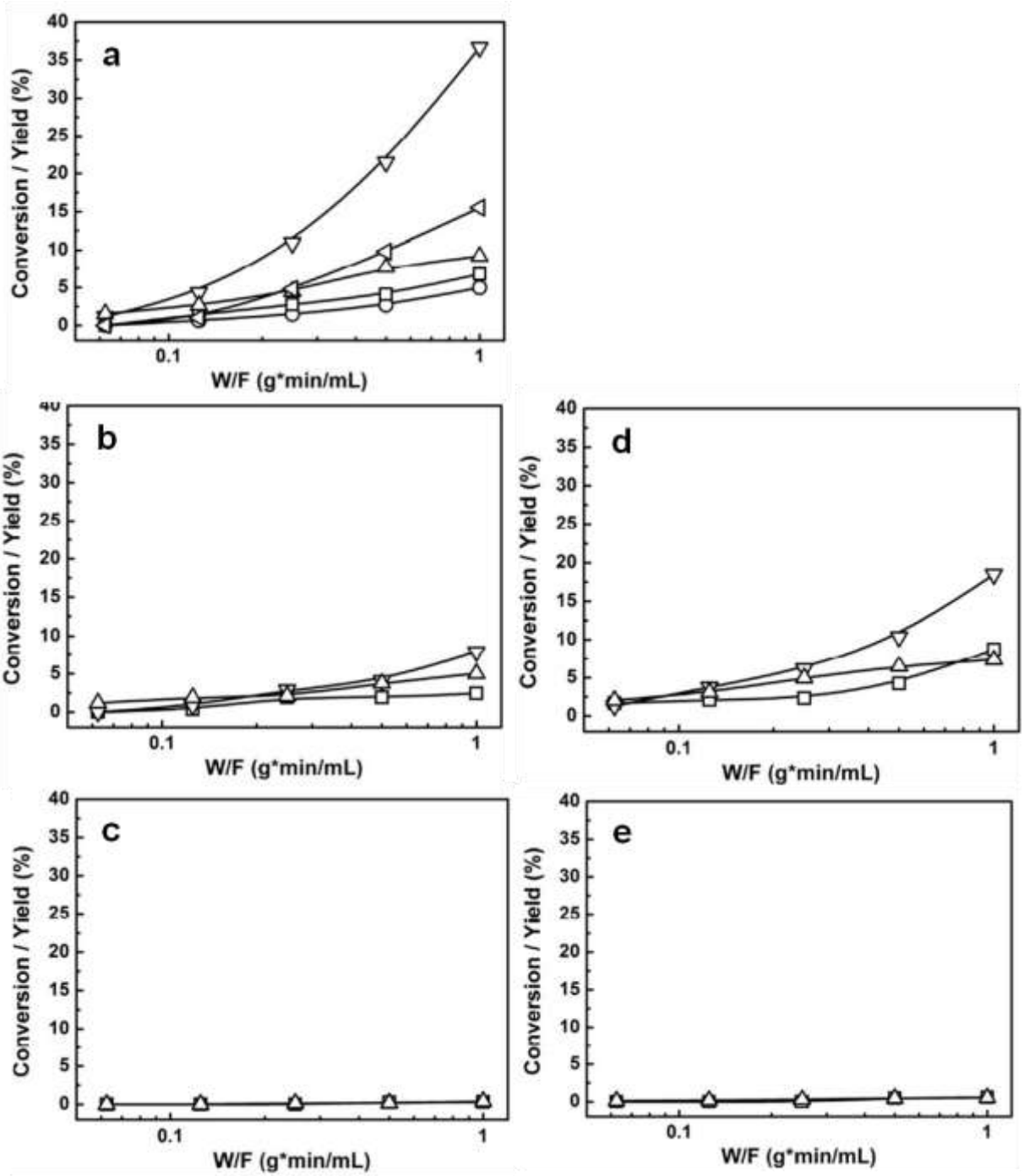

Due to the lower rates observed for the Pt-Co catalysts, additional reaction measurements were performed at 160°C and 33 bar in order determine the evolution of products, with results shown in Figure 4.12. As shown in Figure 4.12a, the HMF conversion was nearly 90% on the Pt_3Co NCs-based catalyst, even at the lowest space time. The B-products again declined steadily with increasing space time but DMF yield went through a maximum of about 75% at this temperature, with over-hydrogenated products being produced from DMF. On the other hand, DMF yields up to 98% were obtained over the Pt_3Co_2 NCs-based catalyst (Figure 4.12b) for the highest space time.

Figure 4.12 Conversion and product distribution for the HDO reaction of HMF over (a) 10 wt% Pt_3Co NCs/C, (b) 10 wt% Pt_3Co_2 NCs/C, as a function of reactor space time. Reaction conditions: 33 bar and 160 ºC.
(▼) HMF conversion, (▲) product group B, (●) DMF, (■) product group D.

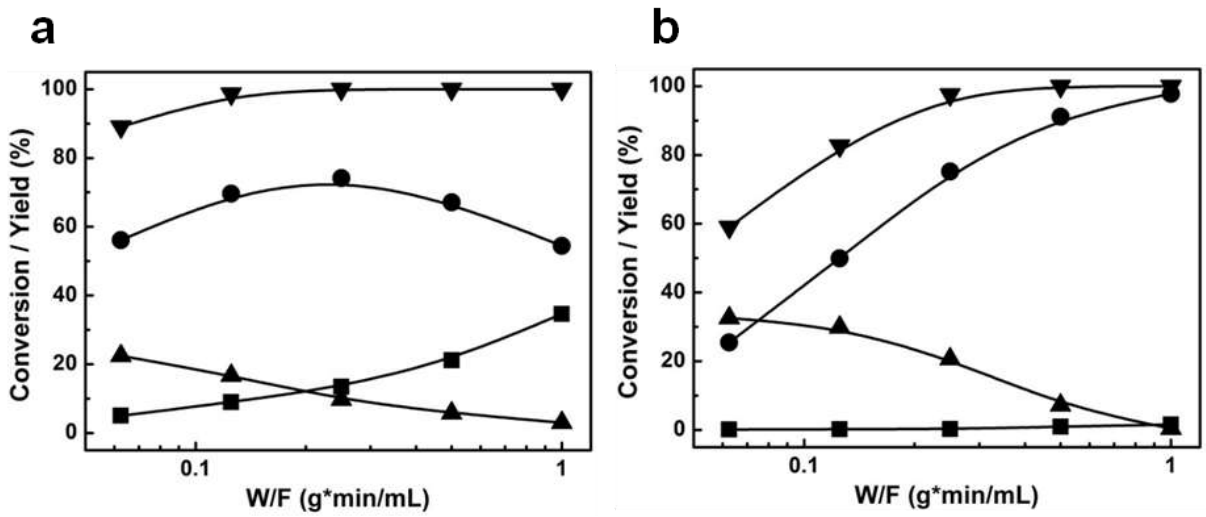

The Pt_3Co_2 sample was also very stable compared to the Pt catalyst. Figure 4.13 shows the HMF conversion and DMF yield for the two catalysts as a function of time at 160°C and a space of 1.0 g min mL^{-1}. The Pt_3Co_2-based catalyst has no observable deactivation or change in selectivity for a period of at least 14 h. By contrast, the Pt-based catalyst deactivated rapidly under the same conditions. It should be noted that Pt/C catalyst was highly active under these conditions, so that the low initial yield is due to the reaction of DMF to over-hydrogenated (D) compounds. The increasing yield with short times results from the lower catalyst activity.

Figure 4.13

Time on stream measurements for HMF hydrodeoxygenation. Reaction conditions: 33 bar, 160 ºC, W/F 1.0 g min mL^{-1}. (■) HMF conversion over 10 wt% Pt_3Co_2 NCs/C, (△) DMF yield over 10 wt% Pt_3Co_2 NCs/C, (●) HMF conversion over 10 wt% Pt NCs/C, (▽) DMF yield over 10 wt% Pt NCs/C.

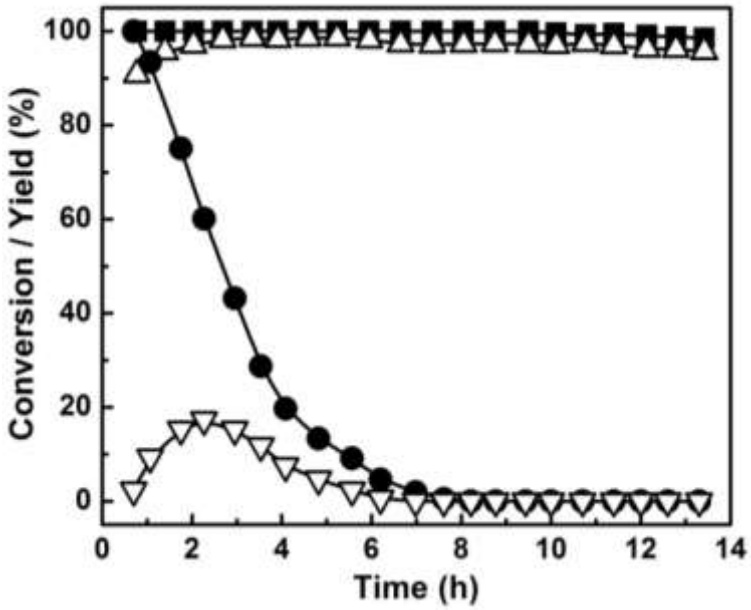

In addition to the stability against coking, the alloy catalyst is also more thermally stable(*204*). Statistical particle size analysis was performed on TEM images for Pt and PtCo catalysts after 5 hours reaction at 160 °C (Figure 4.14). Pt NCs underwent morphological changes, with the average particle size increasing from 2.4 nm to 3.5 nm and a significant size distribution change from 7.3% to 19%. By contrast, Pt_3Co_2 NCs showed almost no morphological change. The average size of the particles were unaffected and the size distribution increased only slightly from 7.3% to 10%.

Figure 4.14 The particle size distribution of (a) Pt and (b) Pt_3Co_2 nanocrystals before and after 5 h of HDO reaction conditions at 160°C.

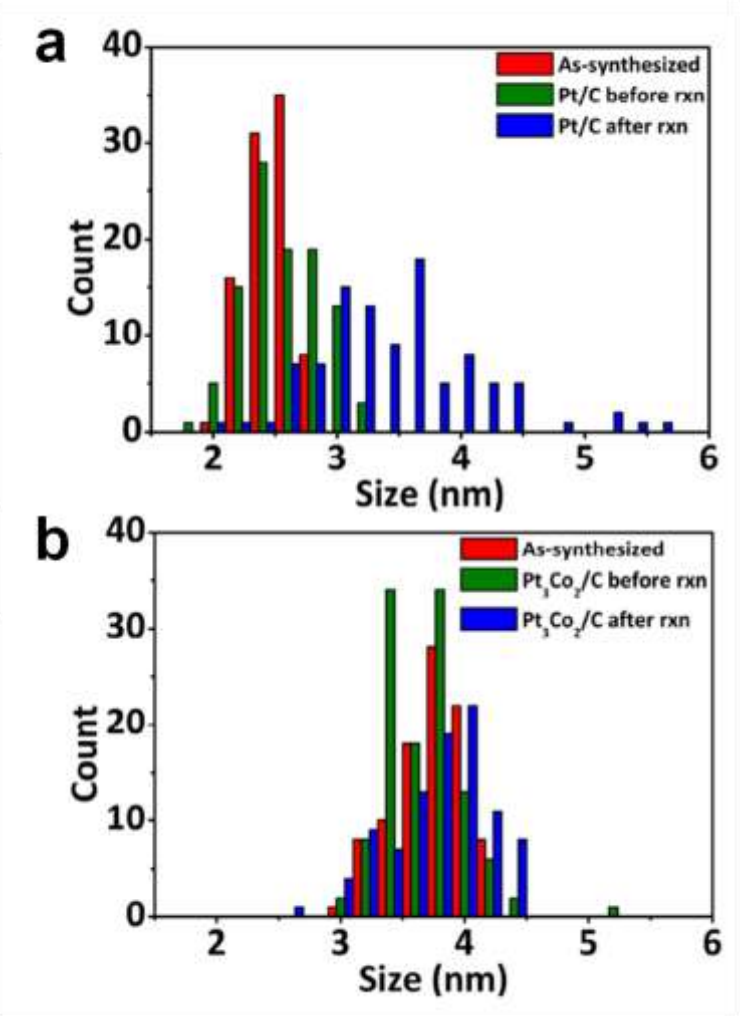

The results in Figure 4.10 and Figure 4.12 indicate that Co alloying with Pt has a modest effect on HDO rates for HMF but strongly suppresses reactions of DMF. To investigate this in more detail, we examined the reaction of DMF on the same three catalysts, with conversions and product distributions shown in Figure 4.15. The reactions were carried out at 33 bar and either 120 °C (for Pt) or 160°C (for the Pt-Co alloys), using 1-propanol solutions with the same DMF molar concentration as that used in the HMF experiments. Since water is formed in the reaction of HMF, these experiments do not perfectly mimic the sequential reaction found in HMF; however, some water was also formed in the DMF reaction measurements by dehydration of alcohols to form dipropyl ether.

Figure 4.15

Conversion and product distribution for the reaction of DMF as a function of space time at 33 bar: (a) 10 wt% Pt NCs/C at 120 ºC; (b) 10 wt% Pt_3Co NCs/C at 160 ºC, (c) 10 wt% Pt_3Co_2 NCs/C at 160 ºC.
(▼) DMF conversion, (□) DMTHF, (▽) 2-hexanone, 2-hexanol and 2-propoxyhexane, (△) 2,5-hexandione, 2,5-dipropoxyhexane, (○) hexane.

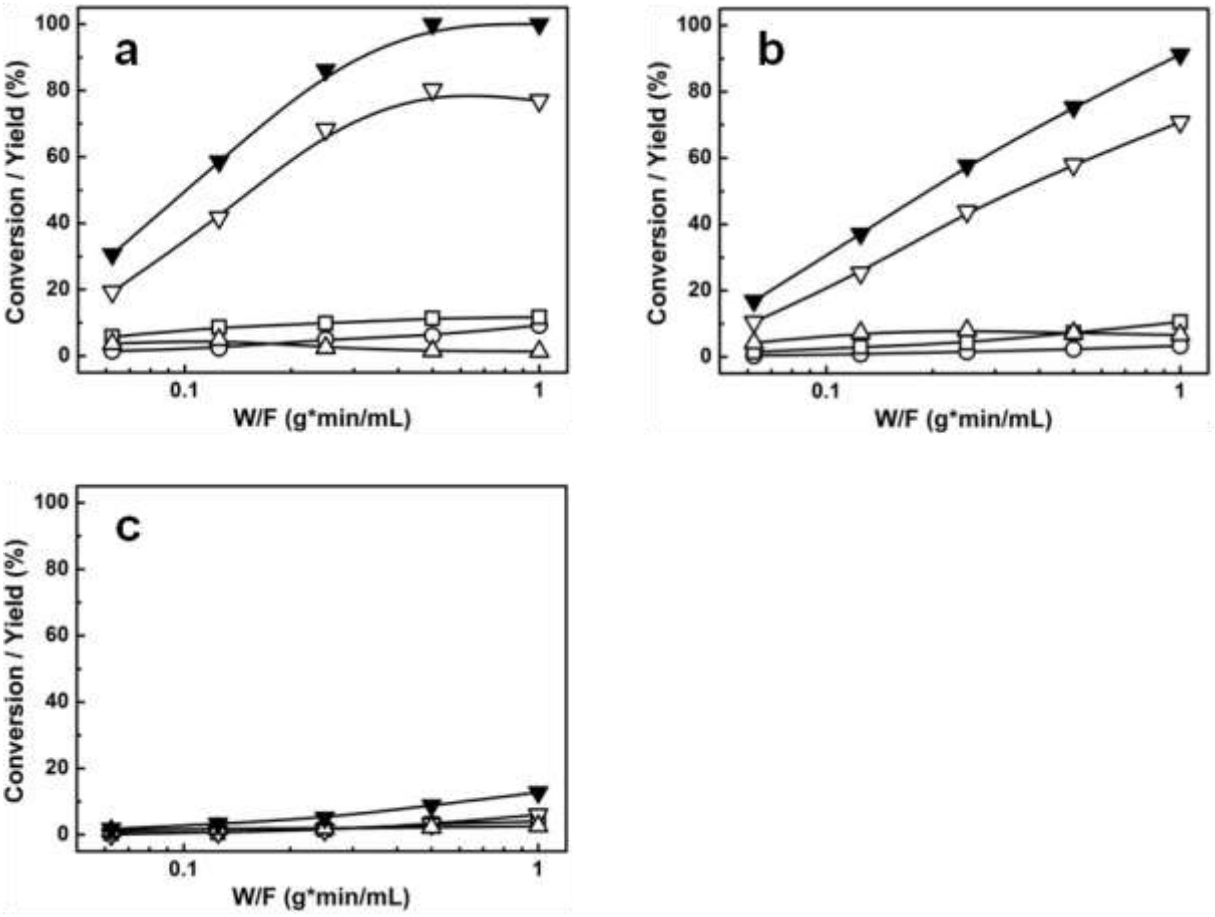

As shown in Figure 4.15a, DMF is converted rapidly on Pt/C, even at 120°C. The main products are the open-ring ketones and ethers, which were also formed at high space times for the reaction of HMF (see Figure 4.11). The reaction of DMF on the Pt-Co catalysts was carried out at 160°C because of their lower activities. Even at this higher temperature, the DMF conversion on the Pt_3Co sample was lower than that observed on the Pt catalyst, although still significant. The products on the Pt_3Co catalyst were essentially the same as the ones observed on Pt. However, the conversion of DMF on the Pt_3Co_2 sample at 160°C, shown in Figure 4.15c, was very low for all space times, reaching a value of only 10% at a space time of 1.0 g min mL^{-1}.

4.3.3 Active Site Structure Investigation

In order to understand the role of Co for high HMF-to-DMF selectivity and elucidate the nature of the active site, a combination of microscopic, spectroscopic, and computational tools were employed, as discussed below. First of all, wide angle X-ray scattering data (Figure 4.7d) show that the (220) peak shifts from 67.6° for Pt NCs to 68.2° and 68.4° for Pt_3Co and Pt_3Co_2, indicating the replacement of Pt by Co in the lattice structure. The lattice constants of the NCs, determined from the position of the (220) peak on the x-ray scattering patterns, are 3.92, 3.87, and 3.87 Å for Pt, Pt_3Co, and Pt_3Co_2 NCs, respectively. Using Vegard's law, the bulk Co fraction in the Pt_3Co and Pt_3Co_2 NCs was estimated to be 13.4 mol.%. The fact that the bulk Co fraction is lower than that of the alloy stoichiometry is an initial indication of Co segregation.

The local environments of the Pt and Co atoms were further investigated using X-Ray Absorption Spectroscopy (XAS). The Pt L_3 near-edge spectra of Pt_3Co_2 samples reduced in H_2 at 250 and 400°C are shown in Figure 4.16a, together with the Co K near-edge spectra (Figure 4.16b). On the Pt edge, the white line and edge positions of the samples coincide with those of the Pt foil for both reduction temperatures, demonstrating that the Pt is fully reduced in all cases. However, the Extended X-Ray Absorption Fine Structure (EXAFS) on the Pt edge suggests that there is surface segregation of Co in the Pt-Co alloy particles, as the Pt:Co ratio in the Pt coordination sphere (3.1 ± 0.6) is greater than the nominal. Considering the fact that the cobalt precursor was injected at 170 °C in the synthesis, it is reasonable that the Pt-Co alloy NCs had cobalt rich shell, because platinum precursor could decompose and nucleate at lower temperature, forming the core of NCs. The fitting parameters for these spectra are reported in Table 4.3. The Co edge EXAFS was not fitted for the sample reduced at 250 °C, as the variables required to completely describe the structure are greater than the number of available independent data points. After reduction at 400 °C, the Pt:Co ratio in the Pt coordination sphere is closer to the nominal (2.1 ± 0.4), consistent with at least partial reverse Co segregation to the bulk. A similar reverse segregation phenomenon has been reported previously for PtNi nanoparticles (*205*).

Figure 4.16 (a) Pt L_3 edge XANES. Pt foil (red), Pt_3Co_2 reduced at 250 ºC (blue) and Pt_3Co_2 reduced at 400 ºC (black). (b) Co K edge XANES. Co foil standard (black), CoO standard (red), Pt_3Co_2 reduced at 250 ºC (yellow) and Pt_3Co_2 reduced at 400 ºC (green).

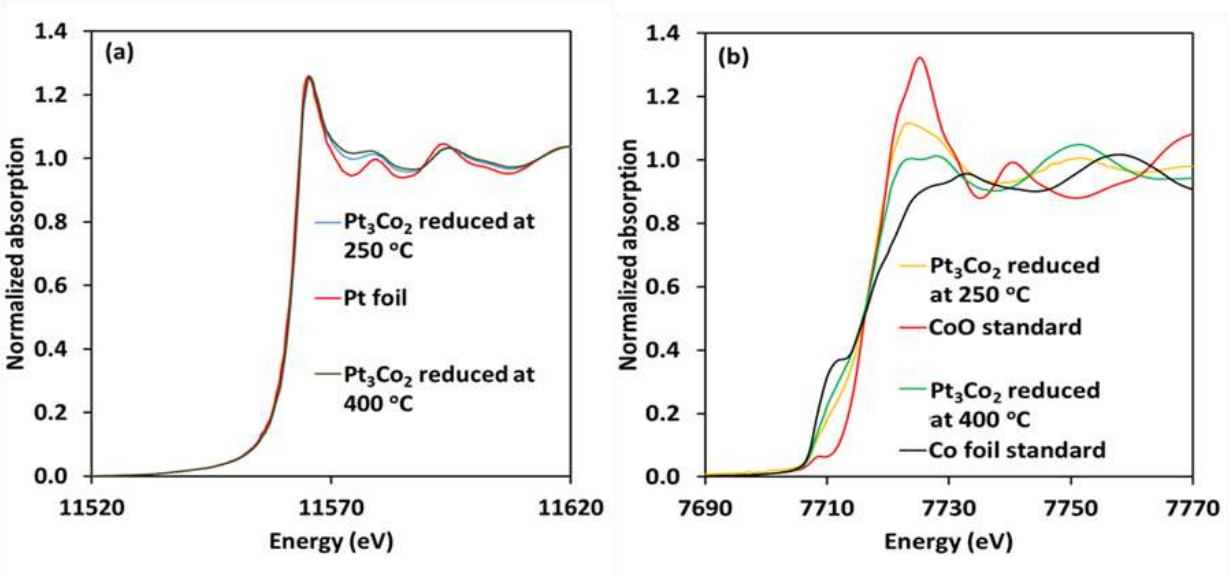

Table 4.3 Fitting of the EXAFS Pt and Co spectra. All distances are in Angstroms.

Pt edge	Pt_3Co_2 400	Pt_3Co_2 250	Co edge	Pt_3Co_2 400
Pt-Pt distance	2.730 ± 0.003	2.743 ± 0.002	*Co-Co distance*	2.554 ± 0.013
Pt-Co distance	2.645 ± 0.005	2.646 ± 0.006	*Co-Pt distance*	2.645
Pt-Pt CN	8.02 ± 0.62	8.98 ± 0.57	*Co-Co CN*	7.69 ± 1.93
Pt-Co CN	3.84 ± 0.47	2.88 ± 0.44	*Co-Pt CN*	6.27 ± 0.98
R^2	0.002	0.001	R^2	0.007
ΔE_0(eV)	6.47 ± 0.33	6.32 ± 0.30	ΔE_0(eV)	-7.60 ± 0.93
σ^2 Pt-Pt ($x10^4$)	65 ± 4	85 ± 12	σ^2 Co-Co ($x10^4$)	171 ± 31
σ^2 Pt-Co ($x10^4$)	90 ± 10	54 ± 3	σ^2 Co-Pt ($x10^4$)	90

The X-Ray Absorption Near Edge Spectra (XANES) of the Co K edge, reported in Figure 4.16b, provides further information on the nature of the alloy NCs. First, the spectra indicate that Co remains partially oxidized, even after reduction at 400°C. Using a linear combination of spectra from CoO and Co standards to fit the results for the alloy catalyst, the average Co oxidation states after reduction at 250°C and 400 °C were 1.2 (60% CoO) and 0.72 (36% CoO), respectively. Surface oxygen is known to induce Co surface segregation in a Pt-Co alloy (*206*). In turn, Co forms a surface monolayer oxide with properties distinct from those of the bulk CoO (*207*). As step sites constitute ca. 30% of all surface sites for 3-4 nm nanoparticles (*208*) and tend to stay more oxidized than terraces (*209*), 30% of surface sites were assumed to be composed of Co in the +2 oxidation state (*210*). Following an analogous Fe_3O_2/Pt(111) structure observed using STM (*211*), the rest of the monolayer surface oxide was assumed to be Co_3O_2 with a honeycomb structure on a Pt-Co metallic core as a nanoparticle model (Figure 4.17a).

Figure 4.17 (a) Pt_3Co_2 nanocrystal model involving an alloy core (88% Pt, 12% Co based on XRD) covered with a Co_3O_2 surface oxide monolayer with a honeycomb structure; (b) and (c) correspond to Pt and Pt_3Co NC models.

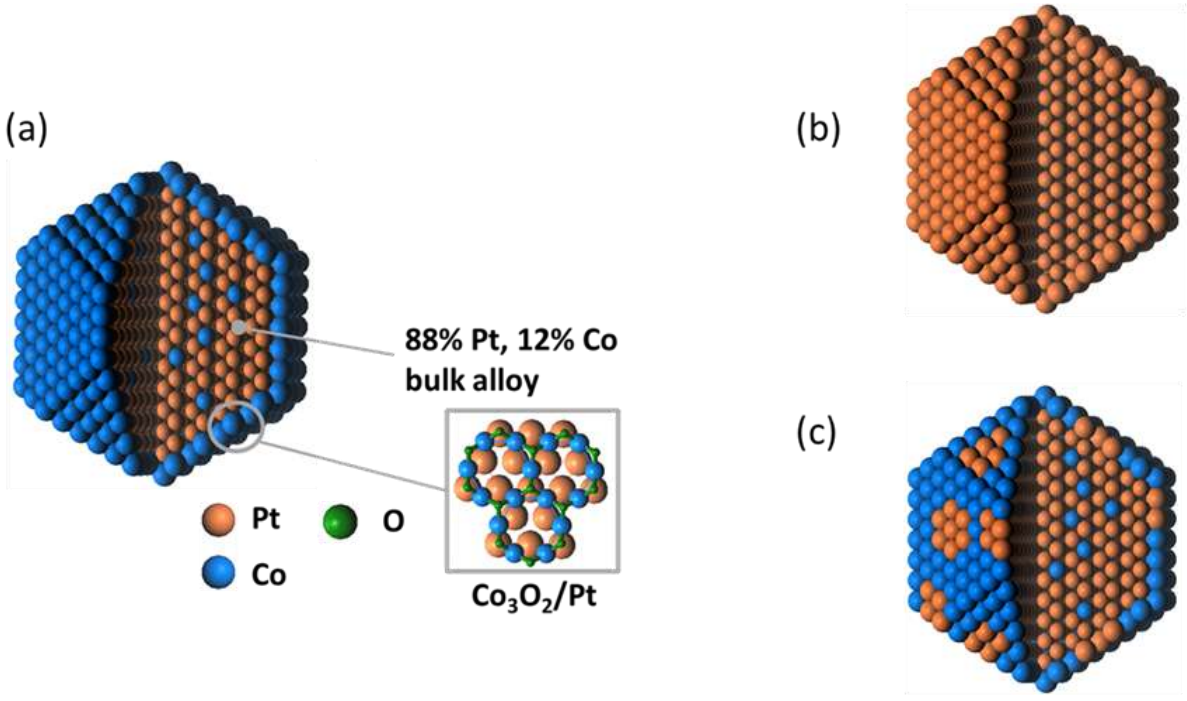

Table 4.4 compares XAS/XRD results with geometric estimates of the alloy core/oxide shell spherical nanoparticle model. Overall, the model exhibits excellent agreement with the experimental data, given the approximations invoked. An average Co oxidation state of 1.18 was

predicted, close to the experimental estimated value of 1.20. The low Co oxidation state is consistent with an O:Co atomic ratio of less than 1 on the majority of surface sites. In contrast, a previously observed surface oxide with CoO stoichiometry (*207*) would yield an average oxidation state >1.5. The predicted Co content in the bulk alloy (14.4 mol%) is close to the Vegard's law estimation from XRD (13.4 mol%). The experimental and geometric Pt-Co and Pt-Pt CNs agree well. The XAS data demonstrate that Pt_3Co_2 NCs, reduced at 250°C, consist of a Pt-rich core with the majority of Co segregated to the surface, forming a CoO_x surface oxide shell. The Co_3O_2 honeycomb monolayer as a dominant surface structure is consistent with XAS results.

Table 4.4 Average coordination numbers and Co oxidation states for Pt_3Co_2 NCs reduced at 250°C, determined by X-ray absorption spectroscopy and estimated using a spherical core/shell NC model with planes covered by a Co_3O_2 surface oxide monolayer (70%) and step sites covered by CoO (30%). CN stands for "coordination number".

	XAS/XRD data	Geometric Model
Co oxidation state	1.20[a]	1.18
Pt-Co CN	2.88[a] ± 0.44	2.92
Pt-Pt CN	8.98[a] ± 0.57	8.91
Co content in the bulk alloy, %	13.4[b]	14.4

[a] XAS data regression
[b] XRD analysis (Vegard's law)

Further evidence for Co_3O_2 surface oxide formation comes from CO chemisorption measurements on NCs supported on γ-Al_2O_3, shown in Table 4.5.

Table 4.5 Metal dispersions of alumina supported catalysts after 250 °C and 400 °C reduction, assuming CO/Pt=1 and no CO adsorption on Co atoms.

Sample	Dispersion (250°C reduction)	Dispersion (400°C reduction)
1 wt% Pt NCs/Al_2O_3	19.4%	12.6%
1 wt% Pt_3Co_2 NCs/Al_2O_3	0%	8.8%

CO chemisorption experiments were performed on alumina supported NCs in order to avoid sorption problems related to active carbon supports (*212*). Before the chemisorption experiment, the samples were evacuated at 400°C and reduced for 30 minutes at 250°C or 400°C in 200 Torr of H_2. In determining the NCs dispersion, an adsorption stoichiometry of one CO molecule per surface Pt was assumed(*213*). Chemisorption of CO on Co was not included in the calculation of the dispersion because control experiments on Co/Al_2O_3 catalysts prepared by impregnation method did not show any CO adsorption. After reduction at 250°C, CO adsorption on the Pt_3Co_2 NCs is negligible, consistently with the Pt atoms being covered. After 400°C reduction, CO chemisorption is comparable to what was observed with Pt NCs, due to reverse segregation of Co to the bulk. DFT results indicate that CO interacts weakly with Co_3O_2/Pt(111) compared to Pt(111) (ca -0.7 vs. ~-2 eV binding energy(*211*), respectively), consistent with the lack of CO adsorption. A similar in magnitude CO binding energy was correlated with no CO adsorption in XPS measurements on Fe_3O_2/Pt(111) honeycomb structure (*211*). The importance of a Co_3O_2 overlayer structure is further supported from DFT calculations, discussed next.

4.3.4 Theoretical Insights into the Reaction Mechanism, Catalyst Composition Effects, and Stability

DFT calculations[9] were performed in order to understand the mechanism of the HDO reaction, catalyst stability issues, and the differences among the three catalysts (Pt, Pt_3Co, and Pt_3Co_2). Regarding the reaction mechanism on the Pt_3Co_2 catalyst, the calculations showed that the Co_3O_2 honeycomb monolayer supported on the Pt rich core is capable of catalyzing key reaction steps involved in the HMF to DMF conversion. The overall reaction is assumed to proceed via the following steps: 1) H_2 dissociation, 2) C=O hydrogenation, and 3) selective HDO with concomitant oxygen removal from the surface in the form of water. The H_2 dissociation step can occur via several homolytic and heterolytic dissociation paths (*210*), but the calculations indicate that the homolytic splitting of a weakly physisorbed H_2 molecule (-0.1 eV binding energy) over a single Co atom is most energetically favorable (a 0.7 eV reaction barrier). The final state (0.3 eV more stable than gaseous H_2) entails both H atoms bound to Co and Pt atoms in bridging configurations.

[9] Calculations have been carried out under the generalized gradient approximation using VASP software (*288–290*). Kohn-Sham *eigenstates* have been expanded in a plane wave basis set with a kinetic energy cutoff of 400 eV. Sampling of the first Brillouin zone has been carried out according to the Monkhurst-Pack (*291*) 3x3x1 k-point mesh. The initial magnetic moment of Co atoms has been set to 2.0 Bohr-magnetons. Exchange, correlation, and dispersion effects have been approximated with a PBE-D3 (*292*, *293*) functional. Threshold value for maximum atomic forces has been set to 0.05 eV $Å^{-1}$. Transition states have been identified via a climbing-image nudged elastic band (CINEB) and/or a dimer (*294–297*) method with the forces' tolerance set to 0.1 eV $Å^{-1}$. A honeycomb Co_3O_2 on a Pt-rich metallic core has been modeled as a Co_3O_2/Pt(111) surface using a (4x4) supercell with a honeycomb Co_3O_2 structure placed on top of three Pt layers (bottom two were fixed). A finite difference method was used to calculate selected vibrational frequencies. DFT energies in a vacuum are reported, unless otherwise stated.

Prior to the C=O hydrogenation step, HMF weakly adsorbs on the surface (-0.8 eV BE); hydrogenation of the C=O carbonyl group exhibits a low reaction barrier when it is weakly bound to the surface (*214*, *215*). Specifically, a concerted addition of two H atoms to HMF occurs with a 0.8 eV barrier, yielding BHMF. The overall hydrogenation is exothermic (reaction energy of -0.6 eV). BHMF can either desorb (0.9 eV desorption energy) or undergo HDO, ultimately forming DMF.

The subsequent HDO mechanism of BHMF on the Pt-rich particle with Co_3O_2 coating is radical in nature, and is depicted in Figure 4.18. A similar mechanism was proposed in the HDO of furfural to form 2-methylfuran on a Ru/RuO_2 catalyst, consistently with a range of experimental and computational data (*210*). BHMF undergoes C-O bond scission on a honeycomb edge site consisting of two Co atoms, forming a loosely bound radical and an OH group, with a reaction energy of +0.9 eV and a barrier of 1.2 eV (Figure 4.18, steps 1-2). A hydrogen atom transfers from the OH to the radical, yielding HMMF and a chemisorbed oxygen atom (Figure 4.18, step 3-4). C-O scission occurs similarly on the second hydroxymethyl group (not shown), forming DMF as the final product. The chemisorbed O atom (+1.7 eV binding energy with respect to H_2 and H_2O) reacts rapidly with H_2 (a -1.2 eV exothermic dissociative adsorption with a 0.3 eV barrier) to form co-adsorbed OH and H that subsequently recombine with a 0.2 eV barrier (-0.9 eV reaction energy) to form water(Figure 4.18, steps 5-6). Finally, water desorbs with a +0.4 eV energy to complete the catalytic cycle.

HMF, BHMF, HMMF, and DMF weakly interact with the Co_3O_2 surface (~ -0.8 eV BE, dominated by dispersion forces (*216*), as opposed to chemisorption on metal atoms with BE of the order of -2 eV(*217*)), largely retaining a gaseous-like molecular geometry(*210*). The absence of covalent bonding of the ring with the metal surface is key to rationalizing the high selectivity of the catalyst, because opening of the furan ring and decarbonylation require strong chemisorption of the ring in a flat geometry, with partial $sp^2 \rightarrow sp^3$ re-hybridization of ring carbon atoms (*184*, *218*–*222*). Lack of covalent bonding between the ring with the Co_3O_2 oxide protects the ring from further side reactions and explains the low reactivity of DMF. The Co_3O_2 surface layer is capable of catalyzing C-O bond hydrogenolysis in HMF that leads to selective production of DMF.

Figure 4.18 Reaction mechanism of BHMF hydrodeoxygenation to HMMF on the Co_3O_2/Pt(111) surface. DFT reaction barriers (energies) are given in eV. The inset depicts a portion of a Co_3O_2/Pt(111) surface. Two Co atoms participating in C-O bond activation are encircled with a white ellipsoid.

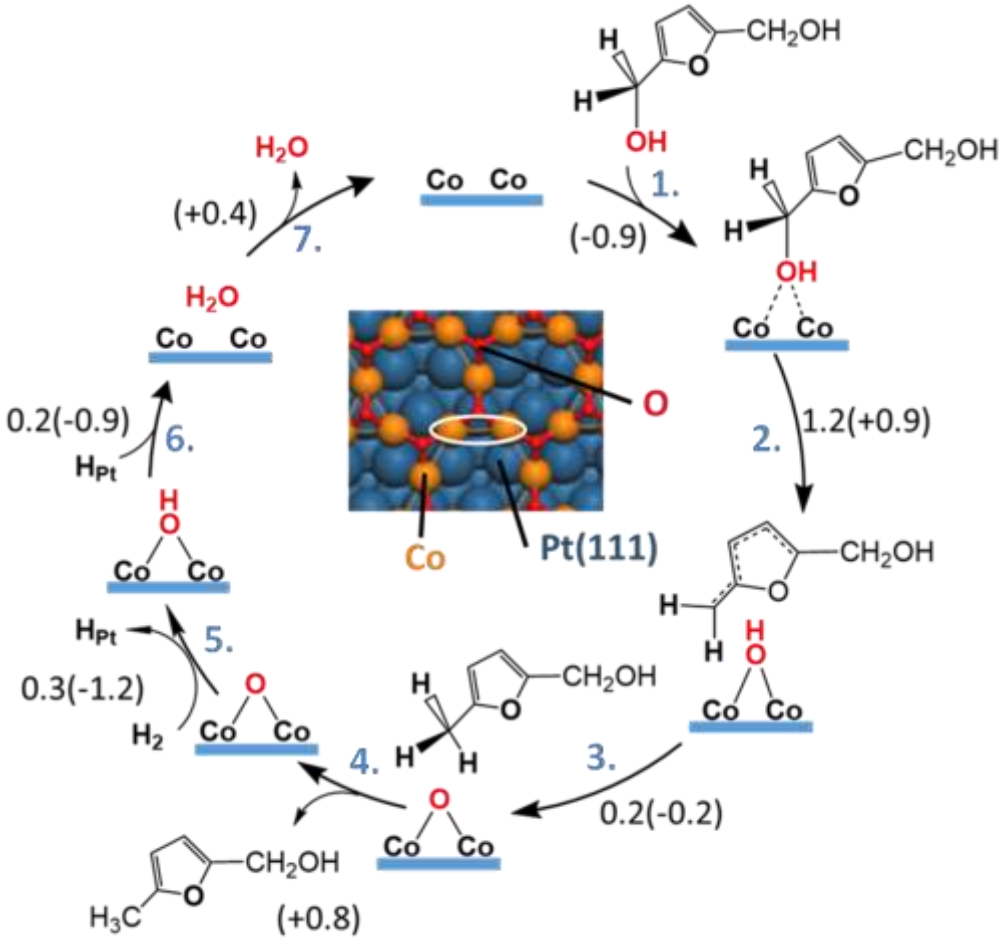

In order to assess the catalyst stability at a H_2-rich environment, the rate of initiation of Co_3O_2 reduction via vacancy formation was calculated (*210*). Under experimental HDO conditions (160°C, 33 bar H_2), the vacancy formation rate is a factor of 2 lower than under *in situ* XAS conditions (250°C, 1 bar H_2). Furthermore, the vacancy, once formed, is easily oxidized by BHMF-to-HMMF reactions. This analysis provides a rationalization as to why the Co_3O_2 surface oxide is stable in a reducing reaction environment.

In contrast to the highly selective, oxide-covered Pt_3Co_2 catalyst, Pt carries out facile hydrogenation of the C=O group to BHMF, but dehydroxylates BHMF to form DMF slowly (*210*). Furthermore, the DMF ring interacts strongly with Pt, promoting ring hydrogenation and ring opening with barriers which are lower than that of the dehydroxylation reaction (*210*). The

computed barriers for HDO of HMF are comparable to the barriers for ring hydrogenation and ring opening of DMF, consistent with the observation that selectivity to DMF is modest.

Pt_3Co NCs exhibit catalytic properties intermediate between Pt and Pt_3Co_2. Unlike the Pt_3Co_2 NCs, there are not enough Co atoms to completely cover the surface with an oxide monolayer. In this catalyst, the surface is predicted to consist of 1/2 Co oxide and ~1/2 Pt atoms. We propose that this difference in structure exposes Pt patches on the surface (Figure 4.17b). The presence of Pt sites at the surface leads to the partial non-selectivity of the Pt_3Co catalyst.

4.3.5 Discussion

The development of better catalysts for HDO of HMF requires an understanding of the reaction mechanism. First, it is important to recognize that the reaction is sequential (*41*, *185*). The poor selectivity that is observed with many metals is due to the fact that they further catalyze reactions of DMF, the desired product. While it is required that a catalyst has good activity for HDO of HMF, a selective catalyst must also be a poor catalyst for reactions of DMF. The sequential nature of the reaction also makes it essential that no part of the catalyst is nonselective. For reactions in which both the desired and side products form in parallel, having a small percentage of the catalyst surface showing a lower selectivity will not dramatically change the overall selectivity. With a sequential reaction, the nonselective part of the catalyst can have a much more dramatic effect. This has important consequences for alloy catalysts. While the catalyst based on Pt_3Co_2 NCs has the necessary properties to achieve a very high selectivity, alloy catalysts prepared by conventional impregnation methods will not be so compositionally uniform. Both Pt and Co are individually nonselective because they are active for reactions of DMF, so that any metal in the catalyst which is not in the form of an alloy will be nonselective. Indeed, a Pt_3Co_2 catalyst prepared by incipient wetness of the metal salts showed a maximum selectivity of less than 80%(*210*). In this context, it is interesting to consider the work from Schüth and co-workers(*188*), who first reported extremely high selectivity for HDO of HMF with PtCo alloys. In their case, the highest selectivity were achieved when the metal particles were encapsulated in porous carbon spheres. We suggest that those carbon spheres were important for achieving a high compositional uniformity in the particles.

Control of the metal composition is essential in order to achieve good HDO selectivity. From the HDO studies, we learned that Pt_3Co was not as selective as Pt_3Co_2. The reason for this is the difference in particle surface structure. Pt_3Co does not have enough Co atoms to completely cover the surface. The incomplete coverage of Co oxide leads to the presence of uncovered Pt sites, and therefore causes partial non-selectivity of the Pt_3Co catalyst. While it may be possible to increase the Co:Pt ratio further, a catalyst with excess of Co is likely to be unselective since monometallic Co catalysts are unselective (*185*).

Catalyst stability is equally important to activity and the present results suggest that there is a direct correlation between stability and selectivity. The most serious and rapid deactivation in the experiments was due to coking which is caused by further reaction of over-hydrogenated products, such as 2,5-hexanedione. The Pt-Co alloy catalyst also seems to be more tolerant against sintering, possibly as a result of the core-shell structure.

4.3.6 Conclusions

High selectivity of DMF from liquid-phase HDO of HMF with H_2 was achieved over a well-controlled Pt-Co /C catalyst. Particularly, over Pt_3Co_2 nanocrystal-based catalyst, 98% of DMF yield was obtained with the optimized reaction temperature and space time. Recognizing the sequential nature of the HMF HDO reaction is the key for catalyst-development strategies. Noble metals interact strongly with the furan ring to promote side reactions. The fundamental principle for the superior performance of Pt_3Co_2 is that the bimetallic alloy forms a monolayer oxide on the surface of the metallic core that interacts weakly with the furan ring to prevent over-hydrogenation and ring opening of DMF to secondary by-products while forming active sites to carry out the HDO process. In this regard, composition control is crucial to cover the entire surface with an oxide layer and avoid exposed metallic patches that could promote side reactions. In the following sections, other metallic alloys will be studied in the HDO of HMF, in order to get further insights in the factors controlling selectivity to DMF.

4.4 Base Metal-Pt Alloys for HDO of HMF

4.4.1 Introduction

There is considerable evidence that bimetallic catalysts can be more selective in HDO reactions than their monometallic counterparts. For example, in the gas-phase reaction of furfural, Ni-Fe catalysts were found to exhibit good selectivity to methylfuran under conditions which resulted in the decarbonylation product, furan, over monometallic Ni catalysts (*38*). As discussed in the previous section, Pt-Co nanocrystals (NCs) exhibited much better selectivity and stability than the monometallic catalysts in the HDO reaction of HMF(*210*). The high selectivity of the Pt-Co catalysts resulted from the fact that DMF is not reactive over the bimetallic catalyst.

It is not entirely clear why the bimetallic catalysts are more selective for HDO and the reasons may vary with the particular alloy or reactor conditions. Several studies have argued that high selectivity is due to the oxophilicity of the secondary metal (*38*, *223–225*). For example, Resasco and coworkers (*38*) observed that NiFe catalysts showed superior selectivity compared to Ni for the reaction of furfural to methyl furan. Their theoretical calculations indicated that the oxophilic nature of Fe stabilizes the η^2(C,O) configuration of the aldehyde carbonyl, weakening the C-O bond and suppressing the formation of acyl intermediates that undergo decarbonylation (*38*). Similarly, for Pt-Co bimetallic catalysts studied in the previous section, Co tends to form a CoO_x shell on a Pt-rich core and this oxide layer prevents interactions between the Pt and the furan ring, enhancing DMF yields from HDO of HMF (*210*).

However, high selectivity has also been reported for HDO reactions over Pd-Cu alloys, for which an oxide overlayer is not expected (*226*). Although Cu is not oxophilic, DFT calculations suggested that Cu atoms at the surface repel the aromatic furan ring (*227*), causing furfural to preferentially adsorb in an η^1(O)-aldehyde configuration via the carbonyl oxygen. Such an orientation of the furan ring prevents side reactions on the ring itself (*38*, *226*, *227*).

In the present section, the catalytic properties of carbon-supported nanocrystalline Pt-Ni, Pt-Zn, and Pt-Cu alloys will be studied, to determine whether Pt-Co is unique among the Pt alloys in providing high selectivity for HDO of HMF. Solvothermal methods (see Section 4.3.1) were employed in order to produce NCs having homogeneous and controlled shape, dimension and composition and to investigate the optimal compositions for selective alloy catalysts. While Ni is oxophilic and catalytically similar to Co, Zn and Cu have properties that contrast sharply with that of Co and provide a test for the properties required for high selectivity to DMF (>95%). Surprisingly, each of the alloys exhibited superior selectivity compared to the monometallic catalysts.

4.4.2 Catalysts Synthesis and Characterization

The following chemicals were used in the synthesis of the investigated NCs: nickel (II) acetate tetrahydrate ($Ni(ac)_2{\cdot}4H_2O$, Sigma-Aldrich, 98 %), platinum (II) acetylacetonate ($Pt(acac)_2$, Acros, 98%), nickel (II) acetylacetonate ($Ni(acac)_2$, Acros Organics, 96 %), copper (II) acetylacetonate ($Cu(acac)_2$, Sigma-Aldrich, ≥99.9 %), zinc (II) acetylacetonate ($Zn(acac)_2$, Acros Organics, 25 % Zn), 1,2-hexadecanediol (HDD, Sigma-Aldrich, 90 %), trioctylamine (TOA, Acros Organics, 97 %), oleylamine (OAm, Sigma-Aldrich, 70 %), oleic acid (OAc, Sigma-Aldrich, 90 %), and trioctylphosphine (TOP, Sigma-Aldrich, 97 %), borane, *tert*-butylamine complex, (BTB, Strem Chemicals, 97 %), diphenyl ether (DPE, Sigma-Aldrich, 99 %) and 1,2-dichlorobenzene (DCB, Acros Organics, 99 %). Nickel(II) nitrate hexahydrate ($Ni(NO_3)_2{\cdot}6H_2O$, Alfa Aesar, 98%), Zinc(II) nitrate hexahydrate ($Zn(NO_3)_2{\cdot}6H_2O$, Alfa Aesar, 99%), Copper(II) nitrate trihydrate ($Cu(NO_3)_2{\cdot}3H_2O$, Alfa Aesar, 98%), and Cobalt(II) nitrate hexahydrate ($Co(NO_3)_2{\cdot}6H_2O$, Aldrich, 99%).

Pt_6Ni and PtNi NCs were synthesized using a scaled-up method reported previously (*228*). For the Pt_6Ni NCs, $Ni(ac)_2{\cdot}4H_2O$ (0.33 mmol) and HDD (1.15 mmol) were dissolved in a solution of DPE (40 mL), OAm (0.8 mL), and OAc (0.8 mL). The reaction mixture was kept at 80 °C for 30 min under vacuum and then heated to 200 °C under a nitrogen atmosphere. $Pt(acac)_2$ (0.67 mmol), dissolved in DCB (2.4 mL), was injected into this mixture at 200 °C. The resulting solution was kept at 200 °C for 1 h before cooling to room temperature. The resulting NCs were then purified by precipitation with ethanol and centrifugation at 8000 rpm for 5 min. The precipitate was washed twice with hexane/ethanol (1:3) mixtures before the final NCs were dispersed in hexane. The same procedure was used to synthesize PtNi NCs, except that the amounts of $Ni(ac)_2{\cdot}4H_2O$ (2 mmol) and OAc (1.0 mL) were adjusted. Also, after the washing steps, the PtNi NCs were re-dispersed in hexane and size-selective precipitation was performed (*229*).

To synthesize Pt_3Ni NCs, $Ni(acac)_2$ (0.4 mmol) and $Pt(acac)_2$ (0.4 mmol) were dissolved in a solution of TOA (40 mL), OAm (5.44 mL), OAc (1.28 mL), and TOP (0.45 mL). The reaction mixture was kept under vacuum at 70 °C for 30 min, then heated to 330 °C under a N_2 atmosphere. After 30 min, the reaction mixture was cooled to room temperature and purified by precipitation with a mixture of isopropanol and ethanol. After being centrifuged at 8000 rpm for 2 min, the precipitate was washed twice with hexane/ethanol (1:3) mixtures. Finally, the NCs were dispersed in hexane.

PtCu and Pt_2Zn NCs were synthesized by modifying a previously reported method (*202*). For PtCu NCs, $Pt(acac)_2$ (0.4 mmol), $Cu(acac)_2$ (0.4 mmol), and BTB (1.1 mmol) were dissolved in OAm (20 mL). The reaction mixture was kept under vacuum at 80 °C for 30 min and then heated to 300 °C at a rate of 5 °C min^{-1}. After 1 h, the reaction mixture was cooled to room temperature. Purification of the NCs was achieved by addition of isopropanol, followed by centrifugation at 8000

rpm for 2 min. The precipitate was washed three times with hexane/ethanol (1:3) mixtures and the final NCs were dispersed in hexane. For Pt_2Zn NCs, $Pt(acac)_2$ (0.5 mmol), $Zn(acac)_2$ (0.5 mmol) and BTB (1.1 mmol) were dissolved in OAm (20 mL). The reaction conditions and purification steps were the same as those for PtCu NCs synthesis.

To prepare the carbon-supported catalysts from the NCs, the NCs, dispersed in hexane, were mixed with carbon powder (Cabot, Vulcan XC72R) to a loading of 10 wt% metal. After sonication for 15 min, the solution was centrifuged at 6000 rpm for 1 min. The supernatant was removed and the precipitate was washed twice with isopropanol, followed by centrifugation. After drying each sample in a vacuum oven overnight at 50 °C, the samples were first treated with an O_2 plasma cleaner (18 W, Harrick Plasma) for 15 min, then transferred for 1 min into a muffle furnace that had been preheated to 500 °C (*40*), as discussed in Section 4.3.1.

Reference 10 wt% Ni/C, Co/C, Cu/C and Zn/C catalyst were prepared by impregnation, using a previously reported procedure (*185*). The Ni, Zn, Cu and Co precursors were $Ni(NO_3)_2{\cdot}6H_2O$, $Zn(NO_3)_2{\cdot}6H_2O$, $Cu(NO_3)_2{\cdot}3H_2O$, and $Co(NO_3)_2{\cdot}6H_2O$, respectively. Each metal precursor was firstly dissolved in a water/ethanol (5:1) solution and then mixed with carbon black (Vulcan XC-72R). After drying the catalyst at room temperature, the resulting powder was heated in flowing He to 500 °C for 6 h, using a heating ramp of 3 °C min^{-1}. The dried powders were reduced by flowing a 5% H_2/He mixture over the catalysts at 60 mLmin^{-1} while ramping the temperature at 2 °C min^{-1} to 400 °C, followed by heating to 500 °C with heating ramp of 1 °C min^{-1}. The catalysts were then held at this temperature for 2 h.

Nearly monodisperse, Pt-based alloyed NCs with various compositions were synthesized by solvothermal synthesis, which enabled us to investigate the composition dependent catalytic behavior of the bimetallic NCs. TEM images of the Pt_6Ni, Pt_3Ni and PtNi NCs are shown in Figure 4.19a-c and indicate that, in each case, the particles are uniform and spherical in shape. Based on the small-angle X-ray scattering (SAXS) data fitted to Rayleigh function (Figure 4.19d), the average sizes and size distributions of the Pt_6Ni, Pt_3Ni, and PtNi NCs were 3.0±0.4, 3.0±0.6 and 6.0±0.8 nm, respectively. As shown in Figure 4.19e, the XRD patterns for each of the NCs showed a face-centered cubic (fcc) crystal structure, and shifts to higher angles in the peaks at 2θ were observed for Pt_6Ni and PtNi NCs, compared with the pure Pt NCs. This results from a contraction of the lattice based on the Vegard's law (*230*) and is a good indication that the NCs are well-mixed bimetallic alloys. In the case of Pt_3Ni NCs, the only observed 2θ peak corresponds to the (111) plane. The absence of additional peaks suggests either polycrystallinity or the presence of a high concentration of defects, as is often seen with NC systems (*231*).

Figure 4.19 The TEM images of (a) Pt_6Ni, (b) Pt_3Ni and (c) PtNi NCs, the corresponding (d) SAXS patterns and (e) XRD patterns. Inset in (a) shows the HRTEM image of Pt_6Ni NCs. The black lines in (d) represent the simulated fits for the size of the catalyst.

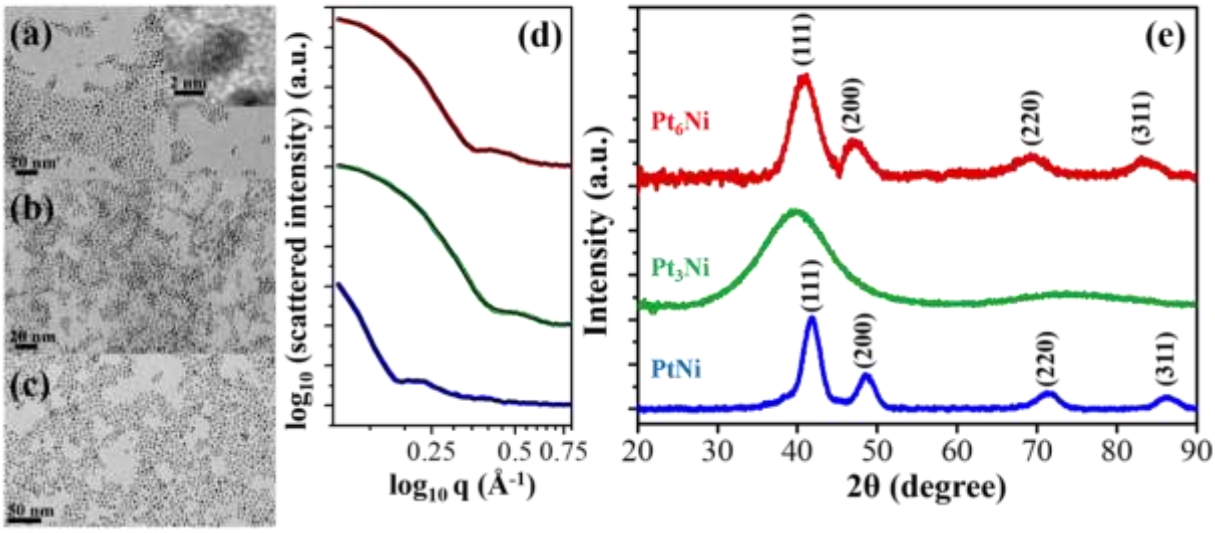

As observed for Pt-Co catalysts in the previous section (Figure 4.8), no change in the morphology or size of the NCs was observed following their addition to the carbon support and their treatment to remove the ligands by O_2 plasma and thermal annealing (*232*). The Pt-Ni NC catalysts also exhibited good stability under HDO reaction conditions. Figure 4.20 shows TEM images of the catalysts based on Pt_6Ni NCs before (Figure 4.20a) and after (Figure 4.20b) 5 h of HDO reaction. The thermal stability of NC catalysts was further confirmed by SAXS measurements (Figure 4.20c). By subtracting out the scattering from carbon support (black curve) and performing fitting with Rayleigh function, the average sizes of Pt_6Ni/C before (green curve) and after (blue curve) the functional testing were 4.1±0.8 and 4.1±0.7 nm, respectively. The results from SAXS measurements indicate no change in the size of the NCs consistently with TEM observations. The XRD patterns (Figure 4.20d) measured before (green curve) and after (blue curve) the catalyst was exposed to the reaction environment also indicated that there was no phase transformation from disordered fcc to ordered face-centered tetragonal (fct) structure. The carbon support was measured as a control (black curve) and peaks near 25° and 43° correspond to graphite (002) and diamond (111) planes for Vulcan carbon supports (*233*). The thermal stability of crystal structure makes it possible to exclude a contribution from structural ordering on the catalytic performance.

Figure 4.20

The TEM images of 10 wt% Pt_6Ni NCs on carbon support (a) before and (b) after reaction. (c) SAXS patterns of Pt_6Ni NCs in solution (red), 10 wt% Pt_6Ni NCs on carbon support before (green) and after (blue) reaction, carbon support (black), and (d) the corresponding XRD patterns. The black lines in (c) represent the simulated fits for the size of the catalyst.

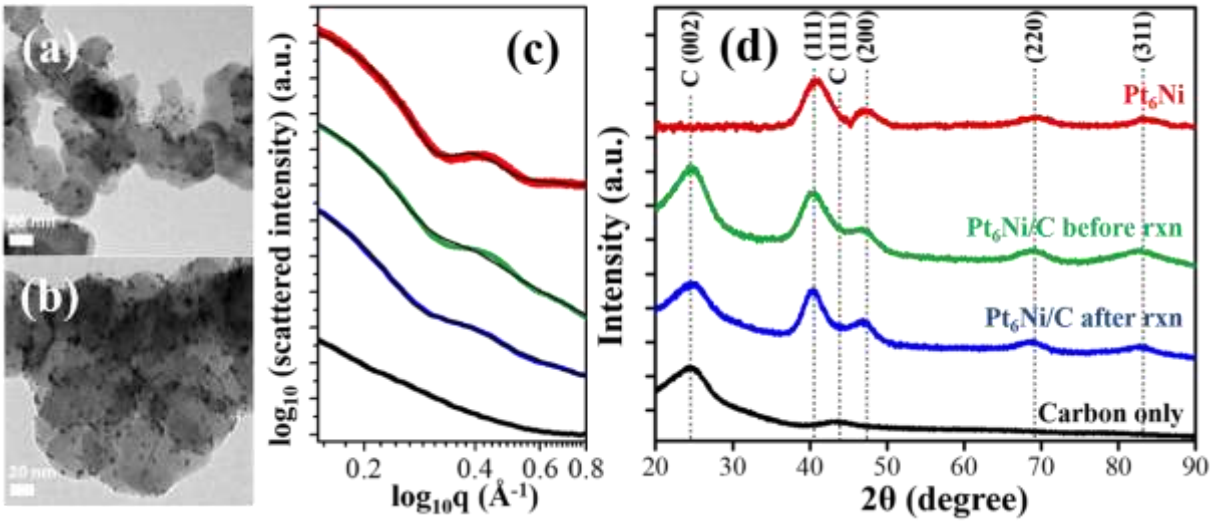

Similar characterization studies were performed with the catalysts prepared from PtCu and Pt_2Zn NCs, with TEM images shown in Figure 4.21a-b. The addition of a stronger reducing agent (BTB) resulted in smaller NCs than the ones prepared without BTB, which is consistent to what previously reported (*202*). XRD patterns of the as-synthesized PtCu and Pt_2Zn NCs also showed fcc structure (Figure 4.21d). Based on SAXS data fitted to Rayleigh function (Figure 4.21c), the average sizes and size distributions of the PtCu and Pt_2Zn NCs are 6.6±1.2 and 2.6±0.6 nm, respectively. The catalyst characterizations discussed above indicate that the NCs synthesized by solvothermal methods were excellent subjects to study the relation between HDO selectivity and bimetallic catalyst composition.

Figure 4.21 The TEM images of (a) PtCu and (b) Pt_2Zn NCs, the corresponding (c) SAXS patterns and (d) XRD patterns. The black lines in (c) represent the simulated fits for the size of the catalyst.

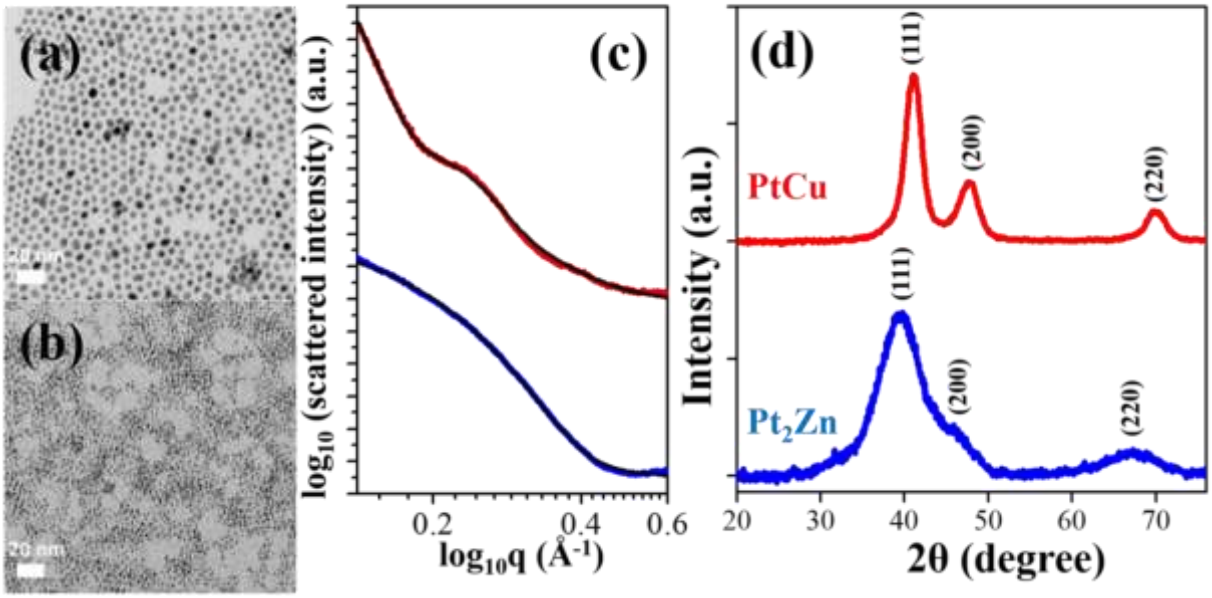

4.4.3 HDO Experiments

In the previous section, the HDO reaction for HMF was shown to be a series reaction, with products forming as shown in Scheme 4.2 (*41*, *185*). Briefly, HMF is converted to a group of partially hydrogenated intermediate species (B), which can react further to form DMF, which in turn may react to over-hydrogenated products (D). Many monometallic catalysts, including carbon-supported Pt, Pd, Ir, Ru, Co, and Ni, were found to exhibit relatively poor selectivity for DMF formation (*41*, *185*, *210*). DMF yields varied with the particular metal catalyst and the reaction conditions but were typically less than about 50%. The products formed by the further reaction of DMF also varied with the metal catalyst, with Pt tending to form open-ring products, primarily 2-hexanone and 2-propoxyhexanone (*185*).

Figure 4.22 shows a comparison of HMF conversions and DMF yields at 180 °C and 33 bar total pressure for conventional 10 wt% Ni/C, Co/C, and Cu/C catalysts. Results for Ni/C and Co/C are similar to what was previously reported (*185*). Both catalysts show high conversions, over 50%, for even short residence times; and the DMF yield goes through a maximum of slightly more than 50% with increasing space time, decreasing with longer space times. The detailed product distributions

are reported elsewhere (*185*), but the major over-hydrogenated product for both metals was 2,5-hexandione. By contrast, the Cu/C was much less active, with a maximum conversion of less than 40% at the longest space time studied. The only products formed over the Cu/C catalyst were those in the B group of Scheme 4.2, including MFu, HMMF and BEF. The low HDO activity observed over Cu agrees with previous literature hydrogenation reactions of furfural over Cu catalysts, which shows that the reaction over Cu tends to stop with formation of furfuryl alcohol [15]. Zn/C catalysts did not show any activity for HDO of HMF under the conditions of this study.

Figure 4.22

Conversion and DMF yield for the HDO reaction of HMF over impregnated 10 wt% monometallic catalyst, as a function of reactor space time. Reaction conditions: 33 bar and 180 ºC. (●) HMF conversion on Ni/C, (○) DMF yield on Ni/C, (■) HMF conversion on Co/C, (□) DMF yield on Co/C, (▲) HMF conversion on Cu/C, (△) DMF yield on Cu/C. Zn/C catalysts did not show any activity (not reported).

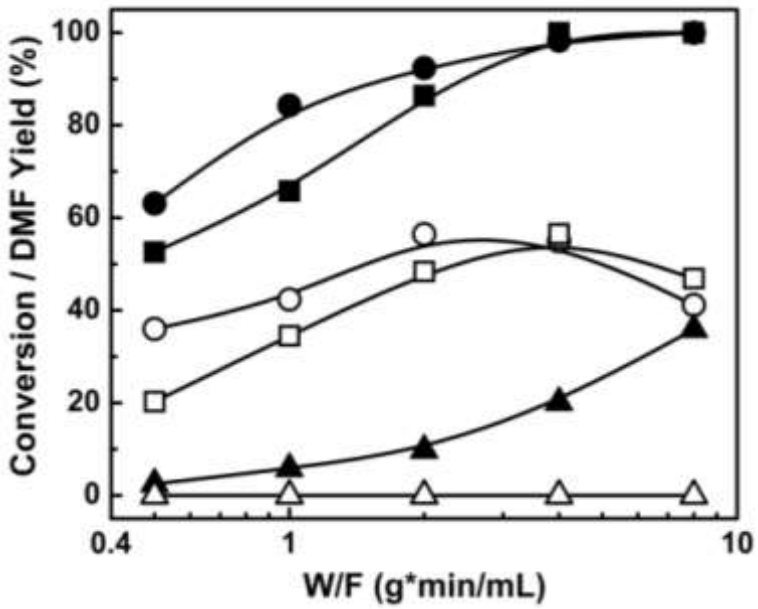

Similar experiments were performed over the Pt-Ni, Pt-Cu, and Pt-Zn bimetallic catalysts, in order to determine how they would perform in comparison to previously discussed Pt-Co catalysts. Figure 4.23 reports the HMF conversion and product yields as a function of space time for the three Pt-Ni NCs/C catalyst at 160 °C and 33 bar. The results are qualitatively similar for all three Pt-Ni catalysts, although the Pt_3Ni NCs/C catalyst in Figure 4.23b) showed somewhat lower conversions. At a space time of 0.5 g min mL^{-1}, the conversion over Pt_3Ni NCs/C was around 85%, while the conversions on the other two Pt-Ni catalysts were over 95%. In general, HMF conversion increased steadily with space time, while partially hydrogenated products (B group) yield diminished in favor

of DMF formation. Except for Pt_3Ni NCs/C, DMF yield reached a value of 80-90% before decreasing due to over-hydrogenated products (D group) formation. The fact that the D products form at the same space times for which DMF yields begin to decrease suggests that they are formed from DMF. The major D product observed with the Pt_6Ni NCs/C catalyst was 2-hexanone, the same major product formed on Pt catalysts (*41*, *185*), while with PtNi NCs/C 2,5-hexandione was observed, which was also the primary product formed on Ni/C catalysts (*185*). Interestingly, no over-hydrogenated products were observed on the Pt_3Ni NCs/C catalyst even for the highest space time examined.

Figure 4.23 Conversion and product distribution for the HDO reaction of HMF over (a) 10 wt% Pt_6Ni NCs/C, (b) 10 wt% Pt_3Ni NCs/C, (c) 10 wt% PtNi NCs/C, as a function of reactor space time. Reaction conditions: 33 bar and 160 ºC. (▼) HMF conversion, (▲) product group B, (●) DMF, (■) product group D.

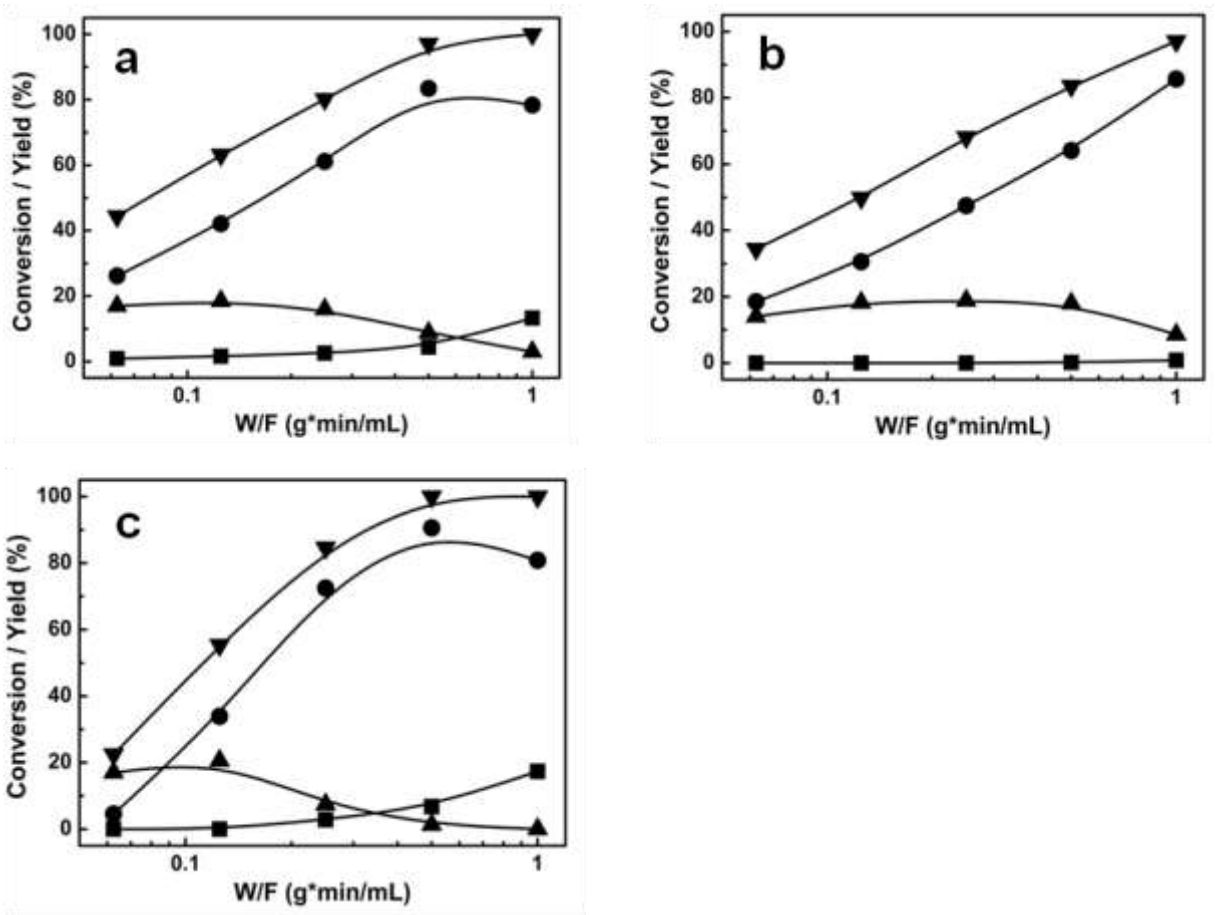

Because the conversions for the Pt_3Ni NCs/C were low at 160 °C, additional measurements were performed on this catalyst at 200 °C, with results reported in Figure 4.24. At this temperature,

the conversions of HMF were much higher. Furthermore, DMF yields reached 98% at the higher space times. It is not likely that the higher yields are due to the increase in temperature. In addition to the fact that previous work indicated that selectivity are not very different between 100 and 200 °C (*41*, *210*) one would expect the reaction of DMF to over-hydrogenated products to increase with temperature. The maximum in the yield as a function of space time in Figure 4.24 is clearly less steep than that found for Pt_6Ni NCs/C and PtNi NCs/C catalysts. Furthermore, the Pt_3Ni NCs/C catalyst was remarkably stable. There was no observable change in either the conversion or the DMF yield over a period of at least 5 h on the Pt_3Ni NCs/C catalyst, while significant changes in both were observed on Pt/C and Ni/C catalysts. The data in Figures 4.23 and 4.24 therefore indicate that the Pt-Ni catalysts are more selective and stable than their monometallic counterparts and that there is an optimum Pt:Ni ratio.

Figure 4.24 Conversion and product distribution for the HDO reaction of HMF over 10 wt% Pt_3Ni NCs/C, as a function of reactor space time. Reaction conditions: 33 bar and 200 ºC. (▼) HMF conversion, (▲) product group B, (●) DMF, (■) product group D.

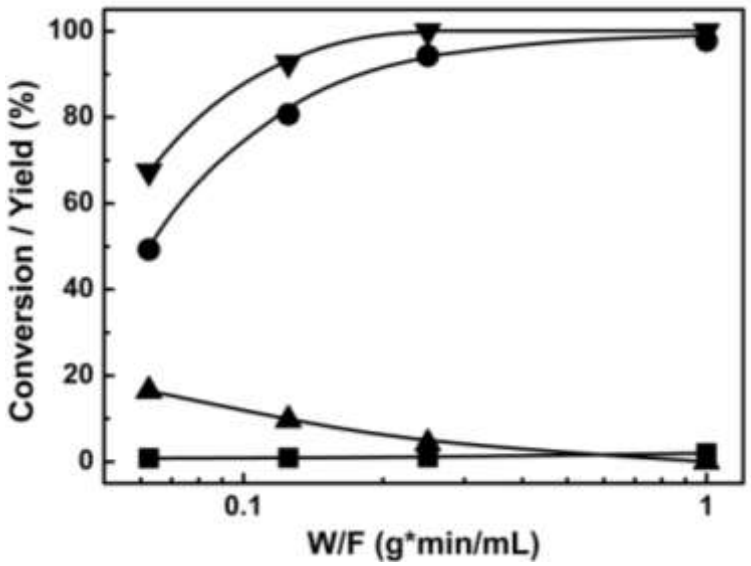

Catalysts based on Pt-Zn and Pt-Cu bimetallic NCs were also investigated, with results shown in Figures 4.25 and 4.26. Because these catalysts were also less active than Pt/C, reactions were carried out at 200 °C and 33 bar. The results for 10 wt% Pt_2Zn NCs/C in Figure 4.25 are very similar to results for Pt_3Ni NCs/C, although the rates were slightly lower. Again, DMF yields as high as 98% were achieved at high space time, with negligible production of over-hydrogenated products. Similar performance was observed over the PtCu NCs/C catalyst, Figure 4.26, with DMF yields again reaching 96%. However, alloying the Pt with Cu did significantly decrease the rates.

Figure 4.25 Conversion and product distribution for the HDO reaction of HMF over 10 wt% Pt_2Zn NCs/C, as a function of reactor space time. Reaction conditions: 33 bar and 200 ºC. (▼) HMF conversion, (▲) product group B, (●) DMF, (■) product group D.

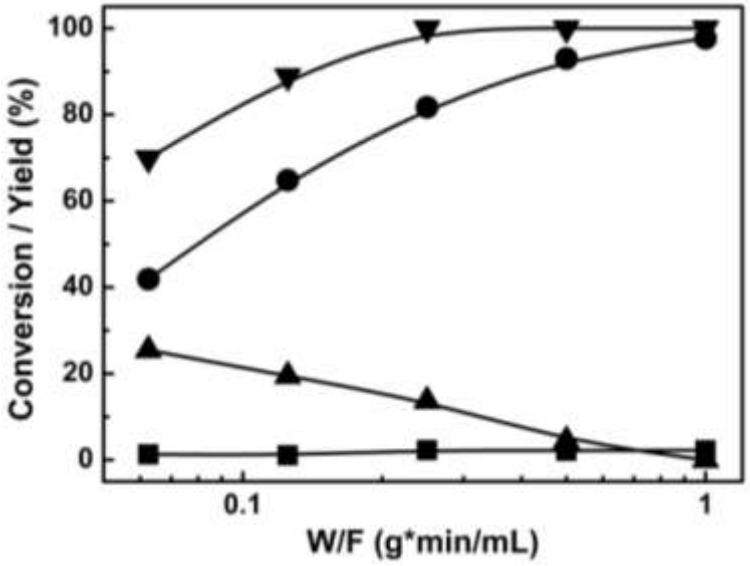

Figure 4.26 Conversion and product distribution for the HDO reaction of HMF over 10 wt% PtCu NCs/C, as a function of reactor space time. Reaction conditions: 33 bar and 200 ºC. (▼) HMF conversion, (▲) product group B, (●) DMF, (■) product group D.

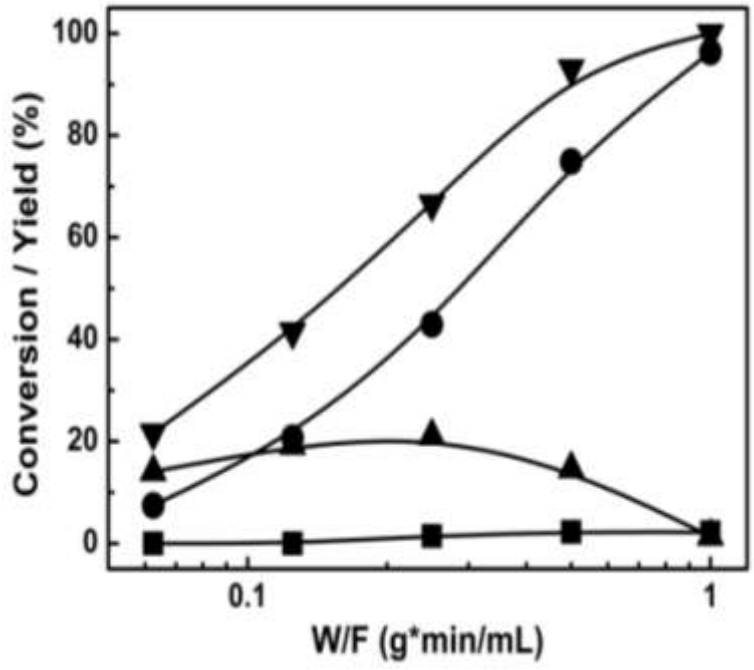

4.4.4 Discussion

The results of the present study clearly demonstrate that the catalysts formed by alloying Pt with a number of metals can significantly increase the yields for the HDO reaction of HMF to DMF. In all cases, the increased yields result from a decreased reactivity of DMF to over-hydrogenated products. The alloying metals appear to do this in different ways, but the net result in each case is that the alloying metal prevents the furan ring from lying down on the catalyst surface. With Pt-Co alloys, the furan ring is prevented from lying down on the surface by a "honey-comb", CoO_x overlayer on the Pt (*210*). Since Ni is more easily reduced than Co, the effect of Ni on the bonding of the furans on the Pt-Ni alloys is likely due to the oxophilicity of the Ni, similar to what was reported for the effect of Fe on Ni-Fe alloy catalysts (*38*). With Cu and Zn, the role of the alloying metals may be to change the Pt ensemble size or otherwise change the way the DMF bonds to the metal surfaces (*224*, *226*).

The selective alloy catalysts were also more stable. In the present study, there was no observable deactivation of a Pt_3Ni/C catalyst, consistent with what was also observed for a Pt_3Co_2 catalyst (*210*). The results corroborate the statement that deactivation by coking in this reaction is caused by the over-hydrogenated products such as di-ketones, which tend to be highly reactive.

With Pt-Ni and Pt-Co alloys, compositional uniformity of the catalyst is critical. Monometallic catalysts based on Pt, Ni, and Co are not selective because all three metals will catalyze the reaction of DMF to over-hydrogenated products (*185*). Furthermore, the selectivity of the Pt-Ni and Pt-Co bimetallic catalysts depends on the Pt:Co (*210*) and Pt:Ni ratios. Synthesis of bimetallic catalysts by conventional methods in which the support is infiltrated with metal salts is not able to produce this uniformity, which is the reason the catalysts in this study were prepared by synthesizing uniform NCs in solution. With Pt alloys of Cu and Zn, the uniformity will be less important, given that Cu and Zn are not active for the reaction of DMF. In this sense, alloy catalysts based on Cu and Zn could be easier to synthesize.

The fact that various Pt alloys show good selectivity raises a number of interesting questions. First, would other alloys, including ones that do not include noble metals, also show high selectivity? Second, can one generalize the high HDO selectivity for HMF that is observed with the Pt alloys to HDO reactions with other reactants, such as those one might associate with lignin? These will be interesting questions to address in the future.

4.4.5 Conclusions

Carbon-supported, monometallic Pt and Ni catalysts exhibit relatively low selectivity, less than 50%, for DMF in the HDO reaction of HMF because DMF is converted to ring-opened or ring-hydrogenated byproducts. On the other hand, Zn and Cu catalysts are not active for HDO reactions. However, catalysts based on bimetallic Pt alloys with Ni, Zn, or Cu show significantly higher selectivity to DMF, up to 98%. With Pt-Ni alloys, controlling the local composition is critically important for achieving high DMF yields due to the non-selectivity of the pure metals. Even though the effects of Ni, Zn, and Cu on Pt are expected to be very different, it is likely that each of the alloys modifies the bonding of DMF so as to prevent the furan ring from lying down on the surface. This appears to be the critical factor in achieving high selectivity for HDO of HMF.

4.5 Ni-Cu Alloys for HDO of HMF

4.5.1 Introduction

As discussed in the previous sections, bimetallic catalysts based on Pt have shown significantly improved HDO selectivity to DMF with respect to single metal catalysts. It was demonstrated for Pt-Co alloys that the reactivity of DMF was greatly suppressed on the alloy compared to monometallic Pt or Co, due to formation of a CoO_x monolayer that dramatically weakened the interactions between the furan ring and the catalyst surface, so that over-hydrogenation of DMF was suppressed (*210*). However, other Pt/base-metal (Pt-Cu, Pt-Zn) alloy catalysts were also shown to give high yields of DMF due to suppressed reactions of DMF (>95%) (*232*); and the alloying metal in the case of Cu is not as oxophilic as Fe or Co. It remains unclear whether an oxide overlayer is needed in order to obtain high DMF yields.

Base-metal alloys have also been shown to be more selective relative to the monometallic catalysts for the vapor-phase reaction of furfural to methyl furan. For example, Resasco and coworkers have demonstrated that Ni-Fe catalysts are superior to monometallic Ni(*38*). In the vapor-phase reaction, decarbonylation of furfural to furan is the major side product but there is evidence that catalysts which are selective for HMF to DMF are also selective for furfural to methyl furan (*234*). Higher yields of DMF from HMF have been reported for Ni-W_2C (*235*) and Cu-Co@C (*236*) catalysts, but there is no indication about the catalysts surface composition under reaction conditions or about the role of the carbon overlayer in controlling the HDO selectivity.

In the present section is reported the reaction of HMF to DMF over Ni-Cu NCs catalysts in a continuous flow reactor at high H_2 pressures. DMF yields as high as 98.7% were achieved with $NiCu_3$ NCs catalyst due to the low catalytic reactivity towards DMF over-hydrogenation. Catalysts prepared by conventional infiltration methods were not as selective as the ones prepared from alloy NCs because the composition of the conventional supported metals was not as uniform. The preparation of alloy NCs via solvothermal methods eliminates catalyst heterogeneity, which also makes it easier to understand how catalyst composition and particle size affect activity and selectivity (*39*). Near Ambient Pressure X-ray photoelectron spectroscopy (NAP-XPS) revealed that the Ni-Cu NCs are completely reduced to the metallic state under reducing conditions. Possible reasons for the high selectivity of this bimetallic alloy catalyst will be discussed.

4.5.2 Catalyst Synthesis and Characterization

NiCu and $NiCu_3$ NCs were synthesized by a solvothermal synthesis under inert atmosphere. To prepare the nanocrystals, nickel (II) acetylacetonate ($Ni(acac)_2$, 95%, Alfa Aesar) and copper (II) acetylacetonate ($Cu(acac)_2$, 97%, Alfa Aesar) were dissolved in 20 mL of OAm (technical grade 70%, Sigma Aldrich) and degassed at 100 °C for 15 min. Then, under N_2 atmosphere, 1.5 mL of TOP (90%, Sigma Aldrich) was added and the system was quickly heated to 230 °C. After 10 min, the reaction mixture was cooled to room temperature. For the work-up, methanol was used to precipitate the NCs by centrifugation (3 times), and hexane was used to redisperse the NCs after each step. In order to obtain 1:1 and 1:3 Ni:Cu molar ratio, 3:1 and 1:1 molar ratios were used. The NCs were dispersed into the carbon support to prepare 10 wt% of metals on carbon. To remove the organic ligands from the surface of the NCs, we followed previously published procedures (*210*, *232*). Briefly, 100 mg of 10 wt% metal/C catalysts were exposed to O_2 plasma for 15 min. After the plasma treatment, the NC surfaces were further cleaned by rapid thermal annealing (RTA).

Conventional monometallic and bimetallic catalysts were synthesized by incipient wetness impregnation for comparison with the nanocrystal catalysts. The Ni/C and Cu/C catalysts were prepared with a 10 wt% metal loading. The metal precursors were nickel(II) nitrate hexahydrate (98%, Alfa Aesar) and copper(II) nitrate trihydrate (98%, Alfa Aesar). Each metal precursor was dissolved in a pre-mixed water/ethanol (3:1) solvent under vigorous stirring. Carbon black (Vulcan XC-72R) was slowly introduced until uniform slurry was formed. The carbon support used in this work has a BET surface area of 250 $m^2\ g^{-1}$, a typical bulk density of 96 kg m^{-3} and an average particle size of 50 nm. The wet mixture was then dried in air at 60 °C for 12 h, followed by 500 °C reduction using 5% H_2/He flow at 60 mL min^{-1}. The temperature was programmed to reach 500 °C using a 3 °C min^{-1} ramp rate and was maintained at 500 °C for 2 h before cooling. The conventional bimetallic NiCu/C catalyst was prepared by co-impregnation, using a pre-mixed solution of the metal precursors.

TEM images of the NiCu and $NiCu_3$ NCs synthesized by solvothermal methods are shown in Figure 4.27a and 4.27d. In each case, the particles were uniform, with a slightly faceted morphology. The average sizes and size distributions of the NiCu and $NiCu_3$ NCs were 13±1.0 nm and 15±1.2, respectively. The slight difference in the particle sizes for NiCu and $NiCu_3$ NCs is due to the amount of precursors used during the synthesis. The XRD patterns in Figure 4.27g demonstrate that the NCs have a face-centered-cubic (fcc) crystal structure. The diffraction peaks for NiCu NCs were shifted to slightly higher angles compared to that of the $NiCu_3$ NCs, as expected for well-mixed alloys. An extra peak between (111) and (200) planes was observed for NiCu NCs, and this is likely indicative of the presence of hcp-like stacking faults (*237*, *238*).

Figure 4.27 The TEM images of (a) NiCu, (d) $NiCu_3$ and the corresponding size distribution (b) and (e) and diffraction patterns (c) and (f). The powder X-ray diffraction patterns are shown in (g). Scale bars are 100 nm. Model colors: light blue=Cu atoms, green=Ni atoms.

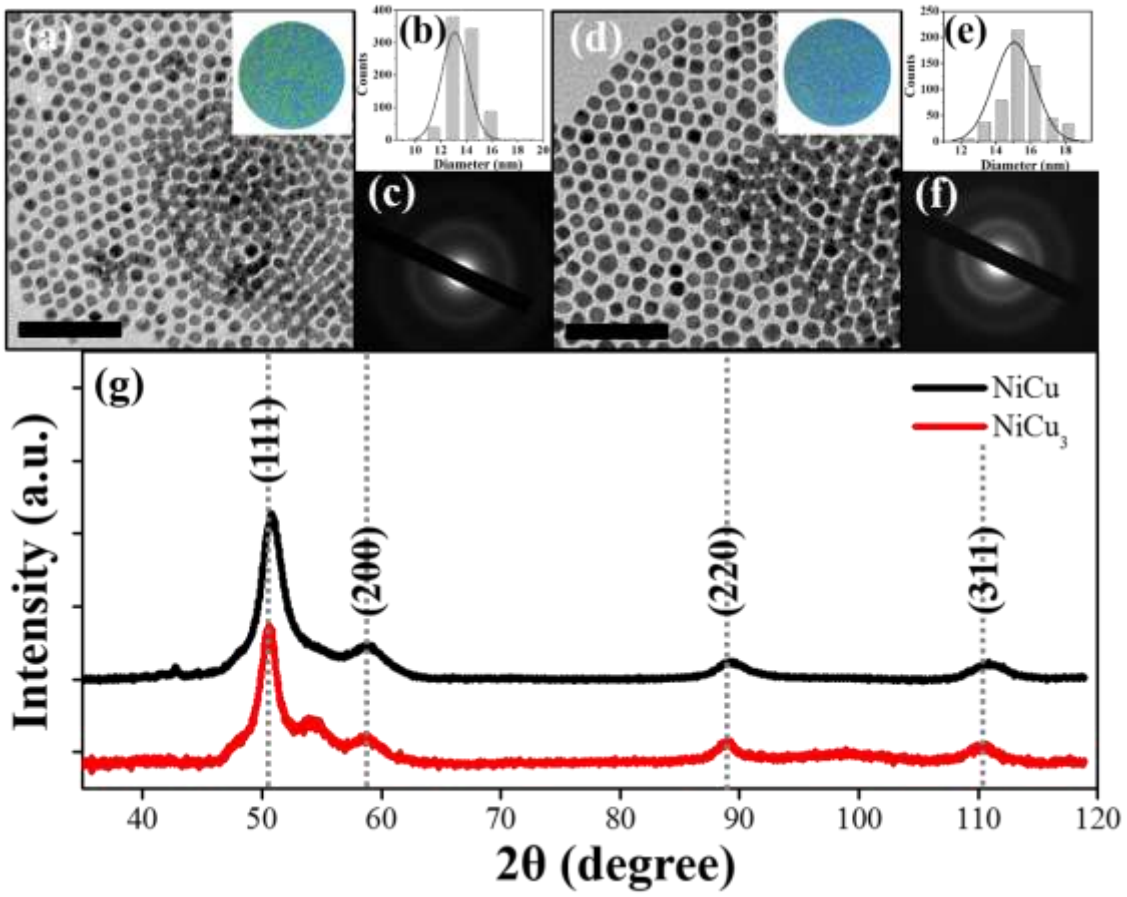

For SEM and NAP-XPS investigation, the NiCu and $NiCu_3$ nanocrystals were deposited on a graphite foil. SEM micrographs (Figure 4.28) showed that the nanoparticles were homogeneously distributed over the surface in a side-by-side fashion, forming a single discontinuous layer. No evidence for second (or higher) layer formation was observed. XPS spectra taken after treating the NCs with oxygen plasma and Rapid-Thermal Annealing (RTA) showed that the pretreatment effectively removed the protecting ligands, so that both N and P signals were below the detection limit in the spectra (not shown).

Figure 4.28

SEM micrographs of graphite supported $NiCu_x$ nanoparticles. (a) NiCu nanoparticles after deposition, (b) NiCu nanoparticles after plasma treatment and annealing to 700 °C. (c) $NiCu_3$ nanoparticles after deposition, (d) $NiCu_3$ nanoparticles after plasma treatment and annealing to 700 °C. Size of the images is 1 × 1 μm^2. Model colors: light blue=Cu atoms, green=Ni atoms, red=oxygen atoms.

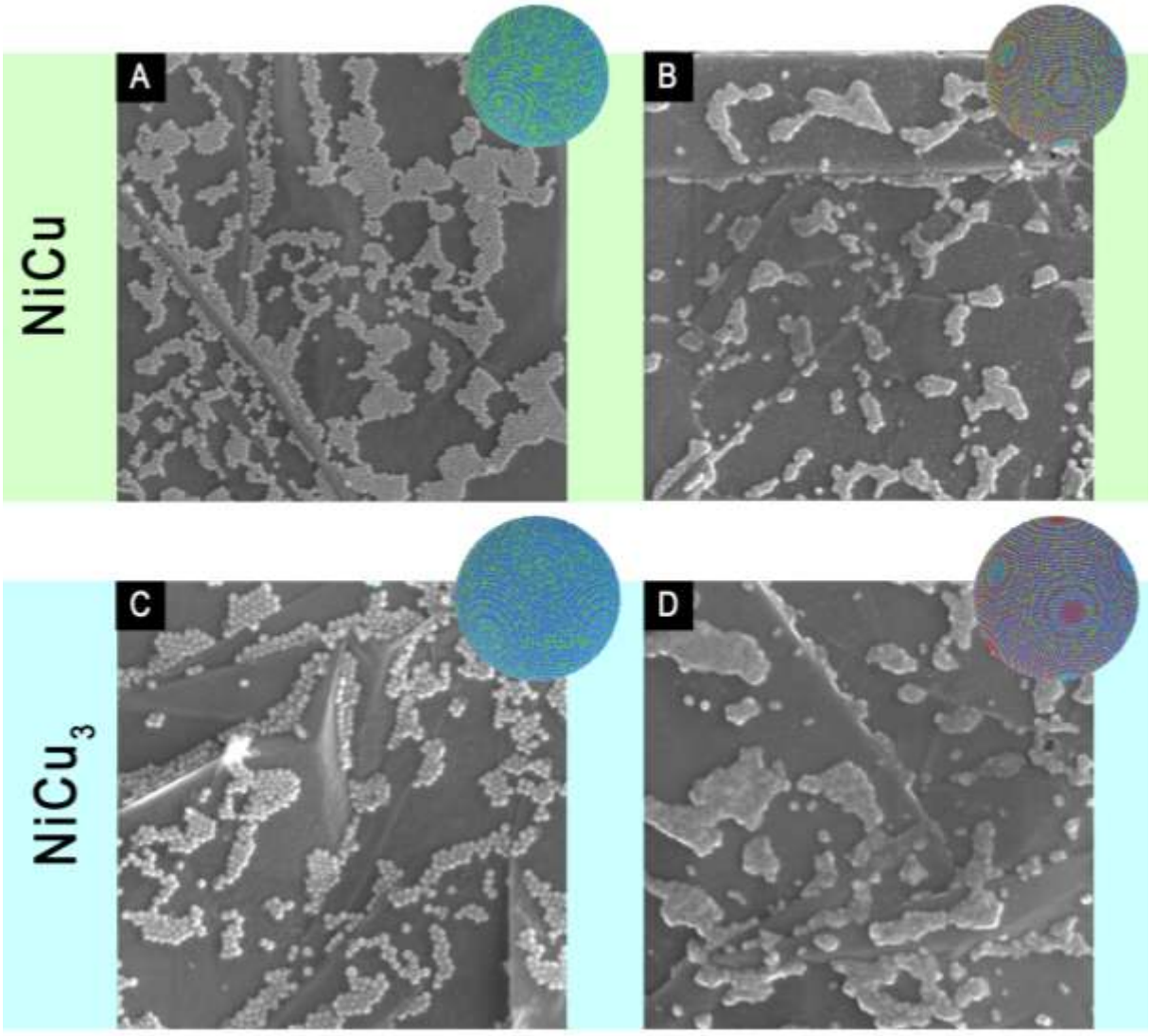

In order to understand the structure and chemical state of the NCs particles under reaction conditions, we performed NAP-XPS characterization for both the NiCu and $NiCu_3$ NCs, with spectra shown in Figure 4.29. Immediately after evacuating the samples at room temperature, the spectra of Cu and Ni showed that both elements were mostly oxidized. For Ni, the XPS signals can be assigned to Ni^{2+} (853.7 eV), indicative of NiO, and Ni^{3+} (855.6 eV), indicative of Ni(OOH) or Ni_2O_3. While the Cu signal has significant contributions from Cu^{2+} (934.7) and metallic Cu^0 (932.4 eV), the presence of Cu^{1+} cannot be ruled out due to its overlap with the metallic signal.

Figure 4.29

NAP-XPS spectra of Cu 2p and Ni 2p core levels of NiCu and $NiCu_3$ nanoparticles measured in UHV and under 1 mbar of H_2 at 250 °C. The spectra are normalized to the metallic Cu $2p_{3/2}$ signal and offset for clarity. XPS colors: light blue=Cu (0), green = Ni (0), red=oxidized metals, grey=satellite signals; model colors: light blue=Cu atoms, green=Ni atoms, red=oxygen atoms.

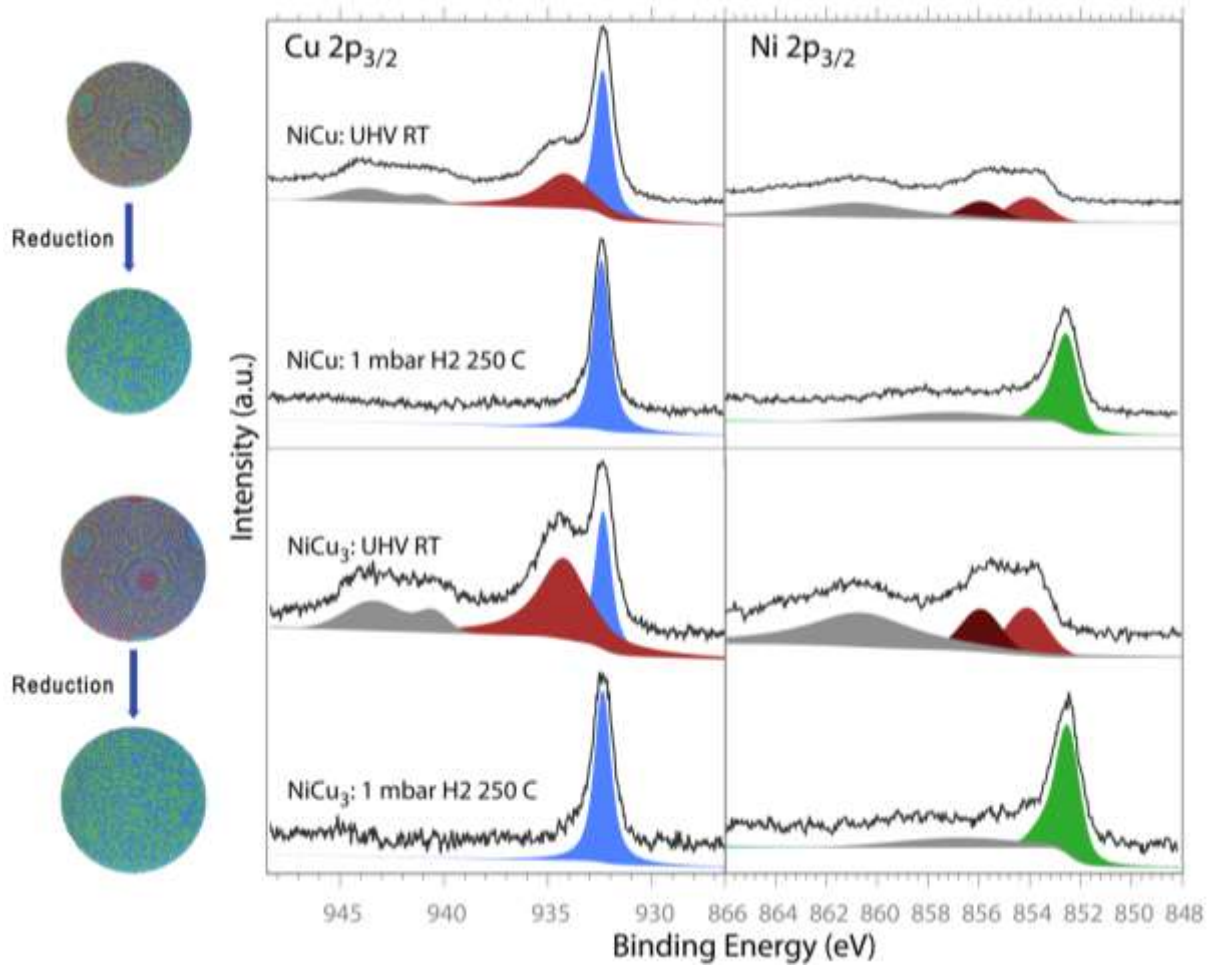

Spectra obtained in 1 mbar of H_2 at 250 °C are also shown in Figure 4.29 and are more indicative of the surfaces under reaction conditions. The reduction treatment led to complete reduction of both Cu and Ni to metallic states in both the NiCu and $NiCu_3$ NCs. Based on photoionization cross-section analysis, both the NiCu and $NiCu_3$ NCs exhibit a Ni:Cu molar ratio close to 1:1 in the surface region mapped by XPS. This result implies that Ni segregates to the surface in the $NiCu_3$ nanoparticles, leading to the formation of a Ni-rich shell on a Cu-rich core. The formation of such a core-shell structure is not surprising. During the sample preparation, the NCs were mildly oxidized by oxygen-plasma and rapid-thermal-annealing treatments in order to

remove the surface organic ligands. Since Ni is easier to be oxidized than Cu, there is a driving force to segregate Ni on the particle surface. After reduction, Ni forms an alloy with Cu, resulting in a Cu-rich core and Ni-rich shell structure. Similar observations have been reported for Pt-Co. However, with Pt-Co NCs spectroscopic data suggested formation of a stable CoO_x layer at the surface that could not be reduced under the conditions of that study (*210*).

4.5.3 Catalytic HDO Study

As previously discussed, high-pressure HDO of HMF in alcohol solvents is a sequential reaction in which DMF is an intermediate product that can go on to form secondary products, as shown in Scheme 4.2(*41*, *185*). The product distributions as a function of reactor space time over 10 wt%, monometallic Ni/C and Cu/C catalysts are shown in Figure 4.30 for reaction at 180 °C and 33 bar total pressure. Results for Ni/C, shown in Figure 4.30(a), are similar to what has been reported previously and are consistent with the sequential reaction scheme discussed above (*41*, *185*). Partially hydrogenated products (B) are formed only at the lowest space times and these rapidly decline. DMF production initially increases with space time, then declines, while the over hydrogenated products are formed only at longer space times. The maximum DMF yield was about 55%.

The Cu/C was much less reactive, as shown in Figure 4.30b. The maximum conversion of HMF was less than 40% at the longest space time and the products were primarily the partial-hydrogenated compounds (B). No DMF was observed on the Cu catalyst under the conditions shown here. The results are consistent with the fact that Cu-based catalysts are used to hydrogenate furfural to furfural alcohol (*226*, *227*). Although the 1-propanol that we used as the solvent in the present study can serve as hydrogen donor in catalyzed transfer hydrogenation (CTH), we did not observe the formation of propanal in the products. Considering the fact that CTH is commonly catalyzed by Lewis acid catalysts (*239*), the transfer hydrogenation likely did not interfere the HDO reaction in this work.

Figure 4.30

Conversion and product yield for the HDO reaction of HMF over 10-wt% impregnated (a) Ni/C, (b) Cu/C, as a function of reactor space time. Reaction conditions: 33 bar and 180 ºC. (▼) HMF conversion, (▲) product group B, (●) DMF, (■) product group D, (◀) 5-methyl furfural (MF), (◆) 2,5-bis(propoxymethyl)furan (BEF), (×) 2-hydroxylmethyl-5-methyl furan (HMMF).

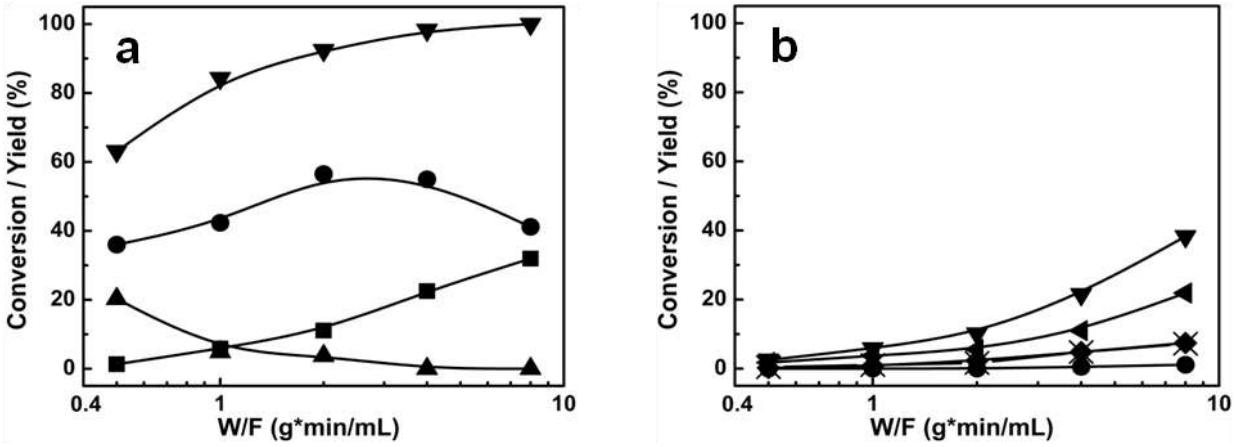

Similar continuous-flow reaction experiments were carried out over the NiCu and $NiCu_3$ bimetallic catalysts prepared by conventional impregnation method. Figure 4.31 presents data for HMF conversion and product yields as a function of space at 180 °C and 33 bar for 10 wt% IMP-NiCu/C and IMP-$NiCu_3$/C catalysts. The product curves for IMP-NiCu, Figure 4.31a, and IMP-$NiCu_3$, Figure 4.31b, are qualitatively similar to the results shown earlier for the monometallic Ni catalyst, but with different yields. Surprisingly, rates on all three Ni-containing catalysts were similar as shown by the fact that conversions at any given space time were similar. For example, at a space time of 0.5 g min mL^{-1}, the conversion over IMP-NiCu/C was 85% and 60% on both $NiCu_3$ and Ni catalysts. This relatively small difference could be due to differences in metal dispersions, which are difficult to measure on Ni-Cu alloys in general (*240*), especially when using a carbon support.

Figure 4.31 Conversion and product distribution for the HDO reaction of HMF over 10 wt% (a) IMP-NiCu/C, (b) IMP-$NiCu_3$/C, as a function of reactor space time. Reaction conditions: 33 bar and 180 ºC. (▼) HMF conversion, (▲) product group B, (●) DMF, (■) product group D.

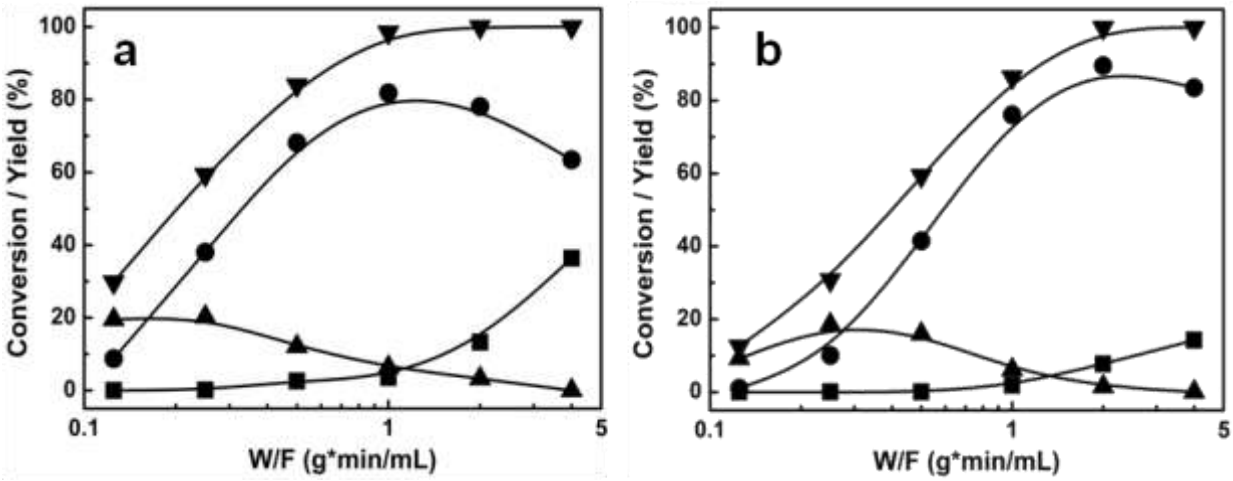

Both the NiCu and $NiCu_3$ catalysts exhibited greatly improved DMF selectivity, with maximum yields in the range of 80 to 90%. However, at longer space time, the DMF yields on both Ni-Cu catalysts decreased, an indication that DMF was reacting to form over-hydrogenated products (D group). The main over-hydrogenated products on the Ni-Cu catalysts were 2,5-hexandione and DMTHF, which were also the primary products formed by reaction of DMF on Ni/C. Unlike the reaction of HMF on Pt (*185*), the etherification by-products, 2-propoxyhexane or 2,5-dipropoxyhexane, were formed in small amounts on the Ni-based catalysts.

In previous HDO studies of Pt-Ni and Pt-Co catalysts, compositional uniformity was shown to be a critical factor in determining selectivity (*210*, *232*); and NCs catalysts prepared by solvothermal methods with the optimal composition showed greatly improved yields compared to catalysts having the same overall composition but prepared by conventional impregnation. To determine whether this would also be true with the Ni-Cu catalysts, we investigated the HDO reaction on the highly uniform, 10 wt% NiCu and $NiCu_3$, NCs catalysts, with conversions and yields shown in Figure 4.32. Both NCs catalysts achieved better selectivity to DMF compared to impregnated catalysts, with yields of 96.1% for the NiCu NCs/C catalyst and 98.3% for the $NiCu_3$ NCs/C catalysts.

Figure 4.32 Conversion and product distribution for the HDO reaction of HMF over 10 wt% (a) NiCu NCs/C, (b) $NiCu_3$ NCs/C, as a function of reactor space time. Reaction conditions: 33 bar and 180 ºC. (▼) HMF conversion, (▲) product group B, (●) DMF, (■) product group D.

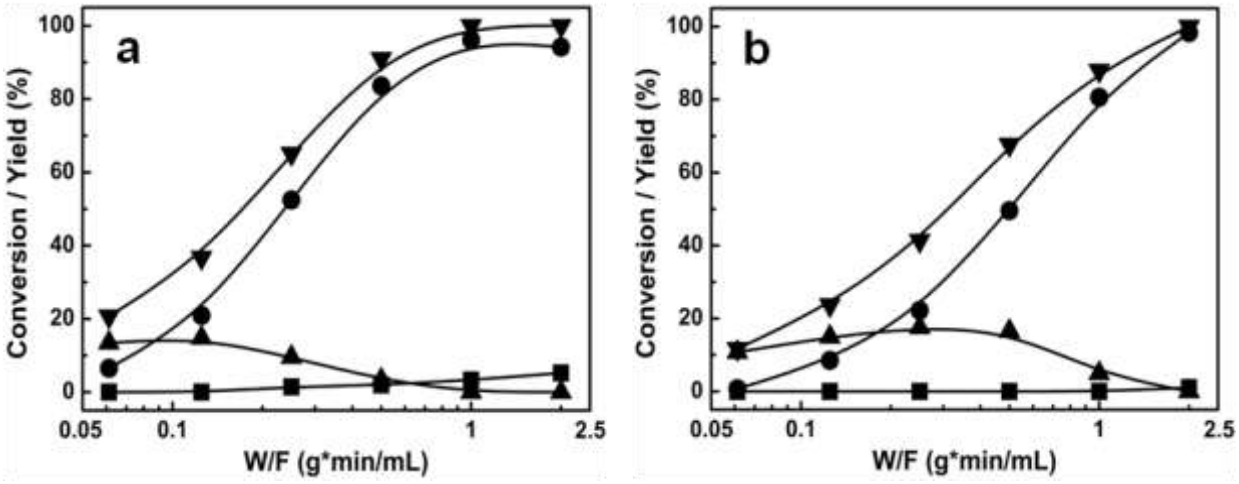

Some deactivation of the HDO activities was observed over the Ni-Cu NCs. For example, at 180°C, 33 bar and 0.5 g min mL^{-1} W/F, the HMF conversion after 4 h decreased of about 10% over NiCu NCs and nearly 50% over a conventional Ni catalyst. However, selectivity was not affected by time-on stream. In previous work, it was argued that the deactivation is due to coking and blocking of the metal active sites, based on the fact that stability scaled with the carbon balances on various catalysts (*210*).

4.5.4 DMF Feeding Study

Because HDO of HMF is a sequential reaction in which DMF can undergo additional reaction, high selectivity for DMF require that DMF be unreactive. Therefore, the reaction of DMF over the various Ni-Cu alloy catalysts was investigated by feeding DMF in a solution with 1-propanol at the same molar concentration as that used in the HMF reaction studies. The experiments were carried out under the same reaction conditions, 180 °C with 33 bar H_2; and the data are summarized in Figure 4.33. The most notable difference between the catalysts was in their activity, following the order: IMP-NiCu/C > IMP-$NiCu_3$/C > NiCu NCs/C> $NiCu_3$ NCs/C.

Figure 4.33 Conversion and product distribution for the reaction of DMF over 10 wt% (a) IMP-NiCu/C, (b) IMP-$NiCu_3$/C, (c) NiCu NCs/C, (d) $NiCu_3$ NCs/C, as a function of space time. Reaction conditions: 33 bar and 180 ºC. (▼) DMF conversion, (□) DMTHF, (▽) 2-hexanone, (△) 2,5-hexandione.

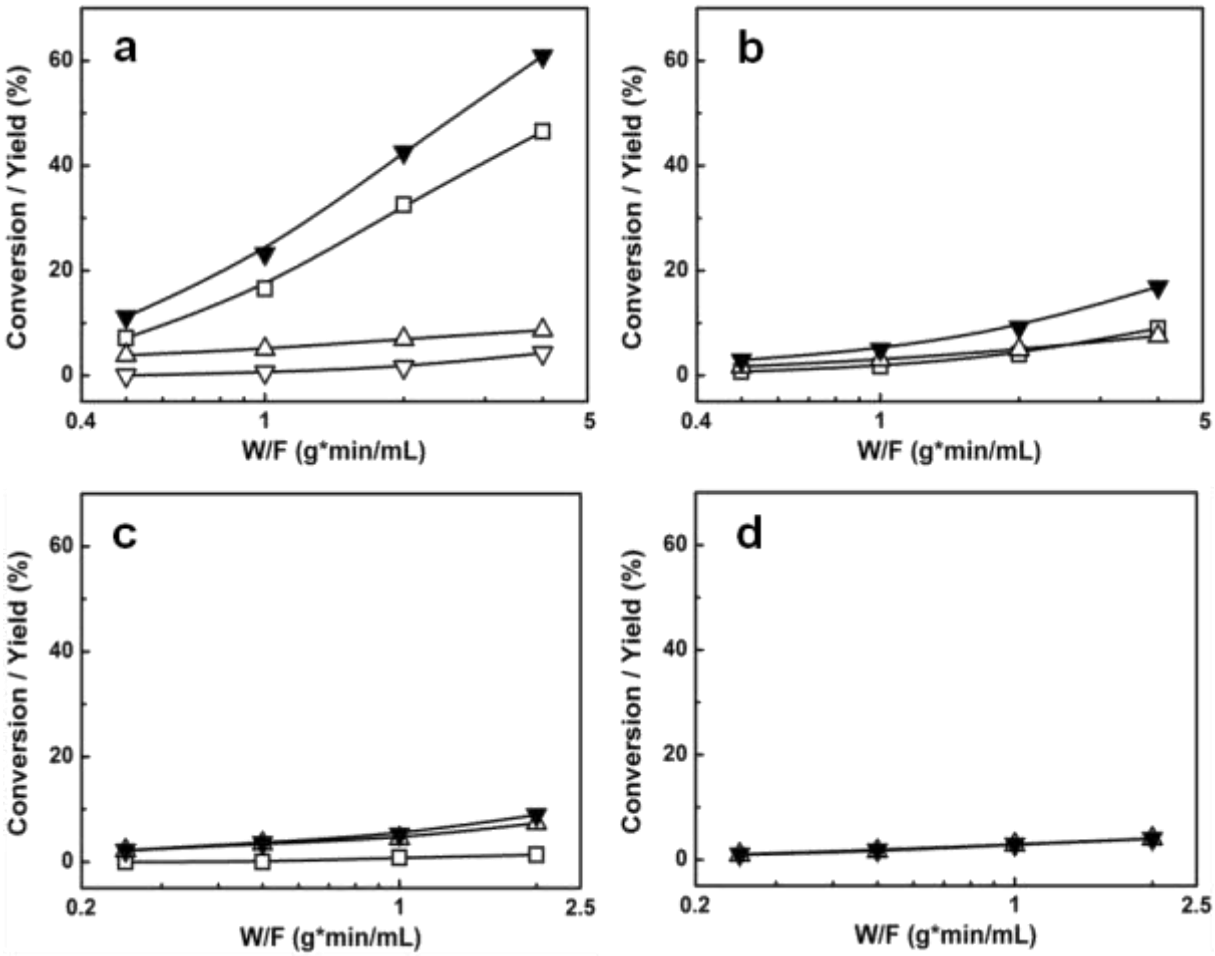

The data in Figure 4.33 are consistent with the sequential reaction mechanism and the reaction data for HMF. There is a direct relationship between the catalyst selectivity and the reactivity of DMF. Furthermore, the products from the reaction of DMF were primarily DMTHF and 2,5-hexanedione, which were also the primary products that formed from HMF on these catalysts at longer space times. Since less water is formed in the reaction of DMF, the yields of hexanedione tend to be lower with DMF.

4.5.5 Discussion

The results of the present paper confirm that alloy catalysts are capable of higher selectivity to DMF for HDO of HMF. DMF yields above 95% have been achieved over Pt-Co, Pt-Ni, Pt-Zn, Pt-Cu, and, now, over Ni-Cu alloy catalysts (*210*, *232*). In each of these cases, high selectivity have been shown to be related to suppressed reaction of DMF to form over-hydrogenated products. Ni-Fe (*38*) and Co-Cu (*236*) alloys have also been reported to show high selectivity for HDO reactions. Although suppressed reactivity of DMF has not been confirmed in those cases, it seems likely that the Ni-Fe and Co-Cu systems would show this similarity as well.

The important question is why all of these alloys exhibit reaction properties that are so different from their monometallic counterparts. It seems likely that the alloying metal in each case prevents the furan ring from lying down on the catalyst surface. Previous studies suggested that the alloying metal oxophilicity was the key to achieve such conditions (*38*, *210*). A similar explanation cannot apply to the Ni-Cu NCs of the present study since NAP-XPS analysis indicates the particles have a completely reduced surface at 250 °C even at low H_2 pressure.

The role of Cu in the Ni-Cu alloys may be to decrease the ensemble size at the Ni surface (*241*). An alternative explanation is based on results from Ke *et al.* (*242*) who investigated the HDO reactions using adsorption of furfural on Cu(111), Ni(111), and Ni-Cu model surfaces. On Cu(111), they observed that furfural adsorbed only weakly via η^1(O) configuration, whereas furfural was strongly bonded on the Ni(111) surface through an η^2(C, O) configuration and decomposed non-selectively. Selective reaction of furfural to 2-methyl furan was observed on a Cu(111) surface with a Ni overlayer.

The differences between the Ni-Cu catalysts prepared by conventional impregnation and those prepared from nanocrystals are likely due to catalyst homogeneity. The individual metal particles in the impregnated catalysts almost certainly have varying compositions and the presence of some Ni-rich particles will limit the selectivity. This inhomogeneity problem is particularly serious when dealing with sequential reactions in which the desired product is an intermediate. Even if the majority of the catalyst is selective, that part of the catalyst that is not can further promote reaction of the desired product. Compared to alloys like Pt-Ni and Pt-Co, Cu-based alloys will be less sensitive to compositional heterogeneity because Cu is relatively unreactive. However, the advantages of the nanocrystal catalysts prepared by solvothermal methods were still apparent with the Ni-Cu system.

The oxidation state of the catalyst surface during reaction is important to consider. Our present XPS results demonstrate that the Ni-Cu catalysts are reduced with very mild pretreatments,

so that the catalyst is certainly reduced before reaction. A calculation of the bulk thermodynamics for the reaction Ni +H_2O = NiO + H_2 show that equilibrium will occur at a P(H_2) : P(H_2O) ratio ~10^{-3} at 180 °C. Since the P(H_2) : P(H_2O) ratio was never less than 25 in the HDO reactor, the thermodynamics of the nanoparticles would have to be *dramatically* different from that of the bulk for the particles to be oxidized under reaction conditions. In previous work on Pt-Co NCs catalysts, where a surface CoO_x was observed(*210*), bulk thermodynamics would again suggest that the Co should be in its metallic form. In addition to the fact that the thermodynamics of surface Co reduction may be somewhat different from that of the bulk(*243*), it appears that reduction may have been kinetically limited in that case, since the catalyst was not reduced, even by the initial pretreatments.

The fact that Ni-Cu alloys are capable of providing high selectivity for DMF production demonstrates that reasonably inexpensive catalysts can be used for selective HDO of HMF. It is interesting to ask whether these base-metal alloys could also be used for other HDO reactions, such as would be important in the processing of lignin. There are indeed indications for this (*244*).

4.5.6 Conclusions

Monometallic Ni and Cu catalysts exhibit low selectivity for DMF formation in the HDO reaction of HMF due to over-hydrogenation on Ni and low reactivity on Cu. On the other hand, bimetallic Ni-Cu catalysts show very high DMF yield in the same reaction conditions. The surface composition and chemical state of the active phase were clearly identified by state-of-the-art NAP-XPS analysis on Ni-Cu catalysts based on bimetallic nanocrystals of controlled dimension and composition. In both nanocrystal NiCu and $NiCu_3$-based catalysts, Ni and Cu were completely reduced already at 250 °C in 1mbar of H_2 and exposed surface in a 1:1 molar ratio, strongly indicating that an oxide overlayer is not necessary to achieve high DMF yield in the HDO reaction of HMF.

5. Dye-Sensitized Photocatalytic H_2 Production

5.1 Introduction

H_2 is an ideal energy carrier because it has no carbon footprint, it can be obtained from water and it can be used as fuel in fuel-cells or as a reagent to produce fuels, biofuels (see Chapter 4) or chemicals. Nowadays, H_2 is mostly produced by steam reforming of methane or other fossil fuels, but many other technologies are available, such as biomass gasification and electrolytic processes, or in development, such as photoelectrochemical (PEC) or biological processes (*245*). In PEC devices H_2 is produced from water (and usually some sacrificial agent), using sunlight and specialized semiconductors called photoelectrochemical materials. PEC water splitting is a promising pathway for H_2 production at semi-central and central scales, but solar-to-hydrogen efficiencies are still very low, and continued improvements in efficiency, durability, and cost are still needed for market viability (*246*).

One reason for low efficiency is that water splitting is a multi-electronic, multi-atomic, thermodynamically demanding and kinetically hampered process with a high activation barrier. The standard potential ($\Delta E°$) of water splitting or water electrolysis to H_2 and O_2 (Equation 5.1) is 1.23 V at any pH. Moreover, under operation the voltage required for water splitting is higher than predicted (up to 1.8–2.0 V), due to thermodynamic losses and overpotentials associated with the reaction kinetics (*247*). Another drawback is that hydrogen and oxygen are produced in the same environment and easily recombine before they can be separated. Therefore, a common approach for testing new materials is to limit the process to either one of the half-reactions: water reduction to hydrogen or oxidation to oxygen, by the use of a sacrificial electron donor (SED) or acceptor (SEA), respectively. SEDs and SEAs act as holes and electron scavengers, respectively, replacing water in one of the two half-reaction.

$$H_2O \rightarrow H_2 + \frac{1}{2}O_2 \qquad (5.1)$$

Another reason for low efficiency of PEC devices is related to the semiconductor used and its electronic properties. Titanium dioxide,TiO_2 , is the most investigated and employed material in

both fundamental research and practical applications, because it is a cheap, nontoxic, chemically and biologically inert, and photo-stable material; especially when coupled with a co-catalyst, such as Pt, TiO_2 performs very well in many photocatalytic reactions (*42*). However, TiO_2 does not absorb visible light, because of its large band gap (~3.2 eV, depending on polymorph and nanostructure), so that only a narrow, UV (Ultraviolet) portion of the solar spectrum can contribute to electron excitation from the valence band (VB) to the conductive band (CB). Many methods have been adopted in order to extend the light absorption of TiO_2 in the visible (Vis) range, such as doping with metals and non-metals (*248*), addition of plasmonic nanoparticles (Au in particular) (*249*), reduction to black TiO_x (*250*) and nanostructural engineering by preparation of nanocrystals (*200*). Extended light absorption was shown to improve the catalytic performance of TiO_2 , but it isn't always effective for enhancing water splitting performance in PEC applications.

Coupling TiO_2 with visible light-absorbing moieties such as colored dyes is an alternative approach to enhance the photocatalytic efficiency of TiO_2, largely employed in the field of solar cells (*i.e.* dye-sensitized solar cells (DSSCs)) (*32*). Instead of changing the optical properties of the semiconductor, a dye acts as a photosensitizer, or antenna, whose main purposes are to efficiently absorb Vis light and to trigger the remaining steps of the water splitting process by electron injection into TiO_2 CB. Figure 5.1 illustrates the working mechanism of a dye-sensitized Pt/TiO_2 photocatalyst for H_2 production, summarized in Equations 5.2-5.5.

Figure 5.1 Graphical representation of the working mechanism for H_2 production over dye-sensitized Pt/TiO_2 photocatalysts.

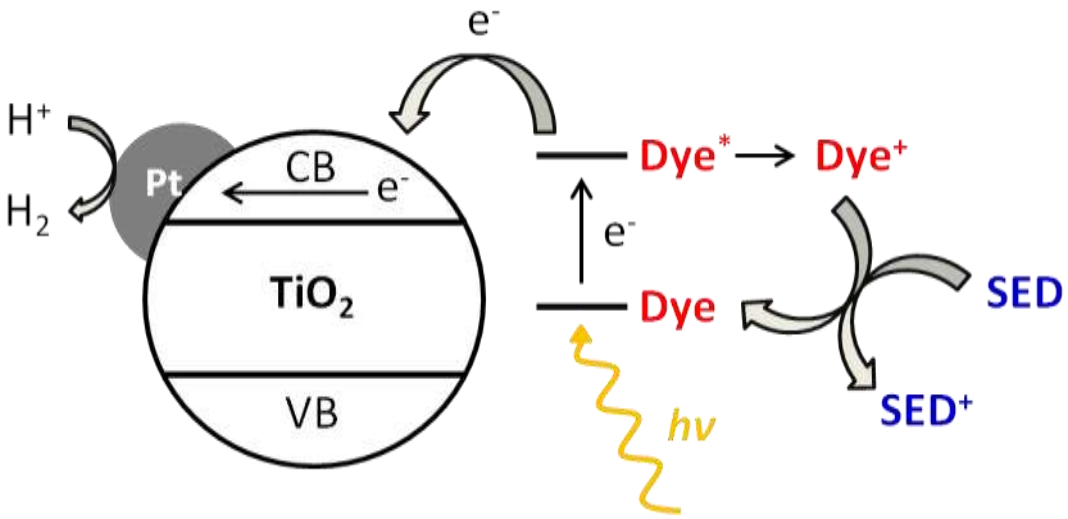

$$Pt/TiO_2/Dye \xrightarrow{h\nu} Pt/TiO_2/Dye^* \quad (5.2)$$

$$Pt/TiO_2/Dye^* \rightarrow Pt/TiO_2(e^-)/Dye^{+\cdot} \quad (5.3)$$

$$Pt/TiO_2(e^-)/Dye^{+\cdot} + SED \rightarrow Pt/TiO_2(e^-)/Dye + SED^+ \quad (5.4)$$

$$Pt/TiO_2(e^-)/Dye + H^+ \rightarrow Pt/TiO_2/Dye + \frac{1}{2}H_2 \quad (5.5)$$

$$Pt/TiO_2/Dye^* \rightarrow Pt/TiO_2/Dye + h\nu \quad (5.6)$$

$$Pt/TiO_2(e^-)/Dye^{+\cdot} \rightarrow Pt/TiO_2/Dye \quad (5.7)$$

The dye absorbs a photon and enters an excited state (5.2). Electron injection into the CB of TiO_2 results in charge separation (5.3). Fast regeneration of the dye by oxidation of the SED agent must take place for an efficient process and high durability of the dye (5.4). Electrons are then transferred to Pt(0) nanoparticles adsorbed on the TiO_2 surface, on which water (H^+) is reduced to molecular hydrogen (5.5). The ideal process can be hindered by some unwanted events. The two main causes of loss in activity are reported in Equations 5.6-5.7: the relaxation of the dye to its ground state before electron injection into the CB of the semiconductor (5.6) and hole–electron recombination between TiO_2 and dye (5.7), which is in competition with H_2 generation (5.5) and dye regeneration (5.4) steps.

Most photocatalytic studies are performed in a suspension of dye-sensitized TiO_2 particles covered by Pt, which is deposited through impregnation or photodeposition from H_2PtCl_6 under UV irradiation conditions (*251*). Dye staining is performed by suspending Pt/TiO_2 powders in a dye solution (usually, less than 1 g of powder in some mL of a mM solution of the dye) for a few hours in the dark. The powders are then separated through centrifugation, washed and dried. In order to estimate the amount of adsorbed dye, its concentration in the residual staining solution can be ascertained by UV/Vis spectroscopy.

In order to test the dye/Pt/TiO_2 catalytic activity, the material is suspended in an aqueous medium containing the SED agent. Typical SEDs are triethylamine (TEA), triethanolamine (TEOA), and ethylenediaminetetraacetic acid (EDTA), but also other inorganic (*e.g.*, S^{2-}, SO_3^{2-}, Fe^{2+}, Ce^{3+}, I^-, Br^-, and CN^-) and organic (alcohols, aldehydes, acids) SEDs have also been investigated (*252*). The pH of the reaction mixture is typically adjusted to neutral. The photoreactor is then evacuated to remove oxygen and irradiated with a Xenon lamp or a solar simulator provided with a UV filter at ca. 400–410 nm in order to cut off the UV portion of the irradiation to avoid direct TiO_2 excitation of electrons to the CB of the semiconductor. The produced hydrogen gas is finally quantitatively

determined with a gas chromatograph equipped with a thermal conductivity detector (TCD). The amount of hydrogen evolved over time and the relative rates of production (typically in the order of μmol h^{-1}) are usually normalized to the weight of the catalytic powder (μmol h^{-1} g^{-1}) for practical reasons or to the surface area of the semiconductor for a correct comparison between different materials (*253*). Since the light absorption is correlated to the presence of dyes, the obtained values of hydrogen production can be compared only among catalysts having similar loadings of dye and co-catalyst. In order to evaluate and compare the performance of photocatalytic systems having the same surface area, some specific parameters are used, such as TON, TOF and LFE which are defined in Section 2.11.

Sensitizers for photocatalytic H_2 production can be classified in three main categories: organometallic complexes, natural or bio-inspired dyes, and metal-free organic dyes. Organometallic complexes have been widely investigated in DSSCs applications, but in spite of the high performances in DSSCs, their activity in H_2 production is (with some exception) not exceptional (*254*). The first class of organic dyes that was deeply investigated is that of emissive dyes, but the donor–acceptor molecular architecture represents a more general and interesting approach for the design of organic sensitizers. A donor–acceptor structure is composed of three sub-molecular units: an electron-donor group (D), a π-spacer (π), and an electron-acceptor group (A). The D–π–A framework has often been used in material science because it is associated with efficient charge separation. Donor–acceptor dyes follow an oxidative quenching mechanism, in which the donor is excited, injects an electron to the CB of TiO_2 and the oxidized dye (dye^+) is then regenerated by the sacrificial agent (*46*). After electron donation from the excited state, the hole of the oxidized dye resides in the HOMO, localized in the D moiety. Therefore, the D group should lie as far from the TiO_2 surface as possible, in order to prevent charge recombination, and as close to the SED as possible in order to favor dye regeneration. π-Spacers are polarizable conjugated aromatic and heteroaromatic groups able to efficiently transfer charge between D and A moieties and to extend the π-conjugated framework for improved optical properties and light harvesting. The nature of the spacer unit plays an important role in stabilizing the dye under irradiation. The A group is a strong electron-withdrawing moiety, able to promote charge separation in the excited state. The molecular LUMO, from where electron injection into TiO_2 takes place, is typically located in the terminal A component. Therefore, the A group is covalently anchored to the semiconductor surface by a functional group, to keep it in close proximity to the catalytic center (*46*).

Careful molecular design of the sensitizer is of fundamental importance to develop efficient and stable hydrogen production photocatalysts. The efficiency of a dye depends in first place on its optical properties. In order to be efficient, a sensitizer requires precise tuning of HOMO/LUMO energetic levels (*46*, *251*). In particular, the energy of the LUMO should be higher than the CB of the

semiconductor to allow electron donation, while dye regeneration can only take place if the HOMO energy level of the dye is lower than that of the SED. HOMO and LUMO energies can be experimentally determined electrochemically (*e.g.* Cyclic Voltammetry – CV) or optically (Tauc plots) and their shapes and energies can be calculated via *ab initio* computations, mostly based on the DFT method (*46*). Many other factors influence the performance of a dye-sensitized photocatalyst, such as dye stability upon irradiation, wettability of the semiconductor surface by water after staining (dictated by ancillary functionalities of the dye), anchoring unit stability and injection efficiency (*46*).

The most widely investigated donor–acceptor sensitizers for dye-sensitized photocatalytic H_2 production are based on triarylamines (TAA) and phenothiazines (PTZ) D moieties (*46*) (Figure 5.2). The PTZ core has particular features associated with its non-planar butterfly conformation along the S–N axis. This arrangement helps to minimize the negative effects associated with self-quenching molecular aggregates on the TiO_2 surface. PTZ contains two symmetric benzene rings which can be conveniently functionalized, allowing the design of symmetric di-branched dyes. Such dyes present high anchoring stability and electron injection efficiency, improved optical properties, and enhanced device stability (*255*). Furthermore, the nitrogen atom of the central heteroaromatic ring can be conveniently functionalized in order to tune additional properties, such as water solubility. Finally, in comparison with other donor groups, the PTZ ring radical cation form is very stable, thereby facilitating electron donation and regeneration by SED.

Figure 5.2

Typical PTZ-based sensitizers structure: the N-functionality (R) can be an alkyl chain of variable length, or a hydrophilic moiety. The π spacer units, here for di-branched dyes, are usually composed of one or more functionalized or simple heterocyclic groups (*e.g.* thiophene, 2,2'-bithiophene, 1,4-thiophthene). The most common anchoring group (cyanoacrylic) is also depicted.

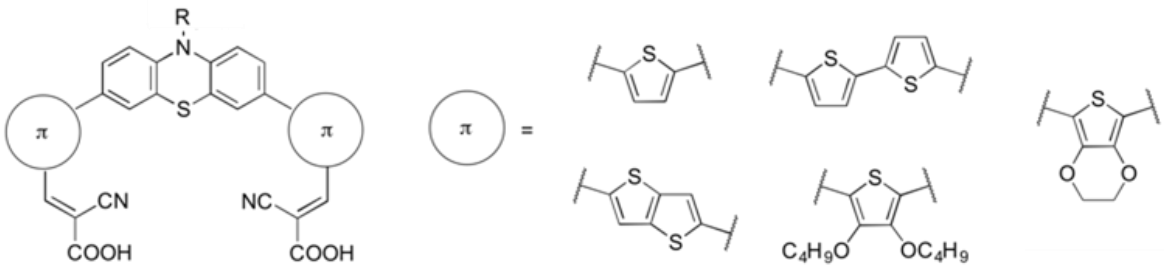

In the following sections, we report the rational molecular design of donor-acceptor dyes based on the PTZ D core aimed to enhance the H_2 production performances of Pt/TiO_2 sensitized photocatalysts. In particular, the effect of peripheral functionalization (aimed to increase surface wettability) and heteroatom substitution in the D core and π-spacers will be discussed. Finally, some future perspective on H_2 sustainable photocatalytic production from EtOH/water mixtures will be presented.

5.2 Phenothiazine-based Sensitizers: N-functionalization Effect

5.2.1 Introduction

In this section, we investigate the effect of hydrophilic substituents of the PTZ moiety of a dye-sensitized TiO_2 photocatalyst (TiO_2-NP) on the photocatalytic hydrogen production from aqueous solutions. One of the most common strategies to induce hydrophilicity to organic dyes is the introduction of a polyethylene glycol functionality, such as the widely used tris(ethylene glycol) monomethyl ether (TEG) group (*256*). More recently, the use of poly-glycolic functionalities as substituents in organic molecules for dye-sensitized hydrogen generation has been also reported (*257*). In this study, TEG (**PTZ-TEG**), sugar methyl α-D-glucopyranoside (**PTZ-GLU**) and (*n*-octyl) (**PTZ-ALK**) derivatives of a thiophene-based PTZ dye were synthesized, characterized and tested for sensitization of Pt/TiO_2 (Figure 5.3).

Figure 5.3 PTZ-based sensitizers investigated in this work.

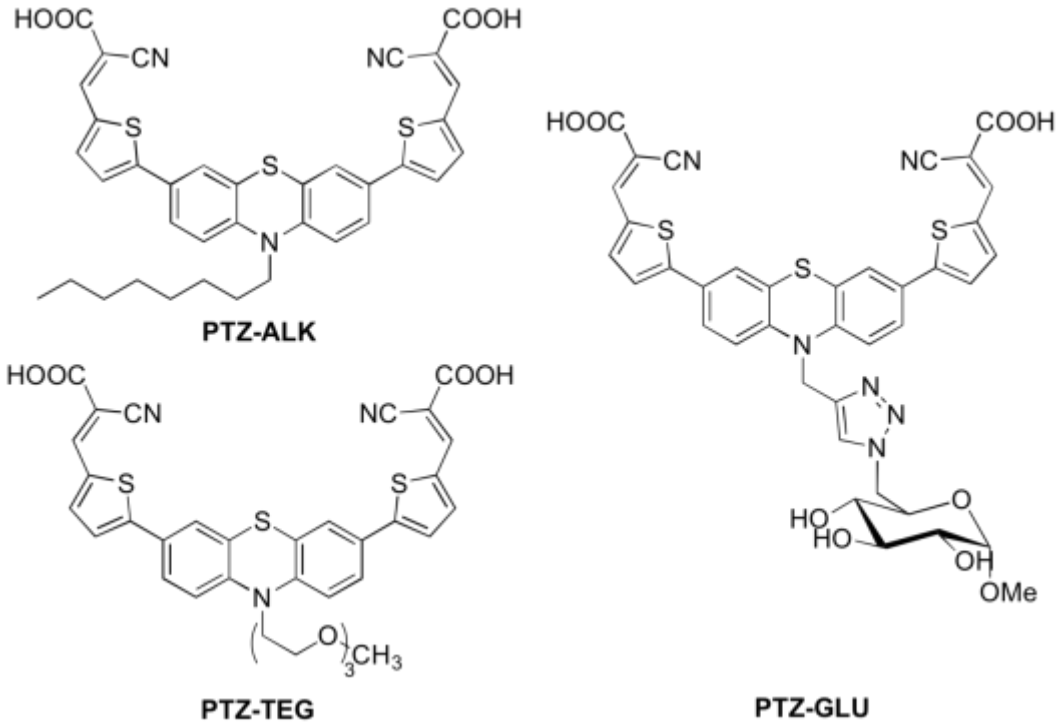

The multifunctional scaffold methyl α-D-glucopyranoside was employed in order to further tune water affinity of sensitizers and to induce additional properties such as intermolecular self-assembly. Carbohydrates are excellent hydrogen bond donors and acceptors because of their multiple hydroxyl functions and can therefore induce self-assembly (*258*). The unprecedented use of a sugar functionalization in this field was demonstrated to improve the wettability of TiO_2

materials after staining, compared to both **PTZ-ALK** and **PTZ-TEG**. The sunlight-driven H_2 production can be related to the chemical structure of the dyes and to the distinct features of the side functionalities, both in terms of evolution rates and TON.

5.2.2 Catalyst Synthesis and Characterization

In order to modify the wettability properties of the catalyst surface without interfering with the conjugated π skeleton of the sensitizer (which is responsible for the light harvesting step of the photocatalytic process), the hydrophilic groups were introduced on the terminal electron-rich D core of PTZ by exploiting the nitrogen site of the heterocyclic ring. A methylene linker was used in order to block communication with the π system. In this way no modification of on the π-conjugated system was induced and the effect of the terminal groups on H_2 production was only related to wettability of the sensitized photocatalyst. The sugar functionality of **PTZ-GLU** has been introduced by exploiting click chemistry and Cu-assisted azide–alkyne Huisgen cycloaddition (*259*, *260*). Although alternative synthetic paths could be envisaged, click chemistry approach was chosen in order to ensure design flexibility, extension to a library of glycoconjugated dyes (*261*), and complete transfer to the industrial scale. The sugar is in form of α-methyl glucopyranoside in order to prevent any possible redox interference of the anomeric free aldehyde with the photocatalytic cycle of the sensitizer. For details about dyes synthesis procedure and characterization, see Ref. (*262*).

The absorption spectra of dyes **PTZ-ALK**, **PTZ-TEG**, and **PTZ-GLU** are reported in Figure 5.4 and the main optical and energetic (HOMO–LUMO energies) parameters are listed in Table 5.1. As expected, the optical properties of the three dyes were not significantly affected by the nature of the functionality. The three dyes showed a typical intense π–π* absorption band in the Vis region attributed to the intramolecular charge-transfer transition. The position of the absorption maximum is about 470 nm whereas peak molar absorptivity is slightly different for the three dyes.

Figure 5.4 Absorption spectra of dyes **PTZ-ALK**, **PTZ-TEG** and **PTZ-GLU** in THF

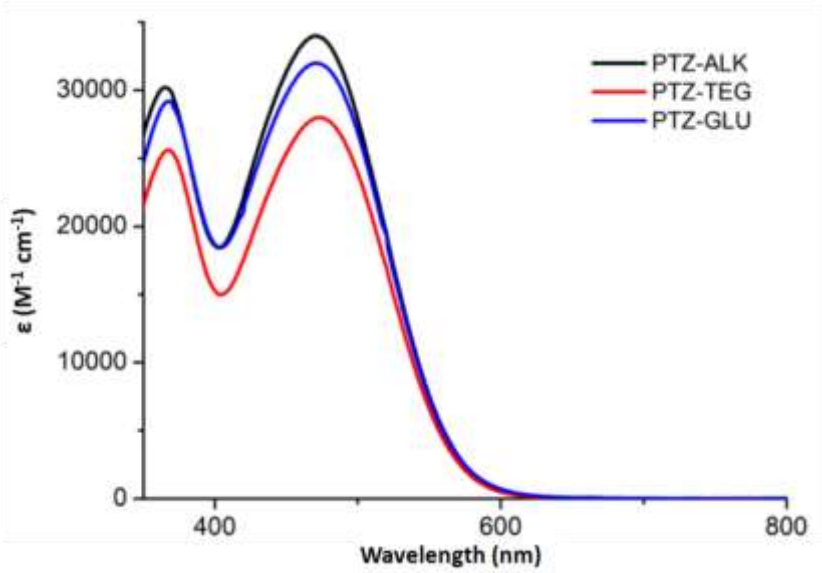

Table 5.1 Optical and electrochemical characterization of dye **PTZ-ALK, PTZ-TEG** and **PTZ-GLU**. **PTZ-ALK** values from Ref. (*262*); for CV and DPV plots: Ref. (*262*).

Sample	λ[a] (nm)	ε (M^{-1} cm^{-1})	V_{ox} (V vs. Fc) ± 10 mV	HOMO[b] (eV) ± 0.1 eV	V_{red} (V vs. Fc) ± 10 mV	LUMO[b] (eV) ± 0.1 eV
PTZ-ALK	470	34000 ± 1000	0.15	-5.4	-	-3.3
PTZ-TEG	470	28000 ± 1000	0.33	-5.5	-1.52	-3.7
PTZ-GLU	471	32000 ± 1000	0.30	-5.5	-1.49	-3.7

[a] Dye solution 10^{-3} M in THF
[b] Vacuum potential = Fc/Fc^{+} + 5.2V

Contact angle analysis was used to investigate the hydrophilicity properties of the sensitized TiO_2 nanoparticles. The contact angles of a DI water drop on the surface of a film of sintered TiO_2 and the corresponding dyes-sensitized films are shown in Figure 5.5. Data are summarized in Table 5.2. The bare TiO_2 and the hydrophilic dyes-sensitized films have contact angles lower than 35°, compared to 117° for the hydrophobic dye **PTZ-ALK**. The sugar functionality in **PTZ-GLU** is able to improve water affinity by further decreasing the angle from 34° in the **PTZ-TEG** dye to 27°, thus going closer to the bare TiO_2-NP surface character.

Figure 5.5 Cross-sectional images of a film of sintered TiO_2-NP (a) and corresponding samples sensitized with **PTZ-ALK** (b), **PTZ-TEG** (c) and **PTZ-GLU** (d).

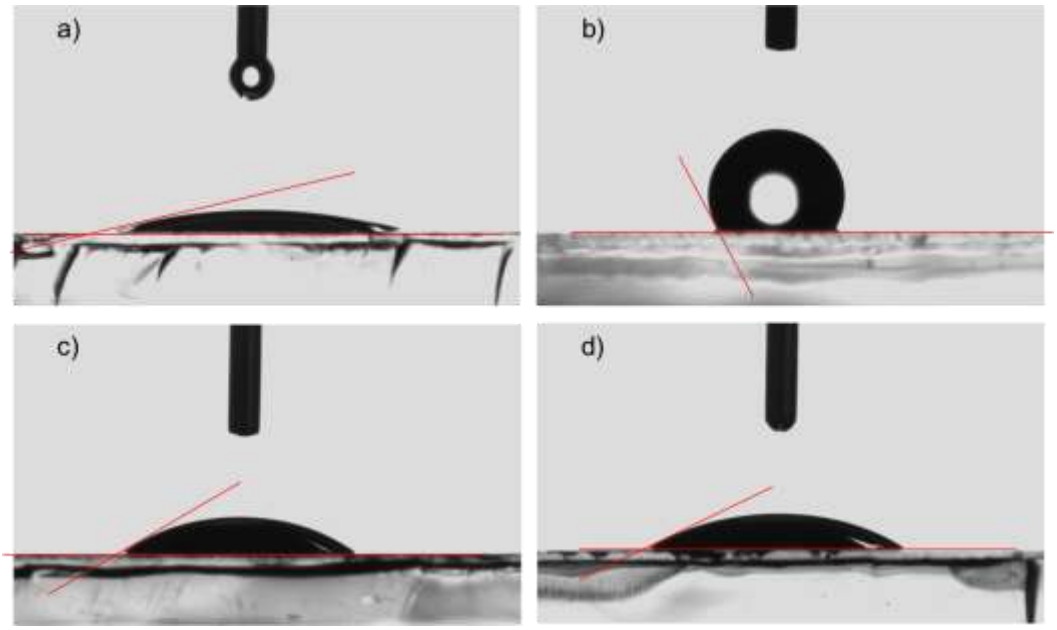

Table 5.2 Contact angle and photocatalytic performance of the dye/Pt/TiO_2 materials in H_2 production from TEOA 10% v/v solution at pH = 7.0 under irradiation with visible light (λ > 420 nm).

Sample	Dye loading (μmol g^{-1})	Contact angle θc (°)	H_2 amount [a] (μmol g^{-1})
Pt/TiO_2-NP	-	13.9	-
PTZ-ALK	30.0	117.3	1060
PTZ-TEG	30.0	33.9	421
PTZ-GLU	30.1	26.8	865

[a] Overall H_2 amount produced after 20 h of irradiation

A Pt/TiO_2 nano-powder was used as benchmark material to test the comparative sensitization ability of the new synthesized dyes under irradiation with visible light (λ > 420 nm). The deposition of Pt nanoparticles on TiO_2 Degussa P25 was done through a previously reported photodeposition method (*257*, *263*). 32.7 mg of $Pt(NO_3)_2$ was dissolved in 300 mL of a solution of water/methanol 1:1 v/v. 2.0 g of TiO_2 Degussa P25 were suspended in the Pt solution in order to

achieve a metal loading of 1.0 wt%. After stirring for 1 h in the dark, the suspension was irradiated with a 450 W medium pressure lamp for 4 h. The Pt/TiO_2 nanocomposites were collected by centrifugation, washed 3 times with water and finally dried at 80 °C overnight. The TiO_2 P25 support was an anatase/rutile mixture (~70/30 by weight) with mean crystallite sizes of 20 nm for both phases. Textural analysis revealed a surface area of 55 $m^2 g^{-1}$ with pores diameters around 48 nm and a pore volume of 0.242 mL g^{-1}. HAADF-STEM analysis (Figure 5.6) evidenced the irregular shape of TiO_2 particles (12–45 nm), with Pt nanoparticles with mean size of 2.4 nm homogenously distributed on the surface of the support.

Figure 5.6 Representative HAADF-STEM images of the Pt/TiO_2 nanocomposite.

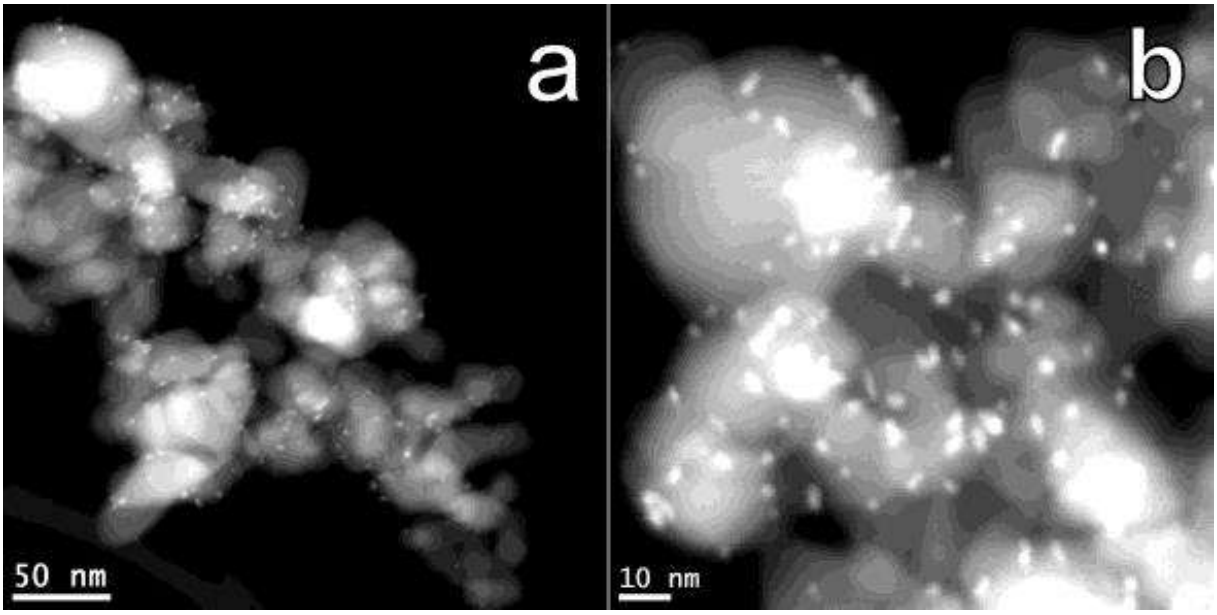

The PTZ-based dyes (**PTZ-ALK**, **PTZ-TEG** and **PTZ-GLU**) have been adsorbed on Pt/TiO_2 nanocomposite by suspending 200 mg of Pt/TiO_2 nanocomposite in 10 mL of dye solution in ethanol for 24 h in the dark. The concentration of the dye was adjusted in order to obtain the desired loading, between 1.0 and 30.0 μmol g^{-1}. The obtained materials were recovered by centrifugation, washed 2 times with 10 mL EtOH each and dried under vacuum at room temperature overnight. UV-vis spectra of the solutions after dye adsorption showed that the amount of residual dyes is negligible, confirming the quantitative adsorption of the dyes on Pt/TiO_2.

5.2.3 H_2 Photocatalytic Production Experiments

The Pt/TiO_2 photocatalysts sensitized by **PTZ-ALK**, **PTZ-TEG** and **PTZ-GLU** were tested for H_2 production under Vis light ($\lambda > 420$ nm) from a triethanolamine (TEOA)/HCl aqueous buffer solution at pH = 7.0. Following the "best practice in photocatalysis" reported by Kisch and Bahnenmann (*45*), the experimental conditions have been optimized measuring the H_2 production rate after stabilization (see below) using different amounts of the photocatalyst. This preliminary optimization was performed using the **PTZ-GLU**/Pt/TiO_2 photocatalyst with a dye loading of 30 μmol g^{-1} (Figure 5.7). Maintaining constant all the other experimental factors (geometry of irradiation and reactor, volume of the TEOA/HCl solution, temperature, *etc.*), the maximum H_2 production rate has been obtained using 60 mg of the photocatalyst, with a slight decrease for higher amounts likely due to increased scattering of the incoming photons.

Figure 5.7 Optimization of the experimental conditions for photocatalytic H_2 production.

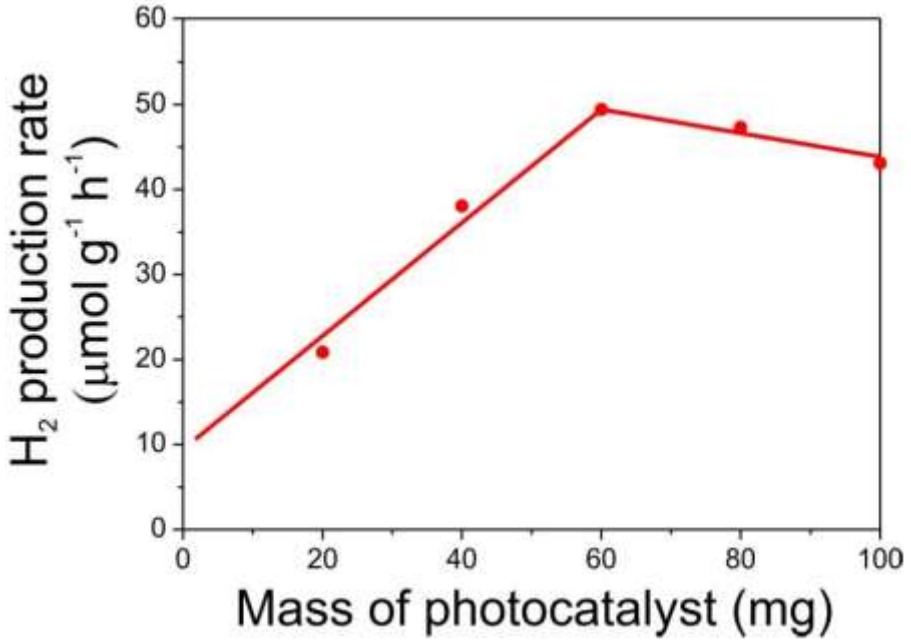

For all the sensitized photocatalysts investigated in this study, the H_2 production rates increased in the first hours of irradiation until reaching a constant mean value (Figure 5.8). This phenomenon arises from the combination of two factors. First, diffusion of produced H_2 in the dead volume of the photoreactor resulted in the progressive increase of H_2 concentration in the gaseous effluent for the system, which typically accounts for the first 1–2 h of time-on-stream. Second, activation of the photocatalyst took place at the beginning of each photocatalytic experiment, likely because the Pt nanoparticles were passivated by the adsorbed oxygen resulting

from exposure to air after photodeposition. The activation period is significantly lower for the hydrophilic dye, likely because of the better interaction with the aqueous reactants. Notably, no H_2 production was observed using the bare Pt/TiO_2 under the same experimental conditions. Moreover, the contribution of degradation of the glucose group in the photocatalytic process can be reasonably ruled out: a **PTZ-GLU**/Pt/TiO_2 catalyst (loading = 10 μmol g^{-1}) without the sacrificial donor TEOA afforded a H_2 production rate below the instrument detection limit (~3 μmol H_2 g^{-1} h^{-1}).

Figure 5.8 H_2 production rates from TEOA 10% v/v solution at pH 7.0 under irradiation with visible light (λ > 420 nm) measured over the dye/Pt/TiO_2 materials. Numbers in the legends correspond to the dye loading in μmol g^{-1}.

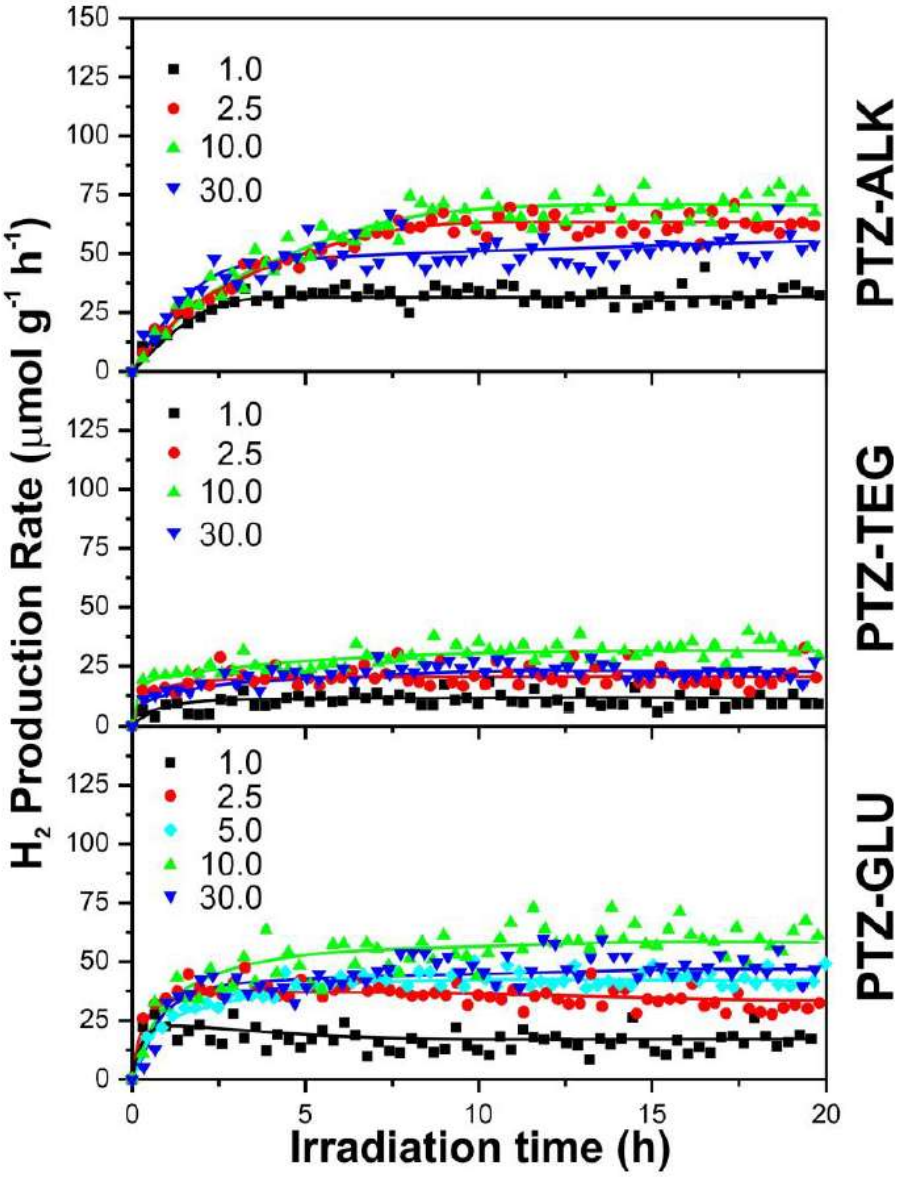

The comparison of the H_2 production rates as a function of the dye loading showed different behavior for the photocatalysts sensitized with the investigated dyes (Figure 5.9). The effect of dye loading on the performance of photocatalysts with **PTZ-ALK** and **PTZ-TEG** shows the same trend, although the hydrophobic dye afforded a better performance. A sharp increase in the activity is observed for dye loadings below 2.5 μmol g^{-1}, while for higher loading the activity increment is modest. The photocatalysts sensitized by **PTZ-GLU** showed a different trend, with the H_2 productivity increasing up to the loading of 10 μmol g^{-1}.

Figure 5.9 Production rates in H_2 evolution from TEOA 10% v/v solution at pH = 7.0 under irradiation with visible light (λ > 420 nm) using the Pt/TiO_2 materials sensitized with **PTZ-ALK**, **PTZ-TEG** and **PTZ-GLU**.

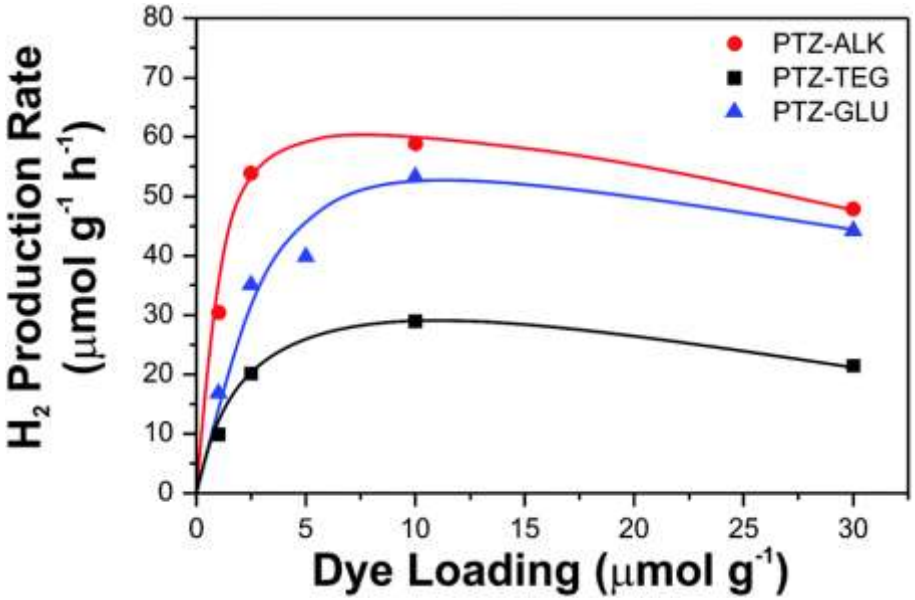

The different behavior of the dyes in sensitizing Pt/TiO_2 photocatalysts can be rationalized in terms of their structure. The comparative trends are in agreement with the similar molecular geometry of **PTZ-ALK** and **PTZ-TEG**, in which a linear and flexible terminal chain is present. In the case of **PTZ-ALK**, the chain is reasonably coiled up because of repulsion from the aqueous solution, suppressing intermolecular quenching. This phenomenon does not take place in the case of **PTZ-TEG**, where the polar group is likely unrolled allowing π–π interaction between the heteroaromatic units.

The **PTZ-GLU** sensitized photocatalysts showed H_2 production rates comparable to **PTZ-ALK** for high loadings (>10 μmol g^{-1}), while at small loadings the rates were much lower. **PTZ-GLU** has a bulky side chain, with a considerably smaller degree of freedom compared to the ALK and TEG chains. In fact, whereas a rigid cyclic substituent is present for **PTZ-GLU**, in **PTZ-**

ALK and **PTZ-TEG** the side chains are endowed with free rotation along single bonds. This suggests a distinct arrangement of **PTZ-GLU** on the surface of Pt/TiO_2. At high loadings, the organization of **PTZ-GLU** becomes somewhat more similar to that of **PTZ-ALK**, with the PTZ units interacting with the Pt/TiO_2 surface and the bulky lateral chains avoiding intermolecular quenching. Notably, the glucose functionality could also induce some sort of supramolecular organization on the surface (*258*, *264*). For low loading of **PTZ-GLU**, the glucose unit could interact directly with the TiO_2 surface through the remaining OH groups and this might change the orientation of the PTZ scaffold, affecting the electron transfer to TiO_2.

TON values and Light-to-Fuel Efficiency (LFE_{20}) measured after 20 h of irradiation (Figure 5.10 and Table 5.3) showed that the efficiency of light conversion into effective electrons to H_2 increased as the dye loading decreased, in agreement with the aforementioned discussion relating the molecular structure to the photocatalytic activity.

Figure 5.10 TON in H_2 evolution from TEOA 10% v/v solution at pH = 7.0 under irradiation with visible light (λ> 420 nm) using the Pt/TiO_2 materials sensitized with PTZ-ALK, PTZ-TEG and PTZ-GLU.

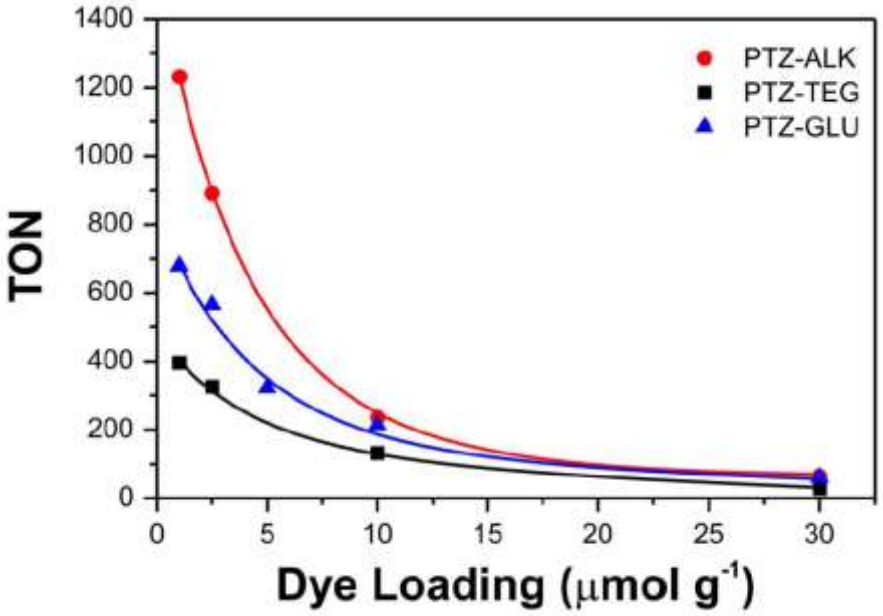

Table 5.3 TON values and Light-to-Fuel Efficiencies (LFE) of dye **PTZ-ALK**, **PTZ-TEG** and **PTZ-GLU**.

Dye Loading ($\mu mol\ g^{-1}$)	TON (20 h)			LFE (%)		
	PTZ-ALK	PTZ-TEG	PTZ-GLU	PTZ-ALK	PTZ-TEG	PTZ-GLU
1.0	1232	396	678	0.017	0.005	0.008
2.5	892	326	566	0.034	0.011	0.016
10.0	236	132	213	0.040	0.017	0.031
30.0	64	29	59	0.029	0.013	0.026

5.2.4 Conclusions

In conclusion, a sugar derivative of a multi-branched organic sensitizer (**PTZ-GLU**) has been efficiently used in the dye-sensitized photocatalytic production of H_2 through careful catalyst design. The insertion of the glucose unit yielded a higher affinity towards the aqueous medium compared to the commonly used hydrophilic TEG functionality, while maintaining the high activity recorded for the alkyl derivative. On the basis of contact angle measurements, photocatalytic data, and the peculiar structural features of the side substituents, the distinct behavior of **PTZ-GLU** was ascribed to the rigid, bulky, hydrophilic geometry of the glucose ring. The lower degrees of freedom and the extra-wettability of the **PTZ-GLU** dye favored the interaction with the reactants in aqueous solution, suppressing intermolecular quenching. The general and scalable synthetic approach can be adapted to a large variety of sugar derivatives, to synthesize photosensitizers having finely tuned properties, and to study their effect on the efficiency of H_2 photocatalytic production.

5.3 Carbazole-based Sensitizers

5.3.1 Introduction

In this section, we report a rational investigation of the effect of heteroatoms replacement (or removal) in a previously reported **PTZ** dye on the H_2 production over sensitized Pt/TiO_2 photocatalysts. In particular, new sensitizers were prepared by replacing the **PTZ** donor core with either a carbazole (**CBZ**) or a phenoxazine (**POZ**) moiety, and by replacing the thiophene spacers with furan spacers. The **CBZ**-based dyes were demonstrated to be much more efficient as Pt/TiO_2 sensitizers in the H_2 photocatalytic production, compared to both **PTZ** and **POZ** based dyes. The amount of produced H_2 and turnover numbers (TON) are top-ranked amongst studies on dye-sensitized photocatalytic hydrogen production (*46*).

CBZ-based systems are widely studied in the fields of materials science (*44*, *265*, *266*), and in dye-sensitized solar cell (DSSCs) (*267–269*), only very few studies on photocatalysis have been reported (*270–272*). Whereas **PTZ** has a bent, butterfly structure (*273*), **CBZ** is planar and contains a 5-member electron-rich heteroaromatic ring, with a pyrrole-like N atom (*274*). The planar structure could enhance the photocatalytic efficiency of the sensitized Pt/TiO_2 system because of favoured charge generation and transport in the dye. In order to separate the effects of S atom replacement and of dye structure, **POZ** donor groups (having a butterfly structure and an O atom instead of S) were investigated. To study the role of sulfur in the spacer unit, new dyes were designed by replacing thiophene (**Th**) π-spacers with furan rings (**Fu**), which have many electronic and structural properties in common, with the exception of the nature of the ring heteroatom (*274*). The structures of the dyes reported in this section are summarized in Figure 5.11.

Figure 5.11 The sensitizers investigated in this work and their structure.

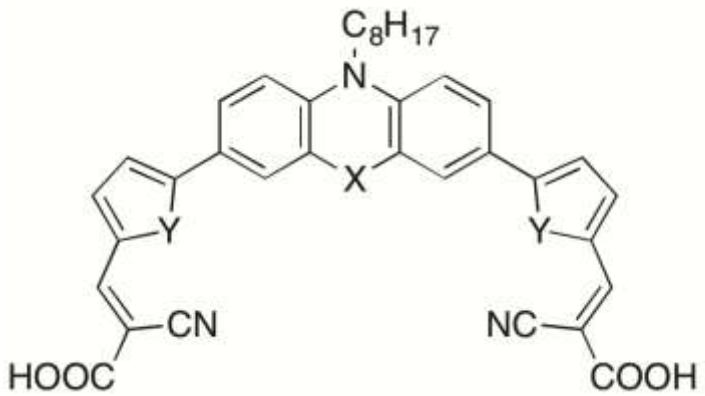

PTZ-Th: X = S, Y = S
PTZ-Fu: X = S, Y = O
POZ-Th: X = O, Y = S
POZ-Fu: X = O, Y = O
CBZ-Th: X = none, Y = S
CBZ-Fu: X = none, Y = O

5.3.2 Catalyst Synthesis and Characterization

The dyes investigated in this work were synthesized in the research group of Professor Alessandro Abbotto (Bicocca University - Milan) by modifying the previously reported procedure for the synthesis of **PTZ-Th** (**PTZ-ALK** in the previous section) (*262*). The same synthetic scheme (Figure 5.12) was adopted for all the dyes. A detailed discussion on the synthesis is out of the purpose of the present thesis. Briefly, Suzuki cross-coupling (Figure 5.12i) was adopted to react the D-core organobromide derivative **1** with the desired π-spacer precursor (commercially available 2-furanaldehyde-5-boronic acid for **Fu** dyes and 2-thiophenealdehyde-5-boronic acid for **Th** dyes). In order to functionalize the dye with the anchoring unit, a Knoevenagel condensation was employed (Figure 5.12 ii), starting from the dye aldehyde precursor **2**, which was reacted with cyanoacetic acid and piperidine to yield the final dye upon purification. Although the synthesis of **CBZ-Th** and a molecule similar to **CBZ-Fu** (bearing a different *N*-alkyl functionalization) have been previously reported in the literature (*269*, *275*), the **CBZ**-based sensitizers were synthesized by the aforementioned general approach using 3,6-dibromocarbazole as a starting reagent while **POZ** derivatives were synthesized from 10-octyl-10H-phenooxazine-3,7-dibromo.

Figure 5.12 General synthetic procedure for dyes **PTZs**, **POZs**, **CBZs**. Reagents and conditions: (i) 5-formyl-2-arylboronic acid, $Pd(dppf)Cl_2 \cdot CH_2Cl_2$ [dppf = 1,1′-bis(diphenylphosphino)ferrocene], K_2CO_3, DME/MeOH, microwave 100 °C, 90 min; (ii) cyanoacetic acid, piperidine, $CHCl_3$, reflux, 5 h.

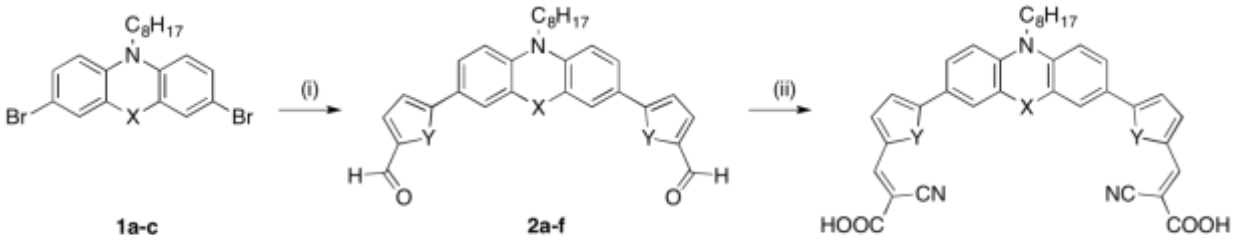

1a-c

a: X = S
b: X = O
c: X = none

2a-f

a: X = S, Y = S
b: X = S, Y = O
c: X = O, Y = S
d: X = O, Y = O
e: X = none, Y = S
f: X = none, Y = O

PTZ-Th: X = S, Y = S
PTZ-Fu: X = S, Y = O
POZ-Th: X = O, Y = S
POZ-Fu: X = O, Y = O
CBZ-Th: X = none, Y = S
CBZ-Fu: X = none, Y = O

The absorption spectra of the dyes (1.0 10^{-5} M in DMSO) are shown in Figure 5.13 and the detailed main optical and energetic parameters (HOMO-LUMO energies) are listed in Table 5.4. In general, the three families of **PTZ**, **POZ** and **CBZ** dyes exhibited 2 typical bands, related to π-π* absorption in the 300 – 450 nm range and to the intramolecular charge transfer (ICT) transition in the 400-600nm range (*43*, *269*). The π-π* band shows a progressive red-shift in the order **POZ**-**PTZ**-**CBZ**, as a result of increased electron delocalization in the core. On the other hand, the ICT transition is subjected to a progressive blue-shift. As a result, π-π* and ICT transitions significantly overlap for the **CBZ** derivatives. The absorption maxima are centered around *ca.* 470 nm for **PTZ**, ca. 410 nm for **CBZ** and ca. 530 nm for the **POZ** dyes. The maximum molar absorptivity is higher for the **CBZ** derivatives, whereas marginal differences (less than 10%) are recorded between **PTZ** and **POZ** dyes. Finally, the introduction of the **Fu** spacer in place of **Th** did not significantly affect the absorption properties.

Figure 5.13 Absorption spectra of the **PTZs**, **CBZs** and **POZs** dyes recorded in DMSO solution.

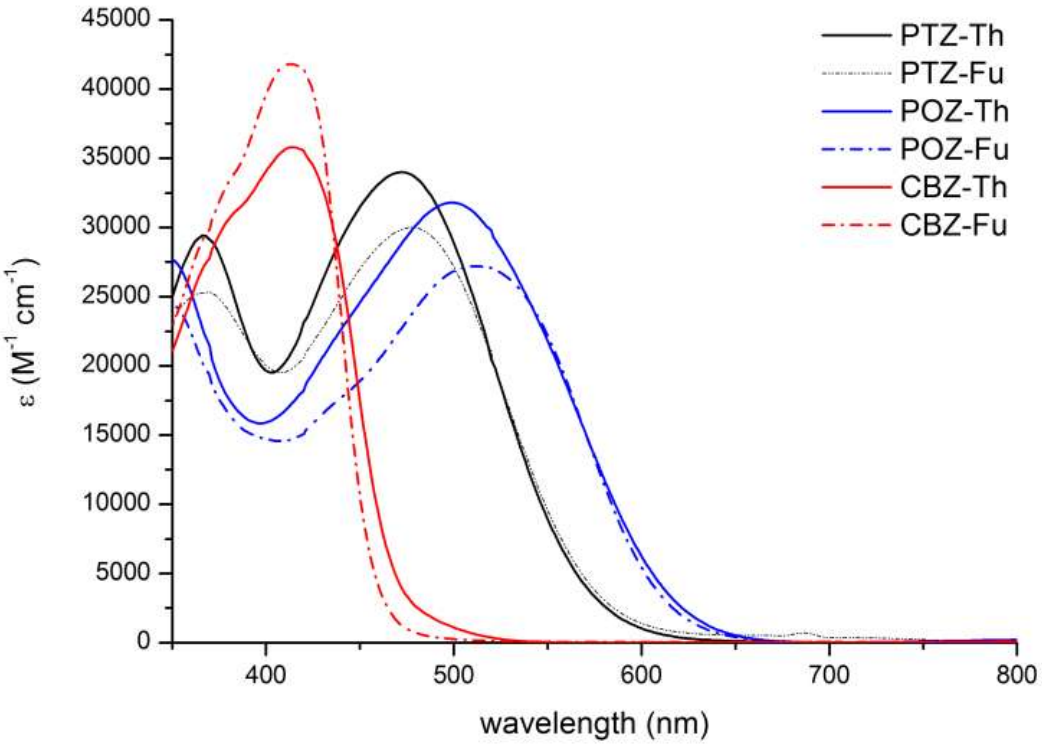

Table 5.4 Main optical and electrochemical characterization of the **PTZs**, **CBZs** and **POZs** dyes. Values for **PTZ-Th** from (*262*); for CV DPV plots see: Ref. (*262*).

Sample	$\lambda^{[a]}$ (nm)	ε (M^{-1} cm^{-1})	V_{ox} (V vs. Fc) ± 10 mV	HOMO[b] (eV) ± 0.1 eV	E_{gap}^{opt} (eV)	LUMO[b] (eV) ± 0.1 eV
PTZ-Th	470	34000 ± 1000	0.15	-5.38	2.05	-3.33
PTZ-Fu	481	30200 ± 700	0.36	-5.59	1.98	-3.61
POZ-Th	534	31800 ± 1500	0.41	-5.64	1.87	-3.77
POZ-Fu	524	27200 ± 200	0.38	-5.61	1.90	-3.71
CBZ-Th	414	35800 ± 100	0.41	-5.64	2.26	-3.38
CBZ-Fu	409	41800 ± 600	0.43	-5.66	2.28	-3.38

[a] Dye solution 10^{-3} M in THF
[b] Vacuum potential = Fc/Fc^+ + 5.23 V.

Differential Pulsed Voltammetry (DPV) was used to determine the HOMO energy levels from the current onset, while LUMO levels have been derived from electrochemical HOMO values and optical band gaps, measured by means of Tauc plots (*276*). Levels are pictorially shown in Figure 5.14. Even though the HOMO energy levels are quite similar for most of the dyes (~ -5.60 eV), their LUMO energies and, accordingly, the electron injection capabilities to the Pt/TiO_2 system are different. In particular, the LUMO energy of the **POZ** dyes, as well as that of **PTZ-Fu**, are very close to the conduction band (CB) of TiO_2 (-4.0eV) (*277*).

Figure 5.14 Experimental HOMO/LUMO energy levels for the dyes investigated in this work (CB level of TiO2 is included as a reference for electron injection from the dye to the semiconductor).

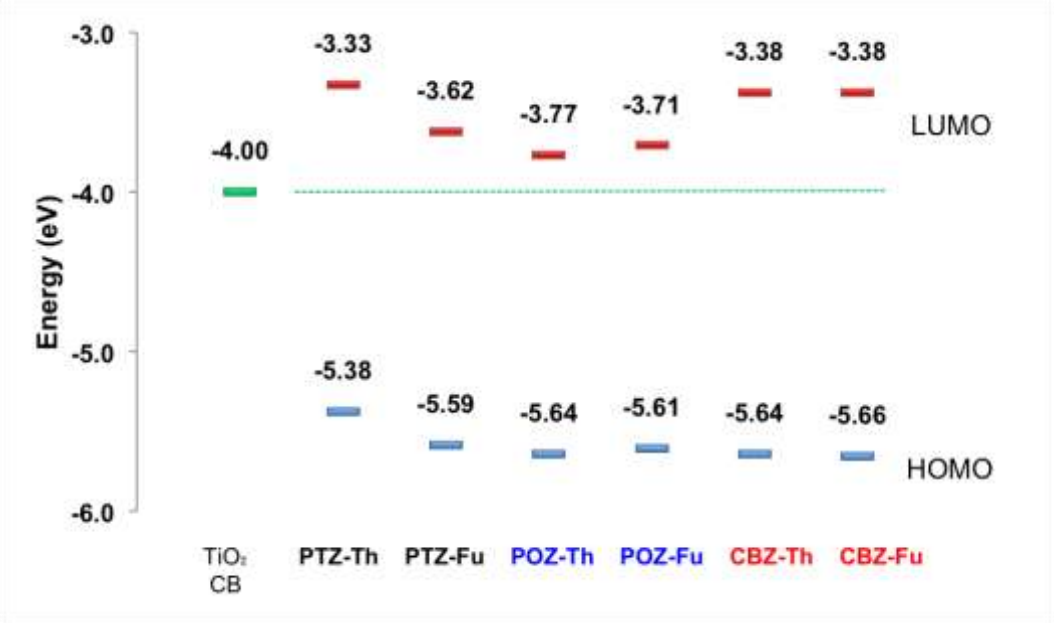

Sensitized Pt/TiO_2 nano-powder were prepared according to the procedure described in Section 5.4.2. Briefly, Pt nanoparticles were photodeposited on TiO_2 Degussa P25 and the dyes were adsorbed on Pt/TiO_2 nanocomposite by suspending the powder in a diluted dye solution. The concentration of the dyes was adjusted in order to obtain a loading of 10.0 μmol g^{-1}. UV-vis spectra of the solutions after dye adsorption showed that the amount of residual dyes is negligible, confirming the quantitative adsorption of the dyes on Pt/TiO_2.

5.3.3 Photocatalytic H_2 Production Experiments

The sensitized Pt/TiO_2 photocatalysts prepared were tested for H_2 production under Vis light irradiation (λ > 420 nm) from a triethanolamine (TEOA)/HCl aqueous buffer solution at pH = 7.0. The experiments were performed adopting the same conditions previously optimized for **PTZ**-based photocatalysts (*262*). No H_2 production was observed using the bare Pt/TiO_2 under the same experimental conditions. Measured H_2 production rates and H_2 productivity versus irradiation time are presented in Figure 5.15 and 5.16, respectively. TON and LFE_{20} calculated after 20 h of irradiation are presented in Figure 5.17 (obtained values are listed in Table 5.5).

All of the investigated catalysts showed remarkable stability over a reasonable irradiation time of 20 h (Figure 5.15). **CBZ**-sensitized photocatalysts showed by far the highest H_2 productivity, TON and LFE values. Namely, performances were at least one order of magnitude higher than

those referred to the benchmark **PTZ-Th** dye. Amongst **CBZ** based dyes, the photocatalytic activity of **CBZ-Th** was considerably higher than that of **CBZ-Fu**. The same relative trend was recorded for the **PTZ** family. Both **POZs**-sensitized photocatalysts demonstrated very small activity in H_2 production.

Figure 5.15 H_2 production rates from TEOA 10% v/v solution at pH = 7.0 under irradiation with visible light (λ> 420 nm) over Pt/TiO_2 materials sensitized with **PTZs**, **POZs** and **CBZs** dyes.

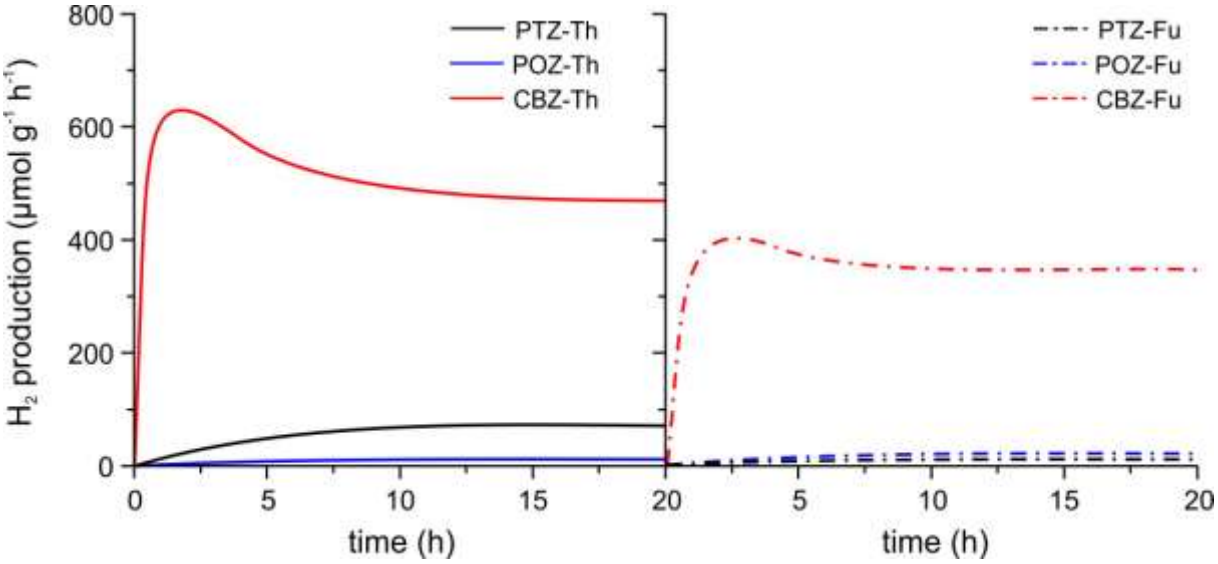

Figure 5.16 H_2 production from TEOA 10% v/v solution at pH = 7.0 under irradiation with visible light (λ> 420 nm) over Pt/TiO_2 materials sensitized with **PTZs**, **POZs** and **CBZs** dyes.

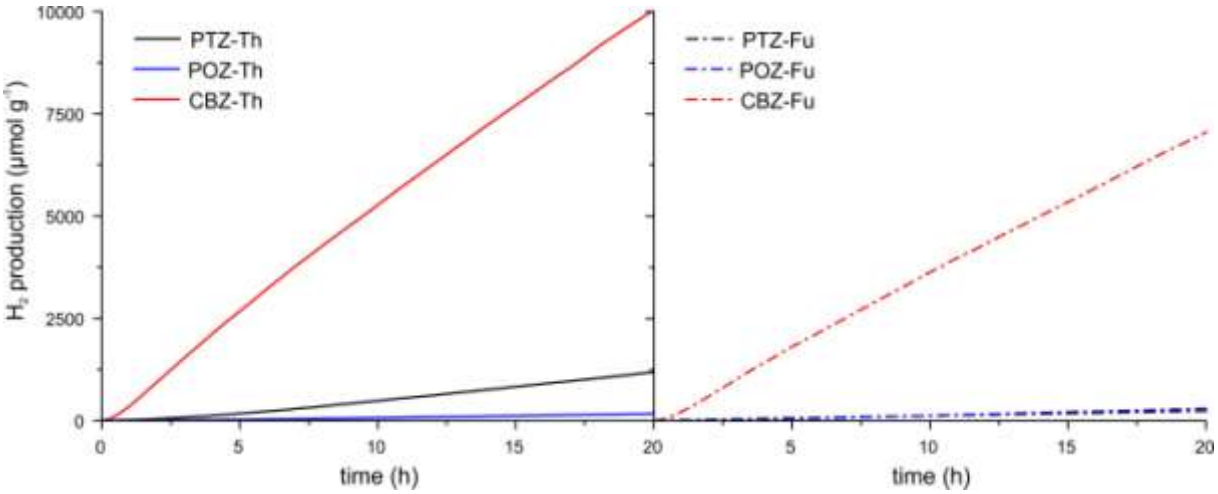

Figure 5.17 Turnover number (TON) and Light-to-Fuel Efficiencies (LFE) calculated from H_2 production using TEOA/HCl solution at pH = 7.0 under irradiation with visible light (λ> 420 nm) over Pt/TiO_2 materials sensitized with **PTZs**, **POZs** and **CBZs** dyes.

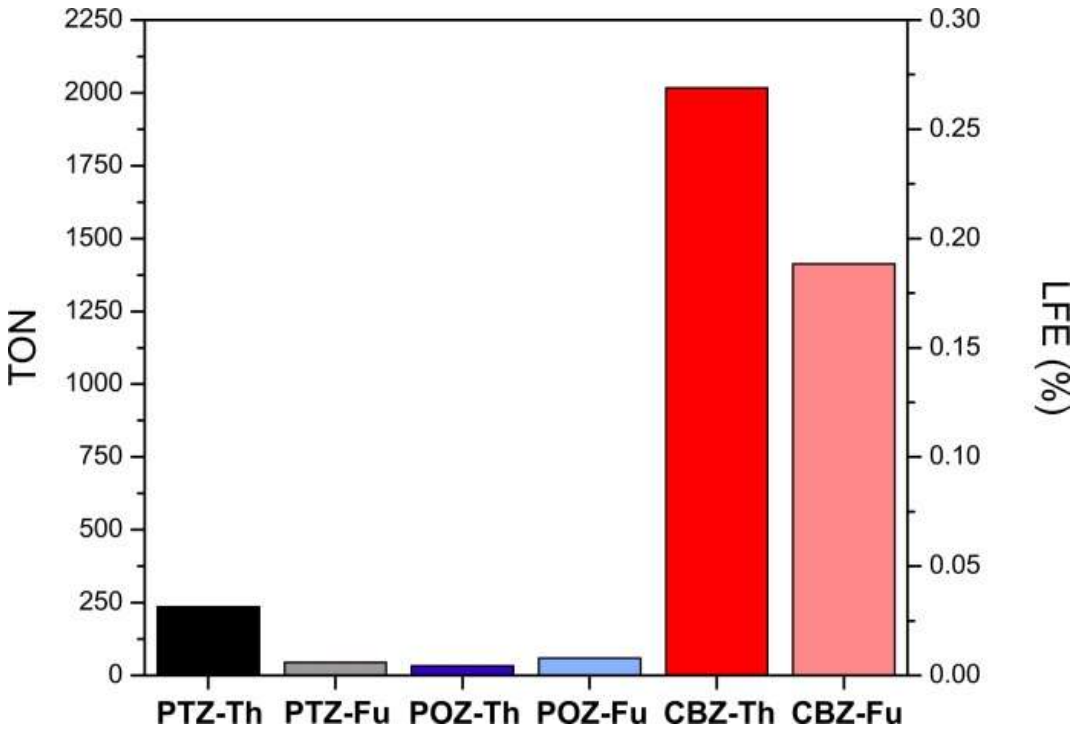

Table 5.5 TON values and LFE_{20} for **PTZs**, **POZs**, and **CBZs** sensitized catalysts.

Dye Sensitizer	H_2 amount ($\mu mol\ g^{-1}$ at 20h)	TON ($\mu mol(H_2)\ \mu mol(dye)^{-1}$ at 20h)	LFE_{20} (%)
PTZ-Th	1178	236	0.032%
PTZ-Fu	227	45	0.006%
POZ-Th	163	33	0.004%
POZ-Fu	294	59	0.008%
CBZ-Th	10083	2017	0.272%
CBZ-Fu	7064	1413	0.190%

The extraordinary high activity of **CBZ**-sensitized systems may be explained by the visible light-induced charge transfer method according to which they operate. Two methods of charge transfer are known in the literature: dye-sensitization and ligand-to-metal charge transfer (LMCT) (*278*, *279*). In the first case, the dye molecules located at the TiO_2/solution interface are photoexcited and subsequently inject electrons from their $LUMO^*$ into the TiO_2 CB. On the other hand, the LMCT mechanism is obtained if charge transfer takes place after the formation of a complex between TiO_2 and the adsorbed dye. In this case there is a strong coupling between the molecular orbital (HOMO) of the adsorbate and the energy band of the semiconductor, so that excited electrons go directly from the ground state of the adsorbate to the semiconductor CB, without involving the excited state of the adsorbate. It was shown in the literature that **CBZ** derivatives (with a molecular structure very similar to that of **CBZ-Fu** and **CBZ-Th**) give a red-shifted visible light absorption (up to 600 nm) when adsorbed on the surface of TiO_2, typical of the sensitization by LMCT (*269*). Such improved visible light absorption was not reported for **PTZ** and **POZ** molecules (*280*), suggesting that these molecules operate mainly through the dye-sensitization pathway.

Preliminary results of photocatalytic H_2 generation using a cut-off filter at 515 nm (Figure 5.18) suggest that **CBZ**-based systems may operate following a different mechanism than **PTZ** and **POZ**-based ones. In these experiments, a cut-off filter at 515 nm was added after activation of the photocatalysts for 8 h under usual conditions. Under irradiation using $\lambda > 515$ photons, **CBZ-Th**-based systems showed an appreciable photocatalytic activity, even if free **CBZ** in solution does not absorb photons having $\lambda > 515$ (Figure 5.13). This result is an indication a new electron transition, based on LMCT, should be involved in the photoexcitation of the system at such wavelengths. This hypothesis will be tested by Diffused Reflectance Spectroscopy (DRS) experiments on the dye/Pt/TiO_2 systems, which will allow to observe the final system UV-vis spectra.

On the other hand, **PTZ-Th** sensitized photocatalysts were completely inactive, despite UV-vis spectra of **PTZ** compounds show an intense light absorption up to 600 nm, due to ICT. This observation suggests that the ICT band, responsible for HOMO-LUMO transition and dye-sensitization of Pt/TiO_2, is not efficient in promoting the photocatalytic H_2 production (at least in the part at higher wavelength). Taking this into account, the activity observed under irradiation with $\lambda > 420$ nm using **PTZ** and **POZ** dyes as sensitizers (Figure 5.15-5.17) could be related to absorption of light by the π-π^* band. This would also explain the very low activity observed using **POZ** sensitizers, since electrons in **POZ** π-π^* band cannot be excited by visible light.

Figure 5.18 H_2 production rates from TEOA 10% v/v solution at pH = 7.0 over Pt/TiO_2 materials sensitized with **PTZ-Th** and **CBZ-Th** dyes: after activation under irradiation with visible light ($\lambda \geq$ 420 nm) for 8h, the photocatalytic activity under irradiation with photons with $\lambda >$ 515 nm is presented.

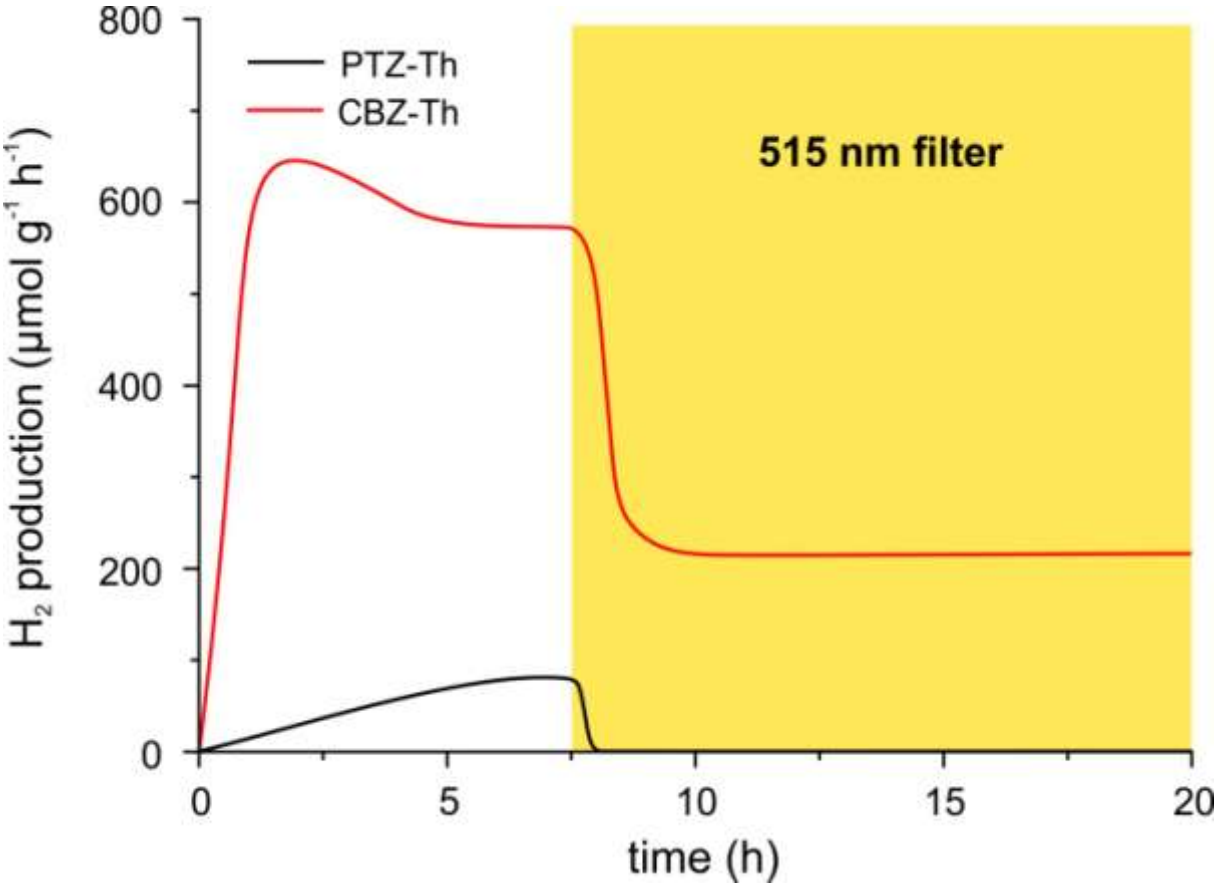

5.3.4 Conclusions

In conclusion, a rational design of the sensitizers was shown to be the key to obtain greatly enhanced performances in H_2 photogeneration under visible light irradiation. The presence of heteroatoms in the donor group and π-spacer moieties of the investigated sensitizers dramatically affected the photocatalytic H_2 production in the visible range over Pt/TiO_2. In particular, the combination of planar donor cores (**CBZ**) with thiophene heterocyclic spacers (**Th**) afforded state-of-the-art efficiency for dye-sensitized H_2 generation.

5.4 Future Perspectives for Sustainable H_2 Production

The sustainability of a process is a complex property to estimate: it encompasses economical, environmental and social aspects of every step involved in the production of the final commodity, and the metrics for its measurements are many, contextual, and still evolving. In chemistry, a series of sustainability principles and guidelines were established in the 90's to guide the practice of so-called *green chemistry*, in the context of increasing attention to problems of chemical pollution and resource depletion. Photocatalysis meets many of the green chemistry practical guidelines, and is surely one of the most green technologies existing for energy production. Photocatalytic systems operate at room temperature, in water solutions, utilizing clean, renewable solar light as the driving force, and cheap, nontoxic, chemically and biologically inert TiO_2-based materials as photocatalysts. Nonetheless, the sustainability of photocatalytic processes, such as H_2 production over sensitized photocatalysts, may be further improved.

The factors limiting the sustainability of the photocatalytic H_2 production process studied in the previous sections are the utilization of Pt noble metal as co-catalyst, of complex organic dyes as sensitizers (even if in very little amounts) and of corrosive and irritating TEOA as a sacrificial agent. In the context of this work, Pt/TiO_2 systems were chosen as a benchmark in order to study the performance of a series of sensitizers and rationalize the photocatalytic activity and stability in terms of their structure. However, more sustainable alternatives to Pt exist (*e.g.* Pd (*281*), Ni (*282*), Cu (*283*)) and the amount of co-catalyst can be diminished to 0.1 wt%, retaining photocatalytic activity (*282*).

The intrinsic impact of organic sensitizers on the process sustainability is dependent on the dye loading in the final catalyst (typically 0.5-1 wt% herein), the efficiency and modality of the staining process, the dye stability against decomposition and leaching over irradiation time, dye toxicity and synthesis procedure. In this work, the dye loading was optimized (see Section 5.2) and a simple staining process was followed to prepare efficient and stable sensitized photocatalysts. The optimization of the dye synthetic procedures and an evaluation of their impact on the environment and human health are out of the scope of this thesis. However, the synthetic procedures employed by the group of Professor Alessandro Abbotto comprise only a few steps and have been optimized keeping in mind the principles of green chemistry. It is also worth noting that, being the photocatalyst stable, the process sustainability is affected much more by (continuative) operational conditions than it is by (ideally, one-time) catalyst preparation.

TEOA was chosen as a sacrificial agent because it is a consolidated benchmark for sensitized photocatalytic H_2 production studies (*46*). However, for real applications, 10 v/v solutions of TEOA would not be a very green choice, since the industrial synthesis of TEOA requires ethylene

oxide, a widely used chemical in view of its reactivity, which is also very harmful and hazardous on the downside (*284*). A much greener class of sacrificial agents is that of oxygenated compounds. Sugars, glycerol (side product of biodiesel production) and alcohols such as ethanol (EtOH – from sugars fermentation) and methanol (MeOH – from glycerol steam reforming) can all be obtained by biomass upgrading, and were demonstrated to work as sacrificial agents in photocatalytic H_2 production (*282*, *285*). However, to the best of our knowledge, except for one study of methanol photoreforming (*286*), none of these compounds was studied in dye-sensitized photocatalytic H_2 production.

Figure 5.20 shows preliminary results of photocatalytic H_2 production using TEOA or EtOH as a sacrificial agent, for Pt/TiO_2 sensitized with a series of triphenilamine-based dyes containing the spacer unit thiazolo[5,4-d]thiazole (**TTZ**), prepared in Dr. G. Reginato research group (ICCOM-CNR, Florence), and previously studied in DSSC (*287*), namely **TTZ3**, **TTZ4** and **TTZ5** (Figure 5.19)[10]. The systems were active with both TEOA and EtOH, and H_2 production was very stable over irradiation time. In TEOA solutions, the Pt/TiO_2 sensitized with **TTZ** dyes performed slightly better than **PTZ**-based systems (see Figure 5.15-5.16), with **TTZ5** showing an activity almost double as those of **TTZ3** and **TTZ4**. When EtOH was used as sacrificial agent, the rates of H_2 production were lower, and interestingly, the activity trend was opposite than with TEOA, **TTZ3**>**TTZ4**>**TTZ5**. Notably, when tested for H_2 production with EtOH as a sacrificial agent, the previously reported **CBZs** and **PTZs**-based dyes showed very modest activity (about the detection limit for the chosen conditions) or no activity at all.

Figure 5.19 Molecular structure of **TTZ3**, **TTZ4** and **TTZ5**.

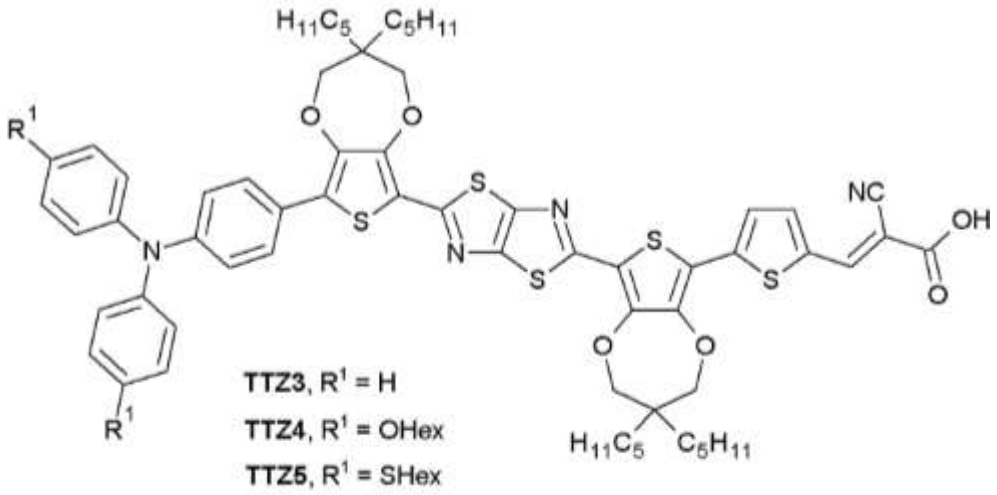

[10] For details on dyes synthesis and optical/redox properties, see reference (*287*)

Figure 5.20

H_2 production rates (A,C) and amount (B,D), from TEOA 10% v/v solution at pH = 7.0 (up) or EtOH 10% v/v solution, under irradiation with visible light ($\lambda \geq$ 420 nm) over Pt/TiO_2 materials sensitized with **TTZ3** (blue), **TTZ4** (black) and **TTZ5** (red).

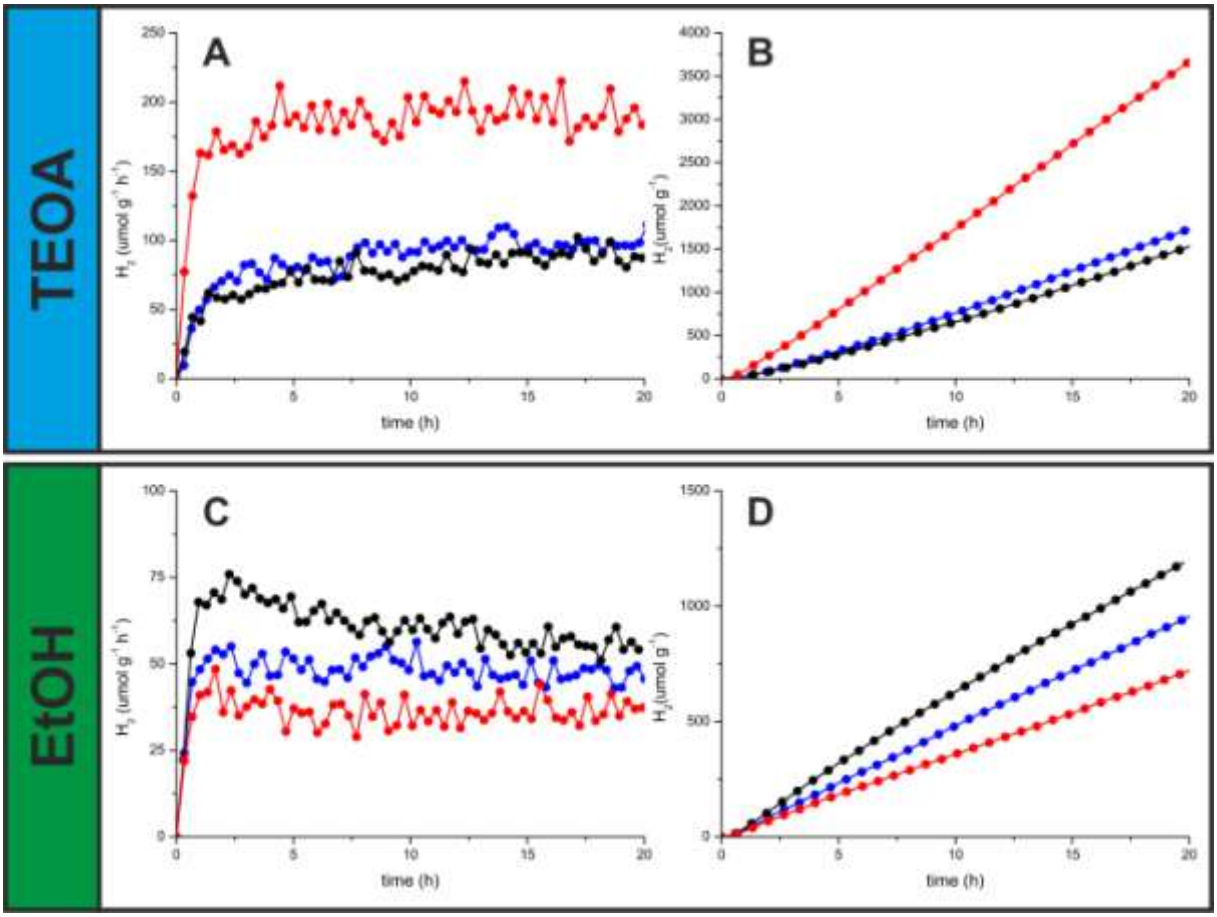

The differences observed between TEOA and EtOH can be due to a number of factors, such as different redox and adsorption properties of the sacrificial agents. A detailed study on EtOH photoreforming by dye-sensitized photocatalysts and the mechanism of operation is under way.

6. Conclusions

In conclusion, the present work provides new insights into some important environmental and energy-related catalytic reactions, taking advantage of well-defined nanostructured materials and of state-of-the-art spectroscopic and imaging techniques in order to rationalize catalytic performances. Three catalytic reactions were studied: methane catalytic oxidation, catalytic hydrodeoxygenation of biomass-derived compounds and photocatalytic hydrogen production.

Regarding methane catalytic oxidation, nanostructured Pd@MO_x-based catalysts were synthesized by slightly modifying a self-assembly method (*92*), and their catalytic activity was evaluated in conditions approaching the ones of industrial effluent gases and combustion engines exhausts. In particular, the effect of the presence of H_2O, phosphates or SO_2 in the reaction mixture was studied. Model catalysts based on Pd@MO_x units were also developed in order to carry out advanced photoelectron spectroscopy surface studies, essential to understand the deactivation processes observed in the presence of the above mentioned poisoning compounds.

Hierarchical Pd@CeO_2/Si-Al_2O_3 catalysts - otherwise stable under ideal conditions - are progressively deactivated in the presence of water (Section 3.3). While at temperatures below 500 °C deactivation is easily reversed by removing the water, at higher temperatures an irreversible deactivation process is observed. This is attributable to lower active phase accessibility, PdO decomposition to Pd, and to the formation of stable cerium hydroxides, which are decomposed only by high-temperature treatment. Lowering the amount of CeO_2 in hierarchical catalysts leads to enhanced stability thanks to the retention of more accessible active phase. The results show that design of catalysts for methane oxidation must maximize metal-support interactions to favor oxygen transfer from a reducible promoter, while keeping the active phase accessible to gas phase reactants. Indeed, Pd@ZrO_2 showed much greater hydrothermal stability (*115*).

The effect of phosphorus poisoning on the catalytic oxidation of methane over model Pd@CeO_2/graphite catalysts was found to be dramatically influenced by temperature and presence of H_2O (Section 3.4). While P-free Pd@CeO_2/graphite catalysts were active and stable under all studied conditions (500-600 °C; dry and wet conditions), P-poisoned catalysts were less active and stable because of partial thermal sintering, worsening at higher temperatures and in the presence of water vapor. The combination of XPS/SRPES, *operando* XANES measurements, SEM/EDS and AFM techniques provided evidence of a temperature dependent, water-driven P-poisoning of Pd-

CeO_2-based oxidation catalysts, proceeding via severe aggregation of ceria nanoparticles, incorporation of Pd active phase in the bulk of the crystallites and exposure of $CePO_4$ to the catalyst surface.

Nanostructured $Pd@Ce_xZr_{1-x}O_2$ ($Pd@MO_x$) units were synthesized in the whole compositional range ($0<x<1$) (Section 3.5). The synthesis of dispersed $Pd@MO_x$ allowed the preparation of a series of high-surface-area $Si\text{-}Al_2O_3$ supported catalysts and model catalysts having similar nanostructure and surface chemistry. Comparison of results on the two types of catalysts allowed the SO_2 poisoning of methane oxidation on Pd-based catalysts to be systematically studied to elucidate the role of the MO_x promoter and the aging conditions. At lower temperatures (<450 °C), the PdO active phase is irreversibly poisoned by SO_2 due to interaction with sulfates which are not able to spillover to the support/promoter. At higher temperatures (>500 °C), poisoning is slowed by formation of sulfate species on the oxide promoter. Due to partial decomposition of sulfates at 500 °C, $Pd@ZrO_2$-based catalysts showed the best sulfur-poisoning resistance, attaining complete regeneration even after prolonged aging, and thus they are the best candidates for real application. $Pd@Ce_{0.6}Zr_{0.4}O_2$ catalysts showed intermediate sulfur tolerance compared to $Pd@CeO_2$ and $Pd@ZrO_2$, in agreement with previously reported results (*142*). The high chemical sensitivity of PES techniques provided direct evidence for previously suggested formation of sulfate species on individual metal cations in $Ce_xZr_{1-x}O_2$ mixed oxides (*142*). Finally, we proved that the model-catalyst approaches developed here allow the study of metal-support interactions in other catalytically relevant systems by simply varying the ALD-deposited thin film composition.

The present study suggests that new technological breakthroughs are needed in order to solve the methane emission issue in vehicles. The hierarchical catalysts investigated herein are an important step in the process of seeking a solution, but, despite their enhanced activity and thermal stability, they suffer from deactivation in a similar way to traditional Pd-based catalysts. Given the severity of the environment of vehicles exhausts and the low reactivity of methane, an effective solution for methane abatement will require not only thermally stable catalysts but also improvement in fuel quality and in engine and after-treatment engineering (*e.g.* electronically controlled fuel injection to reduce unburned HCs emissions).

Regarding HDO catalytic reaction studies, we first demonstrated that the products distribution for furfural HDO is greatly influenced by H_2 pressure (Section 4.2). While at lower H_2 pressures decarbonylation is a major reaction pathway, higher H_2 pressures strongly favor the HDO reaction. When studied under the same conditions, HDO of furfural and HMF are very similar, both following a sequential reaction network, with the desired products (MF or DMF) formed as

intermediates. The development of unifying concepts for different reactants and reaction conditions are important for understanding these reactions.

In a series of studies (Sections 4.3-4.5), we investigated the performances of well-defined metal nanocrystalline alloys in the liquid-phase HDO reaction of HMF in order to understand the factors affecting the catalysts selectivity and stability. Pt-based (Pt-Co, Pt-Zn, Pt-Cu, Pt-Ni) and Ni-Cu nanocrystalline alloys of controlled size and compositions were synthesized by advanced solvothermal methods and supported on high-surface area carbon. Thanks to the uniformity of the synthesized materials, the performances observed in HDO reactions were rationalized on the basis of nanocrystals composition. Alloying was shown to have a positive effect on catalyst selectivity and stability, and optimal compositions were found for each alloy. The critical factor for achieving high selectivity to DMF in the HDO reaction of HMF appears to be the bonding mode of DMF, which has to prevent furan ring from lying down on the surface and be activated. However, there may be multiple ways to achieve such preferential bonding.

In the case of Pt-Co nanocrystal-based catalyst, an optimal DMF yield (98%) was obtained over Pt_3Co_2/C, for which a Co oxide monolayer formed on the surface of the metallic core. The thin overlayer induces high DMF yields because it weakly interacts with the furan ring, preventing over-hydrogenation and ring opening of DMF to secondary by-products while forming active sites to carry out the HDO process. In this regard, composition control is crucial to cover the entire surface with an oxide layer and avoid exposed metallic patches that could promote side reactions (*185*). However, this oxide overlayer model is not expected to be suitable for Pt-Ni, Pt-Zn, and Pt-Cu alloys, not as oxophilic as Co but just as selective. Indeed, the results of the HDO study over Ni-Cu base-meal catalysts strongly indicate that an oxide overlayer is not necessary to achieve high DMF yield in the HDO reaction of HMF.

The fact that high DMF yields were observed over Ni-Cu alloys catalysts demonstrates that reasonably inexpensive materials can be used for selective HDO of HMF. It is interesting to ask whether these base-metal alloys could also be used for other HDO reactions, such as would be important in the processing of lignin. There are indeed indications for this (*244*).

Regarding H_2 photocatalytic production experiments, benchmark Pt/TiO_2 photocatalysts were sensitized with a series of donor-acceptor organic dyes. A rational design of the sensitizers was shown to be the key to obtain greatly enhanced performances in H_2 photocatalytic production under visible light irradiation. We investigated the effect of ancillary substituents hydrophilicity, of the D-core nature (**PTZ**, **CBZ**, **POZ**) and of heteroatoms substitution in the spacer units. The combination of planar donor cores (**CBZ**) with thiophene heterocyclic spacers (**Th**) afforded state-of-the-art efficiency for dye-sensitized H_2 generation using benchmark TEOA as sacrificial agent.

Moreover, the general and scalable synthetic approach can be adapted to a large variety of derivatives, to synthesize photosensitizers having finely tuned properties, and to study their effect on the efficiency of H_2 photocatalytic production.

Finally, stable and sizeable H_2 production was observed over **TTZ**-sensitized Pt/TiO_2 photocatalysts using EtOH as a sacrificial agent, which is a very promising result for the development of photocatalytic systems of improved sustainability.

7. Acknowledgments

Voglio ringraziare il Professor Paolo Fornasiero per essere stato in questi anni non solo un grande mentore scientifico, ma anche un esempio di vita e un amico. Grazie per quel dollaro portafortuna, che ancora porto con me. Avrà forse poco valore sulla carta, ma è un simbolo prezioso, delle possibilità che mi hai offerto e dei momenti divertenti passati assieme.

A tutti i componenti del gruppo di ricerca di Fornasiero, grazie. Grazie Tiziano, Valentina, Alessandro, Michele, Marta e Anne varie ed eventuali. Grazie anche al Professor Mauro Graziani, per i preziosi consigli e gli aneddoti, scientifici e non. Un giorno, quando le querce di Paolo saranno alte e non andranno più potate ogni inverno, spero di sedermi lì nel suo campo con voi tutti e ricordare questi anni magnifici.

In particolare, ringrazio il Dott. Tiziano Montini per avermi insegnato a fare un sacco di cose che un bravo ricercatore dovrebbe fare. Ad esempio, a farmi le domande giuste. Ad essere tempestivo, ma anche a badare ai dettagli. A trattare gli strumenti con cura, e ad aprirli all'occorrenza. Per tutte le avventure passate assieme, da amico, ti ringrazio di cuore.

I would like to thank Professor Ray Gorte, for the great and valuable time I spent in his lab. It's been a great honor for me to work there. It was very inspiring to see him step into the lab every morning to discuss with each of his students, being always very smart and kind. I will also never forget my trip to Baltimore, which I visited thanks to his advice.

I'm also grateful to Professor Chris Murray for giving me the opportunity to work in his awesome lab. It has been a great professional and human experience.

Grazie a Emiliano Fonda e ai suoi colleghi della linea Samba al sincrotrone di Soleil. Con la sua simpatia, pazienza e perseveranza Emiliano riesce a rendere leggere le più lunghe giornate di *beamtime*, quando ormai ogni cognizione del giorno e della notte è andata persa.

Oggi come tre anni fa voglio ringraziare tutti i chimici del C11, passati, presenti e futuri. Fra di loro, un pensiero affettuoso è rivolto a Massimo (Pessimo) Rigo, Giulio Ragazzon (Picio!), Margherita Macino (tha-tha-tha Morgue!) e L.E.M.S. (Lukas Eugen Marsoner Steinkasserer).

Grazie alla mia famiglia, per il sostegno e l'aiuto insostituibile.

Grazie ai miei amici, vicini e lontani. Grazie a Seba, Nick, Braida e Pier. Thank you Cong, for being a great friend in a stranger land - we shall go to another rock concert one day! Thanks to Ming, Jing, Jennifer, and all the guys from Gorte's lab and Murray's lab. Thank you Tomaš, Peter, and everyone in Matolin's group.

Grazie, Serena (RNH_2).

A tutti voi, grazie.

8. Bibliography

(1) Monastersky, R. Anthropocene: The human age. *Nature* **2015**, *519*, 144–147.

(2) Lazarus, R. J. *The Making of Environmental Law*; University of Chicago Press, 2004.

(3) Whitesides, G. M. Reinventing Chemistry. *Angew. Chemie Int. Ed.* **2015**, *54*, 3196–3209.

(4) Ham, D. J.; Phuruangrat, A.; Thongtem, S.; Lee, J. S. Hydrothermal synthesis of monoclinic WO_3 nanoplates and nanorods used as an electrocatalyst for hydrogen evolution reactions from water. *Chem. Eng. J.* **2010**, *165*, 365–369.

(5) Simon, Q.; Barreca, D.; Gasparotto, A.; Maccato, C.; Montini, T.; Gombac, V.; Fornasiero, P.; Lebedev, O. I.; Turner, S.; Van Tendeloo, G. Vertically oriented CuO/ZnO nanorod arrays: from plasma-assisted synthesis to photocatalytic H_2 production. *J. Mater. Chem.* **2012**, *22*, 11739.

(6) Li, S.; Liu, H.; Zhao, X.; Wang, X. A cost-effective preparation method of Ba-hexaaluminate nanoparticles for catalytic combustion of methane. *Mater. Lett.* **2007**, *61*, 3935–3938.

(7) Viñes, F.; Lykhach, Y.; Staudt, T.; Lorenz, M. P.; Papp, C.; Steinrück, H.-P.; Libuda, J.; Neyman, K. M.; Görling, A. Methane activation by platinum: critical role of edge and corner sites of metal nanoparticles. *Chemistry* **2010**, *16*, 6530–9.

(8) Cargnello, M.; Jaen, J. J. D.; Garrido, J. C. H.; Bakhmutsky, K.; Montini, T.; Gamez, J. J. C.; Gorte, R. J.; Fornasiero, P. Exceptional Activity for Methane Combustion over Modular $Pd@CeO_2$ Subunits on Functionalized Al_2O_3. *Science* **2012**, *337*, 713–717.

(9) Heck, R.; Farrauto, R. Automobile exhaust catalysts. *Appl. Catal. A Gen.* **2001**, *221*, 443–457.

(10) Skoglundh, M.; Fridell, E. Strategies for enhancing low-temperature activity. *Top. Catal.* **2004**, *28*, 79–87.

(11) EEA — European Environment Agency. *Air quality in Europe -2011 report*; 2011.

(12) EEA — European Environment Agency. *The contribution of transport to air quality*; 2012.

(13) Seinfeld, J.; Pandis, S. *Atmospheric chemistry and physics: from air pollution to climate change*; 2nd ed.; Wiley, 2006.

(14) Lelieveld, J.; Crutzen, P. J.; Dentener, F. J. Changing concentration, lifetime and climate forcing of atmospheric methane. *Tellus B* **1998**, *50*, 128–150.

(15) Turner, A. J.; Jacob, D. J.; Benmergui, J.; Wofsy, S. C.; Maasakkers, J. D.; Butz, A.; Hasekamp, O.; Biraud, S. C. A large increase in U.S. methane emissions over the past decade inferred from satellite data and surface observations. *Geophys. Res. Lett.* **2016**, *43*, 2218–2224.

(16) Everaert, K.; Baeyens, J. Catalytic combustion of volatile organic compounds. *J. Hazard. Mater.* **2004**, *109*, 113–39.

(17) Li, W. B.; Wang, J. X.; Gong, H. Catalytic combustion of VOCs on non-noble metal catalysts. *Catal. Today* **2009**, *148*, 81–87.

(18) Khan, F. I.; Kr. Ghoshal, A. Removal of Volatile Organic Compounds from polluted air. *J. Loss Prev. Process Ind.* **2000**, *13*, 527–545.

(19) Spivey, J. Complete catalytic oxidation of volatile organics. *Ind. Eng. Chem. Res.* **1987**, 2165–2180.

(20) Wang, J.; Jin, L.; Gao, J.; Shi, J.; Zhao, Y.; Liu, S.; Jin, T.; Bai, Z.; Wu, C.-Y. Investigation of speciated VOC in gasoline vehicular exhaust under ECE and EUDC test cycles. *Sci. Total Environ.* **2013**, *445–446*, 110–6.

(21) Gélin, P.; Primet, M. Complete oxidation of methane at low temperature over noble metal based catalysts: a review. *Appl. Catal. B Environ.* **2002**, *39*, 1–37.

(22) Yin, J.; Su, S.; Yu, X. X.; Weng, Y. Thermodynamic characteristics of a low concentration methane catalytic combustion gas turbine. *Appl. Energy* **2010**, *87*, 2102–2108.

(23) Lampert, J.; Kazi, M.; Farrauto, R. Palladium catalyst performance for methane emissions abatement from lean burn natural gas vehicles. *Appl. Catal. B Environ.* **1997**, *14*, 211–223.

(24) Armstrong, R. C.; Wolfram, C.; de Jong, K. P.; Gross, R.; Lewis, N. S.; Boardman, B.; Ragauskas, A. J.; Ehrhardt-Martinez, K.; Crabtree, G.; Ramana, M. V. The frontiers of energy. *Nat. Energy* **2016**, *1*, 15020.

(25) *Ethanol Benefits and Considerations*; 2014.

(26) *EPA Lifecycle Analysis of Greenhouse Gas Emissions from Renewable Fuels*; 2010.

(27) EASAC. *The current status of biofuels in the European Union, their environmental impacts and future prospects*; 2012.

(28) Fu, C.; Mielenz, J. R.; Xiao, X.; Ge, Y.; Hamilton, C. Y.; Rodriguez, M.; Chen, F.; Foston, M.; Ragauskas, A.; Bouton, J.; Dixon, R. A.; Wang, Z.-Y. Genetic manipulation of lignin reduces recalcitrance and improves ethanol production from switchgrass. *Proc. Natl. Acad. Sci. U. S. A.* **2011**, *108*, 3803–3808.

(29) Furimsky, E. Catalytic hydrodeoxygenation. *Appl. Catal. A Gen.* **2000**, *199*, 147–190.

(30) Luo, J.; Monai, M.; Yun, H.; Arroyo-Ramírez, L.; Wang, C.; Murray, C. B.; Fornasiero, P.; Gorte, R. J. The H_2 Pressure Dependence of Hydrodeoxygenation Selectivities for Furfural over Pt/C Catalysts. *Catal. Letters* **2016**, *146*, 711–717.

(31) Abbasi, T.; Abbasi, S. A. "Renewable" hydrogen: Prospects and challenges. *Renew. Sustain. Energy Rev.* **2011**, *15*, 3034–3040.

(32) Hagfeldt, A.; Boschloo, G.; Sun, L.; Kloo, L.; Pettersson, H. Dye-Sensitized Solar Cells. *Chem. Rev.* **2010**, *110*, 6595–6663.

(33) Albers, P.; Pietsch, J.; Parker, S. F. Poisoning and deactivation of palladium catalysts. *J. Mol. Catal. A Chem.* **2001**, *173*, 275–286.

(34) Larese, C.; López Granados, M.; Mariscal, R.; Fierro, J. L. G.; Lambrou, P. S.; Efstathiou, A. M. The effect of calcination temperature on the oxygen storage and release properties of CeO_2 and Ce–Zr–O metal oxides modified by phosphorus incorporation. *Appl. Catal. B Environ.* **2005**, *59*, 13–25.

(35) Lopez Granados, M.; Galisteo, F.; Lambrou, P.; Mariscal, R.; Sanz, J.; Sobrados, I.; Fierro, J.; Efstathiou, A. Role of P-containing species in phosphated CeO_2 in the deterioration of its oxygen storage and release properties. *J. Catal.* **2006**, *239*, 410–421.

(36) Christou, S. Y.; Álvarez-Galván, M. C.; Fierro, J. L. G.; Efstathiou, A. M. Suppression of the oxygen storage and release kinetics in $Ce_{0.5}Zr_{0.5}O_2$ induced by P, Ca and Zn chemical poisoning. *Appl. Catal. B Environ.* **2011**, *106*, 103–113.

(37) Xu, L.; Guo, G.; Uy, D.; O'Neill, A. .; Weber, W. .; Rokosz, M. .; McCabe, R. . Cerium phosphate in automotive exhaust catalyst poisoning. *Appl. Catal. B Environ.* **2004**, *50*, 113–125.

(38) Sitthisa, S.; An, W.; Resasco, D. E. Selective conversion of furfural to methylfuran over silica-supported NiFe bimetallic catalysts. *J. Catal.* **2011**, *284*, 90–101.

(39) Cargnello, M.; Doan-Nguyen, V. V. T.; Gordon, T. R.; Diaz, R. E.; Stach, E. A.; Gorte, R. J.; Fornasiero, P.;

Murray, C. B. Control of Metal Nanocrystal Size Reveals Metal-Support Interface Role for Ceria Catalysts. *Science* **2013**, *341*, 771–773.

(40) Cargnello, M.; Chen, C.; Diroll, B. T.; Doan-Nguyen, V. V. T.; Gorte, R. J.; Murray, C. B. Efficient Removal of Organic Ligands From Supported Nanocrystals by Fast Thermal Annealing Enables Catalytic Studies on Well Defined Active Phases. *J. Am. Chem. Soc.* **2015**, 137, 6906–6911.

(41) Luo, J.; Arroyo-Ramírez, L.; Gorte, R. J.; Tzoulaki, D.; Vlachos, D. G. Hydrodeoxygenation of HMF over Pt/C in a continuous flow reactor. *AIChE J.* **2015**, *61*, 590–597.

(42) Schneider, J.; Matsuoka, M.; Takeuchi, M.; Zhang, J.; Horiuchi, Y.; Anpo, M.; Bahnemann, D. W. Understanding TiO_2 Photocatalysis: Mechanisms and Materials. *Chem. Rev.* **2014**, *114*, 9919–9986.

(43) Liu, X.; Long, J.; Wang, G.; Pei, Y.; Zhao, B.; Tan, S. Effect of structural modification on the performances of phenothiazine-dye sensitized solar cells. *Dye. Pigment.* **2015**, *121*, 118–127.

(44) Sathiyan, G.; Sivakumar, E. K. T.; Ganesamoorthy, R.; Thangamuthu, R.; Sakthivel, P. Review of carbazole based conjugated molecules for highly efficient organic solar cell application. *Tetrahedron Lett.* **2016**, *57*, 243–252.

(45) Kisch, H.; Bahnemann, D. Best Practice in Photocatalysis: Comparing Rates or Apparent Quantum Yields? *J. Phys. Chem. Lett.* **2015**, *6*, 1907–1910.

(46) Cecconi, B.; Manfredi, N.; Montini, T.; Fornasiero, P.; Abbotto, A. Dye-Sensitized Solar Hydrogen Production: The Emerging Role of Metal-Free Organic Sensitizers. *European J. Org. Chem.* **2016**, *2016*, 5194–5215.

(47) Thomas, J. M. and W. J. *Principle and Practice of Heterogeneous Catalysis*; VCH Publisher: Weinheim (Germany), 1997.

(48) Cheng, H.; Wang, J.; Zhao, Y.; Han, X. Effect of phase composition, morphology, and specific surface area on the photocatalytic activity of TiO_2 nanomaterials. *RSC Adv.* **2014**, *4*, 47031–47038.

(49) Cozzoli, P. D.; Kornowski, A.; Weller, H. Low-Temperature Synthesis of Soluble and Processable Organic-Capped Anatase TiO_2 Nanorods. *J. Am. Chem. Soc.* **2003**, *125*, 14539–14548.

(50) Pierotti, R. A.; Rouquerol, J.; Sing, K. S. W.; Everett, D. H.; Haul, R. A. W.; Moscou, L.; Siemieniewska, T. Reporting physisorption data for gas/solid systems with special reference to the determination of surface area and porosity. *Pure Appl. Chem.* **1985**, *57*, 603–619.

(51) Rouquerol, J.; Avnir, D.; Fairbridge, C. W.; Everett, D. H.; Haynes, J. M.; Pernicone, N.; Ramsay, J. D. F.; Sing, K. S. W.; Unger, K. K. Recommendations for the characterization of porous solids. *Pure Appl. Chem.* **1994**, *66*, 1739–1758.

(52) Barrett, E.; Joyner, L.; Halenda, P. The determination of pore volume and area distributions in porous substances. I. Computations from nitrogen isotherms. *J. Am. Chem. Soc.* **1951**, *73,* 373–380.

(53) Dulaurent, O.; Bianchi, D. Adsorption isobars for CO on a Pt/Al_2O_3 catalyst at high temperatures using FTIR spectroscopy : isosteric heat of adsorption and adsorption model. *Appl. Catal. A Gen.* **2000**, *196*, 271–280.

(54) Gatica, J.; Baker, R.; Fornasiero, P.; Bernal, S.; Kaspar, J. Characterization of the metal phase in $NM/Ce_{0.68}Zr_{0.32}O_2$ (NM: Pt and Pd) catalysts by hydrogen chemisorption and HRTEM microscopy: A comparative study. *J. Phys. Chem. B* **2001**, *2*, 1191–1199.

(55) Zhang, J.; Wang, Z.; Wang, Z. X. Adsorption of carbon monoxide on Pd low-index surfaces and (110) reconstructed surface. *Surf. Interface Anal.* **2011**, *43*, 1038–1045.

(56) Ramos, I. A. C.; Montini, T.; Lorenzut, B.; Troiani, H.; Gennari, F. C.; Graziani, M.; Fornasiero, P. Hydrogen production from ethanol steam reforming on M/CeO_2/YSZ (M=Ru, Pd, Ag) nanocomposites. *Catal. Today* **2012**, *180*, 96–104.

(57) Saghi, Z.; Midgley, P. A. Electron Tomography in the (S)TEM: From Nanoscale Morphological Analysis to 3D Atomic Imaging. *Annu. Rev. Mater. Res.* **2012**, *42*, 59–79.

(58) Goodhew, P. J.; Humphreys, J.; Beanland, R. *Electron Microscopy and Analysis*; Taylor & Francis, 2001; Vol. 54.

(59) Yang, J. C.; Small, M. W.; Grieshaber, R. V; Nuzzo, R. G. Recent developments and applications of electron microscopy to heterogeneous catalysis. *Chem. Soc. Rev.* **2012**, *41*, 8179–8194.

(60) Koningsberger, D. C.; Prins, R. *X-Ray Absorption: Principles, Applications, Techniques of EXAFS, SEXAFS and XANES*; 1987.

(61) Als-Nielsen, J.; McMorrow, D. *Elements of Modern X-ray Physics, 2nd Edition*; 2011.

(62) Bunker, G. *Introduction to XAFS*; 2010.

(63) La Fontaine, C.; Barthe, L.; Rochet, A.; Briois, V. X-ray absorption spectroscopy and heterogeneous catalysis: Performances at the SOLEIL's SAMBA beamline. *Catal. Today* **2013**, *205*, 148–158.

(64) Ankudinov, A.; Ravel, B.; Rehr, J.; Conradson, S. Real-space multiple-scattering calculation and interpretation of X-ray-absorption near-edge structure. *Phys. Rev. B* **1998**, *58*, 7565–7576.

(65) Ravel, B.; Newville, M. ATHENA, ARTEMIS, HEPHAESTUS: data analysis for X-ray absorption spectroscopy using IFEFFIT. *J. Synchrotron Radiat.* **2005**, *12*, 537–541.

(66) van der Heide, P. *X-Ray Photoelectron Spectroscopy*; John Wiley & Sons, Inc.: Hoboken, NJ, USA, 2011.

(67) Barber, J. Photosynthetic energy conversion: natural and artificial. *Chem. Soc. Rev.* **2009**, *38*, 185–196.

(68) Hurtado, P.; Ordóñez, S.; Vega, A.; Díez, F. V. Catalytic combustion of methane over commercial catalysts in presence of ammonia and hydrogen sulphide. *Chemosphere* **2004**, *55*, 681–9.

(69) Colussi, S.; De Leitenburg, C.; Dolcetti, G.; Trovarelli, A. The role of rare earth oxides as promoters and stabilizers in combustion catalysts. *J. Alloys Compd.* **2004**, *374*, 387–392.

(70) Corro, G.; Cano, C.; Fierro, J. L. G. A study of Pt–Pd/γ-Al_2O_3 catalysts for methane oxidation resistant to deactivation by sulfur poisoning. *J. Mol. Catal. A Chem.* **2010**, *315*, 35–42.

(71) Venezia, A. M.; Di Carlo, G.; Pantaleo, G.; Liotta, L. F.; Melaet, G.; Kruse, N. Oxidation of CH_4 over Pd supported on TiO_2-doped SiO_2: Effect of Ti(IV) loading and influence of SO_2. *Appl. Catal. B Environ.* **2009**, *88*, 430–437.

(72) Ciuparu, D.; Lyubovsky, M. R.; Altman, E.; Pfefferle, L. D.; Datye, A. Catalytic Combustion of Methane Over Palladium-Based Catalysts. *Catal. Rev.* **2002**, *44*, 593–649.

(73) Schwartz, W. R.; Pfefferle, L. D. Combustion of Methane over Palladium-Based Catalysts: Support Interactions. *J. Phys. Chem. C* **2012**, *116*, 8571–8578.

(74) Chin, Y.-H. C.; Buda, C.; Neurock, M.; Iglesia, E. Consequences of metal-oxide interconversion for C-H bond activation during CH_4 reactions on Pd catalysts. *J. Am. Chem. Soc.* **2013**, *135*, 15425–42.

(75) Colussi, S.; Trovarelli, A.; Groppi, G.; Llorca, J. The effect of CeO_2 on the dynamics of Pd–PdO transformation over Pd/Al_2O_3 combustion catalysts. *Catal. Commun.* **2007**, *8*, 1263–1266.

(76) Mayernick, A. D.; Janik, M. J. Methane oxidation on Pd–Ceria: A DFT study of the mechanism over $Pd_xCe_{1-x}O_2$, Pd, and PdO. *J. Catal.* **2011**, *278*, 16–25.

(77) Doornkamp, C.; Ponec, V. The universal character of the Mars and Van Krevelen mechanism. *J. Mol. Catal. A Chem.* **2000**, *162*, 19–32.

(78) Mars, P.; van Krevelen, D. W. Oxidations carried out by means of vanadium oxide catalysts. *Chem. Eng. Sci.* **1954**, *3*, 41–59.

(79) Sayle, T.; Cantoni, M.; Bhatta, U. Strain and Architecture-Tuned Reactivity in Ceria Nanostructures; Enhanced Catalytic Oxidation of CO to CO_2. *Chem. Mater.* **2012**, *24*, 1811–1821.

(80) Rocchini, E.; Vicario, M.; Llorca, J.; de Leitenburg, C.; Dolcetti, G.; Trovarelli, A. Reduction and Oxygen Storage Behavior of Noble Metals Supported on Silica-Doped Ceria. *J. Catal.* **2002**, *211*, 407–421.

(81) Trovarelli, A. Catalytic Properties of Ceria. *Catal. Rev.* **2006**, *38*, 439–520.

(82) Zhou, G.; Shah, P. R.; Montini, T.; Fornasiero, P.; Gorte, R. J. Oxidation enthalpies for reduction of ceria surfaces. *Surf. Sci.* **2007**, *601*, 2512–2519.

(83) De Rogatis, L.; Cargnello, M.; Gombac, V.; Lorenzut, B.; Montini, T.; Fornasiero, P. Embedded phases: a way to active and stable catalysts. *ChemSusChem* **2010**, *3*, 24–42.

(84) Mowery, D. L.; McCormick, R. L. Deactivation of alumina supported and unsupported PdO methane oxidation catalyst: the effect of water on sulfate poisoning. *Appl. Catal. B Environ.* **2001**, *34*, 287–297.

(85) Ciuparu, D.; Pfefferle, L. Support and water effects on palladium based methane combustion catalysts. *Appl. Catal. A Gen.* **2001**, *209*, 415–428.

(86) Ciuparu, D.; Katsikis, N.; Pfefferle, L. Temperature and time dependence of the water inhibition effect on supported palladium catalyst for methane combustion. *Appl. Catal. A Gen.* **2001**, *216*, 209–215.

(87) Persson, K.; Pfefferle, L. D.; Schwartz, W.; Ersson, A.; Järås, S. G. Stability of palladium-based catalysts during catalytic combustion of methane: The influence of water. *Appl. Catal. B Environ.* **2007**, *74*, 242–250.

(88) Ciuparu, D.; Perkins, E.; Pfefferle, L. In situ DR-FTIR investigation of surface hydroxyls on γ-Al_2O_3 supported PdO catalysts during methane combustion. *Appl. Catal. A Gen.* **2004**, *263*, 145–153.

(89) Monai, M.; Montini, T.; Chen, C.; Fonda, E.; Gorte, R. J.; Fornasiero, P. Methane Catalytic Combustion over Hierarchical Pd@CeO_2/Si-Al_2O_3: Effect of the Presence of Water. *ChemCatChem* **2015**, *7*, 2038–2046.

(90) Honkane, M.; Kärkkäinen, M.; Kolli, T.; Heikkinen, O.; Viitanen, V.; Zeng, L.; Jiang, H.; Kallinen, K.; Huuhtanen, M.; Keiski, R. L.; Lahtinen, J.; Olsson, E.; Vippola, M. Accelerated Deactivation Studies of the Natural-Gas Oxidation Catalyst – Verifying the Role of Sulfur and Elevated Temperature in Catalyst Aging. *Appl. Catal. B Environ.* **2015**.

(91) Farrauto, R. J. Low-Temperature Oxidation of Methane. *Science* **2012**, *337*, 659–660.

(92) Bakhmutsky, K.; Wieder, N. L.; Cargnello, M.; Galloway, B.; Fornasiero, P.; Gorte, R. J. A versatile route to core-shell catalysts: synthesis of dispersible M@oxide (M=Pd, Pt; oxide=TiO_2, ZrO_2) nanostructures by self-assembly. *ChemSusChem* **2012**, *5*, 140–8.

(93) Cargnello, M.; Wieder, N. Synthesis of Dispersible Pd@CeO_2 Core Shell Nanostructures by Self-Assembly. *J. Am. Chem. Soc.* **2010**, 1402–1409.

(94) Gradeff, P.; Schreiber, F. A simplified method for the synthesis of ceric alkoxides from ceric ammonium nitrate. *Inorg. Chem.* **1985**, 1110–1111.

(95) Adijanto, L.; Bennett, D. A.; Chen, C.; Yu, A. S.; Cargnello, M.; Fornasiero, P.; Gorte, R. J.; Vohs, J. M. Exceptional thermal stability of Pd@CeO_2 core-shell catalyst nanostructures grafted onto an oxide surface. *Nano Lett.* **2013**, *13*, 2252–2257.

(96) Papaefthimiou, P.; Ioannides, T.; Verykios, X. Catalytic incineration of volatile organic compounds present in industrial waste streams. *Appl. Therm. Eng.* **1998**, *18*, 1005–1012.

(97) Burch, R.; Urbano, F.; Loader, P. K. Methane combustion over palladium catalysts: The effect of carbon dioxide and water on activity. *Appl. Catal. A Gen.* **1995**, *123*, 173–184.

(98) Hurtado, P.; Ordonez, S.; Sastre, H.; Diez, F. V. Combustion of methane over palladium catalyst in the

presence of inorganic compounds: inhibition and deactivation phenomena. *Appl. Catal. B Environ.* **2004**, *47*, 85–93.

(99) Kikuchi, R.; Maeda, S.; Sasaki, K.; Wennerström, S.; Ozawa, Y.; Eguchi, K. Catalytic activity of oxide-supported Pd catalysts on a honeycomb for low-temperature methane oxidation. *Appl. Catal. A Gen.* **2003**, *239*, 169–179.

(100) Schwartz, W. R.; Ciuparu, D.; Pfefferle, L. D. Combustion of Methane over Palladium-Based Catalysts: Catalytic Deactivation and Role of the Support. *J. Phys. Chem. C* **2012**, *116*, 8587–8593.

(101) Datye, A. K.; Bravo, J.; Nelson, T. R.; Atanasova, P.; Lyubovsky, M.; Pfefferle, L. Catalyst microstructure and methane oxidation reactivity during the Pd↔PdO transformation on alumina supports. *Appl. Catal. A Gen.* **2000**, *198*, 179–196.

(102) Zhang, F.; Wang, P.; Koberstein, J.; Khalid, S.; Chan, S.-W. S. Cerium oxidation state in ceria nanoparticles studied with X-ray photoelectron spectroscopy and absorption near edge spectroscopy. *Surf. Sci.* **2004**, *563*, 10726–10732.

(103) Keating, J.; Sankar, G.; Hyde, T. I.; Kohara, S.; Ohara, K. Elucidation of structure and nature of the PdO-Pd transformation using in situ PDF and XAS techniques. *Phys. Chem. Chem. Phys.* **2013**, *15*, 8555–65.

(104) Badri, A.; Binet, C.; Lavalley, J. An FTIR study of surface ceria hydroxy groups during a redox process with H_2. *J. Chem. Soc., Faraday Trans.* **1996**, *92*, 4669–4673.

(105) Setiawan, A.; Friggieri, J.; Kennedy, E. M.; Dlugogorski, B. Z.; Stockenhuber, M. Catalytic combustion of ventilation air methane (VAM) - long term catalyst stability in the presence of water vapour and mine dust. *Catal. Sci. Technol.* **2014**, *4*, 1793–1802.

(106) Yang, S.; Maroto-Valiente, A.; Benito-Gonzalez, M.; Rodriguez-Ramos, I. Methane combustion over supported palladium catalysts I . Reactivity and active phase. *Appl. Catal. B Environ.* **2000**, *28*, 223–233.

(107) Esch, F.; Fabris, S.; Zhou, L.; Montini, T.; Africh, C.; Fornasiero, P.; Comelli, G.; Rosei, R. Electron localization determines defect formation on ceria substrates. *Science* **2005**, *309*, 752–725.

(108) Watkins, M.; Foster, A.; Shluger, A. Hydrogen cycle on CeO_2 (111) surfaces: Density functional theory calculations. *J. Phys. Chem. C* **2007**, *2*, 15337–15341.

(109) Fronzi, M.; Piccinin, S.; Delley, B.; Traversa, E.; Stampfl, C. Water adsorption on the stoichiometric and reduced CeO_2(111) surface: a first-principles investigation. *Phys. Chem. Chem. Phys.* **2009**, *11*, 9188–9199.

(110) Vayssilov, G. N.; Lykhach, Y.; Migani, A.; Staudt, T.; Petrova, G. P.; Tsud, N.; Skála, T.; Bruix, A.; Illas, F.; Prince, K. C.; Matolín, V.; Neyman, K. M.; Libuda, J. Support nanostructure boosts oxygen transfer to catalytically active platinum nanoparticles. *Nat. Mater.* **2011**, *10*, 310–315.

(111) Boujana, S.; Dexpert, H.; Majerus, J.; Villain, F.; J, F. L. N. Redox Processes on Pure Ceria and on Rh/CeO_2 Catalyst Monitored by X-ray Absorption (Fast Acquisition Mode). *J. Phys. Chem.* **1994**, 21, 5522–5533.

(112) Calvino, J. J.; Cifredo, A. Comments on "Redox Processes on Pure Ceria and Rh/CeO_2 Catalyst Monitored by X-ray Absorption (Fast Acquisition Mode)." *J. Phys. Chem.* **1995**, *30*, 11794–11796.

(113) Fornasiero, P.; Montini, T.; Graziani, M.; Kašpar, J.; Hungría, A. B.; Martínez-Arias, A.; Conesa, J. C. Effects of thermal pretreatment on the redox behaviour of $Ce_{0.5}Zr_{0.5}O_2$: isotopic and spectroscopic studies. *Phys. Chem. Chem. Phys.* **2002**, *4*, 149–159.

(114) Fornasiero, P.; Kašpar, J.; Graziani, M. On the rate determining step in the reduction of CeO_2–ZrO_2 mixed oxides. *Appl. Catal. B Environ.* **1999**, *22*, L11–L14.

(115) Chen, C.; Yeh, Y.-H.; Cargnello, M.; Murray, C. B.; Fornasiero, P.; Gorte, R. J. Methane Oxidation on Pd@ZrO_2/Si–Al_2O_3 Is Enhanced by Surface Reduction of ZrO_2. *ACS Catal.* **2014**, *4*, 3902–3909.

(116) Martín, L. Simulation three-way catalyst ageing. Analysis of two conventional catalyst. *Appl. Catal. B Environ.* **2003**, *44*, 41–52.

(117) Heo, I.; Choung, J. W.; Kim, P. S.; Nam, I.-S.; Song, Y. I.; In, C. B.; Yeo, G. K. The alteration of the performance of field-aged Pd-based TWCs towards CO and C_3H_6 oxidation. *Appl. Catal. B Environ.* **2009**, *92*, 114–125.

(118) Larese, C. Deactivation of real three way catalysts by $CePO_4$ formation. *Appl. Catal. B Environ.* **2003**, *40*, 305–317.

(119) Uy, D.; O'Neill, A. E.; Xu, L.; Weber, W. H.; McCabe, R. W. Observation of cerium phosphate in aged automotive catalysts using Raman spectroscopy. *Appl. Catal. B Environ.* **2003**, *41*, 269–278.

(120) Benissad-Aissani, F.; Aït-Amar, H.; Schouler, M.-C.; Gadelle, P. The role of phosphorus in the growth of vapour-grown carbon fibres obtained by catalytic decomposition of hydrocarbons. *Carbon N. Y.* **2004**, *42*, 2163–2168.

(121) Larese, C.; Galisteo, F.; Granados, M.; Mariscal, R.; Fierro, J.; Lambrou, P.; Efstathiou, A. Effects of the $CePO_4$ on the oxygen storage and release properties of CeO_2 and $Ce_{0.8}Zr_{0.2}O_2$ solid solution. *J. Catal.* **2004**, *226*, 443–456.

(122) Christou, S. Y.; García-Rodríguez, S.; Fierro, J. L. G.; Efstathiou, A. M. Deactivation of $Pd/Ce_{0.5}Zr_{0.5}O_2$ model three-way catalyst by P, Ca and Zn deposition. *Appl. Catal. B Environ.* **2012**, *111–112*, 233–245.

(123) Larese, C.; Cabello Galisteo, F.; López Granados, M.; Mariscal López, R.; Fierro, J. L G..; Lambrou, P. S.; Efstathiou, A. M. Effects of calcination temperature on the stability of $CePO_4$ detected in vehicle-aged commercial three-way catalysts. *Appl. Catal. B Environ.* **2004**, *48*, 113–123.

(124) Christou, S.; Efstathiou, A. Regeneration of Aged Commercial Three-Way Catalysts Using Cl-Containing Reagents. *Top. Catal.* **2013**, *56*, 255–260.

(125) Özmen-Monkul, B.; Lerner, M. M. The first graphite intercalation compounds containing tris(pentafluoroethyl)trifluorophosphate. *Carbon N. Y.* **2010**, *48*, 3205–3210.

(126) Zhang, Y.; Wang, J.; Zhang, T. Novel Ca-doped $CePO_4$ supported ruthenium catalyst with superior catalytic performance for aerobic oxidation of alcohols. *Chem. Commun.* **2011**, *47*, 5307–5309.

(127) Mullins, D. R.; Albrecht, P. M.; Chen, T.-L.; Calaza, F. C.; Biegalski, M. D.; Christen, H. M.; Overbury, S. H. Water Dissociation on CeO_2(100) and CeO_2(111) Thin Films. *J. Phys. Chem. C* **2012**, *116*, 19419–19428.

(128) Tsud, N.; Johánek, V.; Stará, I.; Veltruská, K.; Matolín, V. CO adsorption on palladium model catalysts: XPS Pd–Al_2O_3 interaction study. *Surf. Sci.* **2000**, *467*, 169–176.

(129) He, H.; Gao, C. A General Strategy for the Preparation of Carbon Nanotubes and Graphene Oxide Decorated with PdO Nanoparticles in Water. *Molecules* **2010**, *15*, 4679–4694.

(130) Zhang, P.; Sham, T. K. X-Ray Studies of the Structure and Electronic Behavior of Alkanethiolate-Capped Gold Nanoparticles: The Interplay of Size and Surface Effects. *Phys. Rev. Lett.* **2003**, *90*, 245502.

(131) Morales, J.; Espinos, J. P.; Caballero, A.; Gonzalez-Elipe, A. R.; Mejias, J. A. XPS Study of Interface and Ligand Effects in Supported Cu_2O and CuO Nanometric Particles. *J. Phys. Chem. B* **2005**, *109*, 7758–7765.

(132) Johánek, V.; Stará, I.; Tsud, N.; Veltruská, K.; Matolín, V. CO adsorption on Al_2O_3-supported Pd clusters: XPS study. *Appl. Surf. Sci.* **2000**, *162*, 679–684.

(133) Wang, H.-F.; Kaden, W. E.; Dowler, R.; Sterrer, M.; Freund, H.-J. Model oxide-supported metal catalysts - comparison of ultrahigh vacuum and solution based preparation of Pd nanoparticles on a single-crystalline oxide substrate. *Phys. Chem. Chem. Phys.* **2012**, *14*, 11525–11533.

(134) Penner, S.; Bera, P.; Pedersen, S.; Ngo, L. T.; Harris, J. J. W.; Campbell, C. T. Interactions of O_2 with Pd

Nanoparticles on α-Al_2O_3(0001) at Low and High O_2 Pressures. *J. Phys. Chem. B* **2006**, *110*, 24577–24584.

(135) Lin, R.; Freemantle, R. G.; Kelly, N. M.; Fielitz, T. R.; Obare, S. O.; Ofoli, R. Y. In situ immobilization of palladium nanoparticles in microfluidic reactors and assessment of their catalytic activity. *Nanotechnology* **2010**, *21*, 325605.

(136) Gélin, P.; Urfels, L.; Primet, M.; Tena, E. Complete oxidation of methane at low temperature over Pt and Pd catalysts for the abatement of lean-burn natural gas fuelled vehicles emissions: influence of water and sulphur containing compounds. *Catal. Today* **2003**, *83*, 45–57.

(137) United States Environmental Protection Agency. *EPA420-F-06-064*; 2006.

(138) Colussi, S.; Arosio, F.; Montanari, T.; Busca, G.; Groppi, G.; Trovarelli, A. Study of sulfur poisoning on Pd/Al_2O_3 and $Pd/CeO_2/Al_2O_3$ methane combustion catalysts. *Catal. Today* **2010**, *155*, 59–65.

(139) Luo, T.; Vohs, J. M.; Gorte, R. J. An Examination of Sulfur Poisoning on Pd/Ceria Catalysts. *J. Alloys Compd.* **2002**, *210*, 397–404.

(140) Rodriguez, J. A.; Jirsak, T.; Freitag, A.; Hanson, J. C.; Larese, J. Z.; Chaturvedi, S. Interaction of SO_2 with CeO_2 and Cu/CeO_2 catalysts: photoemission, XANES and TPD studies. *Catal. Letters* **1999**, *62*, 113–119.

(141) Bazin, P.; Saur, O.; Lavalley, J. C.; Blanchard, G.; Visciglio, V.; Touret, O. Influence of platinum on ceria sulfation. *Appl. Catal. B Environ.* **1997**, *13*, 265–274.

(142) Luo, T.; Gorte, R. J. Characterization of SO_2-poisoned ceria-zirconia mixed oxides. *Appl. Catal. B Environ.* **2004**, *53*, 77–85.

(143) Romano, E. J.; Schulz, K. H. A XPS investigation of SO_2 adsorption on ceria–zirconia mixed-metal oxides. *Appl. Surf. Sci.* **2005**, *246*, 262–270.

(144) Deshmukh, S.; Zhang, M.; Kovalchuk, V. I.; L d'Itri, J. Effect of SO_2 on CO and C_3H_6 oxidation over CeO_2 and $Ce_{0.75}Zr_{0.25}O_2$. *Appl. Catal. B Environ.* **2003**, *45*, 135–145.

(145) Waqif, M.; Bazin, P.; Saur, O.; Lavalley, J. C.; Blanchard, G.; Touret, O. Study of ceria sulfation. *Appl. Catal. B Environ.* **1997**, *11*, 193–205.

(146) Nelson, A. E.; Schulz, K. H. Surface chemistry and microstructural analysis of $Ce_xZr_{1-x}O_{2-y}$ model catalyst surfaces. *Appl. Surf. Sci.* **2003**, *210*, 206–221.

(147) Zhou, R. S.; Snyder, R. L. Structures and transformation mechanisms of the η, γ and θ transition aluminas. *Acta Crystallogr. Sect. B Struct. Sci.* **1991**, *47*, 617–630.

(148) Colón, G.; Valdivieso, F.; Pijolat, M.; Baker, R. T.; Calvino, J. J.; Bernal, S. Textural and phase stability of $Ce_xZr_{1-x}O_2$ mixed oxides under high temperature oxidising conditions. *Catal. Today* **1999**, *50*, 271–284.

(149) Montini, T.; Melchionna, M.; Monai, M.; Fornasiero, P. Fundamentals and Catalytic Applications of CeO_2-Based Materials. *Chem. Rev.* **2016**.

(150) Zhang, S.; Chen, C.; Cargnello, M.; Fornasiero, P.; Gorte, R. J.; Graham, G. W.; Pan, X. Dynamic structural evolution of supported palladium-ceria core-shell catalysts revealed by in situ electron microscopy. *Nat. Commun.* **2015**, *6*, 7778.

(151) Burch, R.; Crittle, D. J.; Southward, B. W. L.; Sullivan, J. A. The effect of SO_2 on the activity of Pd-based catalysts in methane combustion. *Catal. Letters* **2001**, *72*, 153–155.

(152) Monai, M.; Montini, T.; Melchionna, M.; Duchoň, T.; Kúš, P.; Tsud, N.; Prince, K. C.; Matolin, V.; Gorte, R. J.; Fornasiero, P. Phosphorus poisoning during wet oxidation of methane over $Pd@CeO_2$/graphite model catalysts. *Appl. Catal. B Environ.* **2015**.

(153) Priolkar, K. R.; Bera, P.; Sarode, P. R.; Hegde, M. S.; Emura, S.; Kumashiro, R.; Lalla, N. P. Formation of Ce_{1-}

$_xPd_xO_{2-\delta}$ Solid Solution in Combustion-Synthesized Pd/CeO_2 Catalyst: XRD, XPS, and EXAFS Investigation. *Chem. Mater.* **2002**, *14*, 2120–2128.

(154) Hiley, C. I.; Fisher, J. M.; Thompsett, D.; Kashtiban, R. J.; Sloan, J.; Walton, R. I. Incorporation of square-planar Pd^{2+} in fluorite CeO_2: hydrothermal preparation, local structure, redox properties and stability. *J. Mater. Chem. A* **2015**, *3*, 13072–13079.

(155) Venezia, A.; Murania, R.; Pantaleo, G.; Deganello, G. Pd and PdAu on mesoporous silica for methane oxidation: Effect of SO_2. *J. Catal.* **2007**, *251*, 94–102.

(156) Liotta, L. F.; Di Carlo, G.; Pantaleo, G.; Venezia, A. M.; Deganello, G. Insights into SO_2 Interaction with Pd/Co_3O_4–CeO_2 Catalysts for Methane Oxidation. *Top. Catal.* **2009**, *52*, 1989–1994.

(157) Sharma, H. N.; Sharma, V.; Mhadeshwar, A. B.; Ramprasad, R. Why Pt Survives but Pd Suffers From SO_x Poisoning? *J. Phys. Chem. Lett.* **2015**, *6*, 1140–1148.

(158) Yeh, J. J.; Lindau, I. Atomic subshell photoionization cross sections and asymmetry parameters: $1 < Z < 103$. *At. Data Nucl. Data Tables* **1985**, *32*, 1–155.

(159) Ferrizz, R. M.; Gorte, R. J.; Vohs, J. M. TPD and XPS Investigation of the Interaction of SO_2 with Model Ceria Catalysts. *Catal. Letters* **2002**, *82*, 123–129.

(160) O'Neill, B. J.; Jackson, D. H. K.; Lee, J.; Canlas, C.; Stair, P. C.; Marshall, C. L.; Elam, J. W.; Kuech, T. F.; Dumesic, J. A.; Huber, G. W. Catalyst Design with Atomic Layer Deposition. *ACS Catal.* **2015**, *5*, 1804–1825.

(161) Burch, R.; Urbano, F. J. Investigation of the active state of supported palladium catalysts in the combustion of methane. *Appl. Catal. A Gen.* **1995**, *124*, 121–138.

(162) Cargnello, M.; Wieder, N. L.; Canton, P.; Montini, T.; Giambastiani, G.; Benedetti, A.; Gorte, R. J.; Fornasiero, P. A Versatile Approach to the Synthesis of Functionalized Thiol-Protected Palladium Nanoparticles. *Chem. Mater.* **2011**, *23*, 3961–3969.

(163) Nanda, S.; Mohammad, J.; Reddy, S. N.; Kozinski, J. A.; Dalai, A. K. Pathways of lignocellulosic biomass conversion to renewable fuels. *Biomass Convers. Biorefinery* **2014**, *4*, 157–191.

(164) Fukuoka, A.; Dhepe, P. L. Catalytic conversion of cellulose into sugar alcohols. *Angew. Chem. Int. Ed. Engl.* **2006**, *45*, 5161–5163.

(165) Hegner, J.; Pereira, K. C.; DeBoef, B.; Lucht, B. L. *Conversion of cellulose to glucose and levulinic acid via solid-supported acid catalysis*; 2010; Vol. 51.

(166) Gürbüz, E. I.; Wettstein, S. G.; Dumesic, J. A. Conversion of hemicellulose to furfural and levulinic acid using biphasic reactors with alkylphenol solvents. *ChemSusChem* **2012**, *5*, 383–387.

(167) Lanzafame, P.; Temi, D. M.; Perathoner, S.; Spadaro, A. N.; Centi, G. Direct conversion of cellulose to glucose and valuable intermediates in mild reaction conditions over solid acid catalysts. In *Catalysis Today*; 2012; Vol. 179, pp. 178–184.

(168) Alonso, D. M.; Wettstein, S. G.; Mellmer, M. A.; Gurbuz, E. I.; Dumesic, J. A. Integrated conversion of hemicellulose and cellulose from lignocellulosic biomass. *Energy Environ. Sci.* **2013**, *6*, 76–80.

(169) Sutton, A. D.; Waldie, F. D.; Wu, R.; Schlaf, M.; "Pete" Silks, L. A.; Gordon, J. C. The hydrodeoxygenation of bioderived furans into alkanes. *Nat. Chem.* **2013**, *5*, 428–432.

(170) Asadullah, M.; Rahman, M. A.; Ali, M. M.; Rahman, M. S.; Motin, M. A.; Sultan, M. B.; Alam, M. R. Production of bio-oil from fixed bed pyrolysis of bagasse. *Fuel* **2007**, *86*, 2514–2520.

(171) Demirbas, A. The influence of temperature on the yields of compounds existing in bio-oils obtained from biomass samples via pyrolysis. *Fuel Process. Technol.* **2007**, *88*, 591–597.

(172) Elliott, D. C.; Hart, T. R. Catalytic Hydroprocessing of Chemical Models for Bio-oil. *Energy & Fuels* **2009**,

23, 631–637.

(173) Serrano-Ruiz, J. C.; West, R. M.; Dumesic, J. A. Catalytic Conversion of Renewable Biomass Resources to Fuels and Chemicals. *Annu. Rev. Chem. Biomol. Eng.* **2010**, *1*, 79–100.

(174) Nakagawa, Y.; Tamura, M.; Tomishige, K. Catalytic Reduction of Biomass-Derived Furanic Compounds with Hydrogen. *ACS Catal.* **2013**, *3*, 2655–2668.

(175) Román-Leshkov, Y.; Barrett, C. J.; Liu, Z. Y.; Dumesic, J. A. Production of dimethylfuran for liquid fuels from biomass-derived carbohydrates. *Nature* **2007**, *447*, 982–985.

(176) Wang, T.; Nolte, M. W.; Shanks, B. H. Catalytic dehydration of C6 carbohydrates for the production of hydroxymethylfurfural (HMF) as a versatile platform chemical. *Green Chem.* **2014**, *16*, 548–572.

(177) Dashtban, M.; Gilbert, A.; Fatehi, P. Recent advancements in the production of hydroxymethylfurfural. *RSC Adv.* **2014**, *4*, 2037–2050.

(178) Torres, A. I.; Daoutidis, P.; Tsapatsis, M. Continuous production of 5-hydroxymethylfurfural from fructose: a design case study. *Energy Environ. Sci.* **2010**, *3*, 1560.

(179) Chen, G.; Shen, Y.; Zhang, Q.; Yao, M.; Zheng, Z.; Liu, H. Experimental study on combustion and emission characteristics of a diesel engine fueled with 2,5-dimethylfuran–diesel, n-butanol–diesel and gasoline–diesel blends. *Energy* **2013**, *54*, 333–342.

(180) Green, S. K.; Patet, R. E.; Nikbin, N.; Williams, C. L.; Chang, C.-C.; Yu, J.; Gorte, R. J.; Caratzoulas, S.; Fan, W.; Vlachos, D. G.; Dauenhauer, P. J. Diels–Alder cycloaddition of 2-methylfuran and ethylene for renewable toluene. *Appl. Catal. B Environ.* **2016**, *180*, 487–496.

(181) Williams, C. L.; Chang, C.-C.; Do, P.; Nikbin, N.; Caratzoulas, S.; Vlachos, D. G.; Lobo, R. F.; Fan, W.; Dauenhauer, P. J. Cycloaddition of Biomass-Derived Furans for Catalytic Production of Renewable *p* -Xylene. *ACS Catal.* **2012**, *2*, 935–939.

(182) Sitthisa, S.; Resasco, D. E. Hydrodeoxygenation of Furfural Over Supported Metal Catalysts: A Comparative Study of Cu, Pd and Ni. *Catal. Letters* **2011**, *141*, 784–791.

(183) Pushkarev, V. V; Musselwhite, N.; An, K.; Alayoglu, S.; Somorjai, G. A. High Structure Sensitivity of Vapor-Phase Furfural Decarbonylation/Hydrogenation Reaction Network as a Function of Size and Shape of Pt Nanoparticles. *Nano Lett.* **2012**, *12*, 5196–5201.

(184) Pang, S. H.; Schoenbaum, C. A.; Schwartz, D. K.; Medlin, J. W. Directing reaction pathways by catalyst active-site selection using self-assembled monolayers. *Nat. Commun.* **2013**, *4*.

(185) Luo, J.; Arroyo-Ramírez, L.; Wei, J.; Yun, H.; Murray, C. B.; Gorte, R. J. Comparison of HMF hydrodeoxygenation over different metal catalysts in a continuous flow reactor. *Appl. Catal. A Gen.* **2015**, *508*, 86–93.

(186) Hu, L.; Tang, X.; Xu, J.; Wu, Z.; Lin, L.; Liu, S. Selective transformation of 5-hydroxymethylfurfural into the liquid fuel 2,5-dimethylfuran over carbon-supported ruthenium. *Ind. Eng. Chem. Res.* **2014**, *53*, 3056–3064.

(187) Saha, B.; Bohn, C. M.; Abu-Omar, M. M. Zinc-assisted hydrodeoxygenation of biomass-derived 5-hydroxymethylfurfural to 2,5-Dimethylfuran. *ChemSusChem* **2014**, *7*, 3095–3101.

(188) Wang, G.-H.; Hilgert, J.; Richter, F. H.; Wang, F.; Bongard, H.-J.; Spliethoff, B.; Weidenthaler, C.; Schüth, F. Platinum-cobalt bimetallic nanoparticles in hollow carbon nanospheres for hydrogenolysis of 5-hydroxymethylfurfural. *Nat. Mater.* **2014**, *13*, 293–300.

(189) Wang, S.; Vorotnikov, V.; Vlachos, D. G. Coverage-Induced Conformational Effects on Activity and Selectivity: Hydrogenation and Decarbonylation of Furfural on Pd(111). *ACS Catal.* **2015**, *5*, 104–112.

(190) Bradley, M. K.; Robinson, J.; Woodruff, D. P. The structure and bonding of furan on Pd(111). *Surf. Sci.*

2010, *604*, 920–925.

(191) Yan, K.; Chen, A. Selective hydrogenation of furfural and levulinic acid to biofuels on the ecofriendly Cu–Fe catalyst. *Fuel* **2014**, *115*, 101–108.

(192) Hronec, M.; Fulajtarová, K. Selective transformation of furfural to cyclopentanone. *Catal. Commun.* **2012**, *24*, 100–104.

(193) Nishimura, S.; Ikeda, N.; Ebitani, K. Selective hydrogenation of biomass-derived 5-hydroxymethylfurfural (HMF) to 2,5-dimethylfuran (DMF) under atmospheric hydrogen pressure over carbon supported PdAu bimetallic catalyst. In *Catalysis Today*; 2014; Vol. 232, pp. 89–98.

(194) Myint, M.; Yan, Y.; Chen, J. G. Reaction pathways of propanal and 1-propanol on Fe/Ni(111) and Cu/Ni(111) bimetallic surfaces. *J. Phys. Chem. C* **2014**, *118*, 11340–11349.

(195) Lee, J.; Kim, Y. T.; Huber, G. W. Aqueous-phase hydrogenation and hydrodeoxygenation of biomass-derived oxygenates with bimetallic catalysts. *Green Chem.* **2014**, *16*, 708.

(196) Chidambaram, M.; Bell, A. T. A two-step approach for the catalytic conversion of glucose to 2,5-dimethylfuran in ionic liquids. *Green Chem.* **2010**, *12*, 1253.

(197) Thananatthanachon, T.; Rauchfuss, T. B. Efficient Production of the Liquid Fuel 2,5-Dimethylfuran from Fructose Using Formic Acid as a Reagent. *Angew. Chemie Int. Ed.* **2010**, *49*, 6616–6618.

(198) Jae, J.; Zheng, W.; Lobo, R. F.; Vlachos, D. G. Production of Dimethylfuran from Hydroxymethylfurfural through Catalytic Transfer Hydrogenation with Ruthenium Supported on Carbon. *ChemSusChem* **2013**, *6*, 1158–1162.

(199) Shevchenko, E. V; Talapin, D. V; Rogach, A. L.; Kornowski, A.; Haase, M.; Weller, H. Colloidal synthesis and self-assembly of $CoPt_3$ nanocrystals. *J. Am. Chem. Soc.* **2002**, *124*, 11480–11485.

(200) Gordon, T. R.; Cargnello, M.; Paik, T.; Mangolini, F.; Weber, R. T.; Fornasiero, P.; Murray, C. B. Nonaqueous Synthesis of TiO_2 Nanocrystals Using TiF_4 to Engineer Morphology, Oxygen Vacancy Concentration, and Photocatalytic Activity. *J. Am. Chem. Soc.* **2012**, *134*, 6751–6761.

(201) Fievet, F.; Lagier, J.; Blin, B.; Beaudoin, B.; Figlarz, M. Homogeneous and heterogeneous nucleations in the polyol process for the preparation of micron and submicron size metal particles. *Solid State Ionics* **1989**, *32–33*, 198–205.

(202) Yu, Y.; Yang, W.; Sun, X.; Zhu, W.; Li, X. Z.; Sellmyer, D. J.; Sun, S. Monodisperse MPt (M = Fe, Co, Ni, Cu, Zn) nanoparticles prepared from a facile oleylamine reduction of metal salts. *Nano Lett.* **2014**, *14*, 2778–2782.

(203) Wang, D.; Xin, H. L.; Hovden, R.; Wang, H.; Yu, Y.; Muller, D. A.; Di Salvo, F. J.; Abruña, H. D. Structurally ordered intermetallic platinum–cobalt core–shell nanoparticles with enhanced activity and stability as oxygen reduction electrocatalysts. *Nat. Mater.* **2012**, *12*, 81–87.

(204) Ng, Y. H.; Ikeda, S.; Harada, T.; Sakata, T.; Mori, H.; Takaoka, A.; Matsumura, M. High sintering resistance of platinum nanoparticles embedded in a microporous hollow carbon shell fabricated through a photocatalytic reaction. *Langmuir* **2008**, *24*, 6307–6312.

(205) Lonergan, W. W.; Vlachos, D. G.; Chen, J. G. Correlating extent of Pt–Ni bond formation with low-temperature hydrogenation of benzene and 1,3-butadiene over supported Pt/Ni bimetallic catalysts. *J. Catal.* **2010**, *271*, 239–250.

(206) Menning, C. A.; Chen, J. G. Thermodynamics and kinetics of oxygen-induced segregation of 3d metals in Pt-3d-Pt (111) and Pt-3d-Pt (100) bimetallic structures. *J. Chem. Phys.* **2008**, *128*, 164703–164703.

(207) De Santis, M.; Buchsbaum, A.; Varga, P.; Schmid, M. Growth of ultrathin cobalt oxide films on Pt (111). *Phys. Rev. B* **2011**, *84*, 125430.

(208) Blaylock, D. W.; Zhu, Y.-A.; Green, W. H. Computational investigation of the thermochemistry and kinetics of steam methane reforming over a multi-faceted nickel catalyst. *Top. Catal.* **2011**, *54*, 828–844.

(209) Zhu, Z.; Tao, F.; Zheng, F.; Chang, R.; Li, Y.; Heinke, L.; Liu, Z.; Salmeron, M.; Somorjai, G. A. Formation of nanometer-sized surface platinum oxide clusters on a stepped Pt (557) single crystal surface induced by oxygen: a high-pressure STM and ambient-pressure XPS study. *Nano Lett.* **2012**, *12*, 1491–1497.

(210) Luo, J.; Yun, H.; Mironenko, A. V.; Goulas, K.; Lee, J. D.; Monai, M.; Wang, C.; Vorotnikov, V.; Murray, C. B.; Vlachos, D. G.; Fornasiero, P.; Gorte, R. J. Mechanisms for High Selectivity in the Hydrodeoxygenation of 5-Hydroxymethylfurfural over PtCo Nanocrystals. *ACS Catal.* **2016**, *6*, 4095–4104.

(211) Knudsen, J.; Merte, L. R.; Grabow, L. C.; Eichhorn, F. M.; Porsgaard, S.; Zeuthen, H.; Vang, R. T.; Lægsgaard, E.; Mavrikakis, M.; Besenbacher, F. Reduction of FeO/Pt (111) thin films by exposure to atomic hydrogen. *Surf. Sci.* **2010**, *604*, 11–20.

(212) Tengco, J. M. M.; Lugo-José, Y. K.; Monnier, J. R.; Regalbuto, J. R. Chemisorption–XRD particle size discrepancy of carbon supported palladium: Carbon decoration of Pd? *Catal. Today* **2015**, *246*, 9–14.

(213) Scholten, J. J. F.; Pijpers, A. P.; Hustings, A. M. L. Surface Characterization of Supported and Nonsupported Hydrogenation Catalysts. *Catal. Rev. Sci. Eng.* **1985**, *27*, 151–206.

(214) Tuokko, S.; Pihko, P. M.; Honkala, K. First Principles Calculations for Hydrogenation of Acrolein on Pd and Pt: Chemoselectivity Depends on Steric Effects on the Surface. *Angew. Chemie Int. Ed.* **2016**.

(215) Loffreda, D.; Delbecq, F.; Vigné, F.; Sautet, P. Chemo-regioselectivity in heterogeneous catalysis: Competitive routes for CO and CC hydrogenations from a theoretical approach. *J. Am. Chem. Soc.* **2006**, *128*, 1316–1323.

(216) Caratzoulas, S.; Vlachos, D. G. Converting fructose to 5-hydroxymethylfurfural: a quantum mechanics/molecular mechanics study of the mechanism and energetics. *Carbohydr. Res.* **2011**, *346*, 664–672.

(217) Mironenko, A. V.; Gilkey, M. J.; Panagiotopoulou, P.; Facas, G.; Vlachos, D. G.; Xu, B. Ring Activation of Furanic Compounds on Ruthenium-Based Catalysts. *J. Phys. Chem. C* **2015**, *119*, 6075–6085.

(218) Wang, S.; Vorotnikov, V.; Vlachos, D. G. Coverage-Induced Conformational Effects on Activity and Selectivity: Hydrogenation and Decarbonylation of Furfural on Pd (111). *Acs Catal.* **2014**, *5*, 104–112.

(219) Vorotnikov, V.; Mpourmpakis, G.; Vlachos, D. G. DFT study of furfural conversion to furan, furfuryl alcohol, and 2-methylfuran on Pd (111). *Acs Catal.* **2012**, *2*, 2496–2504.

(220) Wang, S.; Vorotnikov, V.; Vlachos, D. G. A DFT study of furan hydrogenation and ring opening on Pd (111). *Green Chem.* **2014**, *16*, 736–747.

(221) Pang, S. H.; Schoenbaum, C. A.; Schwartz, D. K.; Medlin, J. W. Effects of Thiol Modifiers on the Kinetics of Furfural Hydrogenation over Pd Catalysts. *Acs Catal.* **2014**, *4*, 3123–3131.

(222) Schoenbaum, C. A.; Schwartz, D. K.; Medlin, J. W. Controlling the surface environment of heterogeneous catalysts using self-assembled monolayers. *Acc. Chem. Res.* **2014**, *47*, 1438–1445.

(223) McManus, J. R.; Martono, E.; Vohs, J. M. Selective Deoxygenation of Aldehydes: The Reaction of Acetaldehyde and Glycolaldehyde on Zn/Pt(111) Bimetallic Surfaces. *ACS Catal.* **2013**, *3*, 1739–1750.

(224) Shi, D.; Vohs, J. M. Deoxygenation of Biomass-Derived Oxygenates: Reaction of Furfural on Zn-Modified Pt(111). *ACS Catal.* **2015**, *5*, 2177–2183.

(225) Yu, W.; Xiong, K.; Ji, N.; Porosoff, M. D.; Chen, J. G. Theoretical and experimental studies of the adsorption geometry and reaction pathways of furfural over FeNi bimetallic model surfaces and supported catalysts. *J. Catal.* **2014**, *317*, 253–262

(226) Sitthisa, S.; Pham, T.; Prasomsri, T.; Sooknoi, T.; Mallinson, R. G.; Resasco, D. E. Conversion of furfural and 2-methylpentanal on Pd/SiO_2 and Pd–Cu/SiO_2 catalysts. *J. Catal.* **2011**, *280*, 17–27.

(227) Sitthisa, S.; Sooknoi, T.; Ma, Y.; Balbuena, P. B.; Resasco, D. E. Kinetics and mechanism of hydrogenation of furfural on Cu/SiO_2 catalysts. *J. Catal.* **2011**, *277*, 1–13.

(228) Ahrenstorf, K.; Albrecht, O.; Heller, H.; Kornowski, A.; Görlitz, D.; Weller, H. Colloidal Synthesis of Ni_xPt_{1-x} Nanoparticles with Tuneable Composition and Size. *Small* **2007**, *3*, 271–274.

(229) Murray, C. B.; Sun, S.; Doyle, H.; Betley, T. Monodisperse 3d transition-metal (Co, Ni, Fe) nanoparticles and their assembly intonanoparticle superlattices. *Mrs Bull.* **2001**, *26*, 985–991.

(230) Denton, A. R.; Ashcroft, N. W. Vegard's law. *Phys. Rev. A* **1991**, *43*, 3161.

(231) Kang, Y.; Ye, X.; Murray, C. B. Size- and Shape-Selective Synthesis of Metal Nanocrystals and Nanowires Using CO as a Reducing Agent. *Angew. Chemie Int. Ed.* **2010**, *49*, 6156–6159.

(232) Luo, J.; Lee, J. D.; Yun, H.; Wang, C.; Monai, M.; Murray, C. B.; Fornasiero, P.; Gorte, R. J. Base metal-Pt alloys: A general route to high selectivity and stability in the production of biofuels from HMF. *Appl. Catal. B Environ.* **2016**, *199*, 439–446.

(233) Holade, Y.; Morais, C.; Servat, K.; Napporn, T. W.; Kokoh, K. B. Enhancing the available specific surface area of carbon supports to boost the electroactivity of nanostructured Pt catalysts. *Phys. Chem. Chem. Phys.* **2014**, *16*, 25609–25620.

(234) Yu, L.; He, L.; Chen, J.; Zheng, J.; Ye, L.; Lin, H.; Yuan, Y. Robust and Recyclable Nonprecious Bimetallic Nanoparticles on Carbon Nanotubes for the Hydrogenation and Hydrogenolysis of 5-Hydroxymethylfurfural. *ChemCatChem* **2015**, *7*, 1701–1707.

(235) Huang, Y.-B.; Chen, M.-Y.; Yan, L.; Guo, Q.-X.; Fu, Y. Nickel-Tungsten Carbide Catalysts for the Production of 2,5-Dimethylfuran from Biomass-Derived Molecules. *ChemSusChem* **2014**, *7*, 1068–1072.

(236) Chen, B.; Li, F.; Huang, Z.; Yuan, G. Carbon-coated Cu-Co bimetallic nanoparticles as selective and recyclable catalysts for production of biofuel 2,5-dimethylfuran. *Appl. Catal. B Environ.* **2017**, *200*, 192–199.

(237) Huba, Z. J.; Carpenter, E. E. Ethanol assisted reduction and nucleation of ferromagnetic Co and Ni nanocrystalline particles. *CrystEngComm* **2013**, *15*, 8919.

(238) Pellicer, E.; Varea, A.; Sivaraman, K. M.; Pané, S.; Suriñach, S.; Baró, M. D.; Nogués, J.; Nelson, B. J.; Sort, J. Grain Boundary Segregation and Interdiffusion Effects in Nickel–Copper Alloys: An Effective Means to Improve the Thermal Stability of Nanocrystalline Nickel. *ACS Appl. Mater. Interfaces* **2011**, *3*, 2265–2274.

(239) Luo, J.; Yu, J.; Gorte, R. J.; Mahmoud, E.; Vlachos, D. G.; Smith, M. A. The effect of oxide acidity on HMF etherification. *Catal. Sci. Technol.* **2014**, *4*, 3074–3081.

(240) Yao, Y.; Goodman, D. W. Direct evidence of hydrogen spillover from Ni to Cu on Ni–Cu bimetallic catalysts. *J. Mol. Catal. A Chem.* **2014**, *383–384*, 239–242.

(241) Sinfelt, J. H. Catalysis by alloys and bimetallic clusters. *Acc. Chem. Res.* **1977**, *10*, 15–20.

(242) Xiong, K.; Wan, W.; Chen, J. G. Reaction pathways of furfural, furfuryl alcohol and 2-methylfuran on Cu(111) and NiCu bimetallic surfaces. *Surf. Sci.* **2016**, *652*, 91–97.

(243) Bakhmutsky, K.; Wieder, N. L.; Baldassare, T.; Smith, M. A.; Gorte, R. J. A thermodynamic study of the redox properties of supported Co particles. *Appl. Catal. A Gen.* **2011**, *397*, 266–271.

(244) Shi, D.; Arroyo-Ramírez, L.; Vohs, J. M. The use of bimetallics to control the selectivity for the upgrading of lignin-derived oxygenates: Reaction of anisole on Pt and PtZn catalysts. *J. Catal.* **2016**,

340, 219–226.

(245) Press, R. J.; Santhanam, K. S. V.; Miri, M. J.; Bailey, A. V.; Takacs, G. A. *Introduction to Hydrogen Technology*; Wiley, 2008.

(246) Armaroli, N.; Balzani, V. Solar Electricity and Solar Fuels: Status and Perspectives in the Context of the Energy Transition. *Chem. Eur. J.* **2016**, *22*, 32–57.

(247) Kudo, A.; Miseki, Y. Heterogeneous photocatalyst materials for water splitting. *Chem. Soc. Rev.* **2009**, *38*, 253–278.

(248) Zaleska, A. Doped-TiO_2: A Review. *Recent Patents Eng.* **2008**, *2*, 157–164.

(249) Tanaka, A.; Sakaguchi, S.; Hashimoto, K.; Kominami, H. Preparation of Au/TiO_2 with Metal Cocatalysts Exhibiting Strong Surface Plasmon Resonance Effective for Photoinduced Hydrogen Formation under Irradiation of Visible Light. *ACS Catal.* **2013**, *3*, 79–85.

(250) Chen, X.; Liu, L.; Yu, P. Y.; Mao, S. S. Increasing Solar Absorption for Photocatalysis with Black Hydrogenated Titanium Dioxide Nanocrystals. *Science* **2011**, *331*, 746–750.

(251) Zhang, X.; Peng, T.; Song, S. Recent advances in dye-sensitized semiconductor systems for photocatalytic hydrogen production. *J. Mater. Chem. A* **2016**, *4*, 2365–2402.

(252) Chen, X.; Shen, S.; Guo, L.; Mao, S. S. Semiconductor-based Photocatalytic Hydrogen Generation. *Chem. Rev.* **2010**, *110*, 6503–6570.

(253) Qureshi, M.; Takanabe, K. Insights on Measuring and Reporting Heterogeneous Photocatalysis: Efficiency Definitions and Setup Examples. *Chem. Mater.* **2017**, *29*, 158–167.

(254) Youngblood, W. J.; Lee, S.-H. A.; Kobayashi, Y.; Hernandez-Pagan, E. A.; Hoertz, P. G.; Moore, T. A.; Moore, A. L.; Gust, D.; Mallouk, T. E. Photoassisted Overall Water Splitting in a Visible Light-Absorbing Dye-Sensitized Photoelectrochemical Cell. *J. Am. Chem. Soc.* **2009**, *131*, 926–927.

(255) Abbotto, A.; Manfredi, N.; Marinzi, C.; De Angelis, F.; Mosconi, E.; Yum, J.-H.; Xianxi, Z.; Nazeeruddin, M. K.; Gratzel, M. Di-branched di-anchoring organic dyes for dye-sensitized solar cells. *Energy Environ. Sci.* **2009**, *2*, 1094–1101.

(256) Lin, R. Y.-Y.; Wu, F.-L.; Li, C.-T.; Chen, P.-Y.; Ho, K.-C.; Lin, J. T. High-Performance Aqueous/Organic Dye-Sensitized Solar Cells Based on Sensitizers Containing Triethylene Oxide Methyl Ether. *ChemSusChem* **2015**, *8*, 2503–2513.

(257) Lee, S.-H.; Park, Y.; Wee, K.-R.; Son, H.-J.; Cho, D. W.; Pac, C.; Choi, W.; Kang, S. O. Significance of Hydrophilic Characters of Organic Dyes in Visible-Light Hydrogen Generation Based on TiO_2. *Org. Lett.* **2010**, *12*, 460–463.

(258) Pescitelli, G.; Omar, O. H.; Operamolla, A.; Farinola, G. M.; Di Bari, L. Chiroptical Properties of Glucose-Substituted Poly(p-phenylene-ethynylene)s in Solution and Aggregate State. *Macromolecules* **2012**, *45*, 9626–9630.

(259) Haldon, E.; Nicasio, M. C.; Perez, P. J. Copper-catalysed azide-alkyne cycloadditions (CuAAC): an update. *Org. Biomol. Chem.* **2015**, *13*, 9528–9550.

(260) Chabre, Y. M.; Roy, R. Multivalent glycoconjugate syntheses and applications using aromatic scaffolds. *Chem. Soc. Rev.* **2013**, *42*, 4657–4708.

(261) Tornøe, C. W.; Christensen, C.; Meldal, M. Peptidotriazoles on Solid Phase: [1,2,3]-Triazoles by Regiospecific Copper(I)-Catalyzed 1,3-Dipolar Cycloadditions of Terminal Alkynes to Azides. *J. Org. Chem.* **2002**, *67*, 3057–3064.

(262) Manfredi, N.; Cecconi, B.; Calabrese, V.; Minotti, A.; Peri, F.; Ruffo, R.; Monai, M.; Romero-Ocana, I.; Montini, T.; Fornasiero, P.; Abbotto, A. Dye-sensitized photocatalytic hydrogen production: distinct

activity in a glucose derivative of a phenothiazine dye. *Chem. Commun.* **2016**.

(263) Romero Ocaña, I.; Beltram, A.; Delgado Jaén, J. J.; Adami, G.; Montini, T.; Fornasiero, P. Photocatalytic H_2 production by ethanol photodehydrogenation: Effect of anatase/brookite nanocomposites composition. *Inorganica Chim. Acta* **2015**, *431*, 197–205.

(264) Varma, A. J.; Kennedy, J. F.; Galgali, P. Synthetic polymers functionalized by carbohydrates: a review. *Carbohydr. Polym.* **2004**, *56*, 429–445.

(265) Li, J.; Grimsdale, A. C. Carbazole-based polymers for organic photovoltaic devices. *Chem. Soc. Rev.* **2010**, *39*, 2399–2410.

(266) Schmidt, A. W.; Reddy, K. R.; Knölker, H.-J. Occurrence, Biogenesis, and Synthesis of Biologically Active Carbazole Alkaloids. *Chem. Rev.* **2012**, *112*, 3193–3328.

(267) Manfredi, N.; Cecconi, B.; Abbotto, A. Multi-Branched Multi-Anchoring Metal-Free Dyes for Dye-Sensitized Solar Cells. *European J. Org. Chem.* **2014**, *2014*, 7069–7086.

(268) Chen, C.; Liao, J.-Y.; Chi, Z.; Xu, B.; Zhang, X.; Kuang, D.-B.; Zhang, Y.; Liu, S.; Xu, J. Metal-free organic dyes derived from triphenylethylene for dye-sensitized solar cells: tuning of the performance by phenothiazine and carbazole. *J. Mater. Chem.* **2012**, *22*, 8994–9005.

(269) Gupta, K. S. V; Suresh, T.; Singh, S. P.; Islam, A.; Han, L.; Chandrasekharam, M. Carbazole based A-π-D-π-A dyes with double electron acceptor for dye-sensitized solar cell. *Org. Electron.* **2014**, *15*, 266–275.

(270) Abe, R.; Shinmei, K.; Koumura, N.; Hara, K.; Ohtani, B. Visible-Light-Induced Water Splitting Based on Two-Step Photoexcitation between Dye-Sensitized Layered Niobate and Tungsten Oxide Photocatalysts in the Presence of a Triiodide/Iodide Shuttle Redox Mediator. *J. Am. Chem. Soc.* **2013**, *135*, 16872–16884.

(271) Sprick, R. S.; Bonillo, B.; Clowes, R.; Guiglion, P.; Brownbill, N. J.; Slater, B. J.; Blanc, F.; Zwijnenburg, M. A.; Adams, D. J.; Cooper, A. I. Visible-Light-Driven Hydrogen Evolution Using Planarized Conjugated Polymer Photocatalysts. *Angew. Chemie Int. Ed.* **2016**, *55*, 1792–1796.

(272) Su, C.; Tandiana, R.; Tian, B.; Sengupta, A.; Tang, W.; Su, J.; Loh, K. P. Visible-Light Photocatalysis of Aerobic Oxidation Reactions Using Carbazolic Conjugated Microporous Polymers. *ACS Catal.* **2016**, *6*, 3594–3599.

(273) McDowell, J. J. H. The crystal and molecular structure of phenothiazine. *Acta Crystallogr. Sect. B* **1976**, *32*, 5–10.

(274) *Comprehensive Heterocyclic Chemistry: Five-membered rings with two or more nitrogen atoms*; Katritzky, A. R., Ed.; Oxford, 1984.

(275) Grisorio, R.; De Marco, L.; Allegretta, G.; Giannuzzi, R.; Suranna, G. P.; Manca, M.; Mastrorilli, P.; Gigli, G. Anchoring stability and photovoltaic properties of new D(-π-A)$_2$ dyes for dye-sensitized solar cell applications. *Dyes Pigments* **2013**, *98*, 221–231.

(276) Tauc, J. Optical properties and electronic structure of amorphous Ge and Si. *Mater. Res. Bull.* **1968**, *3*, 37–46.

(277) *Dye-sensitized Solar Cells*; Kalyanasundaram, K., Ed.; CRC Press, 2010.

(278) Park, H.; Kim, H.; Moon, G.; Choi, W. Photoinduced charge transfer processes in solar photocatalysis based on modified TiO_2. *Energy Environ. Sci.* **2016**, *9*, 411–433.

(279) Zhang, G.; Kim, G.; Choi, W. Visible light driven photocatalysis mediated via ligand-to-metal charge transfer (LMCT): an alternative approach to solar activation of titania. *Energy Environ. Sci.* **2014**, *7*, 954–966.

(280) Hung, W.-I.; Liao, Y.-Y.; Hsu, C.-Y.; Chou, H.-H.; Lee, T.-H.; Kao, W.-S.; Lin, J. T. High-Performance Dye-

Sensitized Solar Cells Based on Phenothiazine Dyes Containing Double Anchors and Thiophene Spacers. *Chem. Asian J.* **2014**, *9*, 357–366.

(281) Al-Azri, Z. H. N.; Jovic, V.; Chen, W.-T.; Sun-Waterhouse, D.; Metson, J. B.; Waterhouse, G. I. N. Performance evaluation of Pd/TiO_2 and Pt/TiO_2 photocatalysts for hydrogen production from ethanol-water mixtures. *Int. J. Nanotechnol.* **2014**, *11*, 695–703.

(282) Caravaca, A.; Jones, W.; Hardacre, C.; Bowker, M. H_2 production by the photocatalytic reforming of cellulose and raw biomass using Ni, Pd, Pt and Au on titania. *Proc. Math. Phys. Eng. Sci.* **2016**, *472*, 20160054.

(283) Montini, T.; Gombac, V.; Sordelli, L.; Delgado, J. J.; Chen, X.; Adami, G.; Fornasiero, P. Nanostructured Cu/TiO_2 Photocatalysts for H_2 Production from Ethanol and Glycerol Aqueous Solutions. *ChemCatChem* **2011**, *3*, 574–577.

(284) Weissermel, K.; Arpe, H.-J. *Industrial Organic Chemistry*; 4th ed.; WILEY-VCH Verlag, 2003.

(285) Montini, T.; Monai, M.; Beltram, A.; Romero-Ocaña, I.; Fornasiero, P. H_2 production by photocatalytic reforming of oxygenated compounds using TiO_2-based materials. *Mater. Sci. Semicond. Process.* **2016**, *42*, 122–130.

(286) Li, X.; Cui, S.; Wang, D.; Zhou, Y.; Zhou, H.; Hu, Y.; Liu, J.; Long, Y.; Wu, W.; Hua, J.; Tian, H. New Organic Donor–Acceptor–π–Acceptor Sensitizers for Efficient Dye-Sensitized Solar Cells and Photocatalytic Hydrogen Evolution under Visible-Light Irradiation. *ChemSusChem* **2014**, *7*, 2879–2888.

(287) Dessi, A.; Calamante, M.; Mordini, A.; Peruzzini, M.; Sinicropi, A.; Basosi, R.; de Biani, F.; Taddei, M.; Colonna, D.; Di Carlo, A.; Reginato, G.; Zani, L. Organic dyes with intense light absorption especially suitable for application in thin-layer dye-sensitized solar cells. *Chem. Commun.* **2014**, *50*, 13952–13955.

(288) Kresse, G.; Hafner, J. Ab initio molecular dynamics for liquid metals. *Phys. Rev. B* **1993**, *47*, 558.

(289) Kresse, G.; Furthmüller, J. Efficiency of ab-initio total energy calculations for metals and semiconductors using a plane-wave basis set. *Comput. Mater. Sci.* **1996**, *6*, 15–50.

(290) Kresse, G.; Furthmüller, J. Efficient iterative schemes for ab initio total-energy calculations using a plane-wave basis set. *Phys. Rev. B* **1996**, *54*, 11169.

(291) Monkhorst, H. J.; Pack, J. D. Special points for Brillouin-zone integrations. *Phys. Rev. B* **1976**, *13*, 5188.

(292) Perdew, J. P.; Burke, K.; Ernzerhof, M. Generalized gradient approximation made simple. *Phys. Rev. Lett.* **1996**, *77*, 3865.

(293) Grimme, S.; Antony, J.; Ehrlich, S.; Krieg, H. A consistent and accurate ab initio parametrization of density functional dispersion correction (DFT-D) for the 94 elements H-Pu. *J. Chem. Phys.* **2010**, *132*, 154104.

(294) Henkelman, G.; Jonsson, H. Improved tangent estimate in the nudged elastic band method for finding minimum energy paths and saddle points. *J. Chem. Phys.* **2000**, *113*, 9978–9985.

(295) Henkelman, G.; Uberuaga, B. P.; Jónsson, H. A climbing image nudged elastic band method for finding saddle points and minimum energy paths. *J. Chem. Phys.* **2000**, *113*, 9901–9904.

(296) Sheppard, D.; Terrell, R.; Henkelman, G. Optimization methods for finding minimum energy paths. *J. Chem. Phys.* **2008**, *128*, 134106.

(297) Sheppard, D.; Henkelman, G. Paths to which the nudged elastic band converges. *J. Comput. Chem.* **2011**, *32*, 1769–1771.